Mechanisms for the Influence from Ice Nucleus Aerosols on Clouds and their Indirect Effects: Cloud Modelling

DEEPAK WAMAN
DEPARTMENT OF PHYSICAL GEOGRAPHY AND ECOSYSTEM SCIENCE | LUND UNIVERSITY

A significant amount of global precipitation is linked to the formation of ice particles in clouds. In addition, ice microphysical processes affect the Earth's radiation budget. The presence of ice in clouds is a culmination of many complex processes that are still poorly understood. The role of clouds containing ice on global radiation and hydrological budgets is highly uncertain.

In this thesis, the author examines the importance of various ice microphysical processes in mixed-phase clouds using numerical model simulations. It is found that the ice nucleation activity of various biological particles, as well as the time-dependent freezing of ice nucleating particles (INPs), have a minimal effect on the properties of mixed-phase clouds. For the first time, the relative importance of four secondary ice production mechanisms is investigated in various cloud types. Moreover, the thesis investigates how an increase in aerosols through anthropogenic activities leads to changes in cloud radiative properties. Also, this study newly discovered two new indirect effects arising from SIP and from time dependence of INP freezing.

Dr. Sachin G. Patade
(Researcher, INES, Lund University)

**Department of Physical Geography
and Ecosystem Science
Faculty of Science**

LUND
UNIVERSITY

MECHANISMS FOR THE INFLUENCE FROM ICE NUCLEUS AEROSOLS
ON CLOUDS AND THEIR INDIRECT EFFECTS: CLOUD MODELLING

Mechanisms for the Influence from Ice Nucleus Aerosols on Clouds and their Indirect Effects: Cloud Modelling

Deepak Waman

LUND
UNIVERSITY

Organization Lund University Faculty of Science Department of Physical Geography and Ecosystem Science Author: Deepak Meera Balasaheb Waman	Document name DOCTORAL DISSERTATION
	Date of issue 06 October 2023
	Sponsoring organization

Title and subtitle
Mechanisms for the Influence from Ice Nucleus Aerosols on Clouds and their Indirect Effects: Cloud Modelling

Abstract
The role of multiple groups of primary biological aerosol particles (PBAPs) as ice nucleating particles (INPs), and of ice formation processes such as time-dependent freezing of various INPs, and various secondary ice production (SIP) mechanisms in overall ice concentration has been evaluated in a range of cloud systems by simulating them numerically with the state-of-the-art 'Aerosol-Cloud' (AC) model in a 3D mesoscale domain. Also, the mechanisms of aerosol indirect effects (AIEs) arising from anthropogenic INPs, and the responses to these AIEs from time-dependent INP freezing and SIP processes are investigated in the simulated clouds. The cloud systems simulated with AC are: events of summertime deep convection observed over Oklahoma, USA during the Midlatitude Continental Convective Cloud Experiment (MC3E) in 2011 on 1) 11 May, and 2) 20 May, and wintertime 3) orographic clouds observed during the Atmospheric Radiation Measurement Cloud Aerosol Precipitation Experiment (ACAPEX) on 07 February 2015 over North California, and 4) supercooled layer clouds observed over Larkhill, UK, during the Aerosol Properties, Processes And Influences on the Earth's climate (APPRAISE) campaign on 18 February 2009.

AC uses the dynamical core of the Weather Research and Forecasting (WRF) model, modified Geophysical Fluid Dynamic Laboratory (GFDL) radiation scheme, and hybrid bin-bulk microphysics scheme. AC is validated adequately with the coincident aircraft, ground-based, and satellite observations for all four cases. AC forms secondary ice through the Hallett-Mossop (HM) process of rime-splintering, and fragmentation during ice-ice collisions, raindrop freezing, and sublimation of dendritic snow and graupel. A measure of SIP is defined using the term 'ice enhancement' (IE) ratio which is the ratio between the number concentration of total ice particles and active INPs at cloud tops.

For both cases in MC3E, overall, PBAPs have little effect (+1-6%) on the cloud-liquid (droplet mean sizes, number concentrations, and their water contents) properties, overall ice concentration, and on precipitation. AC predicts the activity of various INPs with an empirical parameterization (EP). The EP is modified to represent the time-dependent approach of INP freezing in light of our published laboratory observations. It is predicted that the time dependence of INP freezing is not the main cause for continuous ice nucleation and precipitation in all simulated cases. Rather, the main mechanism of precipitation formation is the combination of various SIP mechanisms (in convection) and recirculation-reactivation of dust particles (in APPRAISE layer cloud episode). Also, for all cases, the inclusion of time dependence of INP freezing causes little increase (about 10-20%) in the total ice concentration and ice from all SIP.

Regarding SIP, in young developing convective clouds of MC3E (11 May), with tops $> -15^{o}C$, the initial explosive growth is from the fast HM process, creating IE ratios as high as 10^3. By contrast, in mature convective clouds (tops $< -20^{o}C$), fragmentation in ice-ice collisions prevails, creating IE ratios of up to about 10^2-10^3. Regarding AIEs from INPs, increasing anthropogenic pollution is predicted to exert a net cooling in APPRAISE, and a strong net warming in MC3E (11 May). Furthermore, these net AIEs are mainly from glaciated clouds. Overall, the contribution to the AIEs from ice formation processes, such as time-dependent INP freezing and SIP, shows a high sensitivity with respect to anthropogenic INPs (about 20-60% increase in net AIEs).

Also, two new indirect effects associated with ice initiation mechanisms are proposed here. These are, 1) the 'SIP' indirect effect, and 2) the 'time-dependent INP' indirect effect. It is predicted that in APPRAISE and MC3E, both SIP and time-dependent INP indirect effects form less than 30%, and more than 50% of the net AIE, respectively.

Key words: Clouds, Ice Nucleating Particles, Primary ice, Secondary ice, Aerosol indirect effects, Cloud radiative effects, Aerosol-Cloud interactions, Cloud Resolving Model

Classification system and/or index terms (if any)		
Supplementary bibliographical information	Language English	
ISSN and key title	**ISBN** 978-91-89187-25-2 (print) 978-91-89187-26-9 (electronic)	
Recipient's notes	**Number of pages**	Price
	Security classification	

Signature   Date 06 October 2023

Mechanisms for the Influence from Ice Nucleus Aerosols on Clouds and their Indirect Effects: Cloud Modelling

Deepak Waman

To my beloved family…

निश्चयाचा महामेरू । बहुत जनासी आधारू ।
अखंडस्थितीचा निर्धारू । श्रीमंत योगी ॥

अनन्याश्चिन्तयन्तो मां ये जनाः पर्युपासते ।
तेषां नित्याभियुक्तानां योगक्षेमं वहाम्यहम् ॥ ९-२२ ॥

Ananyash Chintayanto Mam Ye Janah Paryupasate |
Tesham Nityabhiyuktanam Yoga-Kshemam Vahamyaham ||9–22||

"जे अनन्य प्रेमी दास मज परमेश्वराला निरंतर चिंतन करीत निष्काम भावाने भजतात, त्या नित्य माझे
चिंतन करणाऱ्यांचा योगक्षेम मी स्वतः त्यांना प्राप्त करून देतो. ॥ ९-२२ ॥"

"There are those who always think of Me and engage in exclusive devotion to Me. To
them, whose minds are always absorbed in Me, I provide what they lack and
preserve what they already possess. ||9-22||"

"वेडात जा पुढे तू, शोधीत मुक्त तारे।
पायाखालील काटे, होतील व्यर्थ सारे॥
फिकीर सोड आता, ऋतू कोणता लाभला।
सरेच देणे त्याचे, तू डाव फक्त मांडला॥
आता नको मशाल ती, चटक्यांची उगी सोबत।
मिणमिणती ती पणती, दूरून झोडी नौबत॥
स्पंदने अगणिक मनाचे, अव्यक्त आणि स्तब्ध।
आरक्त नयन आता, होतील तेच शब्द॥
खलात गुरफटले आयुष्य, उरले ना जरी काही।
धमन्यात रुधिर वाहते, दे झुगारून बेबंदशाही॥
असुदे आता कितीही, भयाण वादळवारा।
मस्तीत पुढे तू चाल, हो निढळ ध्रुवतारा॥"
                                                    …दीपक

Contents

List of Papers

Paper *1*

Patade, S., **Waman, D.**, Deshmukh, A., Gupta, A.K., Jadav, A., Phillips, V.T., Bansemer, A., Carlin, J. and Ryzhkov, A., 2022. The influence of multiple groups of biological ice nucleating particles on microphysical properties of mixed-phase clouds observed during MC3E. *Atmospheric Chemistry and Physics*, *22*(18), pp.12055-12075. https://doi.org/10.5194/acp-22-12055-2022.

Paper 2

Waman, D., Deshmukh, A., Jadav, A., Patade, S., Gautam, M., Phillips, V., Bansemer, A. and Jakobsson, J., 2023. Effects from time dependence of ice nucleus activity for contrasting cloud types. *Journal of the Atmospheric Sciences*. https://doi.org/10.1175/JAS-D-22-0187.1.

Paper 3

Waman, D., Patade, S., Jadav, A., Deshmukh, A., Gupta, A.K., Phillips, V.T., Bansemer, A. and DeMott, P.J., 2022. Dependencies of Four Mechanisms of Secondary Ice Production on Cloud-Top Temperature in a Continental Convective Storm. *Journal of the Atmospheric Sciences*, *79*(12), pp.3375-3404. https://doi.org/10.1175/JAS-D-21-0278.1.

Paper 4

Waman, D., Deshmukh, A., Jadav, A., Patade, S., Gautam, M., Phillips, V., 2023: Mechanisms for Indirect Effects from Solid Aerosol Particles on Continental Clouds and Radiation. *Manuscript submitted to the Journal of the Atmospheric Sciences*.

Author contributions

Paper 1

SP and VTJP designed and conceptualized this study. SP and **DW** set-up the simulation and performed the model validation. SP and **DW** processed the observational data from the aircraft and ground-based instruments. SP wrote the paper with contributions from the other authors. VTJP acquired the funding.

Paper 2

DW and VTJP conceptualized the study. **DW** with the help from VTJP and SP modified the model parameterization for heterogeneous ice initiation to represent time dependent approach of ice nucleus freezing. **DW** analyzed the aircraft data, set-up the model together with the other authors and carried out model simulations. **DW** wrote the paper with contributions from the other authors. VTJP acquired the funding.

Paper 3

DW conceptualized this study with guidance from VTJP. **DW** set-up and developed the model and carried out the model validation with the help from AJ and SP. **DW** analyzed the observational data from aircraft and ground-based instruments. **DW** wrote the paper with contributions from the other authors. VTJP acquired the funding.

Paper 4

DW designed and conceptualized this study with guidance from VTJP. **DW** developed the model and carried out simulations. **DW** drafted the manuscript and revised the manuscript with the help from the other authors. VTJP acquired the funding.

Popular Science Summary

This study on the ice phase of the clouds discovered that in continental conditions, the ice nucleating ability of groups of PBAPs is relatively weak compared to mineral dust and soot aerosols. The time-dependent freezing of available INPs is found to have a minimal impact on the overall ice concentration in the simulated cloud systems. Instead, a combination of various ice multiplication mechanisms plays a key role in the quasi-steady ice formation and precipitation over several hours in cloud systems that are convective. This study also revealed that in long-lived layer clouds, recirculation and subsequent reactivation of dust particles, rather than time-dependent INP freezing, is the main source for continuous ice nucleation and precipitation. Also, it is the coordinated combination of various SIP that accurately explains the observed discrepancy between the number concentrations of active INPs and total ice particles. Moreover, this study also explains the role of various SIP mechanisms in the observed dependency of ice enhancement ratio on cloud top temperature in the different stages of the convective clouds. Additionally, this study demonstrated that anthropogenically boosted solid APs can have a substantial impact on cloud micro- and macrophysical as well as radiative properties. The presence of extra INPs in the present-day conditions also causes perturbations in the processes of ice formation (SIP and time-dependent INP freezing), affecting the net solid aerosol indirect effects, mainly from glaciated clouds. This study also found that the indirect effects of solid aerosols are strongly dependent on the cloud system. For example, the inclusion of extra INPs predicts a net cooling of the climate system from supercooled stratiform clouds and strong warming from deep convective clouds.

Populärvetenskaplig sammanfattning

Denna studie om molnmikrofysik upptäckte att i kontinentala förhållanden är isnukleationsförmågan hos grupper av PBAPs relativt svag jämfört med mineraliskt damm och sotpartiklar. Den tidsberoende frysningen av tillgängliga INPs visade sig ha en minimal påverkan på den övergripande iskoncentrationen i de simulerade molnsystemen. Istället spelar en kombination av olika mekanismer för ismångfald en nyckelroll i den kvasi-stabila isbildningen och nederbörden under flera timmar i konvektiva molnsystem. Denna studie avslöjade också att i långlivade skiktmoln utan konvektion är recirkulation och efterföljande återaktivering av dammpartiklar, snarare än tidsberoende INP frysning, den huvudsakliga källan till kontinuerlig isnukleation och nederbörd. Dessutom är det den samordnade kombinationen av olika SIP mekanismer som noggrant förklarar den observerade avvikelsen mellan antalet aktiva INPs och totala ispartiklar. Vidare förklarar denna studie också rollen som olika SIP mekanismer spelar för den observerade beroendet av IE-förhållandet på molnens topptemperatur i olika stadier av konvektiva moln. Dessutom visade denna studie att antropogent förstärkta fasta AP:er kan ha en betydande påverkan på molnens mikro- och makrofysiska samt strålningsmässiga egenskaper. Förekomsten av extra INP:er under dagens förhållanden orsakar också störningar i processerna för isbildning (SIP och tidsberoende INP frysning), vilket påverkar de nettoindirekta effekterna från fasta aerosoler, främst från glaciärmoln. Denna studie fann också att de indirekta effekterna av fasta aerosoler är starkt beroende av molnsystemet. Till exempel förutsäger inkludering av extra INPs en nettoavkylning av klimatsystemet från underkylt skiktmoln och en kraftig uppvärmning från djupa konvektiva moln.

Acknowledgement

List of Figures

List of Tables

List of Abbreviations

2DC	2-Dimensional Cloud probe
2DS	2-Dimensional Spectrometer
AC	Aerosol-Cloud model
ACAPEX	Atmospheric Radiation Measurement Cloud Aerosol Precipitation Experiment
AIEs	Aerosol Indirect Effects
AMF2	ARM Facility 2
APs	Aerosol Particles
APPRAISE	Aerosol Properties, Processes And Influences on the Earth's climate
ARM	Atmospheric Radiation Measurement
CAPE	Convective Available Potential Energy
CCN	Cloud Condensation Nuclei
CDP	Cloud Droplet Probe
CF	Central Facility
CFARR	Chilbolton Facility for Atmospheric and Radio Research
CIP	Cloud Imaging Probe
CRE	Cloud Radiative Effect
CRM	Cloud Resolving Model
DMT	Droplet Measurement Technique
DoE	Department of Energy
EP	Empirical Parameterization
GFDL	Geophysical Fluid Dynamic Laboratory
GPM	Global Precipitation Measurement
HM	Hallett-Mossop
HVPS	High Volume Precipitation Spectrometer
HYSPLIT	Hybrid Single-Particle Lagrangian Integrated Trajectory
IE	Ice Enhancement
INPs	Ice Nucleating Particles
IWC	Ice Water Content
LCL	Lifting Condensation Level
LSF	Large Scale Forcing
LW	Longwave radiation
LWC	Liquid Water Content
MC3E	Midlatitude Continental Convective Cloud Experiment
MCS	Mesoscale Convective System
MSL	Mean Sea Level
NASA	National Aeronautics and Space Administration
NOAA	National Oceanic and Atmospheric Administration
NSF	National Science Foundation
PBAPs	Primary Biological Aerosol Particles

PBL	Planetary Boundary Layer
SGP	Southern Great Plains
SIP	Secondary Ice Production
SW	Shortwave radiation
UND	University of North Dakota
UTC	Coordinated Universal Time
WRF	Weather Research and Forecasting

List of Symbols

Symbol	Description	Unit
X	Aerosol species (X= dust, soot, soluble organic, fungi, pollen, bacteria, algae, detritus)	-
A_X	Proportionality constant for a power law dependence of temperature shift of time	$\text{Ks}^{-\beta}$
T	Temperature of ambient air	$^{\text{o}}$C
S_i	Saturation ratio of vapor with respect to (w. r. t.) ice	-
S_i^w	Value of S_i at water saturation	-
S_w	Saturation ratio of vapor w. r. t. (plane) water	-
s_w	Supersaturation of vapor w. r. t. water	%
s_i	Supersaturation of vapor w. r. t. ice ($s_i = 100 \times [S_i - 1]$)	%
D_X	Diameter of a given aerosol species	μm
H_X	Fraction reducing INP activity at warm T and low S_i for various groups of aerosols in X	-
n_i	Number mixing ratio (m. r.) of ice crystals generated from EP	kg^{-1}
$n_{IN,1,*}$	Background-tropospheric reference activity spectrum number m. r. for water saturation	kg^{-1}
$n_{IN,rain}$	Number m. r. of rain's activated INP	kg^{-1}
$n_{IN,X}$	Number m. r. of X INP species from the EP	kg^{-1}
n_X	Number m. r. of APs in group of X (not depleted by ice nucleation while inside the cloud)	kg^{-1}
$n_{X,a}$	Number of APs in X lost by ice nucleation	kg^{-1}
Q	Passive clock tracer	kg^{-1}
Q_0	Value of Q outside of the cold cloud	kg^{-1}
Q_r	Raindrop's mass m. r.	kg kg^{-1}
t	Time	s
t^*	t since the start of the isothermal phase of the laboratory experiment (Jakobsson et al., 2022)	s
w	Vertical velocity of air	m s^{-1}
z	Height	m
α_X	Fraction of $n_{IN,1,*}$ ($H_X = 1$) from INP activity of AP from X	-
β	Exponent in power-law dependence of temperature shift on time	-
Ω_X	Total surface area of all APs of diameters larger than 0.1 μm from X (not depleted by ice nucleation while inside the cloud)	(aerosol) m^2 (air) kg^{-1}
$\Omega_{X,1,*}$	Background tropospheric component of Ω_X for $0.1 \geq D_X \geq 1$ μm	(aerosol) m^2 (air) kg^{-1}
$\Omega_{X,rain}$	Total surface area of all APs bigger than 0.1 μm in group X immersed in liquid raindrops	(aerosol) m^2 (air) kg^{-1}
Δt	Model time step	s
ΔT_X	Shift in T in time-dependent approach of INP freezing	K
μ_X	Average number of activated ice embryos per AP in group X	-
$\xi(T)$	The function that varies between 0 and 1 for $-5 < T < -2^{\text{o}}$C	-
τ_Q	Relaxation time scale	s
v_t	Fall speeds of raindrops in each size bin	m s^{-1}
RH	Relative Humidity w. r. t. (plane) water	%
RH_i	Relative Humidity w. r. t. ice	%
$\tilde{n}_{IN,X}$	Modified $n_{IN,X}$ representing time dependent INP activity	kg^{-1}
$\tilde{n}_{IN,rain}$	Modified $n_{IN,rain}$ representing time dependent INP activity	kg^{-1}

Abstract

The role of multiple groups of primary biological aerosol particles (PBAPs) as ice nucleating particles (INPs), and of ice formation processes such as time-dependent freezing of various INPs, and various secondary ice production (SIP) mechanisms in overall ice concentration has been evaluated in a range of cloud systems by simulating them numerically with the state-of-the-art 'Aerosol-Cloud' (AC) model in a 3D mesoscale domain. Also, the mechanisms of aerosol indirect effects (AIEs) arising from anthropogenic INPs, and the responses to these AIEs from time-dependent INP freezing and SIP processes are investigated in the simulated clouds. The cloud systems simulated with AC are: events of summertime deep convection observed over Oklahoma, USA during the Midlatitude Continental Convective Cloud Experiment (MC3E) in 2011 on 1) 11 May, and 2) 20 May, and wintertime 3) orographic clouds observed during the Atmospheric Radiation Measurement Cloud Aerosol Precipitation Experiment (ACAPEX) on 07 February 2015 over North California, and 4) supercooled layer clouds observed over Larkhill, UK, during the Aerosol Properties, Processes And Influences on the Earth's climate (APPRAISE) campaign on 18 February 2009.

AC uses the dynamical core of the Weather Research and Forecasting (WRF) model, modified Geophysical Fluid Dynamic Laboratory (GFDL) radiation scheme, and hybrid bin-bulk microphysics scheme. AC is validated adequately with the coincident aircraft, ground-based, and satellite observations for all four cases. AC forms secondary ice through the Hallett-Mossop (HM) process of rime-splintering, and fragmentation during ice-ice collisions, raindrop freezing, and sublimation of dendritic snow and graupel. A measure of SIP is defined using the term 'ice enhancement' (IE) ratio which is the ratio between the number concentration of total ice particles and active INPs at cloud tops.

For both cases in MC3E, overall, PBAPs have little effect (+1-6%) on the cloud-liquid (droplet mean sizes, number concentrations, and their water contents) properties, overall ice concentration, and on precipitation. AC predicts the activity of various INPs with an empirical parameterization (EP). The EP is modified to represent the time-dependent approach of INP freezing in light of our published laboratory observations. It is predicted that the time dependence of INP freezing is not the main cause for continuous ice nucleation and precipitation in all simulated cases. Rather, the main mechanism of precipitation formation is the combination of various SIP mechanisms (in convection) and recirculation-reactivation of dust particles (in APPRAISE layer cloud episode). Also, for all cases, the inclusion of time dependence of INP freezing causes little increase (about 10-20%) in the total ice concentration and ice from all SIP.

Regarding SIP, in young developing convective clouds of MC3E (11 May), with tops $> -15^{\circ}$C, the initial explosive growth is from the fast HM process, creating IE ratios as high as 10^3. By contrast, in mature convective clouds (tops $< -20^{\circ}$C), fragmentation in ice-ice collisions prevails, creating IE ratios of up to about 10^2-10^3. Regarding AIEs from INPs, increasing anthropogenic pollution is predicted to exert a net cooling in APPRAISE, and a strong net warming in MC3E (11 May). Furthermore, these net AIEs are mainly from glaciated clouds. Overall, the contribution to the AIEs from ice formation processes, such as time-dependent INP freezing and SIP, shows a high sensitivity with respect to anthropogenic INPs (about 20-60% increase in net AIEs).

Also, two new indirect effects associated with ice initiation mechanisms are proposed here. These are, 1) the 'SIP' indirect effect, and 2) the 'time-dependent INP' indirect effect. It is predicted that in APPRAISE and MC3E, both SIP and time-dependent INP indirect effects form less than 30%, and more than 50% of the net AIE, respectively.

1. Introduction

1.1 Importance of Clouds: Weather and Climate Perspective

Clouds are one of the influential manifestations of nature. A cloud is composed of hydrometeors that can exist in either the liquid or solid (ice) phase. Cloud hydrometeors form when water vapor condenses on the aerosol particles (APs). APs are small particles (diameters between 0.5 nm and 10 μm) suspended in the atmosphere such as ammonium sulfate, sea salt, black carbon (soot), soluble and insoluble organics, and biological particles (Lohmann et al., 2016; Warneck, 1999). Clouds can be observed in different sizes and shapes. There are different types of clouds, namely, 1) cirrus clouds which are generally composed of ice-crystals and have a feathery, hair-like appearance at high altitudes, 2) cumulus clouds, appearing as fluffy, cauliflower-shaped formations occasionally associated with precipitation, 3) nimbostratus clouds which are low or mid-level rain-bearing clouds characterized by their dark or grey appearance.

Clouds and the associated rainfall are the most important yet least understood components of the climate system (Boucher et al., 2013). Clouds cover about half of the globe (Flossmann, 1998; Liou, 2002; Boucher et al., 2013; King et al. 2013) and are considered one of the most crucial elements of Earth's energy budget, reflecting about 15% of the incident solar radiation to space (Boucher et al., 2013). Clouds control the amount of incoming shortwave (SW) and outgoing longwave (LW) radiation, thereby regulating the earth's temperature, driving the global hydrological cycle, and serving as a source/sink for atmospheric pollutants through precipitation (Hartmann et al., 1992; Flossmann, 1998; Houghton et al., 2001; Ramanathan et al., 2001; Lohmann, 2006; Boucher et al., 2013; Ervens, 2015; Kudzotsa et al., 2016; Ryu and Min, 2022).

Cloud formation in the atmosphere occurs when an air parcel becomes saturated with respect to water/ice. This typically takes place during the ascent of the air parcel caused by various mechanisms. These mechanisms are:

1) *Orographic lifting,*
2) *lifting along frontal boundaries,*
3) *surface-air convergence, and*
4) *surface heating and free convection.*

Also, depending on the presence of hydrometeors and their top temperature, clouds can be classified as:

i.   *liquid* clouds are characterized by warmer tops (> 0ºC) and consists of only liquid particles. These clouds are also known as *warm* clouds.

ii. *Mixed-phase* clouds consist of both liquid and ice particles and their tops can extend up to the −36ºC level, and

iii. *Ice-only* clouds form at levels colder than the −36ºC and consist of only ice particles. They can also form at temperatures as warm as 0ºC, provided that the ascent is weak enough (e.g., Westbrook and Illingworth, 2013 [hereafter 'WI13']).

Initiation of cloud hydrometeors occurs through processes known as *homogeneous* and *heterogeneous* nucleation. However, the homogeneous nucleation of cloud droplets from vapor is not feasible, as the supersaturation with respect to liquid water (s_w) usually does not exceed 10% (Lohmann et al., 2016). By contrast, heterogeneous nucleation of cloud droplets occurs at levels warmer than the −36ºC and in the presence of soluble aerosol particles (diameters about 1 µm) such as ammonium sulfate, sea salt, and soluble organics, depending on s_w. These APs are referred to as cloud condensation nuclei (CCN) (Rogers and Yau, 1996; Lohmann et al., 2016; Flossmann et al., 2018). Typically, CCN concentrations over continents and oceans are on the order of about 10^3 and 10^2 cm^{-3}, respectively (Hobbs and Radke, 1969; Pruppacher and Klett, 1997).

Once a cloud grows above the freezing level (< 0ºC), it may contain both cloud droplets and ice crystals. Mechanisms of ice initiation are fundamental for the climate, as most of the global precipitation is chiefly associated with the ice phase (Lau and Wu, 2003; Lohmann, 2006; Field and Heymsfield 2015). Yet, these mechanisms are uncertain (Cantrell and Heymsfield, 2005; Field et al., 2017). The initiation of ice crystals in the clouds at subzero levels is described below.

1.1.1   Ice Initiation in Clouds

Two phase transitions can initiate ice at subzero levels (Rogers and Yau, 1996; Pruppacher and Klett, 1997). These are briefly described here.

1.1.1.1 Homogeneous Ice Nucleation

In *homogeneous* nucleation (Fig. 1a), an ice crystal forms from the freezing of supercooled liquid droplets without any aerosol activity under sufficiently high supersaturation with respect to ice (s_i) (Rogers and Yau, 1996; Pruppacher and Klett, 1997; Murray et al., 2010). Homogeneous ice nucleation occurs at levels

colder than -36ºC, where a chance collision of vapor molecules leads to the formation of a stable ice embryo. An ice crystal can be formed homogeneously through two types.

The first type involves ice initiation through the spontaneous freezing of supercooled cloud drops/raindrops, and APs at temperatures colder than -36ºC, depending on droplet size. The second type of homogeneous ice nucleation is the homogeneous freezing of solution droplets, which occurs at colder temperatures as soon as s_i exceeds the critical supersaturation (Koop et al., 2000; Phillips et al., 2007). Homogeneous freezing of cloud droplets/raindrops and solution droplets mainly occurs in deep convective and cirrus clouds, respectively.
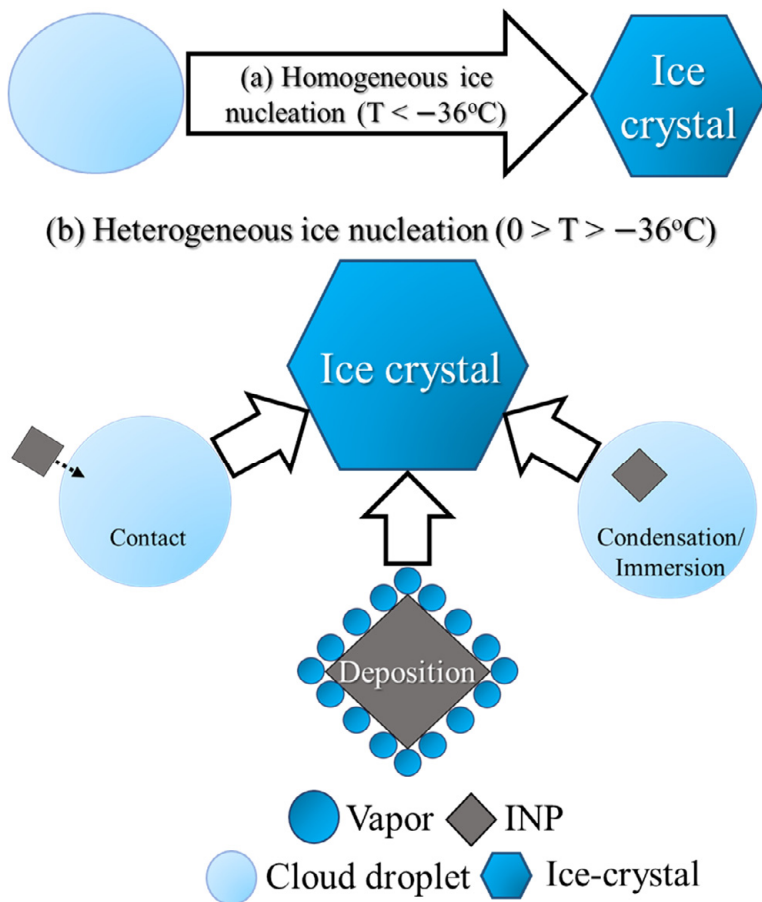
Figure 1. Schematic representation of (a) the homogeneous and (b) various modes of heterogeneous ice nucleation processes.

1.1.1.2 Heterogeneous Ice Nucleation

Heterogeneous ice nucleation involves the formation of an ice crystal due to the activity of solid APs at subzero levels (DeMott, 1990; Rogers and Yau, 1996; Phillips et al., 2008; Murray et al., 2010, 2012; Kanji et al., 2017). These solid APs are commonly referred to as ice nucleating particles (INPs) and are relatively rare in the atmosphere, with typical concentrations between 10^{-5} and 1 L^{-1} at temperatures near $-10^{\circ}C$ (DeMott et al., 2003; Lasher-Trapp et al., 2016). Active sites on the surface of such INPs are required for ice nucleation to occur at temperatures warmer than $-36^{\circ}C$. They are scarce and efficiently absorb water molecules, thus reducing the energy barrier for the formation of ice embryos.

There is a wide variety of sources of INPs in the atmosphere, both natural and anthropogenic. Natural sources include deserts, oceans, volcanic eruptions, and the emission of vegetation debris. Similarly, anthropogenic sources are biomass burning, deforestation, and industrial activities (Kanji et al., 2017). A range of solid APs originating from these sources such as dust (mineral and soil), insoluble organics, soot, and primary biological aerosol particles (PBAPs), which include pollen, bacteria, detritus, algae, fungi, and plant fragments, phytoplankton, lichens may initiate primary ice by acting as INPs (Hobbs and Locatelli, 1969; DeMott, 1990; Phillips et al., 2009, 2013; Kanji et al., 2017; Flossmann et al., 2018; Patade et al., 2021). The chemical composition and concentrations of INPs vary significantly across the globe, and they can significantly alter the microphysical and radiative properties of clouds (Phillips et al., 2003; Cantrell and Heymsfield, 2005; Lohmann 2006; Kudzotsa et al., 2016).

Various heterogeneous nucleation processes (Fig. 1b) can lead to the formation of the first ice crystal above the freezing level (Vali, 1985; DeMott et al., 1983; Pruppacher and Klett, 1997; Lohmann, 2006). These processes include:

i. *Deposition ice nucleation* (Fig. 1b) occurs in an environment supersaturated with respect to ice. In this mode of ice nucleation, water vapor taken up by the INP surfaces can directly transform into an ice phase without any intermediate liquid phase (Kanji et al., 2017). This requires a relative humidity with respect to ice (RH_i) exceeding 100% in the ambient air. Deposition nucleation could be significant in high-level clouds (e.g., cirrus) (Cziczo et al., 2013). However, in mixed-phase clouds, this mode of ice nucleation is less significant as the INPs are first expected to be activated as cloud droplets (Ansmann et al., 2008; Field et al., 2006).

ii. *Contact freezing* in which the ice particle forms upon contact between an active INP and a supercooled droplet (Fig. 1b). There are two ways by which the ice can be nucleated through contact freezing, 1) 'outside-in' in which the INP outside of the droplet collides with it, and 2) the freezing of a droplet occurs when a pre-existing INP touches the droplet surface from within the droplet (Shaw et al., 2005; Fornea et al., 2009).

iii.   *Condensation/Immersion freezing* involves an INP becoming immersed in a cloud droplet, typically at warmer temperatures (> 0°C), and then initiating the ice phase once the droplet reaches subzero levels (Fig. 1b).

In mixed-phase clouds, heterogeneous ice nucleation mainly occurs through deposition, condensation, and immersion freezing while contact nucleation makes a minimal contribution to the total heterogeneous ice formed (Phillips et al., 2007; Ansmann et al., 2008; WI13).

The ice nucleation ability of all INPs varies significantly depending on their type and concentration in the environment. Mineral dust is generally considered the most important type of INP, and its ice nucleation onset can occur at subzero temperatures as warm as −10°C (Hoose and Möhler, 2012; Phillips et al., 2013; Kanji et al., 2017). Furthermore, the activity of dust INPs increases with increasing surface area (Phillips et al., 2008; Kanji et al., 2017).

PBAPs, emitted from land vegetation and oceans (Després et al., 2012), initiate ice at temperatures as warm as −2°C (Patade et al., 2021). Additionally, incomplete combustion of fossil fuels can produce soot, which can also play an important role in ice formation. However, it has been argued that soot is not a significant contributor to heterogeneous ice formation, especially from freshly emitted fossil fuel combustion (Koehler et al., 2009; Bond et al., 2013). Moreover, a modelling study by Schill et al. (2020) demonstrated that soot, from biomass burning, is a minor contributor to INP on the global scale. By contrast, a strong correlation was observed between soot concentrations and in-cloud ice concentrations for thin wave clouds over Wyoming, which were affected by biomass burning (Twohy et al., 2010).

Several previous studies have proposed that the heterogeneous ice nucleation can be: 1) time-independent and, 2) time-dependent in nature (Levine, 1950; Langham and Mason, 1958; Vali and Stansbury, 1966; Vonnegut and Baldwin, 1984; Vali, 1994, 2008; Jakobsson et al., 2022 [hereafter 'JK22']). These are described below.

Time Independent Heterogeneous Ice Nucleation

The time-independent approach of INP activation assumes that ice nucleation is an instantaneous process and occurs at deterministic temperatures at specific 'active' sites (Vali 1994, 2008), resulting in identical INPs nucleating all together. These active sites are characterized by the lowest particle-ice interfacial energy and hence activation takes place at higher temperatures almost instantaneously (Niedermeier et al., 2011). Under isothermal conditions, this hypothesis assumes no time dependence, and any INP activation occurs at the onset of the nucleation (Chen et al., 2008).

Time Dependent Heterogeneous Ice Nucleation

At levels warmer than -36°C, the drops may contain different types of impurities (APs), and the freezing probability of such drops may vary (Vali and Stansbury, 1966), as later observed experimentally by (Vonnegut and Baldwin, 1984). At a given temperature the freezing probability depends on the surface area of the INP and the time for which an INP remains in the favorable environment (Chen et al., 2008; Murray et al., 2012).

Welti et al. (2012) observed that the immersion freezing mode of INP activation exhibits time dependence, which is the basis for WI13 to propose the time dependence of INP freezing being the main source for continuous ice nucleation and precipitation in supercooled stratiform clouds. However, their hypothesis was not supported by any modelling evidence, and the relative importance of the time dependence of INP freezing is not yet well understood. Vali (2014) assessed various laboratory studies and concluded that the time-dependent approach of INP freezing is less important and it can be neglected from numerical models, especially for systems with high cooling rates (about 1-2 K min^{-1}) corresponding to ascent speeds up to about 3 m s^{-1} (Kanji et al., 2017). Nevertheless, this was not conclusively verified with modelling simulations.

1.1.2   Ice Multiplication in Clouds

Previous aircraft studies of natural convective clouds with tops warmer than -36°C (Mossop, 1985; Hobbs et al., 1980; Harris-Hobbs and Cooper, 1987; Cantrell and Heymsfield, 2005) have observed that the number concentrations of ice particles often exceed the number concentrations of INPs by about 10^2 to 10^4 orders of magnitude. It is further observed that the discrepancy in the observed number concentrations of INPs and ice particles remains (Ladino et al., 2017) even with the processing algorithms (Field et al., 2006) and modified optical probes (Korolev et al., 2011) that eliminates possible biases caused by artificial shattering (Field et al., 2017).

Therefore, it has long been proposed that, following initial primary ice nucleation, some mechanisms must exist at subzero temperatures ($> -36^{\circ}$C) that can enhance the number concentrations of ice particles. These mechanisms are known as ice multiplication or secondary ice production (SIP) mechanisms (Hobbs, 1969; Hallett and Mossop, 1974 [hereafter 'HM']; Vardiman, 1978; Oraltay and Hallett, 1989; Takahashi et al., 1995; Lohmann et al., 2016; Phillips et al., 2017a; Miltenberger et al., 2020, 2021; Deshmukh et al., 2022). SIP processes form new ice particles in the presence of pre-existing (primary) ice without requiring the activity of INPs (or homogeneous freezing) (Field et al., 2017) under suitable conditions. Furthermore, the SIP processes must involve precipitation, since wave clouds (e.g., Eidhammer

et al., 2010) and layer clouds (WI13) too thin to precipitate are seen to have little ice enhancement.

The degree of enhancement in the number concentrations of ice particles due to ice multiplication can be defined using the term called '*ice enhancement*' (IE) ratio. This ratio represents the average number concentrations of ice particles to the number concentrations of active INPs at any in-cloud level (Hobbs et al., 1980; Pruppacher and Klett, 1997). There is a range of possible SIP processes proposed so far that depends on temperature, vertical velocity, and particle size distributions, these are:

1.1.2.1 The Hallett-Mossop process of Rime-splintering

The HM process of rime-splintering is an important ice multiplication process in mixed-phase clouds and is the most studied SIP process among all SIP mechanisms known so far. HM (1974) observed that during the riming of supercooled cloud drops (diameters > 24 µm), numerous ice splinters break away for temperatures between −3 and −8°C. The rate of splinter production during riming of a supercooled drop is maximum at about −5°C and for an updraft speed of about 2.7 m s^{-1} (HM 1974, their Fig. 2).

The HM process is temperature-dependent because at subzero temperatures warmer than −3°C, supercooled droplets do not form an ice shell while at temperatures colder than −8°C, ice particle growth becomes rapid and hence the internal pressure is not sufficient to break the ice shells (Griggs and Choularton 1983; Mason 1996). According to the theory proposed by Griggs and Choularton (1983), between −3 and −8°C, pressure built up inside the freezing droplet during its accretion on a large ice particle. This pressure is later released by a crack in the outer frozen shell, releasing an unfrozen freezing liquid that eventually freezes and forms secondary ice.

The HM process is widely studied, evident with both observational and experimental (Harris-Hobbs and Cooper, 1987; Blyth and Latham 1993; Rangno and Hobbs 2001; Crosier et al., 2011 [hereafter 'C11']; Heymsfield and Willys 2014; Patade et al., 2016) and modelling studies (Phillips et al., 2003, 2005; Huang et al., 2017; Miltenberger et al., 2020, 2021; Lasher-Trapp et al., 2021; Gayatri et al., 2022; Waman et al., 2022, 2023a [hereafter 'Wa22' and 'Wa23a']) (Fig. 2). Furthermore, several numerical modelling studies have shown that the HM process and raindrop freezing fragmentation (Sec. 1.1.2.3) dominates the overall ice concentrations typically in young convective clouds with tops warmer than −20°C, creating IE ratios as high as 10^3 (Wa22; Wa23a) in such clouds. However, a recent laboratory study by Hartmann et al. (2023) found no substantial activity of SIP via the HM process.

Apart from the HM process, many alternative ice multiplication mechanisms must exist in clouds that can cause explosive growth of ice crystal concentrations, typically at levels colder than -8°C. These mechanisms are discussed below.

1.1.2.2 Fragmentation during Ice-Ice Collisions

Langmuir (1948) proposed that SIP may occur during the collision between ice particles. This hypothesis was later verified by several field and laboratory studies (Hobbs and Farber 1972; Vardiman 1978; Takahashi et al., 1995, reviewed by Phillips et al., 2017a, b). Production of ice-crystal splinters during ice-ice collisions depends on ambient temperature with a maximum at about -15°C (Takahashi et al., 1995). This can be mainly attributed to the formation of fragile, vapor-grown branches on rimed ice particles in the dendritic regimes.

Fragmentation in ice-ice collisions was also studied theoretically by Hobbs and Farber (1972), Yano and Phillips (2011), Yano et al. (2016), and Phillips et al. (2017a, b). A theoretical formulation proposed by Phillips et al. (2017a) is based on the principle of energy conservation. The formation of secondary fragments during ice-ice collisions depends on the sizes and relative fall velocities of the colliding ice particles, ambient temperature, and riming intensity of ice particles (Korolev and Leisner 2020). Several modelling studies (Fridlind et al., 2017; Sotiropoulou et al., 2021; Zhao et al., 2021; Patade et al., 2022; Wa22; Wa23a) found that fragmentation in ice-ice collisions is a prolific SIP mechanism in the simulated cloud systems (Fig. 2).

The HM process is predicted to prevail in relatively young clouds (tops warmer than -15°C). By contrast, fragmentation in ice-ice collisions prevails at longer times in clouds causing an explosive growth of ice crystal numbers (IE ratios $\sim 10^{3}$-10^{4}) in their mature stage (Yano and Phillips, 2011; Wa22; Wa23a).

1.1.2.3 Fragmentation during Raindrop Freezing

SIP may also occur during the shattering of freezing drizzle or raindrops. Several laboratory studies (Johanson and Hallett 1968; Takahashi and Yamashita 1969, 1970; Pruppacher and Schlamp 1975; Leisner et al., 2014; Wildeman et al., 2017; Keinert et al., 2020) and aircraft observations (Rangno 2008; Lawson et al., 2015; Korolev et al., 2020) have observed fragmentation during droplet freezing (Fig. 2). During raindrop freezing, liquid may get trapped inside an ice shell which may break once the excess pressure built up during freezing exceeds the threshold value, emitting spikes and fragments of secondary ice.

Based on published laboratory observations of drops in free-fall, Phillips et al. (2018) proposed an empirical formulation of SIP during raindrop freezing. They proposed two modes of fragmentation during raindrop freezing. The first mode involves fragmentation during freezing of spherical (0.05-5 mm) drizzles or raindrops. In this mode, the collision of a supercooled drop with a less massive ice

particle initiates quasi-spherical freezing of a drop, which can also be seen during the heterogeneous freezing of raindrops (due to immersed INP). During freezing, the outer ice shell may eventually break, generating fragments of secondary ice. The second mode involves non-spherical freezing when a supercooled raindrop collides with a more massive ice particle, which emits a secondary splash of droplets that eventually freeze to form secondary ice (Phillips et al., 2018; James et al., 2021). Fragmentation during raindrop freezing depends on the ambient temperature and the sizes of colliding hydrometeors.

1.1.2.4 Fragmentation during Sublimation

Another possible source of SIP is fragmentation during the sublimation of ice particles, such as dendritic snow and graupel, in subsaturated cloudy regions, as evident in laboratory studies (Fig. 2) by Oraltay and Hallett (1989), Dong et al. (1994), and Bacon et al. (1998) (Table 1). Oraltay and Hallett (1989) observed that the dendritic ice crystal partially sublimates and generates secondary ice splinters when RH_i is below 70%. These laboratory studies were the basis for Deshmukh et al. (2022) to propose a formulation for fragmentation during the sublimation of dendritic snow and graupel.

Fragmentation during sublimation depends upon particle size and shape, fall velocity, ambient air temperature, and RH_i (Deshmukh et al., 2022) and can be significant in deep convective descents ($w < -2$ m s^{-1}) (Deshmukh et al., 2022; Wa22) creating IE ratios of about 10.

Table 1. Summary of the laboratory studies of SIP during sublimation of ice particles.

Study	T (ºC)	RH_i (%)	Ventilation speed (m s^{-1})	Particle habits
Oraltay and Hallett 1989	−17 to −15	<70	0.1 to 0.2	Dendrites
Dong et al., 1994	−18 to −5	50 to 90	about 1	Rimed ice and needles
Bacon et al., 1998	−30 to 0	85 to 100	-	All ice particles

Apart from these four processes (Sec. 1.1.2) of SIP, two more ice multiplication mechanisms were proposed (Korolev and Leisner, 2020) that are thought to produce secondary ice in clouds. These are,

i.   the activation of pre-existing INPs in the transient supersaturation of falling droplets (Chouippe et al., 2019; Prabhakaran et al., 2019, 2020), and

ii. fragmentation due to thermal shock at the droplet-ice particle interface cause to the release of latent heat during droplet freezing (Dye and Hobbs 1968). The breakup of an ice crystal may also occur without any change in the freezing drop or when the drop is cracked.

Regarding (i), there are reasons to doubt it being prolific, since as soon as the humidity goes well above water saturation any solid INP activates as a cloud droplet, with any subsequent freezing being temperature-dependent and independent of

ambient humidity. Arguably regarding (ii), this mechanism is already active in observed raindrop-freezing in lab experiments of drops in free-fall, since many of these used a cloud of ice crystals in the cloud chamber to induce freezing by collision with the supercooled drops. Hence it is already treated in the scheme by Phillips et al. (2018).

Aircraft*/modelling+ studies of SIP processes

The HM process of rime-splintering
- Hallett et al. (1978*) CC
- Hobbs et al. (1980*) CC
- Phillips et al. (2001+) M-P
- Phillips et al. (2003+) DCC
- Phillips et al. (2005+) DCC
- Phillips et al. (2007+) DCC
- Crosier et al. (2011*) SLC
- Yang et al. (2014*) NStC
- Patade et al. (2016+) M-P
- Gayatri et al. (2016+) M-P
- Huang et al. (2017*) SC
- Young et al. (2019+) AnSt
- Yang et al. (2020*+) MM-P
- Miltenberger et al. (2020+, 2021+) M-P
- Sotiropoulou et al. (2020+, 2021+) AcSt
- Waman et al. (2022+) DCC
- Patade et al. (2022+) DCC
- Waman et al. (2023+) OC

Fragmentation in ice-ice collisions
- Hobbs et al. (1980*) CC
- Yang et al. (2014*) NStC
- Young et al. (2019+) AnSt
- Fridlind et al. (2017+) DCC
- Phillips et al. (2017b+) DCC
- Sotiropoulou et al. (2020+, 2021+) AcSt
- Georgakaki et al. (2022+) OC
- Waman et al. (2022+) DCC
- Patade et al. (2022+) DCC
- Waman et al. (2023+) OC SLC

Fragmentation in raindrop freezing
- Yang et al. (2014*) NStC
- Lawson et al. (2018*) TMC
- Phillips et al. (2018+) DCC
- Yang et al. (2019*+) MM-P
- Zhao et al. (2021+) AcM-P
- Waman et al. (2022+) DCC
- Patade et al. (2022+) DCC

Fragmentation in sublimation
- Waman et al. (2022+, 2023+) DCC SLC OC
- Patade et al. (2022+) DCC
- Deshmukh et al. (2021+) DCC

Figure 2. Flowchart showing the aircraft (asterisks) and modelling (plus) evidence of SIP processes active in various cloud systems such as convective clouds (**CC**), supercooled layer clouds (**SLC**), nimbostratus clouds (**NStC**), mixed-phase clouds (**M-P**), shallow cumulus (**SC**), Antarctic stratocumulus (**AnSt**), Arctic stratocumulus (**AcSt**), deep convective clouds (**DCC**), orographic clouds (**OC**), tropical marine cumulus (**TMC**), maritime mixed-phase (**MM-P**), and Arctic mixed-phase clouds (**AcM-P**).

Figure 2 summarizes aircraft and modeling evidence of SIP processes that are found to be active in different cloud systems.

1.1.3   Processes of Precipitation Formation

The microphysical processes of clouds can greatly affect precipitation (Takahashi and Kawano 1998; Grabowski et al., 1999) which is an important component of the global hydrological cycle (Field and Heymsfield 2015). Precipitation formation mainly occurs through two distinct processes (Rogers and Yau 1996; Rauber et al., 2000). These are, 1) the *warm rain*, and 2) the *ice crystal* process. Both of these processes can co-exist and are briefly described here.

1.1.3.1 Warm-rain (Collision-Coalescence) Process

Once nucleated, a droplet can grow by diffusion of water molecules from the vapor onto its surface, which can only grow cloud droplets up to a few micrometers in size (Rogers and Yau, 1996). Hence, condensation alone cannot grow cloud droplets to a precipitable size. The mechanism responsible for precipitation formation in warm clouds is known as the *collision-coalescence*, or *warm-rain* process (Gao et al., 2021). In this process, cloud droplets of different sizes collide and stick together and form larger drops of precipitation size which may fall with higher terminal velocity collecting more and more cloud droplets serving positive feedback of collision-coalescence whereas droplet breakup limits the growth of droplets.

Typically, a warm-based cloud (> 10ºC) of about 2-3 km depth has sufficient updrafts, liquid water, and a lifetime to sustain collision-coalescence growth. The warm rain process occurs in both shallow and deep convective clouds. In thunderstorm and mesoscale convective systems (MCS), the warm rain process is the source of condensed water (cloud droplets) to precipitable water (drizzle and raindrops) (Gao et al., 2021). The warm-rain process can be significant in tropics and subtropics for shallow clouds (Lau and Wu, 2003; Field and Heymsfield 2015) and is greatly affected by loadings and properties of APs (Dagan et al., 2015).

1.1.3.2 Ice crystal Process

Another mode of precipitation formation associated with cold clouds is the '*ice crystal*' process in which ice crystals formed during nucleation grow to form snow following vapor diffusion or aggregation. Aggregation involves the collection of ice crystals. It is dominant at dendritic levels (-12 to -17ºC), where particles are stickiest (Rogers and Yau, 1996; Phillips et al., 2015). Snow formed during vapor diffusion or aggregation may rime to form graupel which may subsequently melt to form 'cold' rain (Rogers and Yau 1996). Prolonged riming of ice crystals can result in hail formation. The ice crystal process of precipitation can significantly

contribute to surface precipitation globally (Field and Heymsfield 2015), especially in the tropics and midlatitudes (Lau and Wu 2003).

Furthermore, in mixed-phase clouds, snow may form through the Bergeron-Findeisen process. This is a special type of ice crystal process involving the evaporation of supercooled cloud liquid and is chiefly active in mixed-phase clouds, where supercooled liquid and ice coexist. In such clouds, saturation vapor pressure over supercooled liquid is higher than that over ice. This variation in saturation vapor pressures between liquid and ice leads to the growth of ice crystals at the expense of supercooled droplets.

Figure 3 shows a schematic of a convective cloud in its mature stage (top colder than $-36^{\circ}C$), summarizing the microphysical processes described in Sec. 1.1.1-1.1.3. It shows the droplet activation through heterogeneous nucleation of soluble APs at levels near cloud-base, heterogeneous (0 to $-36^{\circ}C$) and homogeneous ice nucleation ($< -36^{\circ}C$), possible SIP processes, and the warm rain and ice crystal processes of precipitation formation active in such convective clouds.
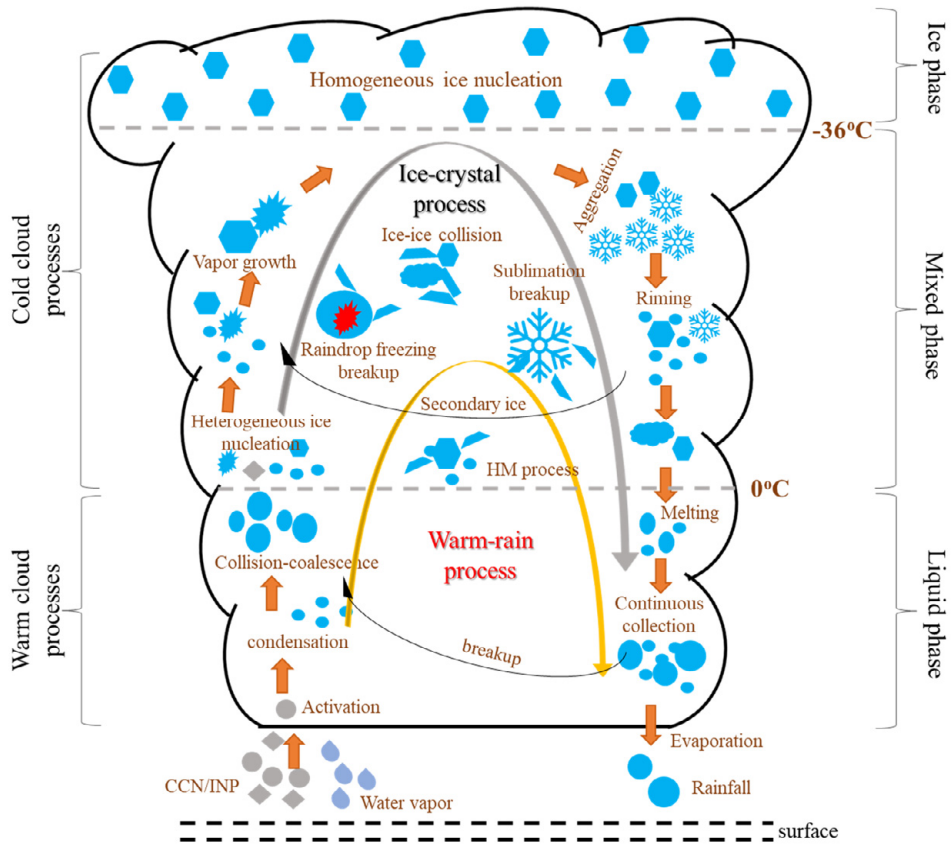
Figure 3. Schematic of a deep convective cloud with its top reaching well above the −36°C level (mature stage) illustrating initiation of cloud hydrometeors, warm rain and ice crystal process of precipitation formation, and mechanisms of SIP.

1.1.4   Radiative Importance of Aerosols and Clouds

Clouds can enhance the planetary albedo by reflecting the incoming SW radiation. Also, they can exert a greenhouse effect by trapping outgoing LW radiation. The net effect of these SW and LW components of radiation is known as the cloud radiative effect (CRE). On the global scale, at the top of the atmosphere (TOA), by enhancing the planetary albedo, clouds exert an annual SW CRE of about −50 W m^{-2} (Boucher et al., 2013). Also, clouds exert a net annual LW CRE of about +30 W m^{-2} (Boucher et al., 2013). Hence, on the global scale, clouds cause a net cooling of the present-day climate system (Yli-Juuti et al. 2021), with an effective CRE of about −20 W m^{-2}. However, the SW and LW CRE depend on the altitude, type, and optical properties of the clouds. For example, high-level clouds (e.g., cirriform) emit less outgoing LW radiation to space because they are colder than the mean emitting

level of the troposphere, thus exerting a strong greenhouse warming of the surface. It arises from the strong dependency of the emitted radiative flux on temperature by the Stefan-Boltzmann law (Liou, 2002). Also, such high-level clouds cause a cooling or warming, depending on whether they are thin or thick. Optically thick mid-level clouds can cause either a warming or a cooling (Sotiropoulou et al., 2021).

The global anthropogenic aerosol loading has significantly increased in the present day compared to pre-industrial times (Haywood and Boucher, 2000; Lohmann and Fiechter, 2005; Takemura, 2012) and is considered an important driver of climate forcing (Boucher et al., 2013). Anthropogenic APs can greatly influence the radiative budget of Earth's atmosphere through direct reflection/absorption of incoming SW and emission/absorption of outgoing LW radiations, known as the *direct effect*.

In their *indirect effect*, APs can modify the radiative impacts of clouds on Earth's radiation budget by altering their microphysical, macrophysical, and hence radiative properties (Twomey, 1974; Flossmann, 1998; Haywood and Boucher, 2000; Penner et al., 2004; Cantrell and Heymsfield, 2005; Gettleman et al., 2012; Wang et al., 2014; Kudzotsa et al., 2016; Wa22). A case study by Romakkaniemi et al. (2012) over Germany has shown that in polluted conditions, aerosol indirect effects (AIEs) dominate, whereas locally, their direct effects are more significant. The change in net radiative flux at the TOA due to changes in APs loading is defined using the term called *radiative forcing* (Kudzotsa et al., 2016; Lohmann, 2006).

In its first indirect effect, known as the *cloud albedo-emissivity effect* (Twomey effect) (Twomey, 1974; Charlson et al., 1992; Lohmann and Lesins, 2002; Lohmann, 2006; Boucher et al., 2013; Kudzotsa et al., 2016b), APs can alter the cloud microphysical structure by acting as CCN or INPs, thereby changing their reflective properties and influencing cloud albedo. Anthropogenic activity can also modify the lifetime of the cloud through precipitation efficiency, affecting its 3D extent. This associated aerosol indirect effect is known as the *lifetime effect* (Albrecht, 1989; Lohmann, 2006; Kudzotsa et al., 2016).

High aerosol loading in Earth's troposphere leads to an increased number of cloud hydrometeors of smaller sizes, resulting in greater reflection of incoming SW radiation and causing net cooling (Lohmann and Feichter, 2005; Christensen et al., 2016). APs can absorb incident radiation, resulting in net heating which may increase the evaporation of cloud hydrometeors, known as the *semi-direct effect* of aerosols (Lohmann and Fiechter, 2001; Johnson et al., 2004; Hill and Dobbie, 2008; Koch and Genio, 2010).

Previous modelling studies (Young et al., 2019; Miltenberger et al., 2021; Wa22) have shown that SIP can affect the radiative properties of clouds by modifying their microphysical and macrophysical structure. Increased SIP activity enhances cloud glaciation rate, thereby reducing cloud cover (Phillips et al., 2017a; Wa22; Wa23b) allowing more solar radiation to reach the earth's surface.

1.2 Importance of Cloud-Resolving Models

The significance of clouds extends beyond their impact on the hydrological cycle or their interaction with radiation. In fact, clouds play a crucial role by releasing latent heat during phase transitions, emerging as a dominant source of energy for atmospheric motions that span over a few mm to thousands of kilometers. Clouds, along with the microphysical, dynamical, and radiative processes associated with them, can occur over a few tens to a few hundred kilometers. Cloud-Resolving models (CRMs) are the state-of-the-art tool to study clouds and associated processes due to their ability to simulate clouds at finer spatial (about a few km) and temporal (about a few seconds) scales. Some important features of CRMs are.

i. CRMs explicitly resolve individual clouds and their microphysical processes that allow a more accurate and realistic representation of the processes such as cloud formation, growth, and dissipation. These processes are crucial for understanding precipitation patterns and CRE.

ii. CRMs allow simulations of small-scale (e.g., single clouds) as well as large-scale (thunderstorm and squall lines) processes with a spatial resolution finer than about 2-3 km (Khain and Pinsky 2018).

iii. These models can explicitly resolve cloud-scale processes and hence an efficient tool to provide better forecasts of short-term weather events.

iv. CRMs provide a more accurate representation of the microphysical processes of the clouds, and their interaction with aerosols and radiation, hence are a powerful tool in atmospheric and climate research.

However, cloud processes remain as one of the largest sources of uncertainties in numerical weather and climate models (Boucher et al., 2013). These uncertainties may arise either from the complete absence or a lack of accurate representation of the cloud microphysical processes. The present study, using the state-of-the-art numerical model, closes the knowledge gaps related to the following aspects:

i. Importance of various biological particles in initiating ice.

ii. The role of time dependence of INP freezing in overall ice formation and precipitation.

iii. Evolution of various ice multiplication processes with clouds.

iv. How anthropogenically increased solid APs influence the cloud radiative properties.

The present work addressed a range of research questions, associated with the ice phase of the clouds, using a CRM model. These include the elucidation of the role of 1) various PBAPs, 2) time-dependent INP freezing in initiating the overall ice, and 3) the relative importance of various SIP mechanisms in different stages of the convective clouds, and 4) effects from solid aerosol pollution on the radiative properties of the simulated clouds. The present study also evaluates the impact from ice formation processes such as SIP and time-dependent INP freezing on the net AIEs, in the simulated clouds. Also, two new indirect effects, associated with these ice formation processes, are proposed here. These are, 1) the 'SIP' indirect effect, and 2) the 'time-dependent INP' indirect effect.

The structure of the thesis is as follows. Sections 2 and 3 describe the proposed research questions and hypotheses, Sec. 4 provides details of the numerical model used, as well as the cases of storms. Section 5 describes the case setup, and modifications made in the numerical model, along with various sensitivity tests performed. Section 6 summarizes the results and conclusions. Finally, Sec. 7 describes the key findings.

2. Scientific Hypotheses and Research Questions

As discussed in Sec. 1, the ice phase in clouds greatly controls precipitation and hence the hydrological cycle and water availability. Also, the interaction between radiation and ice particles can affect climate patterns and temperature distributions by changing the energy balance of the Earth-atmosphere system. Ice particles can also affect the microphysical properties of cloud hydrometeors by altering their sizes, water contents, and number concentrations as well as cloud optical properties by controlling the rates of the processes such as vapor growth, accretion, aggregation, riming, and ice multiplication. Furthermore, the ice phase can significantly alter the cover, age, and lifetime of the clouds through precipitation formation.

Hence, the overarching goal of the present study is to elucidate the fundamental processes and mechanisms that govern the formation and evolution of ice phase in clouds, including both primary and secondary ice production using the Weather Research and Forecasting (WRF) based Aerosol-Cloud (AC) model, which is a state-of-the-art CRM with a 3D mesoscale domain. Furthermore, the indirect effects of various solid aerosols via glaciated clouds have also been studied. Moreover, the present study also investigates the impact on the simulated indirect effects from ice formation processes such as time dependence of INP freezing and SIP.

The research questions and hypotheses of the present study are as follows.

A. How important are various species of PBAPs in initiating ice, controlling precipitation, and altering the microphysical structure of the simulated continental convective storm?

Hypotheses:

    i. PBAPs can be one of the significant types of INPs and can greatly alter the cloud properties such as mass and number concentrations of ice particles.

    ii. PBAPs can significantly alter precipitation efficiency and radiative properties of the clouds.

B. Is the time dependence of INP freezing the main source for continuous ice nucleation and precipitation in a range of cloud systems?

Hypotheses:
   i.   Time dependence of INP freezing is the main cause for the observed ice concentrations in a range of cloud systems simulated numerically.

   ii.   Time dependence of INP freezing is the main mechanism for continuous ice nucleation and precipitation in the simulated cloud systems.

C. How are SIP mechanisms dependent on cloud-top temperature in a continental convective storm? How do various SIP processes differ in relative importance during the evolution of convective clouds?

Hypotheses:
   i.   Various SIP processes can form the observed ice particle number concentrations in the simulated clouds.

   ii.   The evolution of various SIP processes is dependent on the time and cloud-top temperature in the simulated clouds.

   iii.   The aircraft observed classic dependency of the IE ratio is dependent on cloud top temperature.

D. How do anthropogenically increasing solid APs affect the micro-, macrophysical and radiative properties of the simulated clouds compared pre-industrially? Can time dependence of INP freezing and SIP cause any impact on the predicted indirect effects from solid aerosols?

Hypotheses:
   i.   Anthropogenically induced INPs can significantly alter the micro- and macrophysical properties of the simulated clouds.

   ii.   Anthropogenic emission of INPs can exert a strong indirect effect via glaciated clouds.

   iii.   Time dependence of INP freezing and SIP can significantly affect the radiative properties of the clouds.

3. Aims and Objectives

The research questions addressed in the present study are.

1. To understand the relative importance of a range of biological particles in initiating ice and their effects on the microphysical and macrophysical properties in the simulated continental deep convective clouds.

2. To modify the empirical parametrization in AC to represent the time-dependent approach of INP freezing, using our published laboratory observations of time-dependent INP activity. This objective further investigates the role of the time dependence of the INP freezing process in initiating the observed ice concentrations in a range of cloud systems while accounting for all SIP processes.

3. To investigate the role of various SIP processes in overall ice formation in the simulated continental deep convective clouds. This study also explains the possible cause for the aircraft observed classic dependency of the IE ratio on cloud top temperature in the simulated clouds.

4. To study the mechanisms for the indirect effects from ice nucleus aerosols via glaciated clouds. To investigate the impact from time-dependent INP freezing and SIP on the simulated indirect effects.

These objectives are discussed in four separate papers that are.

3.1   **Paper 1**

The Influence of Multiple Groups of Biological Ice Nucleating Particles on Microphysical Properties of Mixed-phase Clouds Observed during MC3E.

3.2   **Paper 2**

Effects from Time Dependence of Ice Nuclei Activation for Contrasting Cloud Types.

3.3   **Paper 3**

Dependencies of Four Mechanisms of Secondary Ice Production on Cloud-Top temperature in a Continental Convective Storm.

3.4   **Paper 4**

Mechanisms for Indirect Effects from Solid Aerosol Particles on Continental Clouds and Radiation.

4. Description of Numerical Model and Field Campaigns

To address the objectives described in Sec. 2, various observed cloud systems have been simulated with the AC model. These are 1) the Midlatitude Continental Convective Cloud Experiment (MC3E) consisting of deep convective clouds, 2) the Atmospheric Radiation Measurement (ARM) Cloud Aerosol Precipitation Experiment (ACAPEX) characterized by orographic clouds, and 3) the Aerosol Properties, Processes, and Influences on Earth's climate (APPRAISE) consisting of supercooled long-lived stratiform clouds (Sec. 4.2). A brief description of AC is provided below:

4.1 Model Description: Aerosol-Cloud model

The present study used the AC model. AC uses the dynamical core and software infrastructure of the Weather Research and Forecasting (WRF) model (Dudhia 1989; Skamarock et al., 2008) to represent aerosols and clouds with hybrid spectral bin-two-moment bulk microphysics, semiprognostic aerosol, and interactive radiation schemes (Phillips et al., 2007, 2009, 2013, 2015, 2017a, b, 2020). AC uses the WRF schemes of the planetary boundary layer ([PBL], Troen and Mahrt, 1986; Hong and Pan, 1996), subgrid-scale mixing, dynamics, and surface layer. AC has been used in many previous studies (e.g., Kudzotsa et al., 2016a, b, Phillips et al., 2017b, 2018, 2020; Patade et al., 2021; Wa22a; Gupta et al., 2023; Wa23b).

AC represents microphysical species as cloud-liquid and ice ('crystal'), snow, graupel or hail, and rain. The total number and mass ('two-moment approach') mixing ratios of each of these species are diffused and advected as bulk prognostic variables in AC. Mass and number concentrations of ice, initiated through various processes (heterogeneous and homogeneous freezing and SIP) are tagged with prognostic, passive variables in AC. These tagging tracers do not interact with any process in AC. AC initiates cloud droplets by soluble APs, such as ammonium sulfate, sea salt, and soluble organics, at cloud-base (Ming et al., 2006) and at in-cloud levels (Phillips et al., 2007, 2009).

In AC, heterogeneous ice nucleation is governed by a total of eight APs, including mineral dust, soot, insoluble organics, and five PBAPs such as fungi, bacteria,

46

detritus, pollen, and algae (Patade et al., 2021, 2022). AC predicts the INP activity of these APs from the 'empirical parameterization (EP)' (Phillips et al., 2008, 2013). The EP encapsulates all modes of INP activation (Sec. 1.1.2.2) as well as heterogeneous raindrop freezing. The EP depends on the temperature, the surface area mixing ratio of each AP, and supersaturation.

No direct measurements of PBAPs were made during the field campaigns of the simulated clouds. The EP (Phillips et al., 2008, 2013) rather assumed that about 50% of the insoluble organics are biological in origin. The basis for this assumption is previous observational studies of biological particles (Matthias-Maser and Jaenicke 1995; Matthias-Maser et al., 1999, 2000) which reported that biological particles form about 20-30% of the total APs. Furthermore, Jaenicke (2005) observed that about 50% of the total APs are cellular particles. These studies were the basis for Phillips et al. (2008, 2013) to consider about 50% of the insoluble organics as biological in origin. The section below provides a brief description of the original EP representing the time-independent approach of heterogeneous ice nucleation (Phillips et al., 2008, 2013).

4.1.1 Representation of Original EP in AC

In AC, for given aerosol species (X = dust, soot, soluble organics, and PBAPs), the EP gives the number mixing ratio ($n_{IN,X}$) of active INPs (Phillips et al., 2013) at temperature (T),

$$n_{IN,X}(T, S_i, \Omega_X) = \int_{\log [0.1 \, \mu m]}^{\infty} \{1 - \exp[-\mu_X(D_X, S_i, T)]\} \times \frac{dn_X}{d\log D_X} \times d\log D_X$$

(1)

Where,

$$\mu_X = H_X (S_i, T)\xi(T) \left(\frac{\alpha_X n_{IN,1,*}}{\Omega_{X,1,*}} \right) \times \frac{d\Omega_X}{dn_X} \quad \text{for T} < 0°C \text{ and } 1 < S_i \leq S_i^w$$

(2)

Here, Ω_X is the surface area mixing ratio for a given X. The average number of activated ice embryos per insoluble AP of size D_X is given by μ_X. The scarcity of heterogeneous ice nucleation in subsaturated conditions is represented by the empirically determined fraction, H_X which is the function of saturation ratio with respect to ice (S_i) and temperature (T), and it varies between 0 and 1. ξ is the temperature-dependent fraction representing freezing of INP immersed drops and it varies from 0 to 1 for temperatures between -2 and $-5°C$. S_i^w is the S_i at water

saturation. $d\Omega_X/dn_X \approx \pi D_X^2$. The term $n_{IN,1,*}$ is the number of active INPs per kilogram of air and represents the reference activity spectrum of the average concentration of INP. More details are from Phillips et al. (2008, 2013).

Also, insoluble APs may be internally mixed with various soluble APs (Clarke et al., 2004). When the saturation ratio with respect to water (S_w) reaches the critical value, such soluble APs can form cloud droplets, and the insoluble part then becomes immersed in the droplet. The raindrop with immersed INPs in it may nucleate heterogeneously at subzero temperatures to form ice. The equation that gives the number concentration of INPs activated during heterogeneous raindrop freezing ($d(\Delta n_{IN,rain})$) (Phillips et al., 2008) for time-step Δt is,

$$d(\Delta n_{IN,rain}(T,S_i,\Omega_X)) \approx \Delta t \, min\left[(w-v_t)\frac{dT}{dz},0\right] \times$$

$$\frac{d}{dT}\{n_{IN,1,*}[T,S_i^w(T)]\}\sum_X\left(\frac{\alpha_X d\Omega_{X,rain}}{\Omega_{X,1,*}}\right) \tag{3}$$

Here, w is the vertical velocity, v_t is the fall speed of raindrops and $d\Omega_{X,rain} = \Omega_{X,rain} \, dQ_r/Q_r$ denotes the surface area mixing ratio of INP immersed in a raindrop. Also, Q_r is the mass mixing ratio of the raindrop. More details can be found in Phillips et al. (2008).

The number of ice crystals initiated (Δn_i) in a time step (Δt) is incremented by,

$$\Delta n_i = \sum_X \text{MAX}(n_{IN,X} - n_{X,a}, 0) \equiv \sum_X \Delta n_{X,a} \tag{4}$$

Here, $n_{X,a}$ is the increment of the number mixing ratio of INPs from group X that has been activated.

In summary, Eqs (1)-(4) represent heterogeneous ice nucleation without time dependence.

AC forms ice homogeneously in two ways. The spontaneous freezing of supercooled cloud drops/rain and APs above the -36°C level forms ice. Homogeneous aerosol freezing occurs as soon as the critical supersaturation exceeds. This critical supersaturation depends on the temperature and size of the AP (Phillips et al., 2007).

AC forms secondary ice by four types of ice multiplication mechanisms which are briefly described in Sec 1.1.2. More details of these mechanisms can be found in Phillips et al. (2001, 2003, 2005, 2007, 2017a and b, 2018), Deshmukh et al. (2022), and Wa22.

Furthermore, AC uses our own implementation of the Geophysical Fluid Dynamics Laboratory (GFDL) radiation scheme (Friedreich and Ramaswamy, 1999) in which scattering of SW and LW radiation depends on the effective and generalized effective size of cloud-liquid and cloud-ice. The GFDL radiation scheme used in

AC takes mean sizes of cloud droplets and ice crystals as inputs to calculate the SW and LW fluxes at model levels. This scheme does not predict the direct effect of aerosols.

4.2   Field Campaigns

4.2.1   MC3E

The MC3E campaign was carried out in north-central Oklahoma, collectively by the U.S. Department of Energy (DoE) and ARM climate research facility, and the National Aeronautics and Space Administration's (NASA) Global Precipitation Measurement (GPM). It made observations for a total of 15 data missions focusing on and around the DoE ARM Southern Great Plains (SGP) Central Facility (CF). MC3E took place from 22 April to 6 June 2011 and involved the collection of data from airborne and ground-based measurements (Jensen et al., 2016).

4.2.1.1 Airborne Measurements

During MC3E, the University of North Dakota (UND) Cessna Citation II jet aircraft (Fig. 4a) carrying a standard suite of meteorological instruments together with precipitation, cloud microphysical and liquid and total water content probes (Table 2) made measurements of in-cloud microphysical properties at levels between about 4 and 8 km. The liquid properties (liquid water content [LWC], droplet sizes, and number concentrations) were measured by the cloud droplet probe (CDP) whereas the sizes and number concentrations of ice particles were measured by the 2D cloud (2DC) probe, cloud imaging probe (CIP), and High volume precipitation spectrometer (HVPS-v3). The Combined Spectrum uses particle size distribution of 2DC or CIP merged with HVPS3. The Citation aircraft flew a total of 15 science flights.

Table 2. Details of the optical probes mounted on the sampling aircraft during the field campaigns and corresponding size range considered in the present study.

Campaign	Aircraft	Instruments mounted on the aircraft to measure cloud properties				
		Ice particle	Size range (mm)	Cloud droplet	Size range (μm)
MC3E (11 and 20 May)	UND Citation	2DC CIP HVPS-v3	0.2-1.0 0.2-1.5 0.2-19.2	CDP	2-20
ACAPEX	DoE G-1	2DS HVPS	0.2-1.28 0.2-19.2		
APPRAISE	CFARR UK BAe146	2DS-128	0.1-1.28		

4.2.1.2 Ground-based measurements

The radiosonde array deployed at 6 sites over a 300 km x 300 km area (Jensen et al., 2016) was used to measure the temperature, humidity, and wind properties. Radiosonde observations (Vaisala RS92-SGP) were conducted four times daily to quantify the diurnal cycle of various atmospheric state variables of the environment surrounding the ARM SGP site. The sounding frequency was increased to eight times per day when aircraft operations were occurring based on forecasted convective conditions.

During the MC3E campaign, the spatial variability of moisture, surface heat, and momentum fluxes were measured by the instrumentation included in extended SGP facilities covering an area of about 150 km × 150 km. Measurement of surface precipitation was done with 16 rain gauge pairs placed within a 6 km radius of the SGP CF. Continuous measurements of aerosols, atmospheric gases, meteorological conditions (e.g., temperature, precipitation, wind), and clouds were conducted by the dedicated instrumentation suite deployed at the ARM SGP CF.

The CCN number concentrations were measured by a CCN counter (DMT) at seven levels of supersaturation (Jefferson, 2011; Uin, 2022) at Lamont, Oklahoma whereas no measurements of INPs were made during the MC3E campaign. Large-scale forcing (LSF), surface heat, and moisture fluxes were derived from a constrained variational analysis approach (Jensen et al., 2016).

The case considered here is a line of convective clouds observed during MC3E on 11 May 2011. These clouds had warm bases near 17°C at about 1.5 km altitude above mean sea level (MSL). The ground level was about 350 m MSL. The convective line, a type of an MCS consisted of different cloud types, most of which were deep convective (e.g., cumulonimbus) with typical cloud depths of 9-13 km and stratiform clouds. Figure 4a shows the study domain. Figure 4b shows the profiles of air and dewpoint temperature on 11 May at 12:00 UTC derived from AC. The lifting condensation level (LCL) was at about 870 hPa (17°C) and the predicted convective available potential energy (CAPE) was about 2200 J kg^{-1} (Fig. 4b), which is mostly attributed to the moistening of the lower troposphere from large-scale advection (Jensen et al., 2016). The horizontal wind speed is relatively high (> 15 m s^{-1}) throughout the atmosphere.

Figure 4(c-e) shows images of ice particle habits from the CIP, mounted on the Citation aircraft (Fig. 4a), at various levels in convective cloudy updrafts ($w > 1$ m s^{-1}). These profiles show that the levels near the cloud base are mostly dominated by raindrops (0.2 to 1 mm, Fig. 4c). Furthermore, the higher levels (-7 to -18°C) are observed to be dominated by aggregates and rimed ice particles (Fig. 4d-e) whereas, pristine ice crystals are relatively less at these levels.
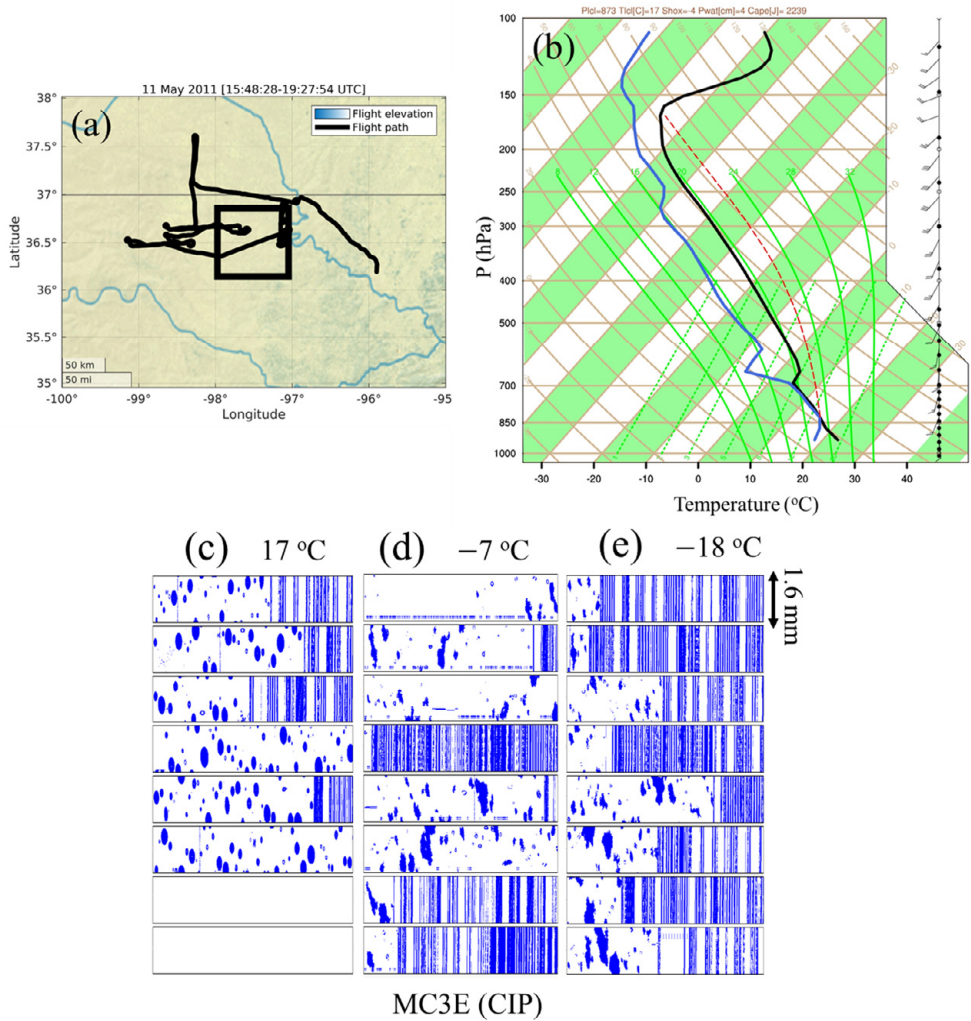
Figure 4. (a) Profiles of geographical area, flight track of the UND Citation aircraft (thin black line) and the simulation domain (solid black box), (b) the vertical profile of the air (solid blue line) and dewpoint (solid black line) temperature, and moist adiabat (dotted red line) on 11 May 2011 at 12:00 UTC. Also shown are the ice particle habits in convective cloudy updrafts (w > 1 m s^{-1}) at (c) 17°C, (d) −7°C, (d) −18°C from the CIP mounted on the UND Citation aircraft during the MC3E campaign on the same day.

Also, another case of a squall line was observed on 20 May 2011 (00:00-24:00 UTC), in which convection was triggered by a flow of moisture from the Gulf of Mexico (Jensen et al., 2016; Patade et al., 2022). The main convective event was observed between 10:30 and 11:00 UTC, with a peak precipitation rate of about 6 mm hr^{-1}, followed by widespread stratiform precipitation. The instruments described above were used to measure the properties of these clouds. The bases of the clouds were at about 20°C whereas their tops were extending up to the

51

tropopause level (about −60ºC). More details about soundings, LSF, and other meteorological conditions are from Patade et al. (2022).

4.2.2 ACAPEX

ACAPEX was a multiagency field campaign designed to understand the effects on the amount and phase of precipitation associated with atmospheric rivers (AR) from aerosols from local pollution and from long-range transport (Leung 2016). ACAPEX was carried out between 12 January and 8 March 2015 as a part of CalWater-2015. The CalWater-2015 project included four aircraft: 1) DoE Gulfstream-1 (G-1), 2) NASA ER-2, and the National Oceanic and Atmospheric Administration (NOAA) 3) G-IV, and 4) P-3 aircraft. The DoE G-1 aircraft sampled clouds between the Central Valley and Sierra Nevada jointly with the NOAA *Ron Brown* ship. The Ron Brown ship made measurements of temperature, humidity, winds, and radiative and surface fluxes and was carrying the ARM Mobile Facility 2 (AMF2) which made the measurements of aerosols and clouds.

The CDP and 2D spectrometer (2DS) and HVPS probes (Table 2) mounted on the DoE G-1 (Fig. 5a) aircraft respectively measured the liquid and ice properties of the ACAPEX clouds. Furthermore, the surface precipitation was measured with rain gauges deployed on the ground at several locations. The case analyzed here involved orographic clouds with embedded convection that brought significant precipitation over the US west coast (Northern California) due to the landfall of an AR on 7 February 2015 (19:00-23:00 UTC).

Figure 5(b-d) shows images of hydrometeor habits observed in the ACAPEX campaign from the 2DS probe at various levels in the cloudy convective updrafts ($w > 1$ m s^{-1}). From these profiles, it is evident that the levels near the cloud base were dominated by raindrops (0.2 to 1 mm, Fig. 5c). Furthermore, mostly pristine ice particles were observed at subzero levels warmer than −7ºC whereas, levels above −7ºC were mostly dominated by aggregates and rimed ice particles.

The Hybrid Single-Particle Lagrangian Integrated Trajectory (HYSPLIT) backward trajectory plotted for 120 hrs shows that over the study domain, APs are mainly marine in origin (Fig. 5e) whereas, dust and black carbon were less (Levin et al., 2019; Lin et al., 2022). The profiles of the air and dewpoint temperatures from AC are shown in Fig. 5e. From this profile, it can be seen that the LCL is at about 10ºC (930 hPa), and the wind speeds were observed to be relatively high (about 10 m s^{-1}) throughout the atmosphere whereas, the CAPE is relatively low (500 J kg^{-1}).
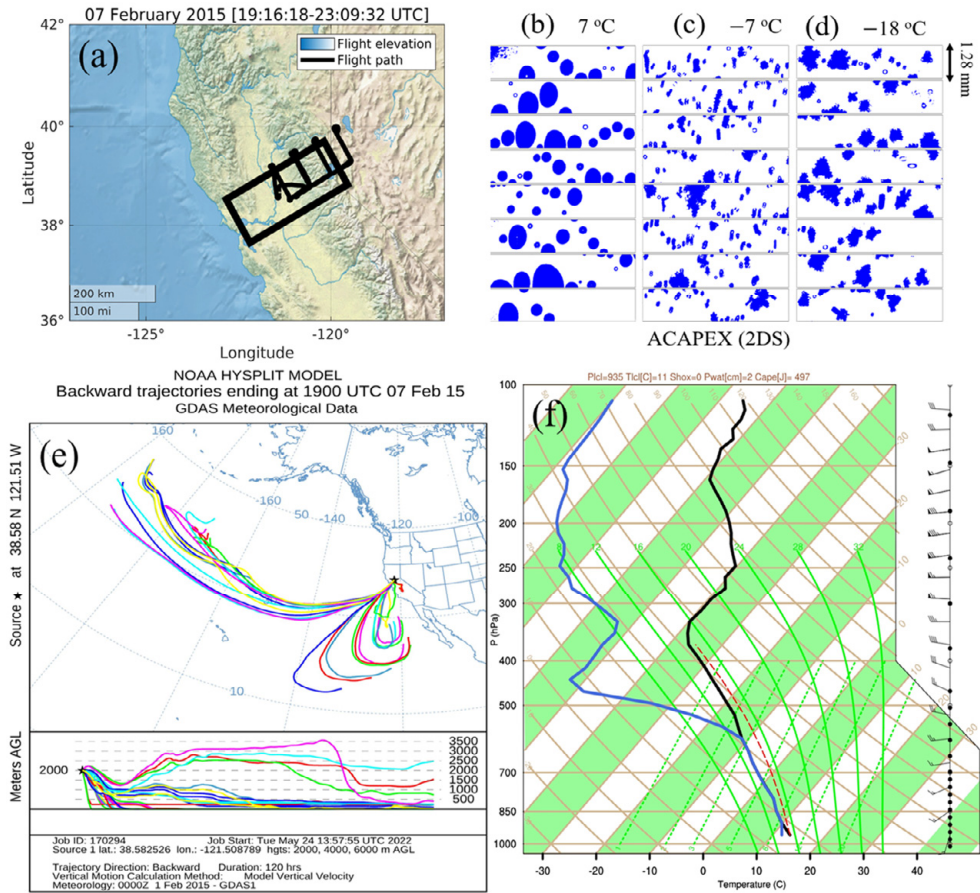
Figure 5. (a) Profiles of geographical area, flight track of the DoE G-1 aircraft (thin black line) and the simulation domain (solid black box), and the ice particle habits in convective cloudy updrafts (w > 1 m s⁻¹) at (c) 7°C, (d) −7°C, (d) −18°C from the 2DS probe mounted on the DoE G-1 aircraft during the ACAPEX campaign on 07 February 2015. Also shown are the (e) HYSPLIT backward trajectory for 120 hrs showing the airflow from the North Pacific Ocean over the study domain (Sacramento, California, USA) and (f) the vertical profile of the air (solid blue line) and dewpoint (solid black line) temperature and moist adiabat (dotted red line) on the same day at 19:15 UTC.

4.2.3   APPRAISE

APPRAISE was carried out in the winter 2009 over the southern UK to study the microphysical processes associated with liquid and ice-phase formation in mixed-phase frontal clouds. A case analyzed here was anticyclonic (surface pressure 1020 hPa) consisting of the episodes of: 1) weak embedded convection (00:00-12:00 UTC), and 2) layer clouds (12:00-24:00 UTC) on 18 February 2009 during the APPRAISE campaign (C11; WI13; Wa23a) and covering an area of more than 100 km in width (C11; WI13). The observed cloud base was at about 6°C whereas the cloud top was quasi-steady throughout the day (cooling by about 1.5 K), extending

up to −15ºC (Fig. 6f). Both the episodes of the APPRAISE clouds were observed to precipitate throughout the day (C11; WI13).

The 2DS and CDP probes (Table 2) mounted on the Chilbolton Facility for Atmospheric and Radio Research (CFARR) BAe-146 aircraft (Fig. 6a) carried out the measurements of ice and liquid properties of the APPRAISE clouds near the CFARR. To validate the AC predicted ice concentrations (> 0.1 mm), corrections are applied to the observations from the 2DS probe by multiplying all measured ice concentrations (WI13, their Fig. 9) by a factor of 0.253 following Korolev et al. (2011, their Fig. 5).

Figure 6(b-e) shows particle habits observed from the 2DS probe on 18 February 2009 between levels −4.3 and −11.7ºC in convective cloudy regions (adopted from C11). These images show the majority of rimed ice particles at about −7ºC level whereas the levels near cloud top (−12ºC, Fig. 6e) were dominated mostly by pristine ice crystals such as plates and aggregates. The lower levels (−4.3ºC, Fig. 6b) were dominated by small columns. This was the basis for C11 to propose the activity of SIP through the HM process in the episode of weak convection of the APPRAISE clouds.

Figure 6f illustrates the profiles of the air and dew-point temperatures on 18 February 2009 at 00:00 UTC derived from AC. The predicted horizontal wind speeds are significantly weak (< 3 m s^{-1}) and are south-westerly in the lower troposphere. Levels above the cloud top show a temperature inversion (temperature difference of about 4ºC) layer characterized by extremely low relative humidity (RH < 50%). For APPRAISE, as reported by WI13 and Wa23a, for the layer cloud episode, two distinct cloudy layers are seen: 1) a saturated layer at levels between about cloud-base and 1.2 km, and 2) a thin, supersaturated layer at levels above 2.5 km extending up to 4 km. These two layers are separated by a subsaturation layer (about 1 km thick). The majority of APs were marine in origin with a mixture of continental aerosols from various parts of Western Europe. C11, WI13, and Wa23a provide more details of the observed system.
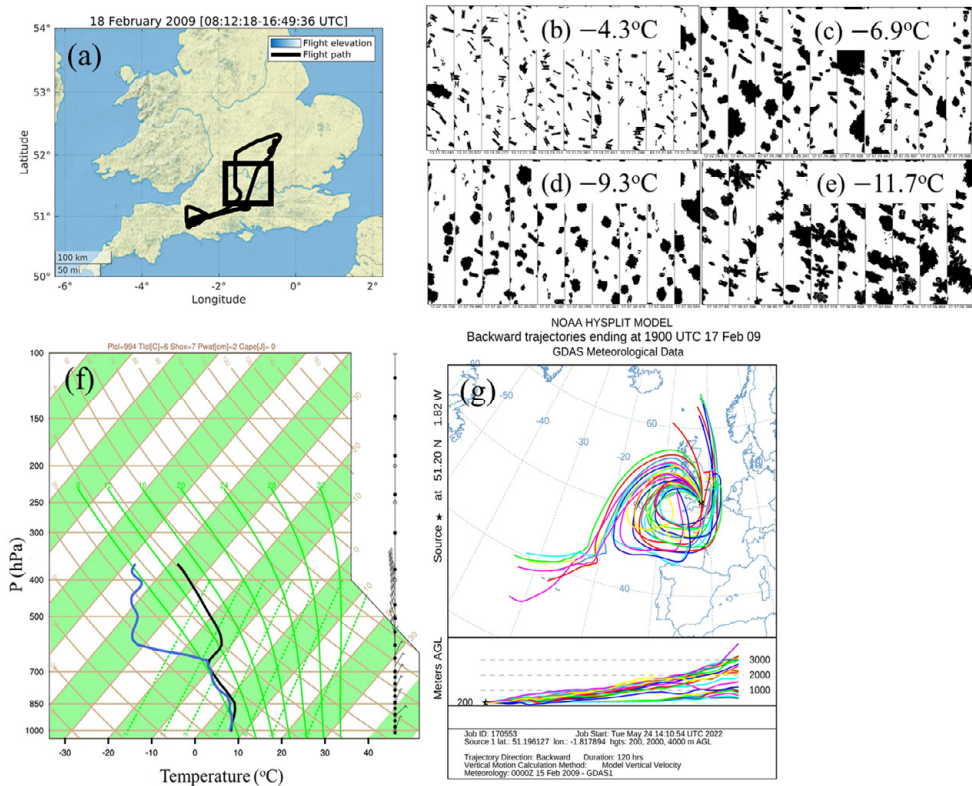
Figure 6. (a) Profiles of geographical area, flight track of the BAe146 aircraft (thick black line) and the simulation domain (solid black box) during the APPRAISE campaign on 18 February 2009, and particle images at (b) −4.3°C, (c) −6.9°C, (d) −9.3°C and, (e) −11.7°C from the 2DS probe mounted on the BAe146 aircraft (adopted from C11), Each image strip is approximately 12.8 mm long and 1.28 mm wide. Also shown are the (f) vertical profile of the air (solid blue line) and dewpoint (solid black line) temperature at 00:00 UTC for the same day and, (g) HYSPLIT backward trajectory for 120 hrs showing the airflow from the North Atlantic Ocean region as well as from polluted regions such as France over the study domain (Larkhill, UK).

5. Methodology

Four cloud cases (Sec. 4.2) were simulated with AC for a 3D mesoscale domain (Sec. 4.1) to address the research questions outlined in Sec. 2. All these cloud cases are simulated in an idealized manner, wherein no attempt was made to estimate the precise cloud locations. The horizontal (along x and y directions) and vertical resolution of the simulation domain are about 2 and 0.5 km respectively, and the model integration time step is about 10 sec. For the simulated APPRAISE and MC3E (both 11 and 20 May 2011) clouds, the lateral boundary conditions are periodic in both x and y directions. On the other hand, for the ACAPEX case, boundary conditions are open and periodic in x and y directions, respectively. The model top was at about 16 km for the MC3E and ACAPEX simulations, and about 8 km for the APPRAISE case.

Regarding the simulation period, during MC3E, an MCS observed on 11 May 2011 is simulated for 72 hours from 10 May 00:00 to 13 May 00:00 UTC whereas a squall line observed on 20 May 2011 is simulated for 48 hours between 20 May 00:00 and 21 May 00:00 UTC. Also, a case of supercooled layer clouds observed during APPRAISE is simulated for 48 hours from 17 February (00:00 UTC) to 19 February 2009 (00:00 UTC). Furthermore, a case of orographic clouds in ACAPEX observed on 7 February 2015, is simulated for 3 hours from 19:15 to 22:15 UTC.

More details about the domain set-up for these simulated cases are from Patade et al. (2022), Wa22, and from Wa23a.

A brief description of the model set-up, modifications made in the scheme of the heterogeneous ice nucleation process, and the sensitivity tests carried out for each paper (Sec. 3) is provided below:

5.1 Paper 1

The Influence of Multiple Groups of Biological Ice Nucleating Particles on Microphysical Properties of Mixed-phase Clouds Observed during MC3E.

To study the influence from various groups of PBAPs on the micro- and macrophysical properties of the convective storm, a case of deep convective clouds observed during the MC3E campaign on 20 May 2011 (Sec. 4.2.1) was simulated with AC.

The EP proposed by Phillips et al. (2008, 2013) initiates ice via the activity of APs such as mineral dust, soot, soluble organics, and PBAPs. However, this EP did not resolve the individual groups of PBAPs. Based on the field observations from Amazonia, Patade et al. (2021) proposed an empirical formulation to predict the INP activity of five types of PBAPs including 1) fungi, 2) bacteria, 3) pollen, 4) algae, and 5) plant/animal detritus. This empirical formulation is an extension of the original EP (Phillips et al., 2008, 2013) (Sec. 4.1.1), and is based on the observed properties of PBAPs such as their sizes, biological composition, number concentrations, and ice nucleating ability. Furthermore, it is dependent on parameters such as T, S_i, and the surface area mixing ratio of a given aerosol species. More details are from Patade et al. (2021, 2022).

5.2 Paper 2

Effects from Time Dependence of Ice Nuclei Activation for Contrasting Cloud Types.

To estimate the effects from time-dependent INP freezing on overall ice concentration in clouds, three cloud cases (Sec. 4.2) have been simulated with AC (Sec. 4.1). These include 1) supercooled layer clouds observed during APRPAISE on 17 February 2009, 2) orographic clouds with embedded convection observed on 7 February 2015 during ACAPEX, and 3) deep convective clouds observed during MC3E on 11 May 2011.

To evaluate the role of time-dependent freezing of various INP species (Sec. 4.1), the original EP (Sec. 4.1.1; Phillips et al., 2013; Patade et al., 2021) was modified by a purely empirical approach in light of the laboratory observations of time dependence by JK22. The modifications made in the original EP (Sec. 4.1.1) to represent the time-dependent approach of INP freezing are described below.

5.2.1   Modification to original EP in AC to Represent Time Dependence of INPs

An experimental study by JK22 quantified the time dependence of INP activity in freezing mode. They considered various aerosol classes such as rural continental, continental polluted, continental pristine, combustion dominated, mineral dust influenced and marine dominated. JK22 observed an increment in INP concentrations by 70 to 100% (70 to 200%) over the period of 2 to 10 hours and the maximum time dependence for dust and rural continental samples.

JK22 proposed the temperature-shift ($\Delta T_X = \Delta T_X(t^*) \leq 0$) approach to represent the time-dependent freezing of active INPs. The original EP (Sec. 4.1.1), representing heterogeneous ice nucleation, was modified by adding the temperature

shift for each AP to represent a time-dependent approach of INP freezing, following JK22 (their Sec. 3.2.2).

The temperature-shift is (JK22),

$$\Delta T_X(t^*) = -A_X t^{*\beta} \tag{5}$$

Here, t^* is the time since the parcel entered the glaciating part of a cloud (the age of the cold parcel). Here, t^* is estimated by a passive tracer (Q) that decays exponentially with time following the motion of any parcel in a cold cloud ($T < 0°C$ and ice water content [IWC] $> 10^{-6}$ kg m^{-3}). The evolution of Q is from numerical integration during the simulation of:

$$\frac{dQ}{dt} = \begin{cases} \dfrac{-Q}{\tau_Q} & \forall\ T\ < 0°C \text{ and } IWC > 10^{-6} \text{ kg m}^{-3} \\\\ 0 & \text{otherwise} \end{cases} \tag{6}$$

Here, τ_Q is an arbitrary relaxation time and is set to 1800 seconds throughout the simulation. For an adiabatic parcel, the analytical solution of Eq (6) gives t^*,

$$t^* \approx -\tau_Q \ln(Q/Q_0) \tag{7}$$

Outside of the cold cloud, $Q = Q_0 = 1$ kg^{-1} is prescribed everywhere. Effects on t^* from dilution of actual simulated parcels are approximately represented by virtue of in-cloud mixing and entrainment being treated in the numerical prediction of Q.

With this temperature-shift ($\Delta T_X(t^*)$), the time-dependent number mixing ratio of active INPs ($ñ_{IN,X}$) in the X-th species from Eq (1) is,

$$ñ_{IN,X}(T, S_i, \Omega_X, t) = n_{IN,X}\left((T + \Delta T_X(t^*)), S_i(T + \Delta T_X(t^*)), \Omega_X\right) \tag{8}$$

Similarly, the time-dependent number mixing ratio of INPs activated in heterogeneous raindrop freezing ($d(\Delta ñ_{IN,rain})$) from Eq (4) is obtained by summing over each raindrop size bin,

$$d\left(\Delta ñ_{IN,rain}(T, S_i, \Omega_X)\right) = d\left(\Delta n_{IN,rain}(T + \Delta T_X(t^*), S_i(T + \Delta T_X(t^*)), \Omega_X)\right) \tag{9}$$

More details can be found in JK22 and in Wa23a.

Two simulations were performed to evaluate the role of the time dependence of INP freezing in forming overall ice in the simulated clouds. These are, 1) the control run which includes time-dependent INP freezing, all SIP mechanisms, and homogeneous ice nucleation, and 2) the 'no time-dependent INP' run in which time dependence of INP freezing is excluded from the control run. Additionally, one more sensitivity test ('no dust from droplet evaporation') was carried out in order to analyze the mechanisms responsible for the continuous nucleation of ice in the episodes of the simulated APPRAISE clouds (Wa23a). In this test, the contribution to dust particles in the air is excluded from droplet evaporation from the control run. More details are from Wa23a.

5.3 Paper 3

Dependencies of Four Mechanisms of Secondary Ice Production on Cloud-Top temperature in a Continental Convective Storm.

Aircraft observations of young, ascending cumulus clouds over Miles City, Montana, USA by Hobbs et al. (1980, their Fig. 25) showed the classic dependency of IE ratio on cloud-top temperature. They observed a classic peak in IE ratio at a characteristic cloud-top temperature of about -12°C. However, the SIP mechanisms responsible for this classic dependency were unknown at that time. In this paper, an attempt was made to analyze the causes for this classic dependency by simulating a similar event of convective clouds observed during MC3E on 11 May 2011 (Sec. 4.2.1), partly using tagging tracers (Sec. 4.1).

Here, the IE ratio is defined as the ratio of the number concentrations of the average non-homogeneous ice (total homogeneous ice minus total ice from cloud ice and snow) at any in-cloud level to that of INPs active at cloud-top. In this study, young, developing cumulus clouds were sampled using the cloud-top algorithm (Wa22, their appendix A). The predicted age of these clouds is between 5 and 30 min. More details are from Wa22.

5.4 Paper 4

Paper 4 involved the study of the net AIEs from ice-nucleating aerosols. Also, the impact from the time dependence of INP freezing and SIP on the predicted net AIEs is investigated. This is achieved by performing a series of sensitivity tests with AC for the simulated APPRAISE and MC3E (11 May) clouds. This involved modifications in the control run to create various perturbation simulations. The control run (Table 3) here is referred to the simulation that includes time-dependence of heterogeneous ice nucleation (Sec. 5.2.1), homogeneous freezing, and all four SIP processes (Sec. 1.1.2). This control run is simulated for the present-

day as well as pre-industrial solid aerosol conditions. Furthermore, both present-day and pre-industrial simulations have been performed with the present-day thermodynamic conditions to eliminate any radiative forcing arising from changing thermodynamic forcing.

In the pre-industrial simulation, solid aerosols are prescribed with an adjustment factor derived from a modelling study of the global distribution of APs from the pre-industrial (1850) to future projection (2100) by Takemura (2012). They reported that the present-day soot concentration is a factor of about 2.5 higher compared to 1800 and is the most affected AP among all solid APs due to anthropogenic activities. Furthermore, in present-day conditions, Takemura (2012) reported a factor of about 1 increase in mineral dust particle concentrations relative to 1800 whereas, no significant change is seen in soluble organics and biological particles.

To estimate the albedo-emissivity and lifetime indirect effects of solid aerosols in the simulated supercooled, mixed-phase layer clouds (APPRAISE) and convective storm (MC3E), various sensitivity tests have been performed following the techniques used in Kudzotsa et al. (2016b). These sensitivity tests are classified as Tests A and B predict the net albedo-emissivity and lifetime indirect effect, respectively for a targeted cloud type. Kudzotsa et al. (2016b) and Wa23b gives more details about these sensitivity tests. However, they are briefly described below.

Table 3. Description of the simulations performed for the simulated APPRAISE and MC3E cases. Each simulation is performed with the present-day and pre-industrial aerosol conditions.

Simulation	Description
Control	Includes time dependent INP freezing, all SIP and homogeneous freezing
No SIP	Excludes all SIP processes from the control run
No time dependent INP	Excludes time dependent INP freezing from the control run

5.4.1 Net Indirect Effects from Anthropogenic Solid Aerosols

A.   Test A: The Total and Albedo-Emissivity AIE

The total or net (Q_{net}) AIE is the difference in net radiative fluxes at the TOA (at the model top) between the present-day ($Q_{PRESDAY}$) and pre-industrial (Q_{PREIND}) run, simulated in the control environment (Gettleman et al., 2012; Lohmann, 2006; Kudzotsa et al., 2016b).

$$Q_{net} = Q_{PRESDAY} - Q_{PREIND} \qquad (10)$$

The albedo of a given cloud is strongly dependent on the mean sizes of cloud hydrometeors (cloud-liquid and ice-crystal), and changing aerosol conditions due to anthropogenic activity can significantly alter the mean sizes of these cloud particles, giving rise to albedo-emissivity AIE. To evaluate the albedo-emissivity AIE of a targeted cloud type, two model runs are performed with two calls to the radiation

scheme. The first call is an active call, in which properties of hydrometeors, such as sizes and number concentrations, are dependent on aerosol loading. By contrast, the second call is a passive call, which means hydrometeor properties are independent of changes in aerosol loading. This passive call does not alter the microphysics of the simulation. This is achieved by creating temperature and vertical-velocity-dependent look-up tables of mean sizes and/or number concentrations of cloud droplets and ice crystals. These look-up tables are designed from the control simulation. The same look-up tables have been used for both the control and pre-industrial simulations.

The difference in the net radiative fluxes at the TOA between the control and pre-industrial runs predicted from the first calls gives the Q_{net}. Furthermore, if the same approach is applied to the second calls of both the control and pre-industrial simulations, a hypothetical net radiative flux (Q_{net_life}) can be estimated, which is the total lifetime AIE. Finally, the albedo-emissivity AIE is given by subtracting Q_{net_life} from Q_{net}.

$$Q_{net\_alb} = Q_{net} - Q_{net\_life} \qquad\qquad (11)$$

If the approach discussed above is applied to a targeted cloud type, then the corresponding albedo-emissivity AIE can be estimated. For example, to estimate the albedo-emissivity indirect effect of glaciated clouds, the cloud-droplet and ice crystal mean sizes are defined using look-up tables in glaciated clouds. Similarly, the albedo-emissivity AIE of ice-only clouds is predicted by prescribing the mean sizes of these hydrometeors in ice-only clouds. At a given time step in the simulation, a grid point is said to be *ice-only* when it has zero cloud-liquid and non-zero cloud-ice mass mixing ratios. On the other hand, above the freezing level (0°C), model grid points containing non-zero cloud-liquid and/or cloud-ice mass mixing ratios are identified as *glaciated* clouds.

B.   Test B: The lifetime AIE

i.   Lifetime AIE for Glaciated Clouds

The lifetime indirect effect for a targeted cloud type is estimated by eliminating the responses of the corresponding microphysical processes using the look-up tables of the mean sizes and/or number concentrations of cloud hydrometeors. For example, to estimate the lifetime effect of glaciated clouds, indirect effects from liquid-only clouds are prohibited by using the look-up tables of the mean sizes and number concentrations of cloud-liquid in the microphysical processes such as collision and coalescence, auto-conversion, sedimentation as well as radiative properties.

The difference in the TOA net radiative fluxes between the present-day and pre-industrial runs performed with look-up tables for these microphysical processes and with passive second calls to the radiation scheme gives the net radiative flux without any indirect effects from water-only clouds at levels warmer than 0°C (Q_{hyp_glc}). Finally, subtracting the Q_{alb_glc} (test A) from Q_{hyp_glc} gives the estimate of the lifetime indirect effects from glaciated clouds (Q_{life_glc}).

ii. Lifetime AIE for Ice-only and Mixed-phase Clouds

To estimate the lifetime indirect effects from ice-only clouds, the responses of the aerosol-dependent microphysical processes of ice-only clouds are eliminated from the present-day and pre-industrial simulations by using the look-up tables of ice crystal number concentrations and sizes. Yet, responses of microphysical processes to changes in aerosol loading are allowed in mixed-phase and liquid-only clouds. The microphysical processes associated with ice-only clouds are auto-conversion of cloud-ice to snow, sedimentation of cloud-ice, aggregation of graupel and cloud-ice, and aggregation of cloud-ice with snow. Additionally, the passive second call to the radiation scheme is used with the same look-up table for ice-only clouds to eliminate their albedo-emissivity effect.

The difference in the TOA net radiative fluxes between the present-day and pre-industrial simulations, performed using the look-up tables for these microphysical processes and radiative properties in ice-only clouds, gives a hypothetical net radiative flux for liquid-only and mixed-phase clouds ($Q_{hyp\_net\_liq\_mix}$). Subtracting $Q_{hyp\_net\_liq\_mix}$ from the Q_{net} determined in Test A gives the net indirect effects from ice-only clouds (Q_{net_ice}). Finally, subtracting Q_{alb_ice} from Q_{net_ice} gives the lifetime indirect effects from ice-only clouds (Q_{life_ice}).

Furthermore, the indirect effects from mixed-phase clouds are determined by subtracting the indirect effects of ice-only clouds from those of glaciated clouds.

5.4.2 SIP and Time dependent INP freezing Indirect Effects

To estimate the effects on the net AIEs predicted above (Sec. 5.4.1, Tests A and B), arising from SIP and time-dependent INP freezing, two perturbation simulations are performed by altering the control simulations (Table 3). These are 1) a 'no SIP' run in which SIP is completely prohibited from the control simulation, and 2) a 'no time-dependent INP' run in which time dependence of INP freezing is prohibited from the control run. These simulations are carried out for the present-day as well as pre-industrial solid aerosol conditions. In these simulations, the indirect effects for each cloud type are estimated by repeating Tests A and B described above (Sec. 5.4.1). Note that separate lookup tables for particle mean sizes and number concentration

are used to perform 'no SIP' simulations. These lookup tables are temperature and vertical velocity dependent and are designed from the present-day 'no SIP' simulation. However, the same look-up tables for particle mean sizes and number concentrations from the present-day control run are used to perform 'no time-dependent INP' simulations. Finally, by subtracting the AIEs from 'no SIP' and 'no time-dependent INP' runs from the net AIEs predicted in the control run, gives the 'SIP' and 'time-dependent INP' indirect effects.

6. Results and Discussion

The study presented here addresses a broad range of research questions in the field of ice microphysics such as, 1) the role of different groups of biological particles in initiating overall ice concentration, and altering the micro- and macrophysics of the clouds (Paper I), 2) the importance of time dependence of INP freezing in initiating overall ice concentration in various cloud systems and its role in precipitation formation (Paper II), 3) dependency of various SIP mechanisms on cloud-top temperature and their evolution in a convective storm (Paper III), and 4) indirect effects from anthropogenically increased solid aerosols and impacts on these AIEs from ice formation processes in the simulated deep convective and supercooled layer clouds (Paper IV).

Such a broad analysis of various ice formation processes and radiative responses of clouds is only made possible with AC which is a state-of-the-art numerical model (Sec. 4.1). AC is designed in the WRF model framework and predicts both number and mass mixing ratios (double-moment approach) of cloud microphysical species such as cloud-liquid, cloud-ice, rain, snow, graupel/hail. Furthermore, AC has a semi-prognostic aerosol scheme and uses the GFDL radiation scheme interactively with cloud properties. AC provides a special advantage to track the number and mass mixing ratios of cloud-ice and snow initiated from various processes (heterogeneous and homogeneous nucleation and all four mechanisms of SIP) by prognostic variables known as tagging tracers (Sec. 4.1).

To address the research questions and to test the hypotheses described in Sec. 2, four cloud systems have been simulated using AC for a 3D mesoscale domain. These include events of summertime deep convection observed over Oklahoma, USA during the MC3E campaign on 1) 11 May 2011 and on 2) 20 May 2011, and wintertime 3) orographic clouds with embedded convection observed during the ACAPEX campaign over California on 7 February 2015, and 4) supercooled stratiform clouds observed on 17 February 2009 over Larkhill, UK during the APPRAISE campaign.

A striking feature of AC is that it adequately predicts the observed filtered ice particle number concentrations at all sampled levels in all four simulated cases. The reason for this adequate validation of ice particle number concentrations is mainly the general realism of the representation of all four SIP mechanisms in AC. Furthermore, other cloud properties such as LWC, cloud droplet mean sizes and

number concentrations, surface precipitation, TOA radiative fluxes, and radar reflectivity have also been validated adequately with the coincident observations from aircraft, ground-based instruments and from satellite for the simulated cases. It is further predicted that all these validated microphysical and macrophysical properties differ by less than ±30% from the coincident observations in all the simulated cloud systems.

A brief summary of results and discussions from each paper are given below:

6.1 Paper 1

The Influence of Multiple Groups of Biological Ice Nucleating Particles on Microphysical Properties of Mixed-phase Clouds Observed during MC3E

In this objective, the role of various groups of PBAPs as INPs is investigated in a simulated squall line observed on 20 May 2011 during MC3E. This is done by modifying the original EP (Phillips et al., 2013) in light of the formulation proposed by Patade et al. (2021), which is based on the field observations of various groups of PBAPs from Amazonia. The groups of biological particles analyzed here include fungal spores, pollen, bacteria, animal and plant detritus, and algae.

In the simulated MC3E clouds, it is predicted that the ice nucleus activity of all PBAPs forms only about 1% of the overall active INPs (Fig. 7a, b). The overall weakness of the simulated activity of PBAP INPs can be attributed to their low concentrations compared to other INPs over the study domain.
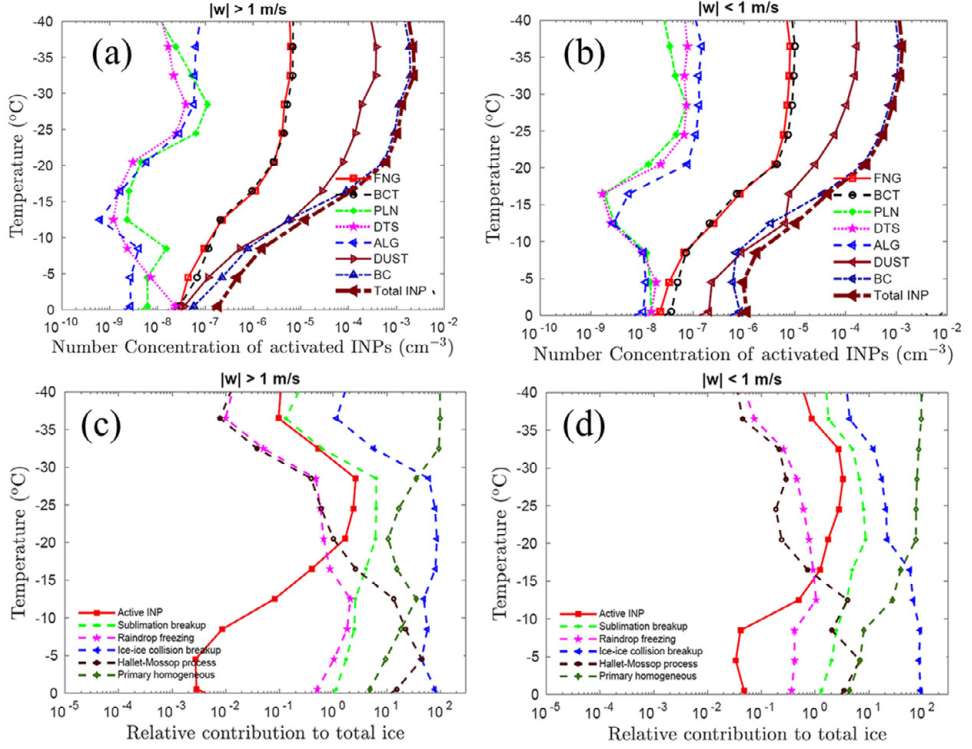
Figure 7. Predicted number concentrations of activated INPs from various PBAP species such as fungi (squares), bacteria (circles), pollen (asterisks), detritus (stars), and algae (backward pointing triangles) along with dust (forward pointing triangles) and black carbon (upward pointing triangles) as well as the total INPs, conditionally averaged for (a) convective ($|w| > 1$ m s^{-1}), and (b) stratiform ($|w| < 1$ m s^{-1}) regions in the simulated squall line observed during the MC3E (20 May 2011) campaign. Also shown is the relative contributions to the total ice concentrations from active INPs (squares), ice from homogeneous (pluses) and from various SIP processes such the HM process (circles), and from fragmentation during ice-ice collisions (backward pointing triangles), raindrop freezing (stars), and sublimation of dendritic snow and graupel (green line). All these quantities (a-d) from advective tagging tracers for the given process and are conditionally averaged for the (c) convective ($|w| > 1$ m s^{-1}), and (d) stratiform ($|w| < 1$ m s^{-1}) regions (adopted from Patade et al., 2022).

The conclusions from the validated simulation of a squall line from MC3E are as follows:

i. Regarding INP activity, at subzero levels warmer than -12°C, the overall INP concentration is chiefly (about 70-80%) from soot and mineral dust INPs. On the other hand, at levels colder than -12°C, soot INPs initiate about 95% of the total INP concentrations (Fig. 7a, b).

ii. At subzero levels warmer than -36°C, primary ice and SIP (through the HM process and fragmentation in ice-ice collisions) are predicted to initiate about 1% and 99% of the overall ice concentration respectively (Fig. 7c, d).

iii. Each PBAP group has different ice nucleation properties in terms of their efficiency of nucleating ice and onset temperatures.

iv. Processes of ice initiation such as heterogeneous and homogeneous ice nucleation and SIP have the least sensitivity with respect to PBAP INPs (Fig. 7c, d).

In summary, it is predicted that the groups of PBAPs predict the modest ice nucleus activity in the simulated convective storm. It is instead predicted that, in such continental convective clouds, the active INP number concentrations of mineral dust and soot are higher by about 1 (at -15°C) and 2 (-30°C) orders of magnitude than PBAP INPs. A more detailed discussion is from Patade et al. (2022). To conclude, PBAPs cause no significant change in the predicted microphysical and macrophysical properties of the simulated MC3E clouds.

6.2 Paper 2

Effects from Time Dependence of Ice Nuclei Activation for Contrasting Cloud Types

This paper investigates the role of time-dependent heterogeneous ice nucleation in overall ice initiation in the simulated summertime deep convection (MC3E, 11 May 2011), and wintertime orographic clouds with weak embedded convection (ACAPEX) and supercooled stratiform (APPRAISE) clouds. This is achieved by modifying the original EP in AC (Phillips et al. 2013) in light of the formulation proposed for time-dependent INP freezing by JK22, as discussed in Sec. 5.2. Furthermore, properties such as the mean sizes and number concentrations of cloud droplets, their LWC, and number concentrations of ice particles larger than 200 µm (in ACAPEX and MC3E), and 100 µm (in APPRAISE) predicted from the control simulations of the simulated cloud cases have been validated adequately with the coincident aircraft and ground-based measurements.

For all the simulated cases (MC3E, ACAPEX, and APPRAISE), it is predicted that the overall ice concentration is mostly dominated by various SIP mechanisms (Fig. 8b, d, f). By contrast, the inclusion of time-dependent INP freezing in the control runs of the simulated cases initiates about half an order of magnitude (in APPRAISE), and about 10% (in ACAPEX and MC3E) more ice particles. This is mostly due to the activity of dust and soot APs (10-50% increase, Fig, 8a, c, e), which is consistent with the previous laboratory observations (Wright et al., 2013; JK22).
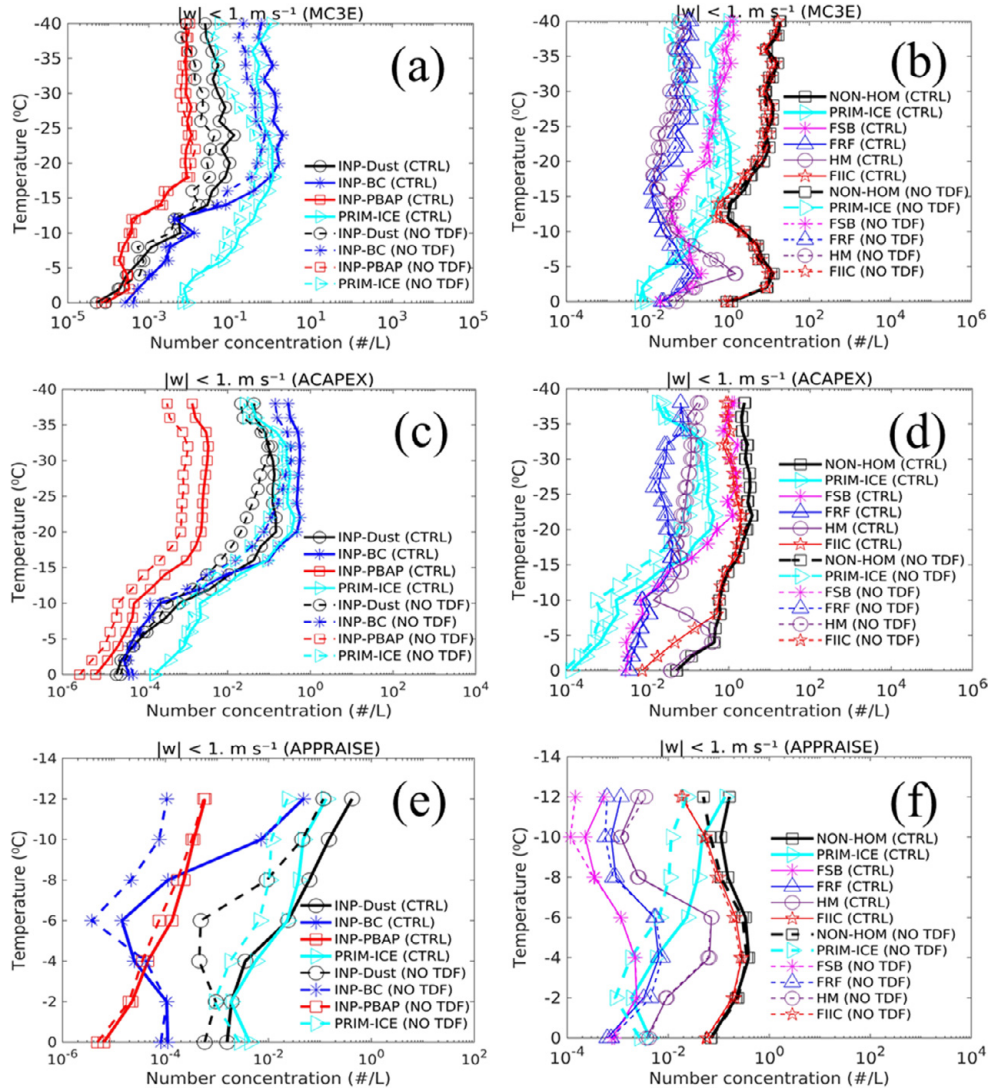
Figure 8. (left) The predicted number concentrations of active INPs conditionally averaged over stratiform regions ($|w| < 1$ m s^{-1}) from mineral dust (solid line with open circles), soot (solid line with asterisks), and PBAP (solid line with squares), and concentrations of heterogeneously nucleated ice (PRIM-ICE, forward-pointing triangles) for the (a) MC3E, (c) ACAPEX, and (e) APPRAISE cases. The same information is shown with dotted lines for the "no time-dependent INP" run. (right) The concentrations of total nonhomogeneous ice (total cloud ice and snow minus total homogeneous ice; solid line with squares) and various tracer terms defining SIP processes such as fragmentation during sublimation (FSB; solid line with asterisks), ice–ice collisions (FIIC; solid line with pentagrams) and raindrop freezing (FRF; solid line with upward-pointing triangles), and the HM process (HM; solid line with open circles) for the (b) MC3E, (d) ACAPEX, and (f) APPRAISE case, respectively. The same information is shown with the dotted lines for the "no time-dependent INP" run. To compare the number concentrations of heterogeneously nucleated ice and total nonhomogeneous ice, heterogeneously nucleated ice (PRIM-ICE; forward-pointing triangles) is also shown in the right column (adopted from Wa23a).

68

The conclusions of this paper are as follows:

i.   In the convective updrafts of ACAPEX and MC3E, at subzero levels warmer than -36°C, SIP (through the HM and fragmentation in ice-ice collisions) contribute about 80% (in ACAPEX, Fig. 8d) and 99% (in MC3E, Fig. 8b) to the overall ice concentration. While in their convective downdraft regions, fragmentation in sublimation form about 20-40% of the total ice concentration at these levels.

ii. For the simulated supercooled layer clouds in APPRAISE, the inclusion of time dependence in the control run predicts an increase of about 30% in the overall ice concentrations (Fig. 8f).

iii. In the episode of weak embedded convection, at subzero levels ($> -15^{\circ}$C), the SIP activity (through the HM process and fragmentation in ice-ice collisions) initiates about 75% of the overall ice concentration.

iv. By contrast, in the layer cloud episode of such clouds, the overall ice concentration is mostly dominated by heterogeneously nucleated ice (about 80% of the total ice concentration) whereas, in such clouds, the SIP activity is relatively weak, initiating only about 20% of the overall ice concentration. This is mainly due to relatively weak vertical velocities (few cm s^{-1}) and low water contents of cloud-liquid and ice-crystals in such clouds.

v.   Also, in the layer cloud episode, it is further predicted that droplets falling from the upper cloudy layer (-7 to -15°C) in the subsaturation region (0 to -7°C) evaporates and releases dust particles embedded in them. These dust particles form about 45% of the total dust mass in the subsaturated region. These dust particles, following weak vertical motions, may reactivate and nucleate ice once they reach the upper mixed-phase cloudy layer (-7 to -15°C).

vi. This reactivation following the recirculation of dust particles in such long-lived layer clouds is predicted to happen over 1-2 hours, which is less than the time (> 10 hours) required for time-dependent INP freezing to alter the predicted overall ice concentration appreciably.

vii. Hence, in the long-lived layer cloud episode of APPRAISE, the recirculation and reactivation of dust particles is the main source for continuous ice nucleation and precipitation production, and not the time dependence of INP freezing, as claimed by WI13.

To conclude, for the simulated cases (APPRAISE, ACAPEX, and MC3E), this paper suggests that, the presence of time dependence cause only a slight increase, by about 10-30%, in the overall ice concentration. In ACAPEX and MC3E, and in weak embedded convection episode of the APPRAISE, SIP is the main source for

the quasi-steady state of ice formation and precipitation. However, in the layer cloud episodes of APPRAISE, reactivation following the recirculation of dust INPs is the main cause of continuous ice nucleation and precipitation. This recycling of INPs is consistent with previous studies such as those by Fan et al. (2009) and Raatikainen et al. (2022). Hence, the time dependence of INP freezing can be neglected in numerical simulations of natural clouds. More details are from Wa23a.

6.3 Paper 3

Dependencies of Four Mechanisms of Secondary Ice Production on Cloud-Top temperature in a Continental Convective Storm.

In this paper, the dependency of various SIP mechanisms (Sec. 1.1.2) on cloud top temperature and their evolution with time in the simulated continental deep convection (MC3E 11 May 2011) have been studied. A measure of SIP is defined using the term known as the IE ratio which in the present study is defined as the ratio between the number concentrations of the total non-homogeneously nucleated ice and active INPs. Based on this metric, the development of convective clouds to become cumulonimbi is expected to exhibit a corresponding evolution in the overall intensity of ice multiplication (Sec. 1.1.2). Also, the activity of various SIP mechanisms is predicted to evolve with the age of the clouds. It is predicted that in the simulated deep convection (MC3E), at subzero levels warmer than -36^oC, the overall ice concentration is chiefly from SIP (about 80-95% of the total ice).
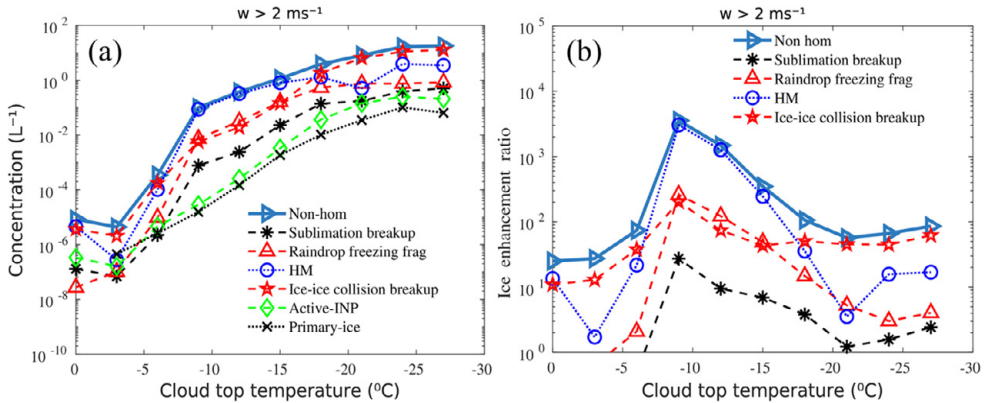
Figure 9. (a) Conditionally averaged ($w > 2$ m s^{-1}) predictions of concentrations of the active INPs (diamonds), primary ice (crosses), total nonhomogeneous ice (total ice from cloud ice and snow minus total homogeneous ice) (right-pointing triangles) as a function of cloud top temperatures and ice concentrations from various SIP processes tracked using tagging tracers such as the HM process (circles) and fragmentation during ice-ice collisions (stars), raindrop freezing (upward-pointing triangles), and sublimation of dendritic snow and graupel (asterisks). All these concentrations are at temperatures warmer than (by 1 to 7°C) the cloud top. All the terms are the geometric means of non-zero values. Also shown is a profile of (b) the predicted IE ratio as a function of cloud top temperature for convective cloudy updraft regions ($w > 2$ m s^{-1}) of the simulated MC3E (11 May 2011) clouds sampled using the cloud-top algorithm (Wa22, Appendix A).

The conclusions of this paper are as follows:

i. In the simulated deep convection (MC3E), the IE ratios are typically between 10 and 10^3 and are dependent on cloud-top temperatures (Fig. 9b). Furthermore, these IE ratios are mostly dominated by young developing convective turrets with top temperatures between -4 and $-20^{\circ}C$.

ii. Also, the simulated IE ratios are between 10 and 10^3 for cloud tops between 0 and $-30^{\circ}C$ with a peak (10^3) at about $-10^{\circ}C$ and a minimum (about 50) at cloud tops of about $-20^{\circ}C$. These predicted IE ratios are consistent with the previous aircraft study of a summertime continental convective storm by Hobbs et al. (1980) who reported a peak in IE ratio at cloud-top of about $-12^{\circ}C$.

iii. For such deep convection with relatively warm bases ($17^{\circ}C$), in young developing convective clouds (with tops warmer than $-15^{\circ}C$), the HM process of rime-splintering is predicted to dominate (about 70%) the overall ice concentration (Fig. 9a), creating IE ratios as high as 10^3. By contrast, fragmentation in ice-ice collisions prevails in typically less young convective clouds with tops colder than $-20^{\circ}C$, contributing more than 80% of the overall ice concentration there with IE ratios of about 10^2-10^3 (Fig. 9b).

iv. In convection (updrafts and downdrafts), SIP from fragmentation in ice-ice collisions prevails and forms more than 70% of the total ice concentrations. In downdrafts, fragmentation during sublimation is the second most dominant mechanism of ice multiplication, creating an IE ratio of about 10^2.

v. The simulated IE ratios increase with increasing convective ascent or descent and decrease with decreasing cloud top temperatures down to $-22^{\circ}C$.

vi. During the evolution of the simulated storm, in typically young convective turrets (tops $> -15^{\circ}C$), the initial explosive growth of ice concentrations is mainly from the fast HM process of rime-splintering which is consistent with Yano and Phillips (2011).

vii. According to their order of importance in initiating total ice in young developing convective clouds, the HM process can be ranked as the first, fragmentation during ice-ice collisions as the second, during raindrop freezing as the third, and during sublimation as the fourth most prolific SIP mechanism.

viii. In mature convective clouds (tops $< -40^{\circ}C$), fragmentation in ice-ice collisions is the first most prolific SIP process whereas the HM process is the second, raindrop freezing fragmentation is the third, and fragmentation during sublimation is the fourth important SIP process.

71

To summarize, this study adequately predicts the observed (Hobbs et al., 1980) classic dependency of IE ratio on cloud top temperature in young, developing convective clouds observed during MC3E (11 May 2011). In the simulated storm, the IE ratio peaks ($\sim 10^3$) at a characteristic cloud top temperature of about -10°C, which is consistent with the observations by Hobbs et al. (1980). It is further predicted that SIP (through the HM process of rime-splintering and fragmentation in ice-ice collisions) is the main cause for the explosive growth of ice concentrations, accounting for this pattern of IE ratio. This study also highlights that the age of the cloud, as it goes through its lifecycle, is of paramount importance for the relative balance of activities among various SIP mechanisms. More details are from Wa22.

6.4 Paper 4

Mechanisms for Indirect Effects from Solid Aerosol Particles on Continental Clouds and Radiation.

This paper investigates the mechanisms of the AIE from INPs in the simulated wintertime supercooled layer clouds during APPRAISE (18 February 2009) and summertime deep convective clouds during MC3E (11 May 2011). It is predicted that, in both cases, the inclusion of anthropogenic solid APs causes a decrease in the mean sizes of cloud droplets and ice crystals by about 15-30% at all cloudy levels whereas their number concentration increases by the same fraction. Also, for APPRAISE, anthropogenic INPs cause an increase of about 1% in the surface accumulated precipitation, mainly from the ice-crystal process (about 10% increase) being boosted.

Also, the contribution from the warm rain process to the surface precipitation is weakened by about 8%, mainly due to the relatively small sizes of cloud droplets. By contrast, for MC3E control runs, the inclusion of anthropogenic INPs predicts a decrease of about 1.5% in the surface precipitation due to the corresponding weakening in the precipitation from the warm rain and ice crystal processes, for the reasons noted above. This aerosol sensitivity of the precipitation also significantly alters the extents and optical thicknesses of the simulated clouds. For both cases, the inclusion of anthropogenic INPs causes an increase of about 1-3% in the horizontal and volumetric extent whereas their optical thicknesses increase by about 4% (in APPRAISE) and by 30% (in MC3E) due to weakened removal of condensate by precipitation.

In both simulations, anthropogenically increased solid aerosols significantly affect the net AIE, mainly from glaciated clouds (about 80% of the net AIE) whereas liquid-only clouds contribute only about 20% to the net AIE (Fig. 10a-d). In APPRAISE (layer-clouds) the net AIE is a cloud albedo indirect effect (cooling) since precipitation is so weak. By contrast, in MC3E (deep convection), the net AIE

is chiefly from the lifetime effect (warming). Furthermore, this study also analyses the impact on the simulated AIEs from ice initiation processes such as SIP and time-dependent INP freezing.
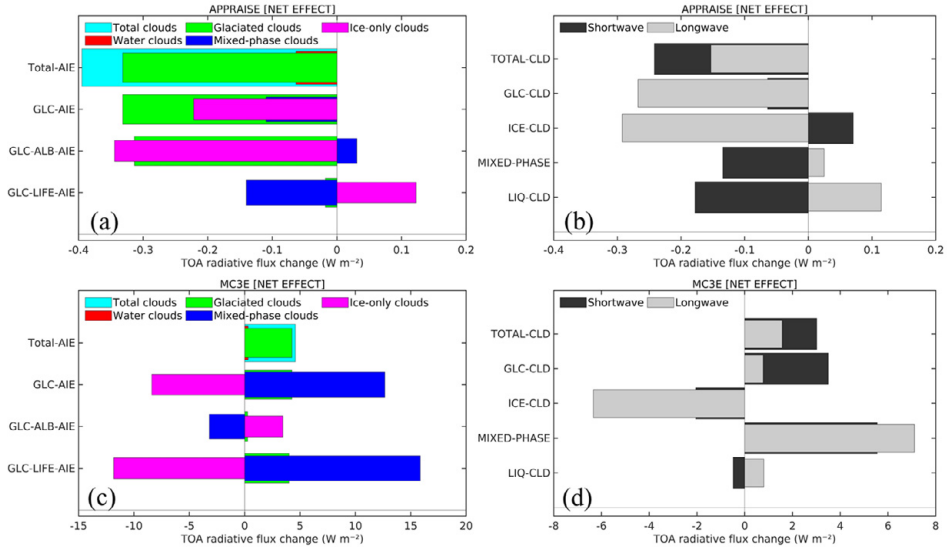
Figure 10. Net aerosol indirect effects at the TOA from solid aerosols on glaciated clouds predicted from Tests A and B (Sec. 5.4) from the control simulations of (a) APPRAISE and (c) MC3E cases. Corresponding changes in the shortwave and longwave components of radiation, unconditionally averaged over the whole domain, at the TOA, are shown for (b) APPRAISE and (d) MC3E cases. Here, abbreviations: GLC-AIE= Glaciated Clouds AIE, GLC-ALB-AIE= Glaciated cloud Albedo-Emissivity AIE, GLC-LIFE-AIE= Glaciated Cloud Lifetime AIE (Adopted from Wa23b).

The conclusions of this study are as follows:

1)   For supercooled layer clouds in APPRAISE, at the TOA:

i.   In the control run (Fig. 10a), anthropogenic solid APs exert a net cooling, with a net AIE of about -0.4 W m^{-2} which is dominated by the albedo-emissivity AIE from glaciated clouds (-0.3 W m^{-2}). This is mainly because increased reflectivity of such clouds due to more numerous cloud droplets and ice crystals, as discussed above.

ii.   Furthermore, this net cooling is mostly due to more reflection (-0.24 W m^{-2}) of downward SW flux to space from optically thick liquid-only and mixed-phase clouds. Moreover, being optically thinner, ice-only clouds allow more LW (-0.3 W m^{-2}) radiation to leave the climate system at the TOA (Fig. 10b).

iii.   By contrast, the lifetime AIE (-0.018 W m^{-2}) from such clouds is relatively low (about 5% of the net AIE), chiefly due to the weakness of precipitation

from such thin layer clouds. This causes a weaker aerosol sensitivity of their horizontal and volumetric extents and of the surface precipitation than in the microphysical properties of these clouds.

iv. Also, artificially prohibiting SIP from such clouds has only a slight impact (about a 2% decrease) on the net AIE from anthropogenic solid aerosols. This is because of the relative weakness of SIP processes in such clouds (Wa23b).

v. Furthermore, in such layer clouds, when time-dependent INP freezing is prohibited, the net AIE from anthropogenic solid APs is weakened to about 65% of its control value (-0.4 W m^{-2}). This weakening is chiefly from the artificially increased reflection of the incoming SW flux from liquid-only (-0.26 W m^{-2}) and mixed-phase (-0.2 W m^{-2}) clouds as they become optically thicker in the present-day condition.

2) For summertime deep convection (MC3E, 11 May 2011), at the TOA:
 i. In the control run, anthropogenic solid APs exert a net warming (4.5 W m^{-2}) of the climate system (Fig. 10c) and is mainly from the lifetime AIE from glaciated clouds (4.3 W m^{-2}). This net warming from such deep convective clouds is consistent with a previous modelling study by Fan et al. (2012).

ii. Also, this net AIE is chiefly because the inclusion of anthropogenic INPs causes mixed-phase clouds to be less extensive, allowing more downward SW flux (5.5 W m^{-2}) to enter the climate system (Fig. 10d). Also, these clouds are optically thicker, causing more partial emission of LW flux (7 W m^{-2}) to the surface, and less emission of outgoing LW radiation to space (Fig. 10d). But overall, the solar warming by mixed-phase cloud changes are more important, as longwave effects cancel out partially among cloud types in MC3E.

iii. In such deep convective clouds, by artificially prohibiting SIP, anthropogenic INPs cause a sharp decrease (by 52%) in the net warming predicted (2.2 W m^{-2}) in the control run (4.5 W m^{-2}). Also, without SIP, the overall AIE (2.2 W m^{-2}) is mainly dominated by the lifetime AIE from glaciated clouds (7 W m^{-2}). Also, both with and without SIP, anthropogenic INPs cause mixed-phase clouds to grow less extensive (by about 3%), allowing more downward SW flux (6-9 W m^{-2}) to enter the climate system.

iv. Also, when time dependence is artificially prohibited from such deep convective clouds, extra INPs cause a weak climate warming (1 W m^{-2}), which, when time dependence is included, would increase by 80% (4.58 W m^{-2}). This is chiefly from a decrease of about 105% in the net AIE from glaciated clouds, due to the inclusion of extra INPs, when time dependence is prohibited from the control run.

74

v.   When time dependence is artificially prohibited from the simulated deep convection, ice-only clouds become less horizontally extensive, allowing more SW flux to enter the climate system (2.3 W m^{-2}). However, this warming from ice-only clouds is canceled out by more reflection of incoming SW flux (-2.2 W m^{-2}) to space from mixed-phase clouds due to a higher mass of cloud condensate in the upper half of the mixed-phase levels.

vi.   By contrast, when time dependence is included in the control run, extra INPs cause a decrease by about 10% in both horizontal and volumetric extent of mixed-phase clouds, allowing more incoming SW radiation (6 W m^{-2}) to enter the climate system. Also, being optically thicker in the present-day condition, these clouds cause more absorption of outgoing LW flux (7.5 W m^{-2}).

vii.   However, with time dependence, in the presence of extra INPs, SW warming from mixed-phase clouds prevail. This is mainly because the net LW warming from mixed-phase clouds is canceled out by a net LW cooling (-6 W m^{-2}) from ice-only clouds, as they are optically thinner (Wa23b).

Additionally, this paper proposes two new indirect effects that are associated with ice formation processes. These are, 1) the 'SIP' indirect effect, and 2) the 'Time-dependent INP' indirect effect. Table 4 below summarizes the net AIE and indirect effects from ice initiation processes such as time dependent INP freezing and SIP. It is predicted that for layer clouds in APPRAISE, both SIP and time-dependent INP indirect effects are weak, forming about 0.25% and 30% of the net AIE. By contrast, for deep convective clouds in MC3E, both SIP and time-dependent INP indirect effects form about 50-80% of the net AIE.

Table 4. The net AIE for the simulated APPRAISE and MC3E clouds and the indirect effects from ice initiation processes such as SIP and time dependent INP freezing.

Simulation	Net AIE	Indirect effect (W m^{-2})	
		from ice initiation process	
		SIP	Time dependent INP freezing
APPRAISE	-0.4	-0.0005	-0.13
MC3E	4.58	2.4	3.6

To conclude, this paper found that at the TOA, increasing anthropogenic pollution of solid aerosols causes a moderate cooling of the climate system via supercooled stratiform clouds. In such wintertime layer clouds, more reflection of SW flux (from liquid-only and mixed-phase clouds) contributes about 60% to the net cooling. Furthermore, in such wintertime layer clouds, more emission of outgoing LW flux

to space, from less extensive and optically thinner ice-only clouds, form about 40% of the net cooling.

On the other hand, from summertime deep convective clouds in MC3E, anthropogenically emitted solid APs cause a strong warming of the present-day climate system which is mainly dominated by more SW flux (about 80% of the net warming) entering the climate system. Furthermore, for both cases, the net AIE has a higher aerosol sensitivity from glaciated clouds. This is also true for AIEs predicted in the absence of ice initiation processes such as SIP and time dependent heterogeneous ice nucleation. Also, for MC3E, the inclusion of anthropogenic INPs causes mixed-phase clouds to exert both SW and LW warming. This is because, being optically thicker in the present-day condition, they reflect more incoming SW radiation to space, causing solar warming at the TOA. Also, these clouds, at relatively lower levels ($> -36^{\circ}$C) in the atmosphere, cause more emission of LW radiation to space than to the surface, hence LW warming of the present-day climate system at the TOA (Fig. 10d).

Generally, since they are cold, high-level clouds (e.g., cirriform) contribute to greenhouse warming as they re-emit less LW flux to space than the clear-sky atmosphere, causing a net LW warming of the troposphere and surface. This is explicable in terms of Stefan-Boltzmann law which states that the amount of energy radiated by an object is proportional to the fourth power of its temperature (Liou, 2002). However, for MC3E, the inclusion of anthropogenic INPs causes high-level clouds to allow more emission of LW flux to space (-6 W m^{-2}, Fig. 10d) at the TOA. This is because for high-level clouds in MC3E, the inclusion of anthropogenic INPs causes a decrease of about 20% in the overall ice concentration. This is explicable in terms of less upwelling of cloud droplets at cirriform levels (levels colder than -36°C), due to weaker ascent (about 5%) and hence less homogeneous freezing. This reduction in the number concentrations of ice particles in such high-level clouds allows more emission of LW flux to space, despite being relatively colder than pre-industrially. This is because the cloud emissivity is reduced, with less absorption of outgoing LW radiation lost to space. In short, with lower cloud emissivity, the greenhouse warming effect of the high-level clouds is weakened, causing an LW cooling of the troposphere. Also, being optically thicker in the present-day conditions (Wa23b, their Fig. 3h), such high-level clouds reflect more incoming SW radiation to space, resulting in a net solar cooling (-2 W m^{-2}).

Finally, this study concludes that anthropogenically boosted solid aerosols can significantly affect the micro- and macrophysical and hence the radiative properties of glaciated clouds. Also, SIP and time-dependent INP freezing can have a higher (up to 80% change) aerosol-sensitivity of the simulated net AIEs. More details are given by Wa23b.

7. Key Findings

- In continental conditions, the ice nucleus activity of PBAPs is weak compared to the relative activities of other INPs such as mineral dust.

- The time dependence of heterogeneous ice nucleation has a negligible contribution to the overall ice concentration in the simulated cloud systems.

- Both MC3E and ACAPEX clouds involved deeper clouds (tops as cold as −36ºC) with more intense precipitation through ice crystal process, driving more vigorous SIP.

- For APPRAISE, when weak embedded convection was present, various SIP processes are responsible for the quasi-steady ice formation and precipitation over long periods of many hours in the wintertime stratiform clouds.

- In layer cloud episode of APPRAISE, SIP is relatively weak and reactivation following recirculation of dust particles is the main source for the observed continuous ice nucleation and precipitation and not the time dependence of INP freezing.

- The concerted combination of various SIP processes adequately explains the observed discrepancy between the number concentrations of the available active INPs and the total ice particles in the simulated clouds.

- The dependency of IE ratio on cloud top temperature in different stages of the convective clouds is strongly dependent on various SIP mechanisms. In young developing convective clouds, the rapid glaciation is mainly from the relatively fast HM process whereas in mature convective clouds, fragmentation in ice-ice collisions prevails over longer times.

- In APPRAISE and MC3E, anthropogenically increased solid APs, through their INP and CCN activity, can significantly affect the micro- and macrophysical and hence radiative properties. Also, for such clouds, the presence of ice formation processes such as SIP and time dependent INP freezing has a great impact on the simulated net AIEs (about 50-80% increase).

- For the simulated APPRAISE clouds, the net AIE is about −0.39 W m⁻². Also, the SIP and time-dependent INP indirect effects are about −0.0005

and -0.13 W m^{-2} respectively. For deep convective clouds in MC3E, the net AIE is 4.58 W m^{-2} whereas the SIP and time-dependent INP indirect effects are about 2.4 and 3.6 W m^{-2} respectively.

- Thus, for deep convection, both SIP and time dependence of INP activity act together to amplify the indirect effect from anthropogenic solid APs, which is predominantly solar warming from mixed-phase clouds becoming less extensive as precipitation from the ice crystal process intensifies, exhibiting the lifetime effect.

- This study disproved the hypothesis that PBAP INPs can greatly affect the micro- (Sec. 2A[i]) and macrophysical (Sec. 2A[ii]) properties of the simulated MC3E clouds. Also, in the simulated clouds (APPRAISE, MC3E, and ACAPEX), the hypothesis that the time dependence of INP freezing forms the overall ice concentrations (Sec. 2B[i]) and is the main cause for the quasi-steady state of ice nucleation and precipitation (Sec. 2B[ii]) are disproved.

- For MC3E clouds, the hypothesis that various SIP processes can form the observed number concentration of ice particles in the simulated clouds is verified (Sec. 2C[i]). Also, the hypothesis that the evolution of various SIP processes strongly depends on the cloud-top temperature is verified (Sec. 2C[ii]). This study also numerically verified the aircraft observed classic dependency of IE ratio on cloud-top temperature in convective clouds (Sec. 2C[iii]).

- Moreover, the hypothesis that anthropogenically increased solid APs, via glaciated clouds, can significantly alter the micro-, macrophysical and radiative properties of the simulated clouds is verified in the present study (Sec. 2D[i, ii]). It is also verified that SIP and time dependence of INP freezing can greatly alter the radiative properties of the simulated clouds (Sec. 2D[iii]).

8. Bibliography

Albrecht, B. A., 1989. Aerosols, cloud microphysics, and fractional cloudiness, *Science*, 245, 1227– 1230.

Ansmann, A., Tesche, M., Althausen, D., Müller, D., Seifert, P., Freudenthaler, V., Heese, B., Wiegner, M., Pisani, G., Knippertz, P. and Dubovik, O., 2008. Influence of Saharan dust on cloud glaciation in southern Morocco during the Saharan Mineral Dust Experiment. *Journal of Geophysical Research: Atmospheres*, *113*(D4).

Bacon, N.J., Swanson, B.D., Baker, M.B. and Davis, E.J., 1998. Breakup of levitated frost particles. *Journal of Geophysical Research: Atmospheres*, *103*(D12), pp.13763-13775.

Blyth, A.M. and Latham, J., 1993. Development of ice and precipitation in New Mexican summertime cumulus clouds. *Quarterly Journal of the Royal Meteorological Society*, *119*(509), pp.91-120.

Bond, T.C., Doherty, S.J., Fahey, D.W., Forster, P.M., Berntsen, T., DeAngelo, B.J., Flanner, M.G., Ghan, S., Kärcher, B., Koch, D. and Kinne, S., 2013. Bounding the role of black carbon in the climate system: A scientific assessment. *Journal of geophysical research: Atmospheres*, *118*(11), pp.5380-5552.

Boucher, O., D. Randall, P. Artaxo, C. Bretherton, G. Feingold, P. Forster, V.-M. Kerminen, Y. Kondo, H. Liao, U. Lohmann, P. Rasch, S.K. Satheesh, S. Sherwood, B. Stevens and X.Y. Zhang, 2013: Clouds and Aerosols. In: Climate Change 2013: The Physical Science Basis. Contribution of Working Group I to the Fifth Assessment Report of the Intergovernmental Panel on Climate Change [Stocker, T.F., D. Qin, G.-K. Plattner, M. Tignor, S.K. Allen, J. Boschung, A. Nauels, Y. Xia, V. Bex and P.M. Midgley (eds.)]. Cambridge University Press, Cambridge, United Kingdom and New York, NY, USA.

Cantrell, W. and Heymsfield, A., 2005. Production of ice in tropospheric clouds: A review. *Bulletin of the American Meteorological Society*, *86*(6), pp.795-808.

Charlson, R.J., Schwartz, S.E., Hales, J.M., Cess, R.D., Coakley Jr, J.A., Hansen, J.E. and Hofmann, D.J., 1992. Climate forcing by anthropogenic aerosols. *Science*, *255*(5043), pp.423-430.

Chen, J.P., Hazra, A. and Levin, Z., 2008. Parameterizing ice nucleation rates using contact angle and activation energy derived from laboratory data. *Atmospheric Chemistry and Physics*, *8*(24), pp.7431-7449.

Chouippe, A., Krayer, M., Uhlmann, M., Dušek, J., Kiselev, A. and Leisner, T., 2019. Heat and water vapor transfer in the wake of a falling ice sphere and its implication for secondary ice formation in clouds. *New Journal of Physics*, *21*(4), p.043043.

Christensen, M.W., Chen, Y.C. and Stephens, G.L., 2016. Aerosol indirect effect dictated by liquid clouds. *Journal of Geophysical Research: Atmospheres*, *121*(24), pp.14-636.

Clarke, A.D., Shinozuka, Y., Kapustin, V.N., Howell, S., Huebert, B., Doherty, S., Anderson, T., Covert, D., Anderson, J., Hua, X. and Moore, K.G., 2004. Size distributions and mixtures of dust and black carbon aerosol in Asian outflow: Physiochemistry and optical properties. *Journal of Geophysical Research: Atmospheres*, *109*(D15).

Crosier, J., Bower, K.N., Choularton, T.W., Westbrook, C.D., Connolly, P.J., Cui, Z.Q., Crawford, I.P., Capes, G.L., Coe, H., Dorsey, J.R. and Williams, P.I., 2011. Observations of ice multiplication in a weakly convective cell embedded in supercooled mid-level stratus. *Atmospheric Chemistry and Physics*, *11*(1), pp.257-273.

Cziczo, D.J., Froyd, K.D., Hoose, C., Jensen, E.J., Diao, M., Zondlo, M.A., Smith, J.B., Twohy, C.H. and Murphy, D.M., 2013. Clarifying the dominant sources and mechanisms of cirrus cloud formation. *Science*, *340*(6138), pp.1320-1324.

Dagan, G., Koren, I. and Altaratz, O., 2015. Aerosol effects on the timing of warm rain processes. *Geophysical Research Letters*, *42*(11), pp.4590-4598.

DeMott, P.J., 1990. An exploratory study of ice nucleation by soot aerosols. *Journal of Applied Meteorology and Climatology*, *29*(10), pp.1072-1079.

DeMott, P.J., Finnegan, W.G. and Grant, L.O., 1983. An application of chemical kinetic theory and methodology to characterize the ice nucleating properties of aerosols used for weather modification. *Journal of Applied Meteorology and Climatology*, *22*(7), pp.1190-1203.

DeMott, P.J., Sassen, K., Poellot, M.R., Baumgardner, D., Rogers, D.C., Brooks, S.D., Prenni, A.J. and Kreidenweis, S.M., 2003. African dust aerosols as atmospheric ice nuclei. *Geophysical Research Letters*, *30*(14).

Deshmukh, A., Phillips, V.T., Bansemer, A., Patade, S. and Waman, D., 2022. New empirical formulation for the sublimational breakup of graupel and dendritic snow. *Journal of the Atmospheric Sciences*, *79*(1), pp.317-336.

Després, V., Huffman, J.A., Burrows, S.M., Hoose, C., Safatov, A., Buryak, G., Fröhlich-Nowoisky, J., Elbert, W., Andreae, M., Pöschl, U. and Jaenicke, R., 2012. Primary biological aerosol particles in the atmosphere: a review. *Tellus B: Chemical and Physical Meteorology*, *64*(1), p.15598.

Dong, Y., Oraltay, R.G. and Hallett, J., 1994. Ice particle generation during evaporation. *Atmospheric research*, *32*(1-4), pp.45-53.

Dudhia, J., 1989. Numerical study of convection observed during the winter monsoon experiment using a mesoscale two-dimensional model. *Journal of Atmospheric Sciences*, *46*(20), pp.3077-3107.

Dye, J.E. and Hobbs, P.V., 1968. The influence of environmental parameters on the freezing and fragmentation of suspended water drops. *Journal of Atmospheric Sciences*, *25*(1), pp.82-96.

Eidhammer, T., DeMott, P.J., Prenni, A.J., Petters, M.D., Twohy, C.H., Rogers, D.C., Stith, J., Heymsfield, A., Wang, Z., Pratt, K.A. and Prather, K.A., 2010. Ice initiation by aerosol particles: Measured and predicted ice nuclei concentrations versus measured ice crystal concentrations in an orographic wave cloud. *Journal of the Atmospheric Sciences*, *67*(8), pp.2417-2436.

Ervens, B., 2015. Modeling the processing of aerosol and trace gases in clouds and fogs. *Chemical reviews*, *115*(10), pp.4157-4198.

Fan, J., Ovtchinnikov, M., Comstock, J.M., McFarlane, S.A. and Khain, A., 2009. Ice formation in Arctic mixed-phase clouds: Insights from a 3-D cloud-resolving model with size-resolved aerosol and cloud microphysics. *Journal of Geophysical Research: Atmospheres*, *114*(D4).

Fan, J., Rosenfeld, D., Ding, Y., Leung, L.R. and Li, Z., 2012. Potential aerosol indirect effects on atmospheric circulation and radiative forcing through deep convection. *Geophysical Research Letters*, *39*(9).

Field, P.R. and Heymsfield, A.J., 2015. Importance of snow to global precipitation. *Geophysical Research Letters*, *42*(21), pp.9512-9520.

Field, P.R., Heymsfield, A.J. and Bansemer, A., 2006. Shattering and particle interarrival times measured by optical array probes in ice clouds. *Journal of Atmospheric and Oceanic Technology*, *23*(10), pp.1357-1371.

Field, P.R., Lawson, R.P., Brown, P.R., Lloyd, G., Westbrook, C., Moisseev, D., Miltenberger, A., Nenes, A., Blyth, A., Choularton, T. and Connolly, P., 2017. Secondary ice production: Current state of the science and recommendations for the future. *Meteorological Monographs*, *58*, pp.7-1.

Flossmann, A.I., 1998. Interaction of aerosol particles and clouds. *Journal of the atmospheric sciences*, *55*(5), pp.879-887.

Flossmann, A.I., Manton, M.J., Abshaev, A., Bruintjet, R., Murakami, M., Prabhakaran, T. and Yao, Z., 2018. *Peer review report on global precipitation enhancement activities* (Doctoral dissertation, WMO).

Fornea, A.P., Brooks, S.D., Dooley, J.B. and Saha, A., 2009. Heterogeneous freezing of ice on atmospheric aerosols containing ash, soot, and soil. *Journal of Geophysical Research: Atmospheres*, *114*(D13).

Freidenreich, S.M. and Ramaswamy, V., 1999. A new multiple-band solar radiative parameterization for general circulation models. *Journal of Geophysical Research: Atmospheres*, *104*(D24), pp.31389-31409.

Fridlind, A.M., Li, X., Wu, D., van Lier-Walqui, M., Ackerman, A.S., Tao, W.K., McFarquhar, G.M., Wu, W., Dong, X., Wang, J. and Ryzhkov, A., 2017. Derivation of aerosol profiles for MC3E convection studies and use in simulations of the 20 May squall line case. *Atmospheric Chemistry and Physics*, *17*(9), pp.5947-5972.

Gao, W., Xue, L., Liu, L., Lu, C., Yun, Y. and Zhou, W., 2021. A study of the fraction of warm rain in a pre-summer rainfall event over South China. *Atmospheric Research*, *262*, p.105792.

Gayatri, K., Patade, S., Fan, J. and Prabhakaran, T., 2022. Pathways of precipitation formation in different thermodynamic and aerosol environments over the Indian Peninsula. *Atmospheric Research*, *266*, p.105934.

Georgakaki, P., Sotiropoulou, G., Vignon, É., Billault-Roux, A.C., Berne, A. and Nenes, A., 2022. Secondary ice production processes in wintertime alpine mixed-phase clouds. *Atmospheric Chemistry and Physics*, *22*(3), pp.1965-1988.

Gettelman, A., Kay, J.E. and Shell, K.M., 2012. The evolution of climate sensitivity and climate feedbacks in the Community Atmosphere Model. *Journal of Climate*, *25*(5), pp.1453-1469.

Grabowski, W.W., Wu, X. and Moncrieff, M.W., 1999. Cloud resolving modeling of tropical cloud systems during Phase III of GATE. Part III: Effects of cloud microphysics. *Journal of the atmospheric sciences*, *56*(14), pp.2384-2402.

Griggs, D.J. and Choularton, T.W., 1983. Freezing modes of riming droplets with application to ice splinter production. *Quarterly Journal of the Royal Meteorological Society*, *109*(459), pp.243-253.

Gupta, A.K., Deshmukh, A., Waman, D., Patade, S., Jadav, A., Phillips, V.T., Bansemer, A., Martins, J.A. and Gonçalves, F.L., 2023. The microphysics of the warm-rain and ice crystal processes of precipitation in simulated continental convective storms. *Communications Earth & Environment*, *4*(1), p.226.

Hallett, J. and Mossop, S.C., 1974. Production of secondary ice particles during the riming process. *Nature*, *249*(5452), pp.26-28.

Hallett, J., Sax, R.I., Lamb, D. and Murty, A.R., 1978. Aircraft measurements of ice in Florida cumuli. *Quarterly Journal of the Royal Meteorological Society*, *104*(441), pp.631-651.

Harris-Hobbs, R.L. and Cooper, W.A., 1987. Field evidence supporting quantitative predictions of secondary ice production rates. *Journal of Atmospheric Sciences*, *44*(7), pp.1071-1082.

Hartmann, D.L., Ockert-Bell, M.E. and Michelsen, M.L., 1992. The effect of cloud type on Earth's energy balance: Global analysis. *Journal of Climate*, *5*(11), pp.1281-1304.

Hartmann, S., Seidel, J., Keinert, A., Kiselev, A., Leisner, T. and Stratmann, F., 2023. *Secondary ice production-No evidence of a productive rime-splintering mechanisms during dry and wet growth* (No. EGU23-11199). Copernicus Meetings.

Haywood, J. and Boucher, O., 2000. Estimates of the direct and indirect radiative forcing due to tropospheric aerosols: A review. *Reviews of geophysics*, *38*(4), pp.513-543.

Heymsfield, A. and Willis, P., 2014. Cloud conditions favoring secondary ice particle production in tropical maritime convection. *Journal of the Atmospheric Sciences*, *71*(12), pp.4500-4526.

Hill, A.A. and Dobbie, S., 2008. The impact of aerosols on non-precipitating marine stratocumulus. II: The semi-direct effect. *Quarterly Journal of the Royal Meteorological Society: A journal of the atmospheric sciences, applied meteorology and physical oceanography*, *134*(634), pp.1155-1165.

Hobbs, P.V. and Locatelli, J.D., 1969. Ice nuclei from a natural forest fire. *Journal of Applied Meteorology and Climatology*, *8*(5), pp.833-834.

Hobbs, P.V. and Radke, L.F., 1969. Cloud condensation nuclei from a simulated forest fire. *Science*, *163*(3864), pp.279-280.

Hobbs, P.V. and Rangno, A.L., 1985. Ice particle concentrations in clouds. *Journal of the atmospheric sciences*, *42*(23), pp.2523-2549.

Hobbs, P.V., 1969. Ice multiplication in clouds. *J. Atmos. Sci*, *26*(2), pp.315-318.

Hobbs, P.V., Politovich, M.K. and Radke, L.F., 1980. The structures of summer convective clouds in eastern Montana. I: Natural clouds. *Journal of Applied Meteorology and Climatology*, *19*(6), pp.645-663.

Hobbs, P.V., R. Farber, 1972. Fragmentation of ice particles in clouds. *J. Rech. Atmos.*, *6*, pp.245-258.

Hong, S.Y. and Pan, H.L., 1996. Nonlocal boundary layer vertical diffusion in a medium-range forecast model. *Monthly weather review*, *124*(10), pp.2322-2339.

Hoose, C. and Möhler, O., 2012. Heterogeneous ice nucleation on atmospheric aerosols: a review of results from laboratory experiments. *Atmospheric Chemistry and Physics*, *12*(20), pp.9817-9854.

Houghton, J.T., Ding, Y.D.J.G., Griggs, D.J., Noguer, M., van der Linden, P.J., Dai, X., Maskell, K. and Johnson, C.A., 2001. *Climate change 2001*.

Huang, Y., Blyth, A.M., Brown, P.R., Choularton, T.W. and Cui, Z., 2017. Factors controlling secondary ice production in cumulus clouds. *Quarterly Journal of the Royal Meteorological Society*, *143*(703), pp.1021-1031.

Jaenicke, R., 2005. Abundance of cellular material and proteins in the atmosphere. *Science*, *308*(5718), pp.73-73.

Jakobsson, J.K., Waman, D.B., Phillips, V.T. and Bjerring Kristensen, T., 2022. Time dependence of heterogeneous ice nucleation by ambient aerosols: laboratory observations and a formulation for models. *Atmospheric Chemistry and Physics*, *22*(10), pp.6717-6748.

James, R.L., Phillips, V.T. and Connolly, P.J., 2021. Secondary ice production during the break-up of freezing water drops on impact with ice particles. *Atmospheric Chemistry and Physics*, *21*(24), pp.18519-18530.

Jefferson, A., 2011. Aerosol observing system (AOS) handbook. *ARMTR-014, US Dep. of Energy, Washington, DC*, *10*.

Jensen, M.P., Petersen, W.A., Bansemer, A., Bharadwaj, N., Carey, L.D., Cecil, D.J., Collis, S.M., Del Genio, A.D., Dolan, B., Gerlach, J. and Giangrande, S.E., 2016. The midlatitude continental convective clouds experiment (MC3E). *Bulletin of the American Meteorological Society*, *97*(9), pp.1667-1686.

Johnson, B.T., Shine, K.P. and Forster, P.M., 2004. The semi-direct aerosol effect: Impact of absorbing aerosols on marine stratocumulus. *Quarterly Journal of the Royal Meteorological Society*, *130*(599), pp.1407-1422.

Johnson, D.A. and Hallett, J., 1968. Freezing and shattering of supercooled water drops. *Quarterly Journal of the Royal Meteorological Society*, *94*(402), pp.468-482.

Kanji, Z.A., Ladino, L.A., Wex, H., Boose, Y., Burkert-Kohn, M., Cziczo, D.J. and Krämer, M., 2017. Overview of ice nucleating particles. *Meteorological Monographs*, *58*, pp.1-1.

Keinert, A., Spannagel, D., Leisner, T. and Kiselev, A., 2020. Secondary ice production upon freezing of freely falling drizzle droplets. *Journal of the Atmospheric Sciences*, *77*(8), pp.2959-2967.

Khain, A.P. and Pinsky, M., 2018. *Physical processes in clouds and cloud modeling*. Cambridge University Press.

King, M.D., Platnick, S., Menzel, W.P., Ackerman, S.A. and Hubanks, P.A., 2013. Spatial and temporal distribution of clouds observed by MODIS onboard the Terra and Aqua satellites. *IEEE transactions on geoscience and remote sensing*, *51*(7), pp.3826-3852.

Koch, D. and Del Genio, A.D., 2010. Black carbon semi-direct effects on cloud cover: review and synthesis. *Atmospheric Chemistry and Physics*, *10*(16), pp.7685-7696.

Koehler, K.A., DeMott, P.J., Kreidenweis, S.M., Popovicheva, O.B., Petters, M.D., Carrico, C.M., Kireeva, E.D., Khokhlova, T.D. and Shonija, N.K., 2009. Cloud condensation nuclei and ice nucleation activity of hydrophobic and hydrophilic soot particles. *Physical Chemistry Chemical Physics*, *11*(36), pp.7906-7920.

Koop, T., Luo, B., Tsias, A. and Peter, T., 2000. Water activity as the determinant for homogeneous ice nucleation in aqueous solutions. *Nature*, *406*(6796), pp.611-614.

Korolev, A. and Leisner, T., 2020. Review of experimental studies of secondary ice production. *Atmospheric Chemistry and Physics*, *20*(20), pp.11767-11797.

Korolev, A., Heckman, I., Wolde, M., Ackerman, A.S., Fridlind, A.M., Ladino, L.A., Lawson, R.P., Milbrandt, J. and Williams, E., 2020. A new look at the environmental conditions favorable to secondary ice production. *Atmospheric Chemistry and Physics*, *20*(3), pp.1391-1429.

Korolev, A.V., Emery, E.F., Strapp, J.W., Cober, S.G., Isaac, G.A., Wasey, M. and Marcotte, D., 2011. Small ice particles in tropospheric clouds: Fact or artifact? Airborne Icing Instrumentation Evaluation Experiment. *Bulletin of the American Meteorological Society*, *92*(8), pp.967-973.

Kudzotsa, I., Phillips, V.T. and Dobbie, S., 2016. Aerosol indirect effects on glaciated clouds. Part 2: Sensitivity tests using solute aerosols. *Quarterly Journal of the Royal Meteorological Society*, *142*(698), pp.1970-1981.

Kudzotsa, I., Phillips, V.T., Dobbie, S., Formenton, M., Sun, J., Allen, G., Bansemer, A., Spracklen, D. and Pringle, K., 2016. Aerosol indirect effects on glaciated clouds. Part I: Model description. *Quarterly Journal of the Royal Meteorological Society*, *142*(698), pp.1958-1969.

Ladino, L.A., Korolev, A., Heckman, I., Wolde, M., Fridlind, A.M. and Ackerman, A.S., 2017. On the role of ice-nucleating aerosol in the formation of ice particles in tropical mesoscale convective systems. *Geophysical research letters*, *44*(3), pp.1574-1582.

Langham, E.J. and Mason, B.J.N., 1958. The heterogeneous and homogeneous nucleation of supercooled water. *Proceedings of the Royal Society of London. Series A. Mathematical and Physical Sciences*, *247*(1251), pp.493-504.

Langmuir, I., 1948. The growth of particles in smokes and clouds and the production of snow from supercooled clouds. *Proceedings of the American Philosophical Society*, *92*(3), pp.167-185.

Lasher-Trapp, S., Leon, D.C., DeMott, P.J., Villanueva-Birriel, C.M., Johnson, A.V., Moser, D.H., Tully, C.S. and Wu, W., 2016. A multisensor investigation of rime splintering in tropical maritime cumuli. *Journal of the Atmospheric Sciences*, *73*(6), pp.2547-2564.

Lasher-Trapp, S., Scott, E.L., Järvinen, E., Schnaiter, M., Waitz, F., DeMott, P.J., McCluskey, C.S. and Hill, T.C., 2021. Observations and modeling of rime splintering in Southern Ocean cumuli. *Journal of Geophysical Research: Atmospheres*, *126*(23), p.e2021JD035479.

Lau, K.M. and Wu, H.T., 2003. Warm rain processes over tropical oceans and climate implications. *Geophysical Research Letters*, *30*(24).

Lawson, R.P., Woods, S. and Morrison, H., 2015. The microphysics of ice and precipitation development in tropical cumulus clouds. *Journal of the Atmospheric Sciences*, *72*(6), pp.2429-2445.

Leisner, T., Pander, T., Handmann, P. and Kiselev, A., 2014, July. Secondary ice processes upon heterogeneous freezing of cloud droplets. In *14th Conf. on Cloud Physics and Atmospheric Radiation*.

Leung, L.R., 2016. *ARM Cloud-Aerosol-Precipitation Experiment (ACAPEX) Field Campaign Report* (No. DOE/SC-ARM-16-012). DOE Office of Science Atmospheric Radiation Measurement (ARM) Program (United States).

Levin, E.J., DeMott, P.J., Suski, K.J., Boose, Y., Hill, T.C., McCluskey, C.S., Schill, G.P., Rocci, K., Al-Mashat, H., Kristensen, L.J. and Cornwell, G., 2019. Characteristics of ice nucleating particles in and around California winter storms. *Journal of Geophysical Research: Atmospheres*, *124*(21), pp.11530-11551.

Levine, J., 1950. *Statistical explanation of spontaneous freezing of water droplets* (No. NACA-TN-2234).

Lin, Y., Fan, J., Li, P., Leung, L.Y.R., DeMott, P.J., Goldberger, L., Comstock, J., Liu, Y., Jeong, J.H. and Tomlinson, J., 2022. Modeling impacts of ice-nucleating particles from marine aerosols on mixed-phase orographic clouds during 2015 ACAPEX field campaign. *Atmospheric Chemistry and Physics*, *22*(10), pp.6749-6771.

Liou, K.N., 2002. *An introduction to atmospheric radiation* (Vol. 84). Elsevier.

Lohmann, U. and Feichter, J., 2001. Can the direct and semi-direct aerosol effect compete with the indirect effect on a global scale?. *Geophysical Research Letters*, *28*(1), pp.159-161.

Lohmann, U. and Feichter, J., 2005. Global indirect aerosol effects: a review. *Atmospheric Chemistry and Physics*, *5*(3), pp.715-737.

Lohmann, U. and Lesins, G., 2002. Stronger constraints on the anthropogenic indirect aerosol effect. *Science*, *298*(5595), pp.1012-1015.

Lohmann, U., 2006. Aerosol effects on clouds and climate. *Space Science Reviews*, *125*, pp.129-137.

Lohmann, U., Lüönd, F. and Mahrt, F., 2016. *An introduction to clouds: From the microscale to climate*. Cambridge University Press.

Lohmann, U., Rotstayn, L., Storelvmo, T., Jones, A., Menon, S., Quaas, J., Ekman, A.M., Koch, D. and Ruedy, R., 2010. Total aerosol effect: radiative forcing or radiative flux perturbation?. *Atmospheric Chemistry and Physics*, *10*(7), pp.3235-3246.

Mason, B.J., 1996. The rapid glaciation of slightly supercooled cumulus clouds. *Quarterly Journal of the Royal Meteorological Society*, *122*(530), pp.357-365.

Matthias-Maser, S. and Jaenicke, R., 1995. The size distribution of primary biological aerosol particles with radii> 0.2 μm in an urban/rural influenced region. *Atmospheric Research*, *39*(4), pp.279-286.

Matthias-Maser, S., Brinkmann, J. and Schneider, W., 1999. The size distribution of marine atmospheric aerosol with regard to primary biological aerosol particles over the South Atlantic Ocean. *Atmospheric Environment*, *33*(21), pp.3569-3575.

Matthias-Maser, S., Obolkin, V., Khodzer, T. and Jaenicke, R., 2000. Seasonal variation of primary biological aerosol particles in the remote continental region of Lake Baikal/Siberia. *Atmospheric Environment*, *34*(22), pp.3805-3811.

Miltenberger, A.K. and Field, P.R., 2021. Sensitivity of mixed-phase moderately deep convective clouds to parameterizations of ice formation–an ensemble perspective. *Atmospheric Chemistry and Physics*, *21*(5), pp.3627-3642.

Miltenberger, A.K., Lüttmer, T. and Siewert, C., 2020. Secondary ice formation in idealised deep convection—source of primary ice and impact on glaciation. *Atmosphere*, *11*(5), p.542.

Ming, Y., Ramaswamy, V., Donner, L.J. and Phillips, V.T., 2006. A new parameterization of cloud droplet activation applicable to general circulation models. *Journal of the atmospheric sciences*, *63*(4), pp.1348-1356.

Mossop, S.C., 1985. Microphysical properties of supercooled cumulus clouds in which an ice particle multiplication process operated. *Quarterly Journal of the Royal Meteorological Society*, *111*(467), pp.183-198.

Murray, B.J., O'sullivan, D., Atkinson, J.D. and Webb, M.E., 2012. Ice nucleation by particles immersed in supercooled cloud droplets. *Chemical Society Reviews*, *41*(19), pp.6519-6554.

Murray, B.J., Wilson, T.W., Dobbie, S., Cui, Z., Al-Jumur, S.M., Möhler, O., Schnaiter, M., Wagner, R., Benz, S., Niemand, M. and Saathoff, H., 2010. Heterogeneous nucleation of ice particles on glassy aerosols under cirrus conditions. *Nature Geoscience*, *3*(4), pp.233-237.

Niedermeier, D., Shaw, R.A., Hartmann, S., Wex, H., Clauss, T., Voigtländer, J. and Stratmann, F., 2011. Heterogeneous ice nucleation: exploring the transition from stochastic to singular freezing behavior. *Atmospheric Chemistry and Physics*, *11*(16), pp.8767-8775.

Oraltay, R.G. and Hallett, J., 1989. Evaporation and melting of ice crystals: A laboratory study. *Atmospheric research*, *24*(1-4), pp.169-189.

Patade, S., Phillips, V.T., Amato, P., Bingemer, H.G., Burrows, S.M., DeMott, P.J., Goncalves, F.L., Knopf, D.A., Morris, C.E., Alwmark, C. and Artaxo, P., 2021. Empirical formulation for multiple groups of primary biological ice nucleating particles from field observations over Amazonia. *Journal of the Atmospheric Sciences*, *78*(7), pp.2195-2220.

Patade, S., Shete, S., Malap, N., Kulkarni, G. and Prabha, T.V., 2016. Observational and simulated cloud microphysical features of rain formation in the mixed phase clouds observed during CAIPEEX. *Atmospheric Research*, *169*, pp.32-45.

Patade, S., Waman, D., Deshmukh, A., Gupta, A.K., Jadav, A., Phillips, V.T., Bansemer, A., Carlin, J. and Ryzhkov, A., 2022. The influence of multiple groups of biological ice nucleating particles on microphysical properties of mixed-phase clouds observed during MC3E. *Atmospheric Chemistry and Physics*, *22*(18), pp.12055-12075.

Penner, J.E., Dong, X. and Chen, Y., 2004. Observational evidence of a change in radiative forcing due to the indirect aerosol effect. *Nature*, *427*(6971), pp.231-234.

Phillips, V.T. and Patade, S., 2022. Multiple Environmental Influences on the Lightning of Cold-Based Continental Convection. Part II: Sensitivity Tests for Its Charge Structure and Land–Ocean Contrast. *Journal of the Atmospheric Sciences*, *79*(1), pp.263-300.

Phillips, V.T., Andronache, C., Christner, B., Morris, C.E., Sands, D.C., Bansemer, A., Lauer, A., McNaughton, C. and Seman, C., 2009. Potential impacts from biological aerosols on ensembles of continental clouds simulated numerically. *Biogeosciences*, *6*(6), pp.987-1014.

Phillips, V.T., Andronache, C., Morris, C.E. and Sands, D.C., 2008. Impacts from ice-nucleating bacteria on deep convection: implications for the biosphere-atmosphere interaction in climate change. *Biogeosciences Discussions*, *5*(2), pp.1035-1067.

Phillips, V.T., Andronache, C., Sherwood, S.C., Bansemer, A., Conant, W.C., Demott, P.J., Flagan, R.C., Heymsfield, A., Jonsson, H., Poellot, M. and Rissman, T.A., 2005. Anvil glaciation in a deep cumulus updraught over Florida simulated with the Explicit Microphysics Model. I: Impact of various nucleation processes. *Quarterly Journal of the Royal Meteorological Society: A journal of the atmospheric sciences, applied meteorology and physical oceanography*, *131*(609), pp.2019-2046.

Phillips, V.T., Blyth, A.M., Brown, P.R., Choularton, T.W. and Latham, J., 2001. The glaciation of a cumulus cloud over New Mexico. *Quarterly Journal of the Royal Meteorological Society*, *127*(575), pp.1513-1534.

Phillips, V.T., Demott, P.J., Andronache, C., Pratt, K.A., Prather, K.A., Subramanian, R. and Twohy, C., 2013. Improvements to an empirical parameterization of heterogeneous ice nucleation and its comparison with observations. *Journal of the Atmospheric Sciences*, *70*(2), pp.378-409.

Phillips, V.T., Donner, L.J. and Garner, S.T., 2007. Nucleation processes in deep convection simulated by a cloud-system-resolving model with double-moment bulk microphysics. *Journal of the atmospheric sciences*, *64*(3), pp.738-761.

Phillips, V.T., Formenton, M., Bansemer, A., Kudzotsa, I. and Lienert, B., 2015. A parameterization of sticking efficiency for collisions of snow and graupel with ice crystals: Theory and comparison with observations. *Journal of the Atmospheric Sciences*, *72*(12), pp.4885-4902.

Phillips, V.T., Formenton, M., Kanawade, V.P., Karlsson, L.R., Patade, S., Sun, J., Barthe, C., Pinty, J.P., Detwiler, A.G., Lyu, W. and Tessendorf, S.A., 2020. Multiple environmental influences on the lightning of cold-based continental cumulonimbus clouds. Part I: Description and validation of model. *Journal of the Atmospheric Sciences*, *77*(12), pp.3999-4024.

Phillips, V.T., Khain, A., Benmoshe, N. and Ilotoviz, E., 2014. Theory of time-dependent freezing. Part I: Description of scheme for wet growth of hail. *Journal of the Atmospheric Sciences*, *71*(12), pp.4527-4557.

Phillips, V.T., Patade, S., Gutierrez, J. and Bansemer, A., 2018. Secondary ice production by fragmentation of freezing drops: Formulation and theory. *Journal of the Atmospheric Sciences*, *75*(9), pp.3031-3070.

Phillips, V.T., Yano, J.I. and Khain, A., 2017. Ice multiplication by breakup in ice–ice collisions. Part I: Theoretical formulation. *Journal of the Atmospheric Sciences*, *74*(6), pp.1705-1719.

Phillips, V.T., Yano, J.I., Formenton, M., Ilotoviz, E., Kanawade, V., Kudzotsa, I., Sun, J., Bansemer, A., Detwiler, A.G., Khain, A. and Tessendorf, S.A., 2017. Ice multiplication by breakup in ice–ice collisions. Part II: Numerical simulations. *Journal of the Atmospheric Sciences*, *74*(9), pp.2789-2811.

Phillips, V.T.J., Choularton, T.W., Illingworth, A.J., Hogan, R.J. and Field, P.R., 2003. Simulations of the glaciation of a frontal mixed-phase cloud with the Explicit Microphysics Model. *Quarterly Journal of the Royal Meteorological Society: A journal of the atmospheric sciences, applied meteorology and physical oceanography*, *129*(590), pp.1351-1371.

Prabhakaran, P., Kinney, G., Cantrell, W., Shaw, R.A. and Bodenschatz, E., 2019. Ice nucleation in the wake of warm hydrometeors. *arXiv preprint arXiv:1906.06129*.

Prabhakaran, P., Shawon, A.S.M., Kinney, G., Thomas, S., Cantrell, W. and Shaw, R.A., 2020. The role of turbulent fluctuations in aerosol activation and cloud formation. *Proceedings of the National Academy of Sciences*, *117*(29), pp.16831-16838.

Pruppacher, H.R. and Schlamp, R.J., 1975. A wind tunnel investigation on ice multiplication by freezing of waterdrops falling at terminal velocity in air. *Journal of Geophysical Research*, *80*(3), pp.380-386.

Pruppacher, H.R., Klett, J.D., 1997. Microphysics of clouds and precipitation.

Raatikainen, T., Prank, M., Ahola, J., Kokkola, H., Tonttila, J., and Romakkaniemi, S., 2022: The effect of marine ice-nucleating particles on mixed-phase clouds, Atmos. Chem. Phys., 22, 3763–3778, https://doi.org/10.5194/acp-22-3763-2022.

Ramanathan, V.C.P.J., Crutzen, P.J., Kiehl, J.T. and Rosenfeld, D., 2001. Aerosols, climate, and the hydrological cycle. *science*, *294*(5549), pp.2119-2124.

Rangno, A.L. and Hobbs, P.V., 2001. Ice particles in stratiform clouds in the Arctic and possible mechanisms for the production of high ice concentrations. *Journal of Geophysical Research: Atmospheres*, *106*(D14), pp.15065-15075.

Rangno, A.L., 2008. Fragmentation of freezing drops in shallow maritime frontal clouds. *Journal of the atmospheric sciences*, *65*(4), pp.1455-1466.

Rauber, R.M., Olthoff, L.S., Ramamurthy, M.K. and Kunkel, K.E., 2000. The relative importance of warm rain and melting processes in freezing precipitation events. *Journal of Applied Meteorology*, *39*(7), pp.1185-1195.

Rogers, R.R., and Yau, M.K., 1996. *A short course in cloud physics*. Elsevier.

Romakkaniemi, S., Arola, A., Kokkola, H., Birmili, W., Tuch, T., Kerminen, V.M., Räisänen, P., Smith, J.N., Korhonen, H. and Laaksonen, A., 2012. Effect of aerosol size distribution changes on AOD, CCN and cloud droplet concentration: Case studies from Erfurt and Melpitz, Germany. *Journal of Geophysical Research: Atmospheres*, *117*(D7).

Ryu, Y.H. and Min, S.K., 2022. Improving Wet and Dry Deposition of Aerosols in WRF-Chem: Updates to Below-Cloud Scavenging and Coarse-Particle Dry Deposition. *Journal of Advances in Modeling Earth Systems*, *14*(4), p.e2021MS002792.

Schill, G.P., Froyd, K.D., Bian, H., Kupc, A., Williamson, C., Brock, C.A., Ray, E., Hornbrook, R.S., Hills, A.J., Apel, E.C. and Chin, M., 2020. Widespread biomass burning smoke throughout the remote troposphere. *Nature Geoscience*, *13*(6), pp.422-427.

Shaw, R.A., Durant, A.J. and Mi, Y., 2005. Heterogeneous surface crystallization observed in undercooled water. *The Journal of Physical Chemistry B*, *109*(20), pp.9865-9868.

Skamarock, W.C., Klemp, J.B., Dudhia, J., Gill, D.O., Barker, D.M., Duda, M.G., Huang, X.Y., Wang, W. and Powers, J.G., 2008. A description of the advanced research WRF version 3. *NCAR technical note*, *475*, p.113.

Sotiropoulou, G., Sullivan, S., Savre, J., Lloyd, G., Lachlan-Cope, T., Ekman, A.M. and Nenes, A., 2020. The impact of secondary ice production on Arctic stratocumulus. *Atmospheric Chemistry and Physics*, *20*(3), pp.1301-1316.

Sotiropoulou, G., Vignon, É., Young, G., Morrison, H., O'Shea, S.J., Lachlan-Cope, T., Berne, A. and Nenes, A., 2021. Secondary ice production in summer clouds over the Antarctic coast: an underappreciated process in atmospheric models. *Atmospheric Chemistry and Physics*, *21*(2), pp.755-771.

Takahashi, C. and Yamashita, A., 1969. Deformation and fragmentation of freezing water drops in free fall. *Journal of the Meteorological Society of Japan. Ser. II*, *47*(6), pp.431-436.

Takahashi, C. and Yamashita, A., 1970. Shattering of frozen water drops in a supercooled cloud. *Journal of the Meteorological Society of Japan. Ser. II*, *48*(4), pp.373-376.

Takahashi, T. and Kawano, T., 1998. Numerical sensitivity study of rainband precipitation and evolution. *Journal of the atmospheric sciences*, *55*(1), pp.57-87.

Takahashi, T., Nagao, Y. and Kushiyama, Y., 1995. Possible high ice particle production during graupel–graupel collisions. *Journal of the atmospheric sciences*, *52*(24), pp.4523-4527.

Takemura, T., 2012. Distributions and climate effects of atmospheric aerosols from the preindustrial era to 2100 along Representative Concentration Pathways (RCPs) simulated using the global aerosol model SPRINTARS. *Atmospheric Chemistry and Physics*, *12*(23), pp.11555-11572.

Troen and Mahrt, 1986: A Simple Model of the Atmospheric Boundary Layer; Sensitivity to Surface Evaporation. Bound. Lay. Met., Vol. 37, pg. 129-148.

Twohy, C.H., DeMott, P.J., Pratt, K.A., Subramanian, R., Kok, G.L., Murphy, S.M., Lersch, T., Heymsfield, A.J., Wang, Z., Prather, K.A. and Seinfeld, J.H., 2010. Relationships of biomass-burning aerosols to ice in orographic wave clouds. *Journal of the atmospheric sciences*, *67*(8), pp.2437-2450.

Twomey, S.J.A.E., 1974. Pollution and the planetary albedo. *Atmospheric Environment (1967)*, *8*(12), pp.1251-1256.

Uin, J., 2022. *Cloud condensation nuclei particle counter (CCN) instrument handbook* (No. DOE/SC-ARM-TR-168). DOE Office of Science Atmospheric Radiation Measurement (ARM) Program (United States).

Vali, G. and Stansbury, E.J., 1966. Time-dependent characteristics of the heterogeneous nucleation of ice. *Canadian Journal of Physics*, *44*(3), pp.477-502.

Vali, G., 1985. Nucleation terminology. *Bulletin of the American Meteorological Society*, *66*(11), pp.1426-1427.

Vali, G., 1994. Freezing rate due to heterogeneous nucleation. *Journal of Atmospheric Sciences*, *51*(13), pp.1843-1856.

Vali, G., 2008. Repeatability and randomness in heterogeneous freezing nucleation. *Atmospheric Chemistry and Physics*, *8*(16), pp.5017-5031.

Vali, G., 2014. Interpretation of freezing nucleation experiments: singular and stochastic; sites and surfaces. *Atmospheric Chemistry and Physics*, *14*(11), pp.5271-5294.

Vali, G., DeMott, P.J., Möhler, O. and Whale, T.F., 2015. A proposal for ice nucleation terminology. *Atmospheric Chemistry and Physics*, *15*(18), pp.10263-10270.

Vardiman, L., 1978. The generation of secondary ice particles in clouds by crystal–crystal collision. *Journal of Atmospheric Sciences*, *35*(11), pp.2168-2180.

Vonnegut, B. and Baldwin, M., 1984. Repeated nucleation of a supercooled water sample that contains silver iodide particles. *Journal of Applied Meteorology and Climatology*, *23*(3), pp.486-490.

Waman, D., Deshmukh, A., Jadav, A., Patade, S., Gautam, M., Phillips, V., Bansemer, A. and Jakobsson, J., 2023. Effects from time dependence of ice nucleus activity for contrasting cloud types. *Journal of the Atmospheric Sciences*.

Waman, D., Deshmukh, A., Jadav, A., Patade, S., Gautam, M., Phillips, V., 2023. Mechanisms for indirect effects from solid aerosol particles on continental clouds and radiation. (Submitted to Journal of the Atmospheric Sciences).

Waman, D., Patade, S., Jadav, A., Deshmukh, A., Gupta, A.K., Phillips, V.T., Bansemer, A. and DeMott, P.J., 2022. Dependencies of Four Mechanisms of Secondary Ice Production on Cloud-Top Temperature in a Continental Convective Storm. *Journal of the Atmospheric Sciences*, *79*(12), pp.3375-3404.

Wang, Z., Schaaf, C.B., Strahler, A.H., Chopping, M.J., Román, M.O., Shuai, Y., Woodcock, C.E., Hollinger, D.Y. and Fitzjarrald, D.R., 2014. Evaluation of MODIS albedo product (MCD43A) over grassland, agriculture and forest surface types during dormant and snow-covered periods. *Remote Sensing of Environment*, *140*, pp.60-77.

Warneck, P., 1999. *Chemistry of the natural atmosphere* (Vol. 71). Elsevier.

Welti, A., Lüönd, F., Kanji, Z.A., Stetzer, O. and Lohmann, U., 2012. Time dependence of immersion freezing: an experimental study on size selected kaolinite particles. *Atmospheric Chemistry and Physics*, *12*(20), pp.9893-9907.

Westbrook, C.D. and Illingworth, A.J., 2013. The formation of ice in a long-lived supercooled layer cloud. *Quarterly Journal of the Royal Meteorological Society*, *139*(677), pp.2209-2221.

Wildeman, S., Sterl, S., Sun, C. and Lohse, D., 2017. Fast dynamics of water droplets freezing from the outside in. *Physical review letters*, *118*(8), p.084101.

Wright, T.P., Petters, M.D., Hader, J.D., Morton, T. and Holder, A.L., 2013. Minimal cooling rate dependence of ice nuclei activity in the immersion mode. *Journal of Geophysical Research: Atmospheres*, *118*(18), pp.10-535.

Yang, J., Lei, H., Hu, Z. and Hou, T., 2014. Particle size spectra and possible mechanisms of high ice concentration in nimbostratus over Hebei Province, China. *Atmospheric research*, *142*, pp.79-90.

Yang, J., Wang, Z., Heymsfield, A.J., DeMott, P.J., Twohy, C.H., Suski, K.J. and Toohey, D.W., 2020. High ice concentration observed in tropical maritime stratiform mixed-phase clouds with top temperatures warmer than− 8 C. *Atmospheric Research*, *233*, p.104719.

Yano, J.I. and Phillips, V.T.J., 2011. Ice–ice collisions: An ice multiplication process in atmospheric clouds. *Journal of the Atmospheric Sciences*, *68*(2), pp.322-333.

Yano, J.I., Phillips, V.T. and Kanawade, V., 2016. Explosive ice multiplication by mechanical break-up in ice–ice collisions: a dynamical system-based study. *Quarterly Journal of the Royal Meteorological Society*, *142*(695), pp.867-879.

Yli-Juuti, T., Mielonen, T., Heikkinen, L., Arola, A., Ehn, M., Isokääntä, S., Keskinen, H.M., Kulmala, M., Laakso, A., Lipponen, A. and Luoma, K., 2021. Significance of the organic aerosol driven climate feedback in the boreal area. *Nature communications*, *12*(1), p.5637.

Young, G., Lachlan-Cope, T., O'Shea, S.J., Dearden, C., Listowski, C., Bower, K.N., Choularton, T.W. and Gallagher, M.W., 2019. Radiative effects of secondary ice enhancement in coastal Antarctic clouds. *Geophysical Research Letters*, *46*(4), pp.2312-2321.

Zhao, X. and Liu, X., 2021. Global importance of secondary ice production. *Geophysical Research Letters*, *48*(11), p.e2021GL092581.

Zhao, X., Liu, X., Phillips, V.T. and Patade, S., 2021. Impacts of secondary ice production on Arctic mixed-phase clouds based on ARM observations and CAM6 single-column model simulations. *Atmospheric Chemistry and Physics*, *21*(7), pp.5685-5703.

Paper 1

Atmospheric
Chemistry
and Physics

Open Access

Research article

The influence of multiple groups of biological ice nucleating particles on microphysical properties of mixed-phase clouds observed during MC3E

Sachin Patade[1], **Deepak Waman**[1], **Akash Deshmukh**[1], **Ashok Kumar Gupta**[2], **Arti Jadav**[1],
Vaughan T. J. Phillips[1], **Aaron Bansemer**[4], **Jacob Carlin**[3], and **Alexander Ryzhkov**[3]

[1]Department of Physical Geography and Ecosystem Science, Lund University, Lund, Sweden
[2]Department of Earth and Environmental Sciences, Vanderbilt University, Nashville, Tennessee, USA
[3]Cooperative Institute for Severe and High-Impact Weather Research and Operations, The University of
Oklahoma and NOAA/OAR National Severe Storms Laboratory, Norman, Oklahoma, USA
[4]Mesoscale and Microscale Meteorology Laboratory, National Center for Atmospheric
Research, Boulder, Colorado, USA

Correspondence: Sachin Patade (sachin.patade@nateko.lu.se)

Abstract. A new empirical parameterization (EP) for multiple groups of primary biological aerosol particles (PBAPs) is implemented in the aerosol–cloud model (AC) to investigate their roles as ice nucleating particles (INPs). The EP describes the heterogeneous ice nucleation by (1) fungal spores, (2) bacteria, (3) pollen, (4) detritus of plants, animals, and viruses, and (5) algae. Each group includes fragments from the originally emitted particles. A high-resolution simulation of a midlatitude mesoscale squall line by AC is validated against airborne and ground observations.

Sensitivity tests are carried out by varying the initial vertical profiles of the loadings of individual PBAP groups. The resulting changes in warm and ice cloud microphysical parameters are investigated. The changes in warm microphysical parameters, including liquid water content and cloud droplet number concentration, are minimal ($<10\%$). Overall, PBAPs have little effect on the ice number concentration ($<6\%$) in the convective region. In the stratiform region, increasing the initial PBAP loadings by a factor of 1000 resulted in less than 40% change in ice number concentrations. The total ice concentration is mostly controlled by various mechanisms of secondary ice production (SIP). However, when SIP is intentionally shut down in sensitivity tests, increasing the PBAP loading by a factor of 100 has an effect of less than 3% on the ice phase. Further sensitivity tests revealed that PBAPs have little effect on surface precipitation and on the shortwave and longwave flux ($<4\%$) for a 100-fold perturbation in PBAPs.

1   Introduction

In most climate models, the largest source of uncertainty for estimating the total anthropogenic forcing is associated with cloud–aerosol interactions (Pörtner et al., 2022). Atmospheric aerosol particles can act as cloud condensation nuclei (CCN), and a few of them act as ice nucleating particles (INPs), thereby influencing the microphysical properties of clouds, and depending on the cloud type (Fan et al., 2010;

Chen et al., 2019), the treatment of INP in climate models can strongly affect the atmospheric radiation budget (DeMott et al., 2010). Various sources of aerosol particles, including dust/metallic, marine aerosols, anthropogenic carbonaceous emissions, and primary biological aerosol particles (PBAPs), contribute to the observed INPs (Kanji et al., 2017).

A significant amount of global precipitation is associated with the ice phase in cold clouds (Field and Heymsfield, 2015; Mülmenstädt et al., 2015, Heymsfield et al., 2020). In

particular, mixed-phase clouds are vital for the global climate (Dong and Mace, 2003; Zuidema et al., 2005; Matus and L'Ecuyer, 2017; Korolev et al., 2017, and references therein). In a multimodel simulation study, Tsushima et al. (2006) showed that the doubling of CO_2 concentrations caused the changes in the distribution of cloud water in the mixed-phase clouds in a climate simulation to be significant.

PBAPs are solid particles of biological origin and are emitted from the Earth's surface (Després et al., 2012). They are highly active in initiating ice as INPs and include bacteria, fungal spores, pollen, algae, lichens, archaea, viruses, and biological fragments (e.g., leaf litter and insects) and molecules (e.g., proteins, polysaccharides, and lipids; Després et al., 2012; Fröhlich-Nowoisky et al., 2015; Knopf et al., 2011; Szyrmer and Zawadzki, 1997). Considering the onset temperature of freezing, some ice nucleation active fungi and bacteria (especially *Pseudomonas syringae*, with an onset freezing temperature around $-3\,°C$) are among the most active INPs present in the atmosphere (Després et al., 2012; Hoose and Möhler, 2012). The potential impact of PBAP INPs on cloud microphysical characteristics has been recognized for many years; however, this topic remains a subject of debate (DeMott and Prenni, 2010; Spracklen and Herald, 2014; Hoose et al., 2010b). Some previous modeling studies have shown that, on a global scale, PBAPs have only a limited influence on clouds and precipitation (Hoose et al., 2010a; Sesartic et al., 2012, 2013; Spracklen and Heald, 2014). On a global scale, the percentage contribution of PBAPs to the immersion freezing (ice nucleation by INP immersed in supercooled water drop) is predicted to be much smaller (0.6 %) compared to dust (87 %) and soot (12 %; Hoose et al., 2010).

Many studies have used cloud models to highlight the potential impact of PBAP INPs on cloud microphysics and precipitation (e.g., Levin et al., 1987; Grützun et al., 2008; Phillips et al., 2009). For example, the mesoscale aerosol–cloud model by Phillips et al. (2009) had a 3-D domain of about 100 km in width, and many cloud types were present in the mesoscale convective system that was simulated. Their simulations revealed that the cloud cover, domain radiative fluxes, and surface precipitation rate were significantly altered by boosting organic aerosols representing PBAPs. According to Hummel et al. (2018), in shallow mixed-phase clouds (i.e., altostratus), when the cloud top temperature is below $-15\,°C$, PBAPs have the potential to influence the cloud ice phase and produce ice crystals in the absence of other INPs.

The quest for insights into the broader atmospheric role of PBAP INPs for cloud microphysical properties and precipitation is hampered by the limited availability of observations of both their ice nucleation activities for various species and their aerosol distributions in the real atmosphere (Huang et al., 2021). More generally, there is incomplete knowledge about the chemical identity of the key INPs, whether biological or otherwise (Murray et al., 2012). In many global and regional models, the ice nucleation activity of bioaerosols is represented either empirically or theoretically, based on laboratory measurements of specific biological species of PBAPs that are assumed as representative candidates (e.g., *Pseudomonas syringae*). This assumption of representativeness introduces uncertainties that would be expected to impact the model results, potentially introducing a bias into the estimation of the effects of bioaerosols on clouds (e.g. Sahyoun et al., 2016; Hoose et al., 2010b; Spracklen and Herald, 2014; Huang et al., 2021, and references therein).

In addition to primary ice nucleation, ice formation in clouds can occur because of processes generating new particles from pre-existing ice, and these are known as secondary ice production (SIP) mechanisms (Korolev and Leisner, 2020; Korolev et al., 2020). SIP can have a considerable impact on cloud micro- and macro-physical properties, such as precipitation rate, glaciation time, cloud lifetime, and cloud electrification by increasing the ice number concentrations by a few orders of magnitude (e.g., Blyth and Latham, 1993; Crawford et al., 2012; Lawson et al., 2015; Phillips et al., 2017b, 2018, 2020; Phillips and Patade, 2022; Sotiropoulou et al., 2021a, b). This, in turn, can influence the global hydrological cycle and climate (Zhao and Liu, 2021).

However, in many cloud models, the representations of these SIP mechanisms are uncertain, as most of the cloud models include only the Hallett–Mossop (hereafter HM; Hallett and Mossop, 1974) process and neglect other SIP mechanisms (e.g., Fan et al., 2017; Han et al., 2019). A few secondary ice formation processes (e.g., the HM process) have been suggested to be active in the temperature range where active PBAP INPs exhibit strong ice nucleation activity. The INPs of biological origin, such as bacteria, are highly active in the temperature range of the HM process (-3 to $-8\,°C$) compared with non-biological INPs (Möhler et al., 2008; Patade et al., 2021; henceforth PT21). At temperatures warmer than $-15\,°C$, some of the PBAPs generated by biologically active landscapes (e.g., forests and woodlands) can promote ice formation and crystal growth in clouds (Morris et al., 2014).

In the USA, about 18 % of the total landmass is used as cropland, farmland, and for agricultural activities (Garcia et al., 2012). These are major sources of biological particles in the atmosphere. Biogenic particles released from crops, either pre- or post-harvest, have previously been shown to serve as INPs (in Colorado and Nebraska; Garcia et al., 2012). Huffman et al. (2013) found that airborne biological particles increase significantly in concentration, by an order of magnitude or more, during rainfall in a forest in the western USA and that bioaerosols are well correlated with INPs. Prenni et al. (2012) observed a similar increase in concentrations of ground-level INPs during rain at a forested site in Colorado, which was associated with increased biological particles. Convective clouds can efficiently transport lower tropospheric aerosol particles into the upper tropo-

sphere where they can affect the cloud properties (Cui and Carslaw, 2006).

The current study aims to simulate realistic concentrations of multiple groups of PBAP INPs, including bacterial and fungal particles, to investigate their interactions with convective clouds observed during the Midlatitude Continental Convective Clouds Experiment field campaign (MC3E) in the USA (Jensen et al., 2016). In view of the literature noted above about the effects of PBAP INPs, there is a need for more detailed analyses of their role in altering cloud microphysical properties and precipitation because the realistic treatment of ice nucleation activity for major PBAP groups was not available prior to our empirical scheme (PT21). Hitherto, laboratory measurements of isolated biological species (e.g., *Pseudomonas syringae* and *Cladosporium* sp.) have been the basis for attempts to simulate biological ice nucleation in clouds, but the representativeness of the choice of such species has been a long-standing issue. For example, Hummel et al. (2018) considered three highly ice nucleation active PBAP species in their model, which may not represent the ice nucleation activity of PBAP in the atmosphere. It is not known which biological species of ice nucleation active (INA) PBAPs contribute the most to biological ice nucleation. Consequently, there is a need for a new approach oriented toward laboratory measurements of biological INPs sampled from the atmosphere, thus optimizing the representativeness of the data for studies of clouds.

In this paper, such an approach is followed to investigate the effect on cloud properties from various major groups of PBAP. We incorporated a recent empirical parameterization for various PBAP groups by PT21 into our 3-D aerosol–cloud model (AC). PT21 created an empirical formulation resolving the ice nucleation of each group of PBAPs, including (1) fungal spores and their fragments, (2) bacteria and their fragments, (3) pollen and their fragments, (4) detritus of plants, animals, and viruses, and (5) algae. We also examine the relative importance of various secondary ice processes in their role in mediating the PBAP effects on cloud microphysical properties, given the weakness of PBAP effects on cloud microphysical properties.

2 Description of observations

2.1 Selected case of a deep convective system

In the current study, we simulated a squall line that occurred on 20 May 2011 during MC3E (Jensen et al., 2016). The MC3E campaign took place from 22 April through to 6 June 2011 and was centered at the Atmospheric Radiation Measurement (ARM) Southern Great Plains (SGP) Central Facility (CF; 36.6° N, 97.5° W) in north-central Oklahoma. The surface meteorological analysis on 20 May indicated a southerly flow at the surface, which provided enough moisture from the Gulf of Mexico to trigger convection. Deep convection, organized in the form of a squall line, passed over the measurement site between 10:30 and 11:00 UTC, resulting in convective precipitation. It was followed by widespread stratiform precipitation that was well observed by both airborne and ground-based measurements. Vertical sounding characteristics of this case are described in Fig. S1 in the Supplement, based on the Skew-T plot.

2.2 Aircraft observations

The in situ cloud microphysical observations used in this study were obtained from a University of North Dakota Citation II aircraft. The aircraft collected observations of cloud microphysical parameters from the cloud base (1.8 km above mean sea level; hereafter a.m.s.l.) to a maximum altitude of 7.5 km a.m.s.l. The MC3E campaign collected extensive airborne measurements of aerosols and cloud microphysical properties over north-central Oklahoma. A detailed description of the scientific objectives of the MC3E program, including the field experiment strategy, airborne, and ground-based instrumentation, is given in the paper by Jensen et al. (2016). A summary of the airborne instrumentation during MC3E is provided in the Supplement.

2.3 Ground-based measurements

A comprehensive instrumentation suite deployed at the ARM SGP central facility provided continuous measurements of atmospheric gases, aerosols, clouds, and local meteorological conditions (e.g., wind, temperature, precipitation, and atmospheric profiles). A cloud condensation nuclei (CCN) counter (CCN-100; DMT) measured the CCN number concentration at seven supersaturation values with a temporal resolution of 1 h. Surface precipitation was measured with 16 rain gauge pairs placed within a 6 km radius of the SGP CF.

During the MC3E campaign, the measurement facility deployed at CF measured the spatial variability in surface fluxes of heat, moisture, and momentum. A radiosonde array of six sites, covering an area of 300 × 300 km, was designed to capture the large-scale variability in the atmospheric state. Radiosonde observations (Vaisala RS92-SGP) were conducted with a 6 h frequency (four times daily) at around 05:30, 11:30, 16:30, and 22:30 UTC, providing vertical profiles of atmospheric state variables (pressure, temperature, humidity, and winds) of the environment surrounding the ARM SGP site. When aircraft operations were planned based on forecasted convective conditions, the sounding frequency was increased to a 3 h frequency, with the starting time at 05:30 UTC.

In addition to airborne observations, the ARM radar network was used to conduct unique radar observations during the MC3E campaign. The information about various radar assets during MC3E is given by Jensen et al. (2016). The surface precipitation used for model validation in this study is a radar-based precipitation estimate, as described by Gi-

angrande et al. (2014). Their radar-based rainfall retrievals were in good agreement with observations, with an absolute bias of less than 0.5 mm for accumulations less than 20 mm.

The Interagency Monitoring of Protected Visual Environments (IMPROVE) network stations close to the location of airborne observations provided ground-level measurements of various chemical species. These included carbonaceous compounds (black and organic carbon), salt, ammonium sulfate, and dust. The details of the measurement techniques used for the mass mixing ratios of these compounds are summarized in Malm et al. (1994). The measurements of these aerosol species from various IMPROVE sites, including sites at Ellis (36.08° N, 99.93° W), Stilwell (35.75° N, 94.66° W), and Wichita Mountains (34.73° N, 98.71° W) in Oklahoma, were averaged to provide inputs to AC.

Initial mass concentrations for the aerosol species of AC (11 species) including sulfate, sea salt, dust, black carbon, soluble organic, and biological and non-biological insoluble organic (five groups of PBAPs) were derived from the Goddard Chemistry Aerosol Radiation and Transport (GOCART) model (Chin et al., 2000). The prescribed mass mixing ratios of aerosol species in our aerosol–cloud model (AC) are based on IMPROVE observations and are listed in Table S2. It should be noted that, for the MC3E case considered in this study, coincident IMPROVE measurements were not available. The mean values of the IMPROVE measurements conducted on 18 and 21 May are used to prescribe the mass of various aerosol species.

3 Methodology

3.1 Model description

The AC used in this study is a cloud-resolving model (CRM) with a hybrid spectral bin/two-moment bulk microphysics, interactive radiation, and semi-prognostic aerosol schemes (Phillips et al., 2017b, 2020). The model predicts the mass and number concentrations for five types of hydrometeors, namely cloud liquid, cloud ice (or crystals), rain, graupel/hail, and snow. The mixing ratios of the total number and mass of all particles in each microphysical species are treated as model prognostic variables. AC treats all known microphysical processes such as droplet nucleation, ice initiation, through primary and secondary processes, and growth processes, such as the deposition/sublimation of ice particles, condensation/evaporation of drops, freezing/melting, and coagulation by collisions between various hydrometeor types. Both the cloud base and in-cloud activation of aerosols to form cloud droplets are treated explicitly, with the predicted in-cloud supersaturation resolved on the model grid being used to activate aerosols aloft. Bin-resolved size distributions of each aerosol species are predicted for the interstitial and immersed components of each aerosol species. Extra prognostic variables track the number of aerosols in each aerosol species that have been lost by INP and CCN activation.

Secondary ice formation is represented by the following four types of fragmentation:

- breakup in ice–ice collisions (Phillips et al., 2017a, b; most active between −10 to −20 °C),

- rime splintering (most active between −3 to −8 °C; Hallett and Mossop 1974),

- fragmentation of freezing rain/drizzle by modes 1 and 2 (Phillips et al., 2018; most active around −15 °C), and

- sublimation breakup (Deshmukh et al., 2021; most active between −0 to −18 °C).

The empirical parameterization (EP; Phillips et al., 2013) of heterogeneous ice nucleation treats all known modes of ice formation (deposition mode, condensation /immersion freezing, and inside-out and outside-in contact freezing) in terms of dependencies on the loading, size, and chemistry of multiple aerosol species. In the previous version of the EP, prior to PT21, there were four species of INP aerosol. One of these was PBAP INPs. However, that version of the EP did not resolve the individual types of PBAP INP, which exhibit a wide range of ice nucleating abilities. The current version of AC also includes the ice nucleation (IN) activity of dust and black carbon. The ice nucleation parameterization of dust, and black carbon, is based on studies by Phillips et al. (2008, 2013). The activation of dust and black carbon INP starts at temperatures colder than −10 and −15 °C.

There are two types of homogeneous freezing represented, i.e., that of cloud droplets near −36 °C and that of solute aerosols at colder temperatures. Both schemes are described by Phillips et al. (2007, 2009). For cloud droplets, a lookup table from simulations with a spectral bin microphysics parcel model treats the fraction of all supercooled cloud droplets that evaporate without freezing near −36 °C, depending on the ascent, initial droplet concentration, and supersaturation. The size dependence of the temperature of homogeneous freezing is represented.

Cloud processes and rainfall formation have been detected using different radar variables, such as a specific differential phase K_{DP}. Moisseev et al. (2015), for example, noted an increase in observed K_{DP} because of aggregation. In addition, a few studies have hypothesized evidence of SIP via K_{DP} (e.g., Sinclair et al., 2016; Kumjian and Lombardo, 2017; Carlin et al., 2021). In this study, we attempted to detect secondary ice formation signatures by implementing K_{DP} estimations into AC. Based on Ryzhkov et al. (2011), K_{DP} values were estimated for various hydrometeor types, including cloud drops, raindrops, cloud ice, snow, and graupel (their Eqs. 22, 23, 24, 26, and 29).

3.2 Empirical formulation for PBAP INPs

In a recent study, PT21 provided an empirical formulation for multiple groups of PBAP INPs based on field observations

over the central Amazon. In this study, we modified AC by implementing the recent empirical parameterization of PBAP INPs by PT21. The empirical formulation by PT21 is based on observations of PBAP collected at the Amazon Tall Tower Observatory (ATTO), a research site located in the middle of the Amazon rainforest in northern Brazil. The empirical formulation by PT21 for multiple groups of PBAPs includes (1) fungal spores (FNG), (2) bacteria (BCT), (3) pollen (PLN), (4) viral particles and plant/animal detritus (DTS), and (5) algae (ALG) and their respective fragments, which are implemented in AC. This formulation has empirically derived dependencies on the surface area of each group (except algae), and it applies to particles with diameters greater than $0.1\,\mu m$. Additional details about the formulation by PT21 are given in the Supplement.

3.3 Model setup

AC was driven by initial and evolving boundary data for meteorological conditions. The large-scale advection of humidity and temperature tendencies maintained the convection. Convection was initiated by imposing perturbations onto the initial field of vapor mixing ratio. The large-scale forcing condition used for the simulation was derived using the constrained variational analysis method described in Xie et al. (2014). Based on this method, the so-called large-scale forcing, including large-scale vertical velocity and advective tendencies of temperature and moisture, were derived from the sounding measurements network. During the MC3E campaign, the sounding network consisted of five sounding stations centered on a sixth site at the ARM SGP central facility. An area with a diameter of approximately $300\,km$ was covered by this sounding network covers. Figure S2 shows the time–height evolution of potential temperature and water vapor mixing ratio from large-scale forcing data. It also shows the time variation of convective available potential energy (CAPE) based on observations. The maximum value of CAPE $2400\,J\,kg^{-1}$ was noticed at around 12:00 UTC on 20 May.

The model simulations were carried out for a three-dimensional domain of $80 \times 80\,km$ with horizontal grid spacings of $2\,km$. In the vertical, the model resolution was $0.5\,km$, and the model top was located at about $16\,km$. The lateral boundary conditions are doubly periodic on all sides of the domain. The initial time of the simulations was at 12:00 UTC on 19 May 2011, and all simulations were performed for $48\,h$ at a time step of $10\,s$.

The GOCART model (Chin et al., 2000) was used to initialize the seven chemical species associated with the EP. The data from the three IMPROVE sites mentioned above (Sect. 2.3) were used to rescale the mass concentration profiles at all levels so that they match the measurements near the surface. Table S2 lists the mass mixing ratios of various aerosol species after the corrections. The corresponding vertical profiles of various aerosol species, including sulfate,

dust, sea salt, black carbon, and total organic carbon, are shown in Fig. S3a–e. The corresponding IMPROVE measurements are also shown in the same figure. There were no direct measurements of PBAP mass during IMPROVE, and therefore, it was derived from the measured mass of the total organic carbon (TOC). The relative contribution of insoluble and soluble organic carbon to TOC was assumed to be 20% and 80%, respectively, by assuming a water-soluble fraction of 80% for carbonaceous aerosol (Phillips et al., 2017b). AC takes into account the soluble fraction of each type of aerosol. The values of this factor are 0.15 for dust and 0.8 for carbonaceous species. The value of this fraction for all PBAP groups is 0.1.

There are very few observations available in the literature that show the fraction of PBAP in the insoluble organics or total aerosol particles. For example, observations by Matthias-Maser et al. (2000) found that 25% of the total insoluble particles are biological. PBAPs can contribute a significant fraction to the number concentrations of total aerosol particles (Mattias-Maser et al., 1999). Mattias-Maser and Jaenicke (1995) showed that PBAPs can amount to 20% and 30% of the total aerosol particles. The observation by Jaenicke (2005) in a semi-rural location showed that cellular particles can contribute up to about 50% of the total particles. Based on these studies, we assumed that 50% of the insoluble organics were biological in origin. The total PBAP loading was prescribed, partly based on observations of insoluble organics. The mass fraction of each PBAP group in the total PBAP mass is prescribed, based on the PT21 observations. The fraction of mass mixing ratio for various PBAP groups is $FNG = 0.39$, $BCT = 0.13$, $PLN = 0.31$, $DTS = 0.17$, and $ALG = 2.5 \times 10^{-4}$.

It should be noted that the observations of PBAPs over different geographical locations (including the region where we carried out the simulation) are rare, which prevents us from using the region-specific PBAP observations for the present study. Hence, PT21's default observations were used to calculate the relative contribution of various PBAP groups to insoluble organics. The parameters for the shape of the particle size distribution (PSD) of each PBAP group (modal mean diameters, standard deviation ratios, and relative numbers in various modes) are prescribed, based on observations from Amazon (PT21). Figure S4 depicts the corresponding size distribution of various PBAP groups in AC. To check the validity of the observation from PT21 over the region considered in the current study, the model-estimated values of one of the major PBAP bacteria are compared with the observations, as shown Fig. S5. It shows that the estimated values of bacterial number concentration are overall in fair agreement with previous observations (e.g. Bowers et al., 2009; Bauer et al., 2002; Burrows et al., 2009). The simulated bacterial ($\sim 10^4\,m^{-3}$) and fungal ($\sim 10^3\,m^{-3}$) number concentration by AC is in good agreement with their typical concentration in the atmosphere (Després et al., 2012). The resulting ver-

tical profiles of mass of the various PBAP groups are shown in Fig. S3f.

From these prescribed loadings of aerosol species, AC predicts their size distribution and, hence, the CCN activity spectrum. Using the initial sounding and aerosol profile, AC can predict the in-cloud size distribution of aerosols in each species and in-cloud supersaturation. Figure S6 shows the predicted CCN spectrum comparison with observations from the CCN counter at the surface at the SGP site. It should be noted that the aerosol mass loading from IMPROVE observations showed variations of 20 %–30 % for the simulated case. The uncertainties in the input aerosol mass loading can result in simulated CCN concentration and are shown by the errors in the CCN concentration predicted by the AC. During 19–20 May, the measured number concentration of active CCN at the SGP CF ranged from 400 to 3000 cm^{-3} at 1 % supersaturation (Fridlind et al., 2017). The measurements were made on 20 May before the start of the rain in clear air. The normalized CCN number concentrations at 1 % supersaturation from observations and AC are ~ 1000 and ~ 940 cm^{-3}, respectively. Given the wide range of observed CCN concentrations at each supersaturation and the uncertainties in the model-predicted CCN concentration, the predicted and observed CCN activity spectra are in acceptable agreement.

4 Results from control simulation and model validation

4.1 Overview of the control simulation

An intense north-to-south-oriented squall line moved over the ARM SGP CF on 20 May 2011, from 11:00 to 14:00 UTC (Sect. 2.1). The new version of AC simulated this case, after implementing the empirical formulation by PT21, for multiple groups of PBAP INPs (control simulation; Sect. 3). It should be noted that five ensemble runs were carried out for the control simulation (see Table S3), varying the perturbation in the initial water vapor mixing ratio.

Figure 1 shows the time–height evolution of various liquid and ice cloud microphysical parameters derived from the control simulation conditionally averaged over cloudy regions. The maximum average cloud droplet number concentration was around 250 cm^{-3}. The liquid water content (LWC) was typically less than 0.5 g m^{-3}. The freezing level (0 °C) was around 4.1 km a.m.s.l. The deep convection began at around 10:00 UTC, followed by intense precipitation at around 11:00 UTC, and reached its peak at around 12:00 UTC. The time–height evolution of cloud ice, snow, and graupel number concentrations shows maxima shortly before 12:00 UTC, which coincides with the time of peak precipitation. This suggests that the ice phase was important in precipitation formation.

The time–height map of simulated radar reflectivity during 20 May, unconditionally averaged over the whole domain, is shown in Fig. 1g. It shows the well-defined squall line passing over the domain from 11:00 to 15:00 UTC. The maximum of this domain-wide simulated reflectivity was around 40 dBZ when deep convection was happening. The instantaneous maximum of reflectivity at any grid point (not shown here) was about 50 dBZ. At other times, the average reflectivity was typical of the stratiform cloud of about 15 dBZ. The cloud top height of the squall line decreases after 14:00 UTC.

4.2 Model validation against coincident observations of the storm

The extended stratiform region of the squall line while in the vicinity of the SGP CF was sampled by the Citation aircraft equipped with a full suite of cloud microphysical instrumentation. The aircraft started sampling the stratiform precipitation region at around 13:00 UTC and continued the observations at sub-freezing temperatures from 13:35 to 15:15 UTC. Occasionally, the aircraft encountered weak convective updrafts (<6 m s^{-1}). The aircraft actively avoided convection that was more vigorous than that. In this section, we validate various microphysical and dynamical quantities from the control simulation against aircraft and ground measurements. The control run includes all primary and SIP processes of ice initiation. The vertical profiles shown here are an average of five ensemble runs.

Figure 2 compares the aircraft observations against predicted microphysical quantities, with both the predictions and observations identically averaged, conditionally over convective ($6 > |w| > 1$ m s^{-1}) and stratiform regions $|w| < 1$ m s^{-1}). The simulated LWC decreases exponentially with height above the cloud base. There is considerable scatter in the observed LWC at each level. The various degrees of dilution of sampled parts of the cloud can cause these variations in LWC at a given altitude. The maximum simulated LWC of 0.5 g m^{-3} was observed in the convective region at temperatures warmer than -5 °C. In the convective region around -5 °C, the measured LWC is lower than the simulated LWC by a factor of 3. For the stratiform region, simulated values of LWC are in adequate agreement with observations. Overall, the means of observed LWC are in acceptable agreement with the model results for convective and stratiform regions.

The vertical profiles of simulated and observed cloud drop number concentration (CDNC; Fig. 2c and d) showed that the CDNC was lower than 300 cm^{-3}. In the convective region, the measured CDNC is 40 % lower than the simulated CDNC at 15 °C. However, an adequate agreement between them is found around -5 °C. For the stratiform region, simulated CDNC is much higher in the mixed-phase region. However, at a temperature warmer than 0 °C the values of observed CDNC are in acceptable agreement with observations. The observed and simulated mean diameter of cloud droplets varied between 6 to 16 μm (Fig. 2e and f). There are few points in the convective region e.g., around -5 °C, where the observed cloud drop diameter is 50 % lower than the sim-
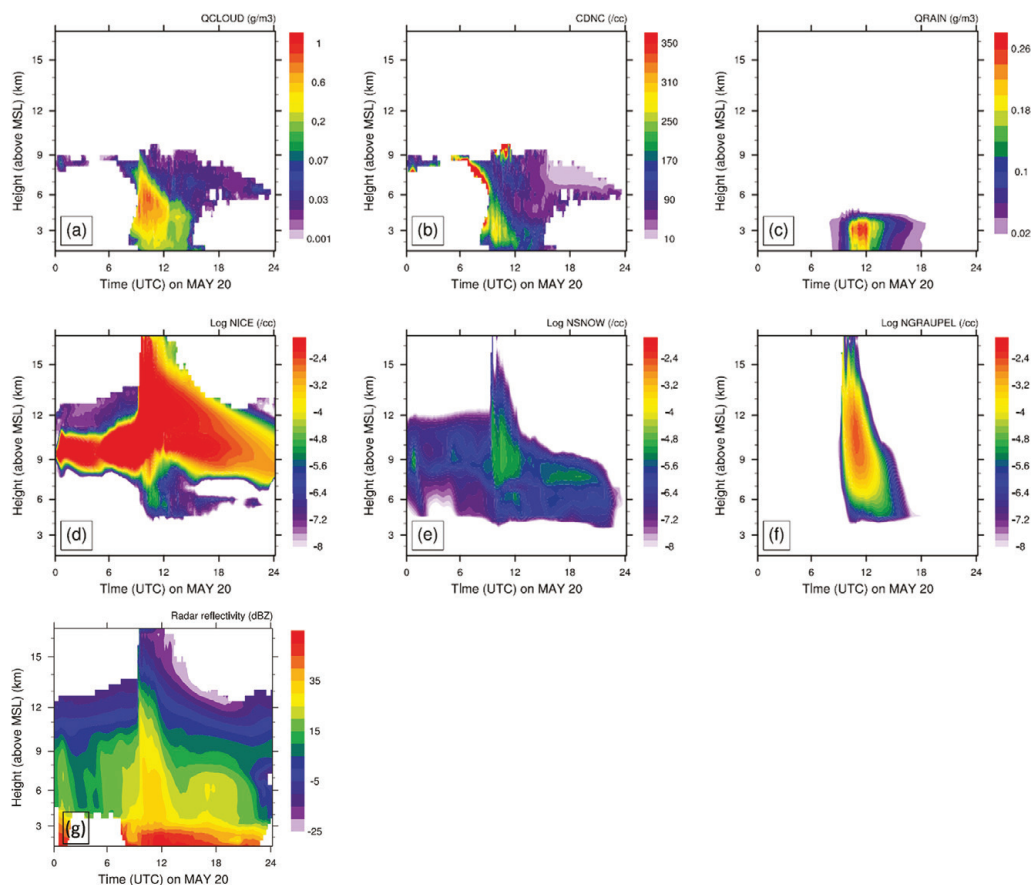
Figure 1. Time–height contours of the domain-averaged **(a)** cloud water mixing ratio (QCLOUD), **(b)** cloud droplet number concentration (CDNC), **(c)** rainwater mixing ratio (QRAIN), **(d)** number concentration of cloud ice (NICE), **(e)** number concentration of snow (NSNOW), and **(f)** number concentration of graupel (NGRAUPEL). Due to a wide range of values, the log values number concentrations are plotted. The surface height is ~ 500 m. The averaging was done for cloud points with LWC>0.001 g m^{-3} or total water content (TWC) $>10^{-6}$ g m^{-3}. Also shown is the time–height evolution of the domain-averaged **(g)** radar reflectivity.

ulated value. An adequate agreement between simulated and observed cloud drop diameter was found for the stratiform region. Overall, the predictions of the average CDNC and cloud droplet diameter, in both convective and stratiform regions, show a fair agreement with observations.

The ice particle number concentration from observations and the control simulation is also compared as shown in Fig. 3a and b for convective and stratiform regions, respectively. It should be noted that the observed number concentration of ice particle particles smaller than 200 µm is prone to shattering, even with the use of the shattering correction

algorithm. This can introduce a significant bias in the observed ice number concentration (Korolev et al., 1991). To avoid these biases, we have compared the number concentration of ice particles with a diameter greater than 200 µm from both observation and model (denoted by NT200). However, in the rest of the paper (in sensitivity studies), the number concentration from the model included ice particles of all size ranges.

Observations show that the concentration of ice particles gradually increases as the temperature decreases, as expected. The maximum ice number concentration from
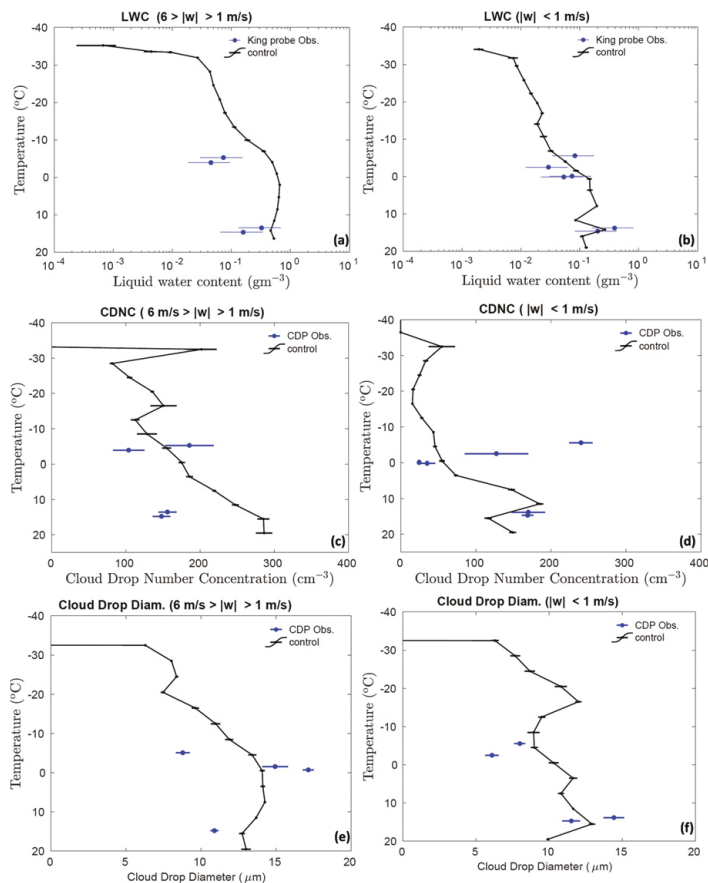
Figure 2. Comparison of the control simulations by AC with aircraft observations for the liquid water content conditionally averaged over **(a)** convective ($6 \, \text{m s}^{-1} > |w| > 1 \, \text{m s}^{-1}$) and **(b)** stratiform ($|w| < 1 \, \text{m s}^{-1}$) regions, cloud drop number concentration over **(c)** convective and **(d)** stratiform regions, and average size of cloud droplets ($< 20 \, \mu\text{m}$) conditionally averaged over **(e)** convective and **(f)** stratiform regions. All the vertical profiles shown here are averaged for the whole domain. The error bars were estimated based on five ensemble runs.

the aircraft observations (with $D > 200 \, \mu\text{m}$) is $\sim 0.06 \, \text{cm}^{-3}$ around $-15\,^{\circ}\text{C}$. Good agreement to within 50 %, at most levels, was found between the model-simulated NT200 and that observed for the convective region.

In the stratiform region, at most levels, model values of NT200 have the same order of magnitude as observations. However, between about the -10 and $-16\,^{\circ}\text{C}$ levels, the stratiform NT200 values are about half an order of magnitude lower than the observations. In similar simulations of the 20 May case, Fan et al. (2015) and Fridlind et al. (2017) also showed an underestimation of simulated ice number concentrations. Compared to the observations, their simula-

tions showed half an order of magnitude bias in ice crystal number concentration. Comparatively, for the convective region, our model-predicted ice number concentrations were in better agreement with the observations. As mentioned in Sect. 2.2, imaging probe data are prone to shattering, and various corrections were used to rectify this. However, there are currently no ways of determining how many undetected artifacts remain after shattering corrections have been applied (Baumgardner et al., 2017). Such uncertainties in measured ice number concentration could result in such bias in observed and simulated ice number concentrations. In sum-
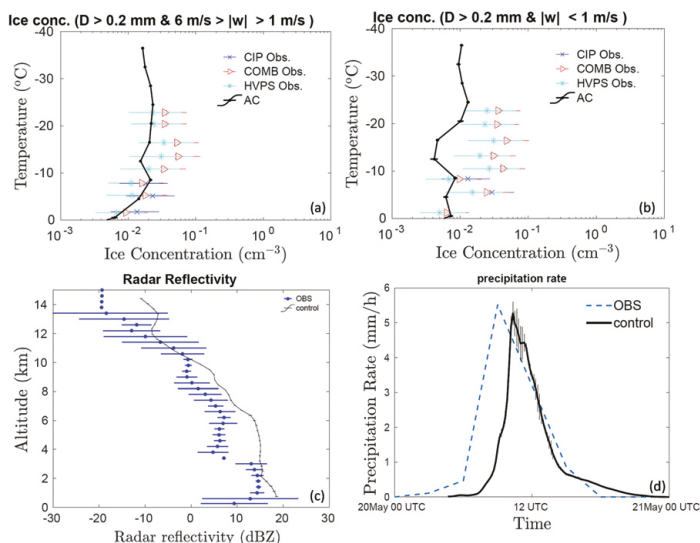
Figure 3. Comparison of the control simulations by AC with aircraft observations for the ice number concentration of all particles >0.2(NT200) mm in the maximum dimension of all microphysical species (cloud ice, graupel/hail, and snow), averaged over **(a)** convective $(6\,\mathrm{m\,s^{-1}} > |w| > 1\,\mathrm{m\,s^{-1}})$ and **(b)** stratiform $(|w| < 1\,\mathrm{m\,s^{-1}})$ regions. **(c)** The vertical profile of simulated radar reflectivity conditionally averaged over all regions of significant reflectivity $(> -20\,\mathrm{dBZ})$ at each level is compared with observations from ground-based radars. The temperature corresponding to each altitude is mentioned on the right axes, and the **(d)** predicted precipitation rate $(\mathrm{mm\,h^{-1}})$ is compared with ground observations at the SGP CF. All the vertical profiles shown here are averaged for the whole domain. The error bars were estimated based on five ensemble runs.

mary, though the AC model is not totally perfect, it did a fair job in simulating observed ice number concentrations.

In Fig. 3c, the radar reflectivity from vertically pointing Ka-band ARM zenith radar is compared with the mean profile from model simulations. This figure illustrates that simulated reflectivity profiles below roughly 3 km and 8 km a.m.s.l. altitudes are in good agreement with observations. Between 3 and 8 km a.m.s.l. (temperatures of 2 and $-30\,^\circ$C), the bias in the reflectivity from model simulations and observations is about 10 dBZ. Thus, the simulated reflectivity is substantially higher than the observed, particularly at levels where the aircraft sampled the clouds. Fridlind et al. (2017), and Fan et al. (2015), noticed similar overestimations of reflectivity within stratiform outflow of the squall line case on 20 May. They attributed the reflectivity biases to significantly larger ice particles in the simulations than in the observed.

Figure 3d compares the time series of the precipitation rate from the control simulation with the radar-based precipitation estimates. In both the control simulation and observations, a maximum precipitation rate of about 5 mm h^{-1} was noticed, with an error in the prediction of less than 5 %. In comparison to observations, the simulated squall line arrives 1–2 h later. The lack of resolution of the 3-D turbulence in the

planetary boundary layer and uncertainties associated with the 3-D structure of initial and boundary conditions can all have an independent impact on the simulated rainfall structure, resulting in a delayed peak. Nonetheless, AC has done a fair job of simulating the peak in the predicted precipitation rate.

4.3 Analysis of simulation with ice particle budgets and tagging tracers

The activated PBAP INPs from the control run are shown in Fig. 4 for the convective and stratiform regions. In addition to the PBAP INPs, Fig. 4 also shows the activated INPs from dust and black carbon. It should be noted that these concentrations shown here are based on advective tagging tracers that follow the diffusion, ascent, and descent inside cloud motions. Overall, bacterial and fungal particles dominate the biological INP concentration in the simulated cloud. For example, at $-20\,^\circ$C, the activated INPs from bacteria and fungi are higher than the other three groups of PBAP INPs (detritus, pollen, and algae) by 2 orders of magnitude in both convective and stratiform regions. At that level in convective regions, the average concentration of simulated active PBAP INPs is about $3 \times 10^{-6}\,\mathrm{cm^{-3}}$, which is 2 orders of

magnitude less than the maximum total for all active INPs (about $3 \times 10^{-4}\,\mathrm{cm}^{-3}$) in the whole simulation. Overall, the predicted total INP concentration is dominated by black carbon and dust. At $-10\,°\mathrm{C}$, the activated INPs from dust and black carbon differ by an order of magnitude from the total PBAP INPs in convection.

The formation of ice in a cloud is a result of several primary and secondary processes. It is important to understand the relative importance of these processes in precipitation formation. To that end, Fig. 5a shows the ice particles initiated from various sources throughout the 3-D domain of the entire simulation. The primary homogeneous (PRIM_HOM) dominates the total ice budget. Among all SIP mechanisms, breakup caused by collisions between various ice particles is the most important in determining the total ice number concentration. The ice production by the sublimation breakup of graupel is slightly lower than PRIM_HOM. However, the contribution of ice production via the sublimation breakup of dendritic ice crystals is negligible.

Figure 5b and c depict the relative importance of ice concentration from various SIP mechanisms and active INPs in determining the total ice number as a function of temperature for convective and stratiform regions. Each source of ice displayed is tracked with advective tagging tracers throughout the simulation. Overall, at temperatures warmer than $-15\,°\mathrm{C}$, the contribution to the total ice number concentration from various SIP is 2–3 orders of magnitude higher than the concentration of active INPs, highlighting the importance of SIP mechanisms in ice formation. At $-25\,°\mathrm{C}$, breakup in ice–ice collisions contributes around 75 % and 20 % of the total ice concentration in the convective and stratiform regions, respectively. At the same temperature, in both the convective and stratiform regions, sublimation breakup and raindrop freezing contribute about 8 % and 0.8 %, respectively. It can be observed that, in the convective regions at temperatures warmer than $-30\,°\mathrm{C}$, SIP mechanisms are important in determining the total ice concentrations, whereas at colder temperatures, homogeneous nucleation is dominant. In the stratiform region, this crossover occurs at a much warmer temperature around $-18\,°\mathrm{C}$. At temperatures colder than this, homogeneous nucleation is a major contributor to the total ice, whereas at warmer temperatures, SIP mechanisms prevail. Overall, the contribution of active INP to the total ice is lower than 3 %.

Secondary ice formation via the HM process of rime splintering contributes significantly to ice production at temperatures warmer than about $-15\,°\mathrm{C}$ (Fig. 5b and c), enhancing the ice concentration beyond the primary ice. In the convective region, the contribution of the HM process in total ice can reach as high as 40 % at around $-5\,°\mathrm{C}$. The simulated cloud droplet diameter is mostly smaller than 15 µm. It is smaller than the cloud droplet size required for the HM process to occur. In AC, the rate of the rime splintering mechanism depends on the concentration of droplets >24 µm. It should be noted that, in the AC model, the HM process is treated with a factor multiplying the fragment emission which depends on the cloud droplet size. This factor is zero for cloud diameter below 16 µm and unity above 24 µm, with linear interpolations in between.

5   Results from sensitivity tests about the influence of PBAP

To quantify the effect of multiple types of PBAPs on cloud properties, sensitivity tests were performed by modifying the control simulation and comparing the perturbed simulations with it. A description of various sensitivity tests carried out in the current study are listed in Table S3. The corresponding figures for each simulation are also mentioned.

Simulations were performed by eliminating all PBAPs from the control (no PBAP case) and by multiplying their initial loadings at all levels by factors of 10 and 100 (high PBAP and very high PBAP cases), respectively. A comparison with the control simulation reveals the overall effect from both the CCN and IN activities of all bioaerosols combined. These factors are justified by considering the variations in PBAP concentrations in the range of about 0.1 to $30\,\mathrm{L}^{-1}$ over North American forests (Huffman et al., 2013). An additional simulation was conducted with a 1000-fold increase in initial PBAP loading (ultra-high PBAP) to investigate if these unrealistically high concentrations of PBAPs could affect the ice phase in a purely hypothetical scenario. A total of five ensemble runs were carried out for all major simulations involving perturbations in PBAP loading. The ensemble runs were carried out by varying the perturbation in initial conditions (water vapor mixing ratio).

Additional simulations were performed by removing the treatment of biological IN activity in the EP (no PBAP INP case) relative to the control run. A comparison of both additional simulations against the corresponding simulations with the full change in the PBAP loadings (no PBAP and high PBAP cases) reveals the separate roles of the INP and CCN activities for the changes in biological material. Apart from these changes in PBAPs, the perturbed simulations are identical to the control run.

Figure 6 reveals the effects of all bioaerosols on cloud properties in the convective region ($|w|>1\,\mathrm{m\,s}^{-1}$). Overall, changes in cloud microphysical properties, including liquid water content, cloud droplet size, cloud drop number concentration, and ice number concentration, are less sensitive to the changes in PBAPs for the convective part of the simulated clouds and are not statistically significant. The LWC, cloud droplet number, and cloud drop diameter in the perturbed simulations do not differ much (<3 %) from the control run. For the whole storm, considerable changes in the spatial distribution of total ice number concentration are observed due to changes in PBAPs (see Fig. S7). However, vertical profiles showed very small changes in the ice number concentrations. In the convective region, changes in ice crystal
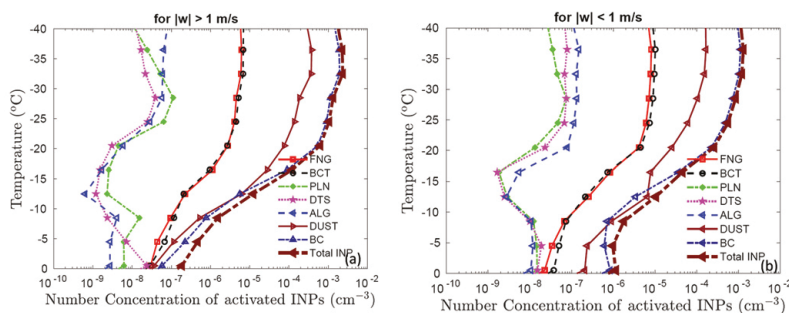
Figure 4. The activated number concentration of INPs from various PBAP groups are shown along with dust (DUST) and black carbon (BC) and total INPs at various temperatures for **(a)** convective and **(b)** stratiform regions. All the vertical profiles shown here are averaged for the whole domain.
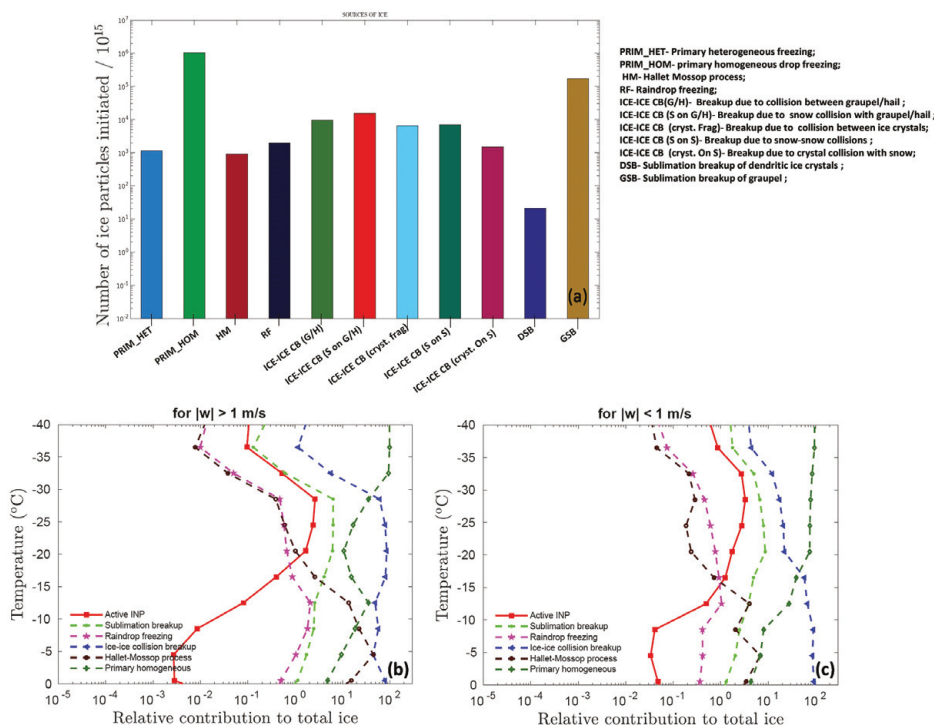
Figure 5. (a) Ice crystal budget for simulated MC3E case. The number of ice crystals produced by various mechanisms (as shown in the legend) per 10^{15} particles is shown. Also shown is the relative contribution of various SIP mechanisms such as sublimation breakup, raindrop freezing, ice–collision breakup, and the Hallett–Mossop process to the total ice number concentration as a function of temperature, averaged conditionally over only **(b)** convective and **(c)** stratiform regions. The relative contribution was calculated based on advective tagging tracers for the given process. The convective and stratiform regions were identified based on criteria $|w|>1$ and $|w|<1$, respectively.
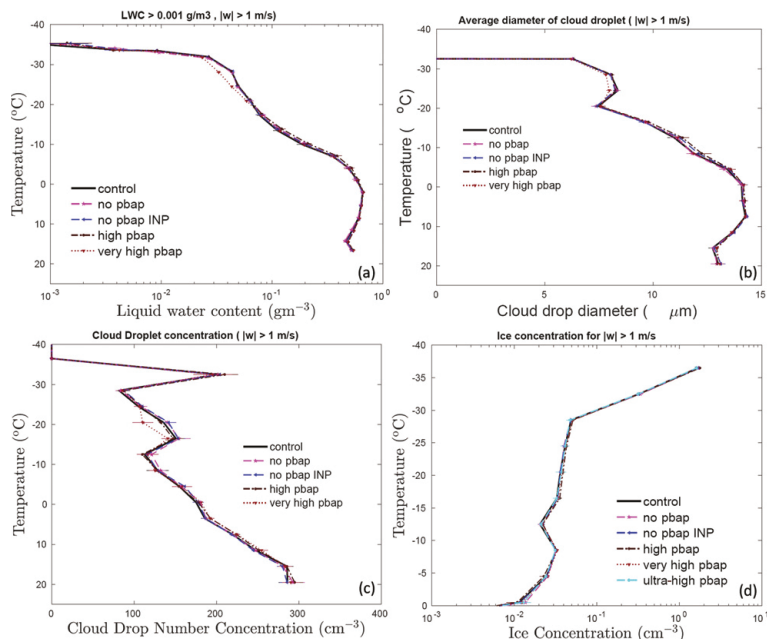
Figure 6. The temperature dependence of the **(a)** liquid water content, the **(b)** cloud droplet number, **(c)** the cloud droplet diameter, and the **(d)** total ice number concentration for control simulation and various sensitivity runs involving a change in total PBAP number concentrations for the convective region. The averaging conditions are mentioned at the top of each figure. The ice number concentration from the ultra-high PBAP is also shown in panel **(d)**. All the vertical profiles shown here are averaged for the whole domain.

number concentration due to changes in PBAPs are negligible ($< 6\%$) from all bioaerosols. This includes the extreme changes in bioaerosol loading (ultra-high PBAP case).

Figure 7 shows the corresponding effects in the stratiform region ($|w| < 1\,\mathrm{m\,s^{-1}}$) from all bioaerosols. The changes in warm microphysical properties because of changes in PBAP loadings are smaller than 10 %. In this part of the cloud, the ice microphysical parameters are comparatively more sensitive to the changes in PBAP than in the convective region. The ultra-high PBAP case predicted a $\sim 40\%$ lower ice number concentration than the control run. However, these changes in the ice number concentration are not significant as the error bars associated with ensemble members overlap. For the stratiform region, all other simulations considered here showed $< 10\%$ change in ice number concentrations compared to the control run. These changes in ice number concentration due to PBAPs are mostly controlled through their effect on homogeneous freezing above the $-36\,^\circ\mathrm{C}$ level, as shown in Fig. 7e, by the tagging tracer for homogeneous nucleation. These ice particles can then advect to lower levels, affecting ice number concentrations in the mixed-phase region.

Figure 8 shows the number of ice particles generated by homogeneous nucleation, various mechanisms of primary nucleation (Fig. 8a), and secondary ice production (Fig. 8b) per 10^{15} ice particles for the entire storm. Homogeneous freezing dominates the ice production among the three broad types of ice formation mechanisms (heterogeneous and homogeneous ice nucleation and SIP). The maximum changes in ice nucleated through the primary ice mechanism are noticed for the very high PBAP case and can be attributed to the 100-fold increase in all PBAP loading. The very high PBAP simulation predicted a 15 % lower number of homogeneously nucleated ice than the control run. The very high PBAP cases predicted about 80 % more primary ice crystals formed at temperatures warmer than $-30\,^\circ\mathrm{C}$. At temperatures colder than $-30\,^\circ\mathrm{C}$, this case predicted 20 % more primary ice crystals than the control run. The very high PBAP case showed an increase in primary heterogeneous ice and a decrease in primary homogenous ice. Since the contribution of primary homogenous ice nucleation is much higher in determining the total ice number concentration when compared with primary homogeneous nucleation, the overall effect of the very high PBAP case is a decrease in total ice number
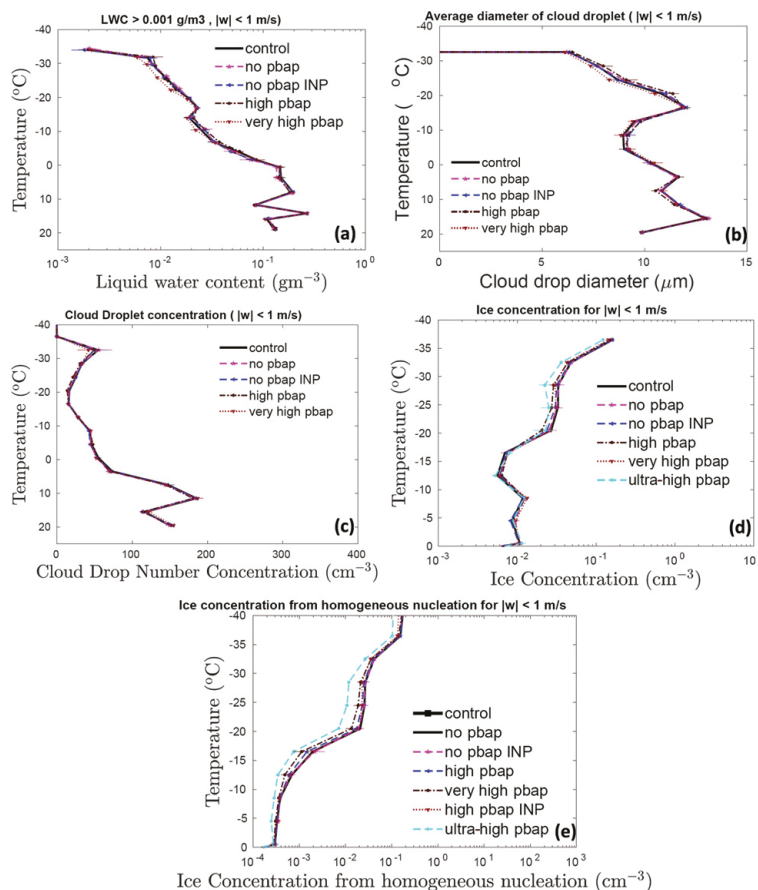
Figure 7. The temperature dependence of **(a)** the liquid water content, **(b)** the cloud droplet number, **(c)** the cloud droplet diameter, and the **(d)** total ice number concentration for the control simulation and various sensitivity runs involving a change in total PBAP number concentrations for in the stratiform region. Also shown is the temperature dependence of **(e)** ice concentration on homogeneous freezing. The averaging conditions are mentioned at the top of each figure. The total ice number concentration and ice number from homogeneous freezing from ultra-high PBAP are also shown in panels **(d)** and **(e)**. All the vertical profiles shown here are averaged for the whole domain. The error bars are based on ensemble runs.

concentration as shown in Fig. 7 and Table S4. However, at temperatures warmer than $-35\,°C$, the ice number concentration in the very high PBAP case was comparable with the control run (Table S5).

Figure 8b shows that, among SIP mechanisms, the contributions of ice–ice collision breakup and sublimation breakup are higher by an order of magnitude than the HM process and raindrop fragmentation. However, the budget analysis (not shown in the plot) showed that about 75 % of the fragments associated with sublimation breakup are prone to evapora-

tion, making the ice–ice collision breakup a major SIP mechanism. The estimated ice enhancement ratio, which is a ratio between the number concentrations of total ice (excluding homogeneous nucleation) and primary ice, is shown in Fig. 8c and d for convective and stratiform regions, respectively. Overall, the ice enhancement ratio varied between 10 to 10^4, which indicates the importance of SIP mechanisms. The budget analysis shows that, overall, the perturbations in bioaerosols resulted in very small changes (with a maximum change of $<40\,\%$) in ice generated by SIP mechanisms.

Figure 8. The number of ice crystals produced during the whole storm by **(a)** primary ice nucleation mechanisms and homogeneous f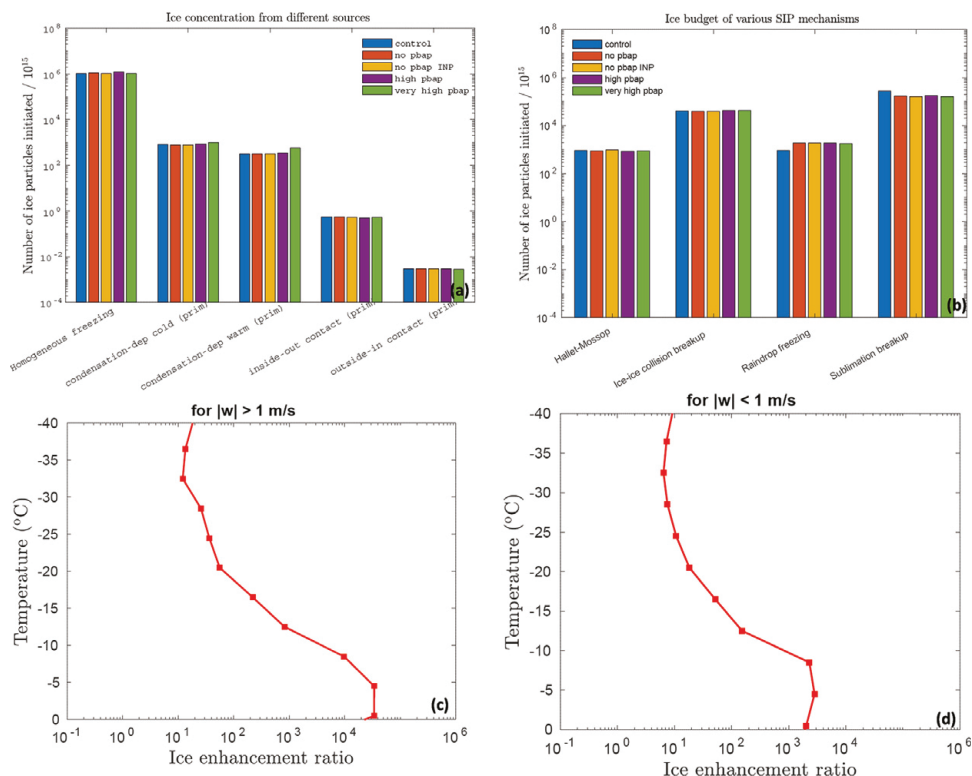reezing, and **(b)** various SIP mechanisms (as shown in the legend) per 10^{15} particles are shown for various sensitivity runs. The ice enhancement ratio for the convective and stratiform regions is shown in panels **(c)** and **(d)**.

The role of PBAPs in altering radar reflectivity and surface precipitation was limited and described briefly in the Supplement (Fig. S8). The overall effect of PBAPs on accumulated surface precipitation was minimal (<4 %; Fig. S8 and Table S4). In addition, the changes in PBAPs do not show a significant impact on shortwave and longwave radiation fluxes and cloud fractions, as discussed in the Supplement (Fig. S9).

6   Results from sensitivity tests about secondary ice production

Various sensitivity experiments were conducted to evaluate the role of SIP mechanisms in determining micro- and macrophysical parameters of the clouds (see Table S3). SIP through sublimation breakup and breakup in ice–ice collisions were switched off in the no sublimation breakup and no collisional ice–ice breakup simulations, respectively. In the no secondary case, no SIP mechanisms were active.

The results from these sensitivity experiments are shown in Fig. 9 for the convective and the stratiform region of the simulated cloud. Overall, in the convective region, the no secondary and no collisional ice–ice breakup cases predicted 5 % and 12 % higher LWC, respectively, than the control run (see Table S4). In the stratiform region, these cases predicted ~ 25 % higher LWC than the control run. Lower ice number concentrations due to the absence of SIP mechanisms may reduce the rate of conversion of liquid to ice via mixed-phase processes, resulting in a higher LWC.

In the convective part, the absence of any SIP increased the ice number concentration by half an order of magnitude at temperatures warmer than $-25\,^\circ$C. Comparing the no SIP and control cases, the effect of the inclusion of SIP mechanisms is to increase the average ice concentration by up to half an order of magnitude at temperatures warmer than $-15\,^\circ$C in the stratiform region. For the stratiform region, at temperatures colder than this, the absence of SIP mecha-
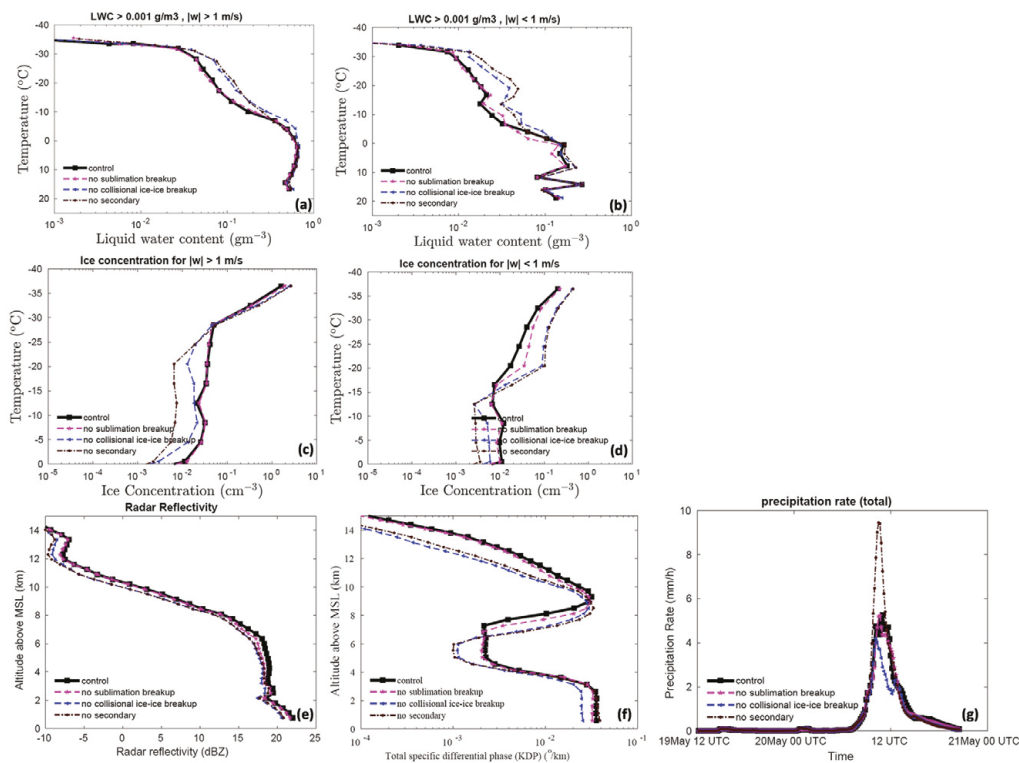
Figure 9. Temperature dependence of the liquid water content in (**a**) the convective and (**b**) the stratiform region for the control simulation and various sensitivity runs involving SIPs. The ice number concentration is also shown for the (**c**) convective and (**d**) stratiform regions. The averaging conditions are mentioned at the top of each figure. The vertical profiles of (**e**) radar reflectivity and (**f**) total specific differential phase are also shown for the same simulations. (**g**) The temporal evolution of the total surface precipitation rate averaged over the domain is also shown. All the vertical profiles shown here are averaged for the whole domain.

nisms resulted in higher ice number concentrations by a similar magnitude. These changes at the colder levels are associated with homogeneous droplet freezing. The changes in ice number concentration in the no collisional ice–ice breakup case are comparable with the no secondary case. Compared to break up in ice–ice collisions, the sublimation breakup has a lower impact (<40 %) on the total ice number concentration in both the convective and stratiform regions.

The changes in simulated radar reflectivity, total specific differential phase, and surface precipitation rate with SIP mechanisms are shown in Fig. 9e, f, and g, respectively, for the whole storm. Overall, the simulated radar reflectivity was 1 dBZ lower in the no SIP and no collisional ice–ice breakup case than in the control run and can be attributed to the overall increase in ice number concentration in the control run.

The no sublimation case predicted slightly higher reflectivity than the control run. The absence of all SIPs resulted in about a 100 % decrease in the K_{DP} at a temperature colder than $-40\,^{\circ}$C. Between -10 and $-30\,^{\circ}$C, the absence of no collisional breakup and no secondary resulted in higher K_{DP} (half an order of magnitude) values than the control run. The absence of all SIP mechanisms results in a higher surface precipitation rate (75 %) during the peak rainfall hour, which occurs around 11:30 UTC compared to the control run. In a previous study, Phillips et al. (2017b) have shown that SIP through ice–ice collision breakup can reduce accumulated surface precipitation in the simulated storm by 20 %–40 %. They attributed it to the increase in snow particles competing for available liquid and the reduction in their growth by riming. It resulted in smaller ice particles and a reduction in surface precipitation.
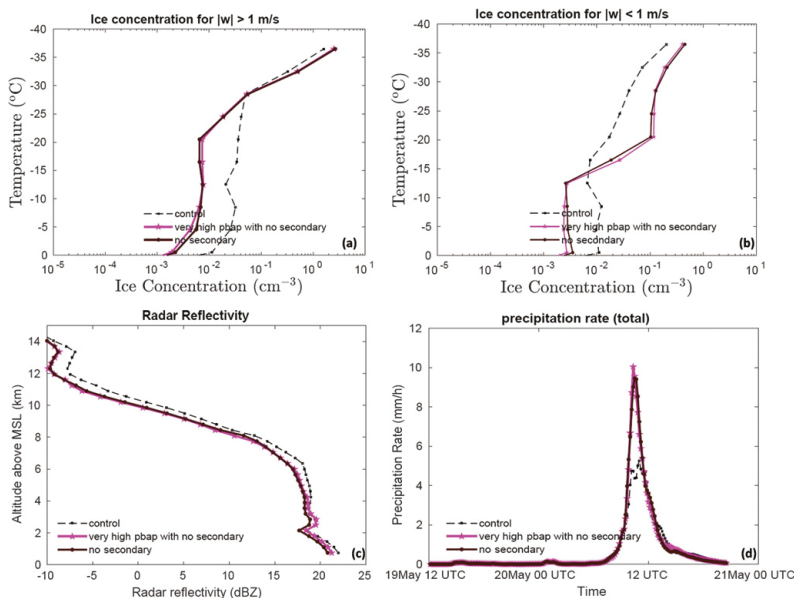
Figure 10. The temperature dependence of the ice number concentration for the control, very high PBAP with no SIP, and no SIP simulations averaged for **(a)** convective and **(b)** stratiform regions. The **(c)** vertical profile of the radar reflectivity and the temporal evolution of the **(d)** surface precipitation rate are shown for the entire simulation. All the vertical profiles shown here are averaged for the whole domain.

7 Results about the influence of PBAPs in the absence of SIP mechanisms

To investigate the role of PBAPs in altering cloud microphysical properties through SIP mechanisms, an additional simulation was performed by eliminating all secondary ice processes from the control run and multiplying the initial loading of all PBAP groups by a factor of 100 (the very high PBAP with no SIP case). The results of this simulation are then compared to the no SIP case, as shown in Fig. 10.

In the absence of any SIP mechanisms, the 100-fold increase in bioaerosols resulted in minimal effect on ice number concentration. Overall, without SIP, the increase in bioaerosol loading by 100-fold resulted in a less than 5 % change in the ice number concentration. This indicates that the ice produced by various SIP mechanisms does not alter the effect of bioaerosols on the ice number concentration in the simulated clouds. The changes in simulated radar reflectivity due to a 100-fold increase in bioaerosols are negligible (<0.5 %; Fig. 10c). The difference in the predicted surface precipitation rate and accumulated precipitation between very high PBAP with no secondary and no secondary cases was lower than 3 %.

8 Discussion

In total, rive PBAP groups have been implemented in the mesoscale AC model to predict their ice nucleation activity based on the empirical formulation by PT21. The simulated concentrations of major PBAPs, including fungi and bacteria, are of the same order of magnitude as results from previous modeling studies (Després et al., 2012; Hoose et al., 2010b). Still, the relative abundance of PBAP groups over the simulated region is unknown due to the lack of measurements. The AC model was run with a higher resolution (2 × 2 km), compared to previous studies on a global scale (Hoose et al., 2010b), to investigate the potential impact of variations in PBAP concentration on the properties of the simulated squall line events more clearly.

Yet the control simulation is not perfectly accurate in all respects. In the stratiform region between −10 and −16 °C, the predicted ice number concentration was lower than that observed by aircraft by half an order of magnitude and in fair agreement at temperatures warmer than −10 °C. This uncertainty factor is similar to the uncertainty in the measurements due to various biases (e.g., Field et al., 2006). Nevertheless, all other simulated cloud microphysical parameters, radar reflectivity, and the surface precipitation rate were in acceptable agreement with aircraft and ground-based observations.

In the control simulation, the average ice concentration above −30 and −18 °C levels is dominated by the downwelling of homogeneously nucleated ice from above the mixed-phase region in convective and stratiform clouds, respectively. Below both levels, SIP prevails. Both processes of ice initiation (homogeneous freezing and SIP) have only weak sensitivity to PBAPs and, hence, the weakness of the impact on simulated cloud glaciation.

Based on the sensitivity experiments, it can be concluded that PBAP INPs have only a limited effect on the average state of the ice phase of the simulated clouds of this mesoscale convective system. Most of the changes in ice number concentration associated with changes in PBAPs are controlled by their effects on homogeneous nucleation and SIPs. The lower dependence of simulated ice number concentration on changes in PBAPs is consistent with the findings of Hummel et al. (2018). Based on ensemble simulations of the regional atmospheric model for Europe, they showed that the changes in the average ice crystal concentration by biological INPs are very small and are not statistically significant, implying that PBAPs play only a minor role in altering the cloud ice phase. The limited effect of PBAPs on cloud properties on a global scale has been highlighted in previous studies (Hoose et al., 2010b; Sesartic et al., 2012, 2013; Spracklen and Heald, 2014).

The weakness of the simulated impact from realistic PBAP fluctuations is explicable mostly in terms of the low contribution from biological ice nucleation compared to non-biological INPs to the overall ice initiation. In terms of ice nucleation efficiency and onset temperatures, each PBAP group has different ice nucleation properties. Based on vertical profiles of active INPs (Fig. 4), the overall contribution of activated INPs from all PBAP groups to the total active INPs was ∼ 1 %. At −15 °C, temperature, the active INPs from dust and black carbon was 1 order of magnitude higher than PBAP INPs. At −30 °C, the predicted INPs from dust and black carbon were higher by 1 and 2 orders of magnitude, respectively, than PBAP INPs. The dust and black carbon INPs activated at these temperatures can be advected down to the levels where PBAP INPs are most important. Overall, this resulted in low sensitivity of the average ice phase to the changes in bioaerosol loading.

The ice production in the simulated cloud system at levels in the mixed-phase region (0 to −36 °C) is largely controlled by various SIP mechanisms, of which the most important is the breakup in ice–ice collisions. Some of these processes are active at temperatures warmer than −15 °C (e.g., the HM process), where PBAP INP are important and expected to enhance the biological ice nucleation. However, our results showed that the ice production associated with SIP mechanisms is less sensitive to the initial PBAP loading because SIP causes a positive feedback of ice multiplication with ice fragments growing to become precipitation-sized particles that then fragment again.

In our study, a 100-fold increase in PBAPs leads to a <4 % change in surface precipitation. Using mesoscale model simulations, Phillips et al. (2009) reported a 10 % increase in accumulated surface precipitation associated with deep convective clouds due to a 100-fold increase in biological particles. Phillips et al. (2009) also noted an effect (up to 4 %) on surface shortwave and top-of-atmosphere (TOA) longwave radiation flux because of changes in PBAP number concentration. In our study, the changes in PBAP loading caused smaller changes in simulated shortwave and longwave fluxes (<3 %). Sesartic et al. (2012, 2013) showed that including fungi and bacteria in the global climate model leads to minor changes (<0.5 %) in the ice water path, total cloud cover, and total precipitation.

It should be noted that the sensitivity experiments carried out in the current study are limited to the small domain (80 × 80 km domain) representing a limited area of the global ecosystem. Also, the model top was located at 16 km, and it may not represent the whole atmosphere. The results presented here are based on a mesoscale model and may not represent the global impact of PBAPs on clouds.

9   Conclusions

A framework describing the ice nucleation activity of five major groups of PBAPs, including fungal spores, bacteria, pollen, viral particles, plant/animal detritus, algae, and their respective fragments, was provided by PT21. The ice nucleation activity of these major PBAP groups in the EP was based on samples from the real atmosphere. The present study implements this EP in AC and investigates the role of these five PBAP groups as INPs in deep convective clouds. The high-resolution (2 km horizontally) simulations over a mesoscale 3-D domain (80 km wide) using AC elucidate the impact of these five PBAP groups on the cloud properties. A series of sensitivity experiments were conducted to test the impact of PBAP groups on cloud properties.

A midlatitude squall line that occurred on 20 May 2011 during MC3E over the USA Southern Great Plains is simulated with the model. The simulated number concentration of ice particles showed good agreement (to within about 50 %) with aircraft observations for the convective clouds within the mesoscale system. In the stratiform region between −10 and −16 °C, the model-predicted ice number concentration was lower than the aircraft observation by half an order of magnitude and in fair agreement at temperatures warmer than −10 °C. Various sensitivity experiments were carried out by perturbing the initial PBAP loading and by altering various SIP mechanisms.

Each PBAP group has diverse properties, including its shape, size, and abundance in the atmosphere. A small fraction of PBAPs is found to be ice nucleation active and can therefore act as PBAP INPs. The relative contribution of each PBAP within the total PBAPs may vary from one ecosystem

to another. In the current study, their relative contribution is based on previous observations from Amazonia and can be considered as the main limitations of this study. However, the simulated number concentrations of major PBAPs, including fungi and bacteria, look reasonable and are close to their typical abundance in the atmosphere.

Any perturbation in the PBAP concentration by factors up to 1000 assumed in the current study resulted in maximum changes in the ice number concentration by $<6\%$ in the convective region and by $<40\%$ in the stratiform region with respect to the control run. The simulations showed that the simulated ice particle number concentration is much higher than the number concentrations of PBAP INPs. Even at temperatures warmer than $-15\,°C$, where PBAP INPs are thought to be the most important INP, ice crystals originating from the primary heterogeneous nucleation of dust and black carbon from higher levels of the cloud frequently perturb the lower levels due to sedimentation. The major ice formation comes from SIP mechanisms and homogeneous nucleation and both are less sensitive to the changes in PBAPs. Therefore, PBAP INPs do not show a significant impact on the average ice phase of the simulated storm.

PBAPs have a minimal effect on the warm microphysical properties of simulated clouds. The effect on liquid water content and cloud droplet number concentration was lower than 10% in both convective and stratiform regions. Since both ice and warm microphysical processes are less sensitive to PBAPs, surface precipitation is not significantly affected by changes in PBAPs. A 100-fold increase in all PBAPs resulted in less than a 5% change in surface precipitation.

Code and data availability. Data and the code for the empirical formulation of PBAPs are available on request by contacting the corresponding author.

Supplement. The supplement related to this article is available online at: https://doi.org/10.5194/acp-22-12055-2022-supplement.

Author contributions. VTJP designed and monitored this study. SP conducted model simulation, did most of the data analysis, and wrote the initial draft. All authors contributed to the scientific discussion and model development.

Competing interests. The contact author has declared that none of the authors has any competing interests.

Disclaimer. Publisher's note: Copernicus Publications remains neutral with regard to jurisdictional claims in published maps and institutional affiliations.

References

Bauer, H., Kasper-Giebl, A., Loflund, M., Giebl, H., Hitzenberger, R., Zibuschka, F., and Puxbaum, H.: The contribution of bacteria and fungal spores to the organic carbon content of cloud water, precipitation and aerosols, Atmos. Res., 64, 109–119, 2002.

Baumgardner, D., Abel, S. J., Axisa, D., Cotton, R., Crosier, J., Field, P., Gurganus, C., Heymsfield, A., Korolev, A., Krämer, M., Lawson, P., McFarquhar, G., Ulanowski, Z., and Um, J.: Cloud Ice Properties: In Situ Measurement Challenges, Meteor. Mon., 58, 9.1–9.23, 2017.

Blyth, A. M. and Latham, J.: Development of ice and precipitation in New Mexican summertime cumulus clouds, Q. J. R. Meteorol. Soc. 119, 91–120, 1993.

Bowers, R. M., Lauber, C. L., Wiedinmyer, C., Hamady, M., Hallar, A. G., Fall, R., Knight, R., and Fierer, N.: Characterization of airborne microbial communities at a high-elevation site and their potential to act as atmospheric ice nuclei, Appl. Environ. Microbiol., 75, 5121–30, https://doi.org/10.1128/AEM.00447-09, 2009.

Burrows, S. M., Elbert, W., Lawrence, M. G., and Pöschl, U.: Bacteria in the global atmosphere – Part 1: Review and synthesis of literature data for different ecosystems, Atmos. Chem. Phys., 9, 9263–9280, https://doi.org/10.5194/acp-9-9263-2009, 2009.

Carlin, J. T., Reeves, H. D., and Ryzhkov, A. V.: Polarimetric Observations and Simulations of Sublimating Snow: Implications for Nowcasting, J. Appl. Meteorol. Climatol., 60, 1035–1054, 2021.

Chen, Q., Yin, Y., Jiang, H., Chu, Z., Xue, L., Shi, R., Zhang, X., and Chen, J.: The roles of mineral dust as cloud condensation nuclei and icenuclei during the evolution of a hail storm, J. Geophys. Res.-Atmos., 124, 14262–14284, 2019.

Chin, M., Rood, R. B., Lin, S. J., Müller, J. F., and Thompson, A. M.: Atmospheric sulfur cycle simulated in the global model GOCART: Model description and global

properties, J. Geophys. Res.-Atmos., 105, 24671–24687, https://doi.org/10.1029/2000JD000384, 2000.

Crawford, I., Bower, K. N., Choularton, T. W., Dearden, C., Crosier, J., Westbrook, C., Capes, G., Coe, H., Connolly, P. J., Dorsey, J. R., Gallagher, M. W., Williams, P., Trembath, J., Cui, Z., and Blyth, A.: Ice formation and development in aged, wintertime cumulus over the UK: observations and modelling, Atmos. Chem. Phys., 12, 4963–4985, https://doi.org/10.5194/acp-12-4963-2012, 2012.

Cui, Z. and Carslaw, K. S.: Enhanced vertical transport efficiency of aerosol in convective clouds due to increases in tropospheric aerosol abundance, J. Geophys. Res., 111, D15212, https://doi.org/10.1029/2005JD006781, 2006.

DeMott, P. J. and Prenni, A. J.: New Directions: Need for defining the numbers and sources of biological aerosols acting as ice nuclei, Atmos. Environ., 44, 1944–1945, 2010.

DeMott P. J., Prenni A. J., Liu, X., Kreidenweis, S. M., Petters, M. D., Twohy, C. H., Richardson, M. S., Eidhammer, T., and Rogers, D. C.: Predicting global atmospheric ice nuclei distributions and their impacts on climate, P. Natl. Acad. Sci. USA, 107, 11217–11222, 2010.

Deshmukh, A., Phillips, V. J. T. P., Bansemer A., Patade, S., and Waman, D.: New Empirical Formulation for the Sublimational Breakup of Graupel and Dendritic Snow, J. Atmos. Sci., 79, 317–336, https://doi.org/10.1175/JAS-D-20-0275.1, 2021.

Després, V. R., Huffman, J. A., Burrows, S. M., Hoose, C., Safatov, A. S., Buryak, G., Fröhlich-Nowoisky, J., Elbert, W., Andreae, M. O., and Pöschl, U.: Primary biological aerosol particles in the atmosphere: a review, Tellus B, 64, 15598, https://doi.org/10.3402/tellusb.v64i0.15598, 2012.

Dong, X. and Mace, G. G.: Arctic stratus cloud properties and radiative forcing derived from ground-based data collected at Barrow, Alaska, J. Climate, 16, 445–461, https://doi.org/10.1175/1520-0442(2003)016<0445:ASCPAR>2.0.CO;2, 2003.

Fan, J., Comstock, J. M., and Ovchinnikov, M.: The cloud condensation nuclei and ice nuclei effects on tropical anvil characteristics and water vapor of the tropical tropopause layer, Environ. Res. Lett., 5, 044005, https://doi.org/10.1088/1748-9326/5/4/044005, 2010.

Fan, J., Liu, Y-C, Xu, K. M., North, K., Collis, S., Dong, X., Zhang, G. J., Chen, Q., Kollias, P., and Ghan, S. J.: Improving representation of convective transport for scale-aware parameterization: 1. Convection and cloud properties simulated with spectral bin and bulk microphysics, J. Geophys. Res. Atmos., 120, 3485–3509. https://doi.org/10.1002/2014JD022142, 2015.

Fan, J., Han, B., Varble, A., Morrison, H., North, K., Kollias, P., Chen, B., Dong, X., Giangrande, S., Khain, A., Lin, Y., Mansell, E., Milbrandt, J. A., Stenz, R., Thompson, G., and Wang, Y: Cloud-resolving model intercomparison of an MC3E squall line case: Part I – Convective updrafts, J. Geophys. Res. Atmos., 122, 9351–9378, 2017.

Field, P. R. and Heymsfield, A. J: Importance of snow to global precipitation, Geophys. Res. Lett., 42, 9512–9520, https://doi.org/10.1002/2015GL065497, 2015.

Field, P. R., Heymsfield, A. J., and Bansemer, A.: Shattering and Particle Interarrival Times Measured by Optical Array Probes in Ice Clouds, J. Atmos. Ocean. Technol., 23, 1357–1371, 2006.

Fridlind, A. M., Li, X., Wu, D., van Lier-Walqui, M., Ackerman, A. S., Tao, W.-K., McFarquhar, G. M., Wu, W., Dong, X., Wang, J.,

Ryzhkov, A., Zhang, P., Poellot, M. R., Neumann, A., and Tomlinson, J. M.: Derivation of aerosol profiles for MC3E convection studies and use in simulations of the 20 May squall line case, Atmos. Chem. Phys., 17, 5947–5972, https://doi.org/10.5194/acp-17-5947-2017, 2017.

Fröhlich-Nowoisky, J., Kampf, C. J., Weber, B., Huffman, J. A., Pöhlker, C., Andreae, M. O., Lang-Yona, N., Burrows, S. M., Gunthe, S. S., Elbert, W., Su, H., Hoor, P., Thines, E., Hoffmann, T., Després, V. R., and Pöoschl, U.: Bioaerosols in the Earth system: climate, health, and ecosystem interactions, Atmos. Res. 182, 346–376, 2016.

Garcia, E., Hill, T. C. J., Prenni, A. J., DeMott, P. J., Franc, G. D., and Kreidenweis, S. M.: Biogenic ice nuclei in boundary layer air over two US high plains agricultural regions, J. Geophys. Res.-Atmos., 117, 1–12, https://doi.org/10.1029/2012JD018343, 2012.

Giangrande, S. E., Collis, S., Theisen, A. K., and Tokay, A.: Precipitation estimation from the ARM distributed radar network during the MC3E campaign, J. Appl. Meteorol. Climatol., 53, 2130–2147, https://doi.org/10.1175/JAMC-D-13-0321.1, 2014.

Grützun, V., Knoth, O., and Simmel, M.: Simulation of the influence of aerosol particle characteristics on clouds and precipitation with LM-SPECS: Model description and first results, Atmos. Res., 90, 233–242, https://doi.org/10.1016/j.atmosres.2008.03.002, 2008.

Hallett, J., and Mossop S. C.: Production of secondary ice particles during the riming process, Nature, 249, 26–28, https://doi.org/10.1038/249026a0, 1974.

Han, B., Fan, J., Varble, A., Morrison, H., Williams, C. R., Chen, B., Dong, X., Giangrande, S. E., Khain, A., Mansell, E., Milbrandt, J. A., Shpund, J., and Thompson, G.: Cloud-resolving model intercomparison of an MC3E squall line case: Part II. Stratiform precipitation properties, J. Geophys. Res.-Atmos., 124, 1090–1117, 2019.

Heymsfield, A. J., Schmitt, C., Chen, C., Bansemer, A., Gettelman, A., Field, P. R., and Liu, C.: Contributions of the Liquid and Ice Phases to Global Surface Precipitation: Observations and Global Climate Modeling, J. Atmos. Sci., 77, 2629–2648, 2020.

Hoose, C. and Möhler, O.: Heterogeneous ice nucleation on atmospheric aerosols: a review of results from laboratory experiments, Atmos. Chem. Phys., 12, 9817–9854, https://doi.org/10.5194/acp-12-9817-2012, 2012.

Hoose, C., Kristjánsson, J. E., and Burrows, S. M.: How important is biological ice nucleation in clouds on a global scale?, Environ. Res. Lett., 5, 024009, https://doi.org/10.1088/1748-9326/5/2/024009, 2010a.

Hoose, C., Kristjánsson, J. E., Chen, J. P., and Hazra, A.: A Classical-Theory-Based Parameterization of Heterogeneous Ice Nucleation by Mineral Dust, Soot, and Biological Particles in a Global Climate Model, J. Atmos. Sci., 67, 2483–2503, https://doi.org/10.1175/2010jas3425.1, 2010b.

Huang, S., Wei, H., Chen, J., Wu, Z., Zhang, D., and Fu, P.: Overview of biological ice nucleating particles in the atmosphere, Environ. Internat., 146, 106197, https://doi.org/10.1016/j.envint.2020.106197, 2021.

Huffman, J. A., Prenni, A. J., DeMott, P. J., Pöhlker, C., Mason, R. H., Robinson, N. H., Fröhlich-Nowoisky, J., Tobo, Y., Després, V. R., Garcia, E., Gochis, D. J., Harris, E., Müller-Germann, I, Ruzene, C., Schmer, B., Sinha, B., Day, D. A., An-

dreae, M. O., Jimenez, J. L., Gallagher, M., Kreidenweis, S. M., Bertram, A. K., and Pöschl, U.: High concentrations of biological aerosol particles and ice nuclei during and after rain, Atmos. Chem. Phys., 13, 6151–6164, https://doi.org/10.5194/acp-13-6151-2013, 2013.

Hummel, M., Hoose, C., Pummer, B., Schaupp, C., Fröhlich-Nowoisky, J., and Möhler, O.: Simulating the influence of primary biological aerosol particles on clouds by heterogeneous ice nucleation, Atmos. Chem. Phys., 18, 15437–15450, https://doi.org/10.5194/acp-18-15437-2018, 2018.

Jaenicke, R.: Abundance of cellular material and proteins in the atmospheric, Science, 308, p. 73, https://doi.org/10.1126/science.1106335, 2005.

Jensen, M. P., Petersen, W. A., Bansemer, A., Bharadwaj, N., Carey, L. D., Cecil, D. J., Collis, S. M., Del Genio, A. D., Dolan, B., Gerlach, J., Giangrande, S. E., Heymsfield, A., Heymsfield, G., Kollias, P., Lang, T. J., Nesbitt, S. W., Neumann, A., Poellot, M., Rutledge, S. A., Schwaller, M., Tokay, A., Williams, C. R., Wolff, D. B., Xie, S., and Zipser, E. J.: The midlatitude continental convective clouds experiment (MC3E), B. Am. Meteorol. Soc., 97, 1667–1686, https://doi.org/10.1175/BAMS-D-14-00228.1, 2016.

Kanji, Z. A., Ladino, L. A., Wex, H., Boose, Y., Burkert-Kohn, M., Cziczo, D. J., and Krämer, M.: Overview of Ice Nucleating Particles, Meteor. Mon., 58, 1.1–1.33, 2017.

Knopf, D. A., Alpert, P. A., Wang, B., and Aller, J. Y.: Stimulation of ice nucleation by marine diatoms, Nat. Geosci. 4, 88–90, https://doi.org/10.1038/ngeo1037, 2011.

Korolev, A. and Leisner, T.: Review of experimental studies of secondary ice production, Atmos. Chem. Phys., 20, 11767–11797, https://doi.org/10.5194/acp-20-11767-2020, 2020.

Korolev, A. V., Kuznetsov, S. V., Makarov, Y. E., and Novikov, V. S: Evaluation of Measurements of Particle Size and Sample Area from Optical Array Probes, J. Atmos. Ocean. Technol., 8, 514–522, 1991.

Korolev, A., McFarquhar, G., Field, P. R., Franklin, C., Lawson, P., Wang, Z., Williams, E., Abel, S. J., Axisa, D., Borrmann, S., Crosier, J., Fugal, J., Krämer, M., Lohmann, U., Schlenczek, O., Schnaiter, M., and Wendisch, M.: Mixed-Phase Clouds: Progress and Challenges, Meteor. Mon., 58, 5.1–5.50, 2017.

Korolev, A., Heckman, I., Wolde, M., Ackerman, A. S., Fridlind, A. M., Ladino, L. A., Lawson, R. P., Milbrandt, J., and Williams, E.: A new look at the environmental conditions favorable to secondary ice production, Atmos. Chem. Phys., 20, 1391–1429, https://doi.org/10.5194/acp-20-1391-2020, 2020.

Kumjian, M. R. and Lombardo, K. A.: Insights into the evolving microphysical and kinematic structure of northeastern U.S. winter storms from dual-polarization Doppler radar, Mon. Wea. Rev., 145, 1033–1061, https://doi.org/10.1175/MWR-D-15-0451.1, 2017.

Lawson, R. P., Woods, S., and Morrison, H.: The microphysics of ice and precipitation 1195 development in tropical cumulus clouds, J. Atmos. Sci., 72, 2429–2445, https://doi.org/10.1175/JAS-D-14-0274.1, 2015.

Levin, Z., Yankofsky, S., Pardes, D., and Magal, N.: J. Clim. Appl. Meteorol., 26, 1188–97, 1987.

Malm, W. C., Sisler, J. F., Huffman, D., Eldred, R. A., and Cahill, T. A.: Spatial and seasonal trends in particle concentration and optical extinction in the United States, J. Geophys. Res., 99, 1347–1370, 1994.

Mattias-Maser, S. and Jaenicke, R.: The size distribution of primary biological aerosol particles with radii >0.2 mm in an urban/rural influenced region, Atmos. Res. 39, 279–286, 1995.

Mattias-Maser, S., Brinkmann, J., and Schneider, W.: The size distribution of marine atmospheric aerosol with regard to primary biological aerosol particles over the South Atlantic Ocean, Atmos. Environ., 33, 3569–3575, 1999.

Matthias-Maser, S., Bogs, B., and Jaenicke, R.: The size distribution of primary biological aerosol particles in cloud water on the mountain Kleiner Feldberg/Taunus (FRG), Atmos. Res., 54, 1–13, 2000.

Matus, A. V. and L'Ecuyer, T. S.: The role of cloud phase in Earth's radiation budget, J. Geophys. Res.-Atmos., 122, 2559–2578, https://doi.org/10.1002/2016JD025951, 2017.

Möhler, O., Georgakopoulos, D. G., Morris, C. E., Benz, S., Ebert, V., Hunsmann, S., Saathoff, H., Schnaiter, M., and Wagner, R.: Heterogeneous ice nucleation activity of bacteria: new laboratory experiments at simulated cloud conditions, Biogeosciences, 5, 1425–1435, https://doi.org/10.5194/bg-5-1425-2008, 2008.

Moisseev, D. N., Lautaportti, S., Tyynela, J., and Lim, S.: Dual-polarization radar signatures in snowstorms: Role of snowflake aggregation, J. Geophys. Res.-Atmos., 120, 12644–12655, https://doi.org/10.1002/2015JD023884.

Morris, C. E., Conen F., Huffman, A. J., Phillips, V. J. T. P., Pöschl, U., and Sands, D. C.: Bioprecipitation: A feedback cycle linking Earth history, ecosystem dynamics and land use through biological ice nucleators in the atmosphere, Global Change Biology, 20, 341–351, https://doi.org/10.1111/gcb.12447, 2014,

Mülmenstädt, J., Sourdeval, O., Delanoë, J., and Quaas, J.: Frequency of occurrence of rain from liquid-, mixed-, and ice-phase clouds derived from A-Train satellite retrievals, Geophys. Res. Lett., 42, 6502–6509, 2015.

Murray, B. J., O'Sullivan, D., Atkinson, J. D., and Webb, M. E.: Ice nucleation by particles immersed in super-cooled cloud droplets, Chem. Soc. Rev., 41, 6519–6554, https://doi.org/10.1039/c2cs35200a, 2012.

Patade, S., Phillips, V. T. J., Amato, P., Bingemer, H. G., Burrows, S. M., DeMott, P. J., Goncalves, F. L. T., Knopf, D. A., Morris, C. E., Alwmark, C., Artaxo, P., Pöhlker, C., Schrod, J., and Weber, B.: Empirical Formulation for Multiple Groups of Primary Biological Ice Nucleating Particles from Field Observations over Amazonia, J. Atmos. Sci., 78, 2195–2220, 2021.

Phillips, V. T. J. and Patade, S.: Multiple Environmental Influences on the Lightning of Cold-based Continental Convection. Part II: Sensitivity Tests for its Charge Structure and Land-Ocean Contrast, J. Atmos. Sci., 79, 263–300, https://doi.org/10.1175/JAS-D-20-0234.1, 2021.

Phillips, V. T. J., Donner, L. J., and Garner, S.: Nucleation processes in deep convection simulated by a cloud-system resolving model with double-moment bulk microphysics, J. Atmos. Sci., 64, 738–761, 2007.

Phillips, V. T. J., DeMott, P. J., and Andronache, C.: An Empirical Parameterization of Heterogeneous Ice Nucleation for Multiple Chemical Species of Aerosol, J. Atmos. Sci., 65, 2757–2783, 2008.

Phillips, V. T. J., Andronache, C., Christner, B., Morris, C. E., Sands, D. C., Bansemer, A., Lauer, A., McNaughton, C., and Se-

man, C.: Potential impacts from biological aerosols on ensembles of continental clouds simulated numerically, Biogeosciences, 6, 987–1014, https://doi.org/10.5194/bg-6-987-2009, 2009.

Phillips, V. T. J., Demott, P. J., Andronache, C., Pratt, K. A., Prather, K. A., Subramanian, R., and Twohy, C.: Improvements to an empirical parameterization of heterogeneous ice nucleation and its comparison with observations, J. Atmos. Sci., 70, 378–409, https://doi.org/10.1175/JAS-D-12-080.1, 2013.

Phillips, V. T. J., Yano, J. I., and Khain, A.: Ice multiplication by breakup in ice-ice collisions. Part I: Theoretical formulation, J. Atmos. Sci., 74, 1705–1719, https://doi.org/10.1175/JAS-D-16-0224.1, 2017a.

Phillips, V. T. J., Yano, J., Formenton, M., Ilotoviz, E., Kanawade, V., Kudzotsa, I., Sun, J., Bansemer, A., Detwiler, A. G., Khain, A., and Tessendorf, S. A.: Ice Multiplication by Breakup in Ice–Ice Collisions, Part II: Numerical Simulations, J. Atmos. Sci., 74, 2789–2811, 2017b.

Phillips, V. T. J., Patade, S., Gutierrez, J., and Bansemer, A.: Secondary ice production by fragmentation of freezing drops: Formulation and theory, J. Atmos. Sci., 75, 3031–3070, https://doi.org/10.1175/JAS-D-17-0190.1, 2018.

Phillips, V. T. J., Formenton, M., Kanawade, V. P., Karlsson, L. R., Patade, S., Sun, J., Barthe, C., Pinty, J., Detwiler, A. G., Lyu, W., and Tessendorf, S. A.: Multiple Environmental Influences on the Lightning of Cold-Based Continental Cumulonimbus Clouds, Part I: Description and Validation of Model, J. Atmos. Sci., 77, 3999–4024, 2020.

Pörtner, H.-O., Roberts, D. C., Poloczanska, E. S., Mintenbeck, K., Tignor, M., Alegría, A., Craig, M., Langsdorf, S., Löschke, S., Möller, V., and Okem, A.: Summary for policymakers, in: Climate change 2022: Impact, adaptation, and vulnerability: Summary for policy makers: Working group II Contribution to the sixth assessment report of the Intergovernmental Panel on Climate Change, Cambridge University Press, in press, 2022.

Prenni, A. J., Tobo, Y., Garcia, E., DeMott, P. J., Huffman, J. A., McCluskey, C. S., Kreidenweis, S. M., Prenni, J. E., Pöhlker, C., and Pöschl, U.: The impact of rain on ice nuclei populations at a forested site in Colorado, Geophys. Res. Lett., 40, 227–231, https://doi.org/10.1029/2012GL053953, 2012.

Ryzhkov, A., Pinsky, M., Pokrovsky, A., and Khain, A.: Polarimetric Radar Observation Operator for a Cloud Model with Spectral Microphysics, J. Appl. Meteorol. Climatol., 50, 873–894, 2011.

Sahyoun, M., Wex, H., Gosewinkel, U., Šantl-Temkiv, T., Nielsen, N. W., Finster, K., Sørensen, J. H., Stratmann, F., and Korsholm, U. S.: On the usage of classical nucleation theory in quantification of the impact of bacterial INP on weather and climate, Atmos. Environ., 139, 230–240, https://doi.org/10.1016/j.atmosenv.2016.05.034, 2016.

Sesartic, A., Lohmann, U., and Storelvmo, T.: Bacteria in the ECHAM5-HAM global climate model, Atmos. Chem. Phys., 12, 8645–8661, https://doi.org/10.5194/acp-12-8645-2012, 2012.

Sesartic, A., Lohmann, U., and Storelvmo, T.: Modelling the impact of fungal spore ice nuclei on clouds and precipitation, Environ. Res. Lett., 8, 014029, https://doi.org/10.1088/1748-9326/8/1/014029, 2013.

Sinclair, V. A., Moisseev, D., and von Lerber, A.: How dual-polarization radar observations can be used to verify model representation of secondary ice, J. Geophys. Res.-Atmos., 121, 10954–10970, https://doi.org/10.1002/2016JD025381, 2016.

Sotiropoulou, G., Vignon, É., Young, G., Morrison, H., O'Shea, S. J., Lachlan-Cope, T., Berne, A., and Nenes, A.: Secondary ice production in summer clouds over the Antarctic coast: an under-appreciated process in atmospheric models, Atmos. Chem. Phys., 21, 755–771, https://doi.org/10.5194/acp-21-755-2021, 2021a.

Sotiropoulou, G., Ickes, L., Nenes, A., and Ekman, A. M. L.: Ice multiplication from ice–ice collisions in the high Arctic: sensitivity to ice habit, rimed fraction, ice type and uncertainties in the numerical description of the process, Atmos. Chem. Phys., 21, 9741–9760, https://doi.org/10.5194/acp-21-9741-2021, 2021b.

Spracklen, D. V. and Heald, C. L.: The contribution of fungal spores and bacteria to regional and global aerosol number and ice nucleation immersion freezing rates, Atmos. Chem. Phys., 14, 9051–9059, https://doi.org/10.5194/acp-14-9051-2014, 2014.

Szyrmer, W. and Zawadzki, I.: Biogenic and anthropogenic sources of ice-forming nuclei: A review, B. Am. Meteorol. Soc., 78, 209–228, 1997.

Tsushima, Y., Emori S., Ogura T., Kimoto, M., Webb, M. J., Williams, K. D., Ringer, M. A., Soden, B. J., Li, B., and Andronova, N.: Importance of the mixed-phase cloud distribution in the control climate for assessing the response of clouds to carbon dioxide increase: a multi-model study, Clim. Dynam., 27, 113–126, 2006.

Xie, S., Zhang, Y., Giangrande, S. E., Jensen, M. P., McCoy, R., and Zhang, M.: Interactions between cumulus convection and its environment as revealed by the MC3E sounding array, J. Geophys. Res., 119, 11784–11808, https://doi.org/10.1002/2014JD022011, 2014.

Zhao, X. and Liu, X.: Global importance of secondary ice production, Geophys. Res. Lett., 48, e2021GL092581, https://doi.org/10.1029/2021GL092581, 2021.

Zuidema, P., Westwater, E. R., Fairall, C., and Hazen, D.: Ship-based liquid water path estimates in marine stratocumulus, J. Geophys. Res., 110, D20206, https://doi.org/10.1029/2005JD005833, 2005.

Paper 2

Effects from Time Dependence of Ice Nucleus Activity for Contrasting Cloud Types

Deepak Waman[a], Akash Deshmukh,[a] Arti Jadav,[a] Sachin Patade,[a] Martanda Gautam,[a]
Vaughan Phillips,[a] Aaron Bansemer,[b] and Jonas Jakobsson[c]

[a] Department of Physical Geography and Ecosystem Science, Lund University, Lund, Sweden
[b] National Center for Atmospheric Research, Boulder, Colorado
[c] Division of Nuclear Physics, Department of Physics, Lund University, Lund, Sweden

ABSTRACT: The role of time-dependent freezing of ice nucleating particles (INPs) is evaluated with the "Aerosol–Cloud" (AC) model in 1) deep convection observed over Oklahoma during the Midlatitude Continental Convective Cloud Experiment (MC3E), 2) orographic clouds observed over North California during the Atmospheric Radiation Measurement (ARM) Cloud Aerosol Precipitation Experiment (ACAPEX), and 3) supercooled, stratiform clouds over the United Kingdom, observed during the Aerosol Properties, Processes And Influences on the Earth's climate (APPRAISE) campaign. AC uses the dynamical core of the WRF Model and has hybrid bin–bulk microphysics and a 3D mesoscale domain. AC is validated against coincident aircraft, ground-based, and satellite observations for all three cases. Filtered concentrations of ice (>0.1–0.2 mm) agree with those observed at all sampled levels. AC predicts the INP activity of various types of aerosol particles with an empirical parameterization (EP), which follows a singular approach (no time dependence). Here, the EP is modified to represent time-dependent INP activity by a purely empirical approach, using our published laboratory observations of time-dependent INP activity. In all simulated clouds, the inclusion of time dependence increases the predicted INP activity of mineral dust particles by 0.5–1 order of magnitude. However, there is little impact on the cloud glaciation because the total ice is mostly (80%–90%) from secondary ice production (SIP) at levels warmer than about $-36°C$. The Hallett–Mossop process and fragmentation in ice–ice collisions together initiate about 70% of the total ice, whereas fragmentation during both raindrop freezing and sublimation contributes $<10\%$. Overall, total ice concentrations and SIP are unaffected by time-dependent INP activity. In the simulated APPRAISE case, the main causes of persistence of long-lived clouds and precipitation are predicted to be SIP in weak embedded convection and reactivation following recirculation of dust particles in supercooled layer cloud.

KEYWORDS: Ice crystals; Ice particles; Secondary ice production; Clouds

1. Introduction

Ice particles in natural clouds affect radiative transfer, precipitation, cloud lifetime, and electrification in the atmosphere worldwide (Takahashi 1978; Cantrell and Heymsfield 2005; Lohmann 2006; Kudzotsa et al. 2016; Phillips et al. 2020, hereafter Ph20). Generally, precipitation can be formed by two processes (e.g., Yau and Rogers 1996): 1) the "warm-rain" process in which water droplets collide and coalesce to form warm rain, and 2) the "ice-crystal" process, which involves vapor growth of ice particles forming snow (or "cold" graupel by riming) which may melt to yield "cold rain." The ice-crystal process may form much of the surface precipitation globally (Field and Heymsfield 2015), even in the midlatitudes and tropics (Lau and Wu 2003).

At temperatures warmer than about $-36°C$ (Phillips et al. 2007, hereafter Ph07), primary ice is initiated by "heterogeneous ice nucleation" from solid aerosol particles (APs) acting as ice nucleating particles (INPs). A range of solid APs, such as dust, insoluble organics, black carbon (soot), and primary biological aerosol particles (PBAPs), may initiate primary ice by acting as INPs (Hobbs and Locatelli 1969; DeMott 1990; Kanji et al. 2017, hereafter Ka17; Patade et al. 2021).

Two approaches for representing heterogeneous ice nucleation proposed so far are the "singular (time-independent)" hypothesis and the "classical (time-dependent)" nucleation theory. The singular hypothesis is an approximation based on the assumption that ice nucleation is practically an instantaneous process occurring at deterministic temperatures on specific "active" sites (Levine 1950; Langham and Mason 1958; Vali 1994, 2008) characterized by the lowest particle–ice interfacial energy and hence activation of ice takes place when its characteristic temperature is reached (Niedermeier et al. 2011). According to the singular hypothesis, under the same environmental conditions, microscopically identical INPs with the same characteristic temperature nucleate all together. When INPs are exposed to isothermal conditions, this hypothesis neglects all time dependence, and any activation is assumed to happen at the start of the nucleation (Chen et al. 2008). Phillips et al. (2008, hereafter Ph08, their Fig. 1) and Connolly et al. (2009) innovated the concept of the surface density of active sites among

Corresponding author: Deepak Waman, deepak.waman@nateko.lu.se

INPs, enabling the application of the singular hypothesis to any size distribution of an aerosol species in cloud models.

Bigg (1953) proposed that nucleation is a stochastic process with the freezing probability of a given drop depending on its volume and rate of cooling. Carte (1959) and Dufour and Defay (1963) further proposed that in a given interval of time, all drops in a given monodisperse population have the same probability of nucleation, either heterogeneously or homogeneously. Carte (1959) reinterpreted the results of Bigg (1953) by proposing that this probability is proportional to the drop volume. It follows that more immersed aerosol material in a larger drop contains more of the most active INPs, which explains those observations of drop volume being proportional to the freezing probability. However, below the $-36°C$ level, different drops contain different kinds of APs, and the freezing probability of such drops cannot be the same (Vali and Stansbury 1966). Vonnegut and Baldwin (1984) experimentally observed that heterogeneous ice nucleation is mainly a stochastic process. They studied the freezing of silver iodide and observed that ice formation in supercooled clouds depends not only on the characteristics of the individual silver iodide particles but also on the probability of water molecules coming together in the ice lattice on the solid surface. This may take from several minutes to hours. Since ice nucleation is a probabilistic process, at a given temperature it depends on the surface area of the INP and on the time during which any INP stays in a favorable environment (Chen et al. 2008; Herbert et al. 2014). Modern laboratory observations have confirmed that the ability of INPs to nucleate ice depends on temperature strongly, and on the surface area of the solid material (DeMott 1990; Murray et al. 2012; Ervens and Feingold 2013).

Yet by assessing previous laboratory experiments in the literature, Vali (2014) concluded that the variations in the time scale of exposure to ambient conditions (e.g., changes in the cooling rate) cause only slight perturbations in the temperatures of each INP compared to the range of all freezing temperatures among the INP population. Thus, this implied that time dependence can often be neglected. As ice nucleation is strongly sensitive to temperature, the suggestion was that numerical models can neglect time dependence (Vali 2014) when cooling rates are sufficiently high ($\sim$1–2 K min^{-1}), which corresponds to updraft speeds of about 1.5–3 m s^{-1} (Ka17). However, this was not conclusively verified with cloud simulations.

Our recent laboratory experiment by Jakobsson et al. (2022, hereafter Jk22) quantified the time dependence of freezing for immersed INPs from ambient aerosol samples from the real troposphere. They observed an increment in active INP concentrations by 70%–100% (70%–200%) for 2–10 h isothermally. The maximum time dependence was for dust and rural continental samples. These observations were the basis for Jk22 to propose a method for including time dependence in numerical models using various empirical types of parameterizations of INP activity (e.g., the EP).

Such laboratory experiments were argued a decade ago to be consistent with the idea of continuous freezing of supercooled cloud droplets being the largest source of ice in mixed-phase, midlevel stratus clouds especially when there is little entrainment of APs from the environment (Crosier et al. 2011, hereafter C11; Westbrook and Illingworth 2013, hereafter WI13). C11 and WI13 observed a case of long-lived, thin stratiform clouds over the southern United Kingdom, by vertically pointing radar and aircraft with quasi-steady precipitation for several hours. WI13 argued that since the vertical motions were weak ($|w| < 1$ m s^{-1}), there was no possibility of significant mixing of environmental INPs into the cloud layer. They further proposed that the cause for this quasi-steady precipitation and the long lifetime of such clouds is that the ice nucleation process is time dependent.

Another possible reason for quasi-steady ice concentrations claimed to have been observed by WI13 is secondary ice production (SIP). Aircraft (Hobbs et al. 1980; Lasher-Trapp et al. 2016, 2021) and modeling (Yano and Phillips 2011; Phillips et al. 2017b; Zhao et al. 2021; Waman et al. 2022, hereafter Wa22) studies of precipitating cold clouds have shown that the observed number concentrations of the total ice particles are typically about three or four orders of magnitude higher than those of available active INPs ($<$1 L^{-1}) at temperatures between $-5°$ and $-25°C$. Since the lifetime of such deep convective clouds is only about 60–90 min (e.g., Wa22) and SIP is prolific, the time-dependent process of heterogeneous ice nucleation might not be an important process of ice initiation by comparison.

The objective of the present study is to investigate the possible role of the time dependence of INP activity in explaining the observed ice concentrations in long-lived, precipitating cloud systems, while accounting for all the alternative explanations such as SIP. In this study, the time dependence is represented in our Aerosol–Cloud (AC) model following the framework proposed by Jk22 that has been proven to be realistic for real tropospheric aerosols, as noted above. A range of precipitating cloud types (deep convection, orographic and thin midlevel stratiform clouds) observed by aircraft are considered in the present study.

2. Field campaigns and observations

The present study focuses on three different campaigns from different locations and periods. These are 1) the Midlatitude Continental Convective Cloud Experiment (MC3E) consisting of deep convective clouds, 2) the Atmospheric Radiation Measurement (ARM) Cloud Aerosol Precipitation Experiment (ACAPEX) consisting of orographic clouds, and 3) the Aerosol Properties, Processes And Influences on the Earth's climate (APPRAISE) campaign which observed supercooled long-lived stratiform clouds. These are described as follows.

a. MC3E

The MC3E campaign was jointly conducted by the National Aeronautics and Space Administration's (NASA) Global Precipitation Measurement program and the U.S. Department of Energy's (DOE) ARM program over north-central Oklahoma, United States, between 22 April and 6 June 2011. The case of a mesoscale convective system (MCS) consisting of deep convective clouds observed during (0900 to 2400 UTC 11 May 2011) MC3E is analyzed here. The aircraft and ground-based measurements and large-scale forcing (LSF) conditions

TABLE 1. Details of optical probes mounted on the sampling aircraft during the field campaigns and corresponding size range considered in the present study.

| Campaign | Aircraft | Instruments used to measure cloud properties | | | |
		Ice particles	Size range (mm)	Cloud droplets	Size range (μm)
MC3E	Citation	2DC	0.2–1.0		
		CIP	0.2–1.5		
		HVPS-v3	0.2–19.2		
ACAPEX	DOE G-1	2DS	0.2–1.28	CDP	2–20
		HVPS	0.2–19.2		
APPRAISE	CFARR U.K. BAe146	2DS-128	0.1–1.28		

of the MC3E campaign are described by Jensen et al. (2016). The case involved a relatively warm cloud base (17°C) with cloud tops reaching up to the −60°C level.

Table 1 provides details about the optical probes mounted on the Citation aircraft (Fig. 1a) which made measurements of hydrometeor properties during the MC3E campaign. The 2D cloud (2DC) and high-volume precipitation spectrometer version 3 (HVPS-v3) probes had shattering corrected tips (Korolev et al. 2011, hereafter K11) while the cloud imaging probe (CIP) had no such tips. The present study included only concentrations of ice particles with maximum dimensions larger than 200 μm ("NI$_{200}$") in the validation of ice number concentrations. Moreover, droplet properties such as size, concentrations, and liquid water content (LWC) were measured by the cloud droplet probe (CDP).

Figures 1b–d show the CIP images at various levels in convective cloudy updrafts. From these images, it is evident that the cloud-base regions were dominated by raindrops (about 0.2–1 mm in diameter, Fig. 1b) whereas abundant rimed ice particles and relatively rare pristine ice crystals were observed at about −7°C level (Fig. 1c). It is also observed that with increasing height, particle size increases and abundant aggregates, and rimed ice particles (>1 mm) were present aloft (Figs. 1c,d).

Figure 1e shows the observed profiles of dewpoint and air temperature at 0300 UTC 10 May 2011. The convective available potential energy (CAPE) was about 3500 J kg^{-1} (Fig. 1e), which is mostly attributed to the moistening of the lower troposphere from large-scale advection (Jensen et al. 2016).

b. ACAPEX

ACAPEX was conducted by DOE ARM to study aerosol–cloud interactions in atmospheric rivers (ARs) of moisture in the environment during wintertime storms (Leung 2016). The case selected involves orographic clouds that brought significant precipitation due to the landfall of an AR on the U.S. West Coast (Northern California) on 7 February 2015 (1900–2300 UTC).

Table 1 summarizes the aircraft and optical probes used to sample the observed clouds. The DOE G-1 aircraft (Fig. 2a) made passes between the Central Valley and Sierra Nevada and sampled the low-level, postfrontal clouds in coordination with the National Oceanic and Atmospheric Administration's (NOAA) Ron Brown research ship. Both the 2D spectrometer (2DS) and HVPS probes had their tips corrected for

shattering (K11). The approach described above (section 2a, NI$_{200}$) is followed to compare the predicted ice concentrations with the coincident aircraft observations. Several rain gauges were deployed on the ground at stations within the study domain to measure the amount of surface precipitation.

Figures 2b–d show images from the 2DS probe in the ACAPEX at various levels in convective cloudy updrafts. It is observed that the cloud-base regions (∼7°C) were characterized by raindrops (about 0.2–1 mm in diameter, Fig. 2b). At subzero levels warmer than −7°C, mostly pristine ice crystals together with rimed ice particles were observed. The average ice particle size is observed to increase from the lower (−7°C) to the upper half (−18°C) of the mixed-phase region.

The observed APs are typically marine in origin (Fig. 2e). The INPs were mainly marine while dust and soot were scarce (Levin et al. 2019; Lin et al. 2022). The Ron Brown ship made observations of atmospheric conditions such as temperature, moisture, winds, aerosols, surface fluxes, and radiative fluxes (Leung 2016). Figure 2f shows observed vertical profiles of air and dewpoint temperatures at 1900 UTC 7 February 2015. The LCL was located at about 953 hPa and the horizontal wind speeds were relatively high (∼10 m s^{-1}) throughout the atmosphere.

c. APPRAISE

A case of supercooled stratiform clouds with embedded convection was observed over southern England covering an area of about 100 km in width on 18 February 2009 during the APPRAISE campaign. The vertical extent of these clouds was about 4 km and such cloudy conditions persisted in the observed location near Chilbolton for more than a day with continuous precipitation (C11; WI13). The U.K. BAe146 Facility for Airborne Atmospheric Measurement (FAAM) aircraft flight track is shown in Fig. 3a which sampled these clouds near the Chilbolton Facility for Atmospheric and Radio Research (CFARR). The cloud base was at about 500 m above mean sea level (MSL) whereas the cloud top was at 4.3 km MSL.

Figure 3c shows observed vertical profiles of air and dewpoint temperatures at 1100 UTC 17 February 2009. The horizontal wind speeds were significantly weak (<5 m s^{-1}) throughout the atmosphere up to the cloud top (∼−13°C). There was an inversion (a temperature difference of about 4°C) layer seen above the cloud top characterized by an extremely dry atmosphere aloft with relative humidity (RH) of

FIG. 1. (a) Profiles of geographical area, flight track of the Citation aircraft (thin black line), and the simulation domain (solid black box), as well as particle images in convective cloudy updrafts ($w > 1$ m s^{-1}) shown at (b) 17°C (cloud base), (c) −7°C, and (d) −16°C levels from the CIP mounted on the Citation aircraft during the MC3E campaign on 11 May 2011. (e) Observed vertical profile of the air (solid black line) and dewpoint (solid gray line) temperature and moist adiabat (thin dotted line) for the MC3E case for the same day at 0300 UTC.

less than about 30%. Figure 3c reveals two distinct cloudy layers. A saturated layer (~1.5 km vertical extent) was seen at lower levels between 1000 and 850 hPa. Above the 850 hPa level, the atmosphere was completely dry (RH < 50%) up to the 700 hPa level. A thin (~400 m) layer of saturated air was observed above the 700 hPa level, extending up to the cloud top (~−13°C). The system was anticyclonic (surface pressure ~ 1020 hPa) and quasi steady, covering most of the United Kingdom with quasi-steady precipitation for more than a day.

C11 and WI13 highlighted most of the features of the observed system.

Although WI13 claimed that there was a quasi-steady state of the glaciated cloud properties and snowfall, their radar measurements and flights during the campaign did not follow the motions in a Lagrangian sense. WI13 claimed there was minimal cooling in cloud-top temperature (by about 1.5 K) over Chilbolton for a period of more than a day. They further hypothesized that this cooling of the cloud top might have
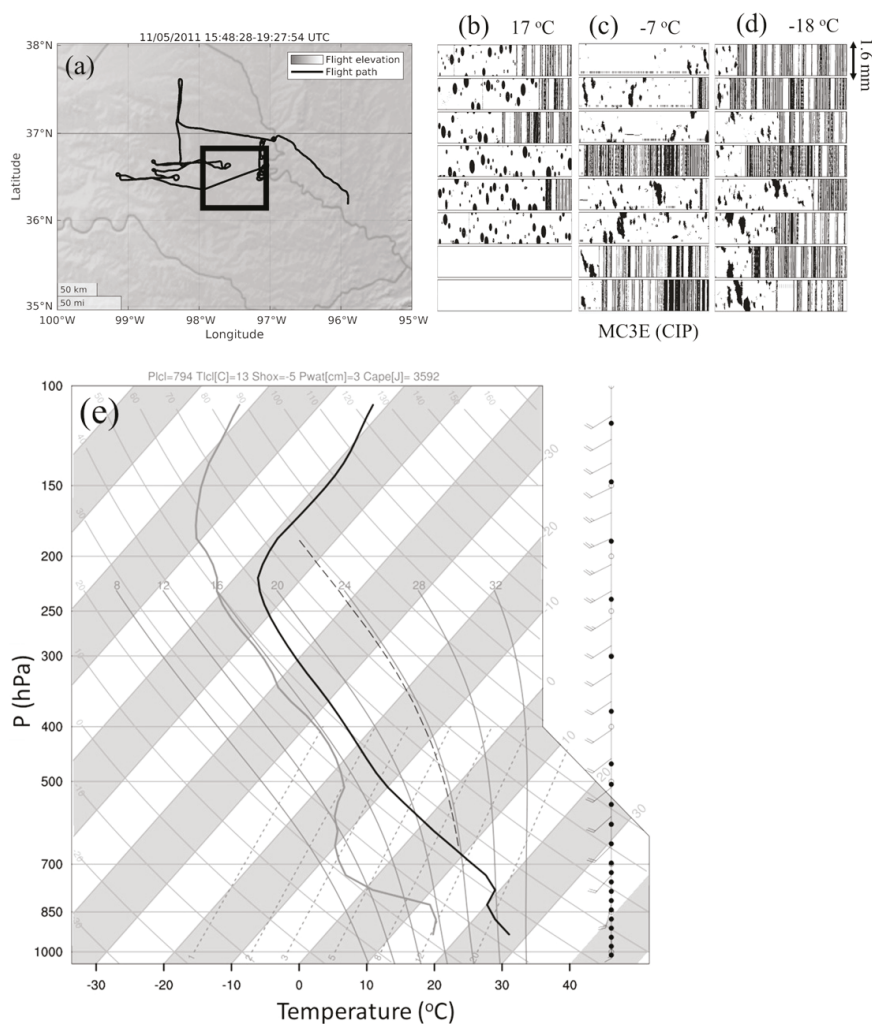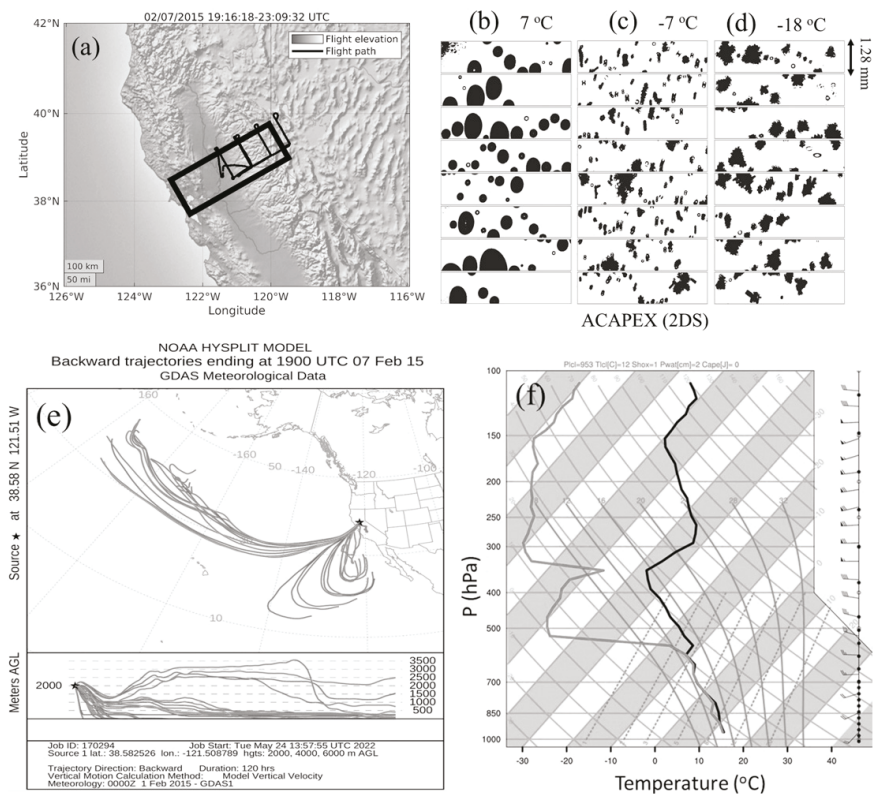
FIG. 2. (a) Profiles of geographical area, flight track of the DOE-G1 aircraft (thin black line), and the simulation domain (solid black rectangle), as well as particle images in convective cloudy updrafts ($w > 1$ m s^{-1}) at (b) 7°C (cloud base), (c) −7°C, and (d) −18°C levels from the 2DS probe mounted of the DOE-G1 aircraft during the ACAPEX campaign on 7 Feb 2015. (e) Hybrid Single-Particle Lagrangian Integrated Trajectory (HYSPLIT) backward trajectory for 120 h showing the airflow from the North Pacific Ocean over the study domain (Sacramento, California, United States) on the same day at 1900 UTC. (f) Observed vertical profile of the air (solid black line) and dewpoint (solid gray line) temperature for the same day and time.

increased active INPs. The radar used in WI13 was fixed at one location and pointing vertically. Most of the aerosols were marine in origin as the Hybrid Single-Particle Lagrangian Integrated Trajectory (HYSPLIT) back-trajectory shows the long-range transport over the study domain was mainly from the North Atlantic Ocean (Fig. 3b) with a mixture of continental APs from France.

In reality, the horizontal wind speed was about 3 m s^{-1} southward in the lower troposphere, and this must have advected the sampled clouds by about 300 km in 24 h. This distance is far greater than the span of the aircraft flights and radar sampling. Consequently, it cannot be ruled out that there was substantial time evolution of cloud properties and surface precipitation following the motion. The appearance of a quasi-steady state is explicable in terms of an approximate steady state of the synoptic-scale flow, combined with the time evolution of cloud properties along parcel trajectories.

In fact, WI13 did not actually prove the quasi-steady state of cloud properties following the air motion for more than a day, given the aircraft flights.

Observations from the 2DS probe (Table 1) were corrected for artificial shattering by applying corrections following Field et al. (2006) and only particles larger than 100 μm ("NI$_{100}$") were included in the plotted ice concentrations. However, K11 suggests that even after applying these corrections the uncertainty due to the artificial shattering remains. Hence, we further corrected the 2DS data (WI13, their Fig. 9) by multiplying all measured ice concentrations by a factor of 0.253 inferred from K11 (their Fig. 5, comparison of solid blue and red lines).

3. Description of AC model

The present study used AC which was created to represent radiation (Geophysical Fluid Dynamics Laboratory radiation
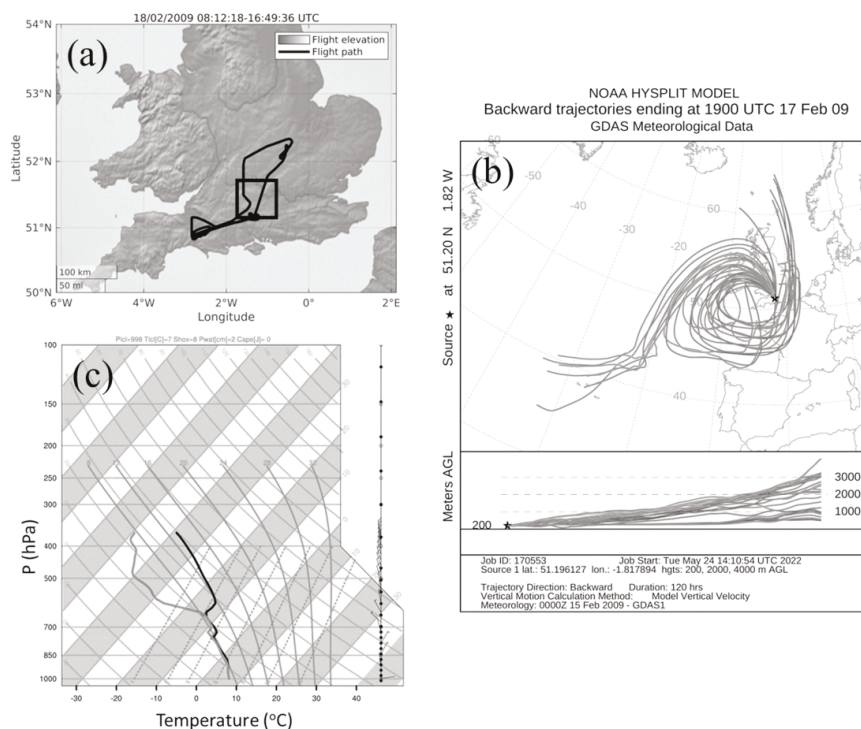
FIG. 3. (a) Profiles of geographical area, flight track of the BAe146 aircraft (thin black line), and the simulation domain (solid black box) during the APPRAISE campaign on 18 Feb 2009. (b) HYSPLIT backward trajectory for 120 h showing the airflow from the North Atlantic Ocean region as well as from the continent (France) over the study domain (Larkhill, United Kingdom) in the APPRAISE case on the same day at 1900 UTC. (c) Observed vertical profile of the air (solid black line) and dewpoint (solid gray line) temperature at 1100 UTC on the same day.

scheme; Freidenreich and Ramaswamy 1999) interactively with cloud properties and has a semiprognostic aerosol scheme. AC treats cloud properties with a hybrid spectral bin–two-moment bulk microphysics scheme (Ph07; Ph08; Phillips et al. 2009, 2013, hereafter Ph13, 2015, 2017a, 2018; Ph20). AC treats the cycling of aerosols through clouds and changes in AP concentrations due to cloud and precipitation by a two-way aerosol–cloud coupling, and tracks components of APs in the air interstitially, immersed in clouds and in precipitation (Phillips et al. 2009).

AC uses the dynamical core of the WRF Model and its software infrastructure (Dudhia 1989; Skamarock et al. 2005). AC treats turbulence using the Medium Range Forecast (MRF) model planetary boundary layer (PBL) scheme which resolves the vertical subgrid-scale fluxes (Hong and Pan 1996) and uses some other standard WRF schemes such as for the surface layer (Monin and Obukhov 1954) and dynamics. AC has been used in previous studies (e.g., Phillips et al. 2017b; Ph20; Patade et al. 2022; Wa22).

AC represents microphysical species as cloud liquid, cloud ice ("crystals"), snow, graupel/hail, and rain. The total number

and mass ("two-moment approach") mixing ratios of each of these species are diffused and advected as bulk prognostic variables in AC. The components of mass and number concentrations of cloud ice and snow initiated in various processes (heterogeneous and homogeneous freezing, four mechanisms of SIP) are tracked by extra prognostic variables in AC. Soluble APs such as ammonium sulfate, sea salt, and soluble organics (sO) initiate cloud droplets in AC at cloud base (Ming et al. 2006) and at in-cloud levels far above cloud base from the supersaturation resolved on the model grid, ("in-cloud droplet activation") (Ph07; Phillips et al. 2009).

Insoluble APs such as mineral dust (DM), soot (BC), and five types of PBAPs (Patade et al. 2021, section 3.1 therein) initiate primary ice in AC at levels warmer than $-36°C$ through heterogeneous ice nucleation. These insoluble APs also initiate cloud droplets as they tend to have hydrophilic coatings or are wettable. AC predicts the INP activity of these insoluble APs with the EP [section 3a(1)] (Ph08; Ph13). The EP represents all modes of INP activation (deposition mode, freezing modes of contact, condensation, and immersion) depending on the temperature, surface area mixing ratio

of each AP type and supersaturation. Both inside-out and outside-in contact freezing is treated.

AC forms ice homogeneously by two mechanisms. First, spontaneous freezing of supercooled cloud drops and rain-drops above about −36°C level forms ice depending on the drop size. There is preferential evaporation of the smaller cloud droplets in the size distribution that freeze later during ascent through the layer of homogeneous freezing of cloud liquid (about −35° to −37°C), with a lookup table (Ph07). Second, homogeneous aerosol freezing occurs at colder tem-peratures as soon as a critical supersaturation is exceeded with respect to ice. This critical supersaturation depends on the temperature and size of APs (Koop et al. 2000; Ph07).

a. Time-dependent heterogenous ice nucleation in AC

1) PREVIOUS REPRESENTATION WITH EP IN AC
    WITHOUT TIME DEPENDENCE

In AC, for the Xth (X = DM, BC, sO, and PBAPs) species of APs that are or can become solid (section 3a), the EP gives the number mixing ratio ($n_{\mathrm{IN},X}$) of active INPs (Ph08; Ph13) at the ambient temperature (T) and humidity (related to s_i),

$$n_{\mathrm{IN},X}(T, S_i, \Omega_X) = \int_{\log(0.1\,\mu\mathrm{m})}^{\infty} \{1 - \exp[-\mu_X(D_X, S_i, T)]\}$$
$$\times \frac{dn_X}{d\log D_X} \times d\log D_X. \quad (1)$$

For X = DM, BC, and sO,

$$\mu_X = H_X(S_i, T)\xi(T)\left(\frac{\alpha_X n_{\mathrm{IN},1,*}}{\Omega_{X,1,*}}\right) \times \frac{d\Omega_X}{dn_X} \quad \forall\, T < 0°\mathrm{C} \quad \text{and}$$
$$1 < S_i \leq S_i^w. \quad (2)$$

Here, Ω_X is the surface area mixing ratio for the Xth AP species, and μ_X gives the average number of activated ice em-bryos per solid AP of size D_X. The scarcity of heterogeneous ice nucleation in subsaturated conditions is represented by the empirically determined fraction H_X, which is a function of saturation ratio of water vapor with respect to ice (S_i) and T, varying between 0 and 1. The next term, ξ, is the temperature-dependent fraction representing freezing of INPs immersed in drops and also varies from 0 to 1 for temperatures between −2° and −5°C; S_i^w is the value of S_i at exact water saturation S_w. Also, $d\Omega_X/dn_X \approx \pi D_X^2$. The term $n_{\mathrm{IN},1,*}$ is the number of active INPs per kg of air and represents the reference activity spectrum (denoted by *) of the average concentration of INPs. Symbols used in the present study are listed in the appendix (Table A1). More details can be found in Ph08 and Ph13.

Also, for X = FNG, PLN, BCT, and DTS,

$$\mu_X = H_X(S_i, T)\xi(T) \times \mathrm{MIN}\{[\exp(-\gamma_X T) - 1], 40\}$$
$$\times \frac{1}{\omega_{X,1,*}} \times \frac{d\Omega_X}{dn_X} \quad \forall\, T < 0°\mathrm{C}. \quad (3)$$

Here, $\omega_{X,1,*}$ is the baseline coefficient of the group of Xth spe-cies in the PBAP group. A different approach is followed to

predict the INP activity from algae. More details can be found in Patade et al. (2021).

The number of ice crystals initiated (Δn_i) in a time step (Δt) is incremented by

$$\Delta n_i = \sum_X \mathrm{MAX}(n_{\mathrm{IN},X} - n_{X,a}, 0) \equiv \sum_X \Delta n_{X,a}. \quad (4)$$

Here, $n_{X,a}$ is the number mixing ratio of INPs from group X that has already been activated.

Insoluble APs are internally mixed with various types of solu-ble material (Clarke et al. 2004). When the s_w reaches a critical value, they form cloud droplets, and the insoluble part becomes immersed in the droplet. A raindrop containing immersed INPs may nucleate ice heterogeneously at subzero temperatures. The number concentrations of INPs activated during heterogeneous raindrop freezing (Ph08) during a time step (Δt) is

$$d[\Delta n_{\mathrm{IN,rain}}(T, S_i, \Omega_X)] \approx \Delta t\, \mathrm{MIN}\left[(w - v_t)\frac{\partial T}{\partial z}, 0\right]$$
$$\times \frac{d}{dT}\{n_{\mathrm{IN},1,*}[T, S_i^w(T)]\}$$
$$\times \sum_X \left(\frac{\alpha_X\, d\Omega_{X,\mathrm{rain}}}{\Omega_{X,1,*}}\right). \quad (5)$$

Here, w is the vertical velocity, v_t is the fall speed of raindrops, and $d\Omega_{X,\mathrm{rain}} = \Omega_{X,\mathrm{rain}}\, dQ_r/Q_r$ denotes the surface area mixing ra-tio of INPs immersed in raindrops. Also, Q_r is the mass mixing ra-tio of rain. More details can be found in Ph08.

In summary, Eqs. (1)–(5) represent heterogeneous ice nu-cleation with the singular approximation.

2) MODIFICATION OF EP TO INCLUDE TIME
    DEPENDENCE OF INP ACTIVITY

Jk22 proposed an empirical approach relying on a temperature shift [$\Delta T_X = \Delta T_X(t^*) \leq 0$] to represent the time-dependent freezing of active INPs. This was based on their laboratory observations during isothermal experiments over many hours with drop populations (section 1). The temperature input to the EP [section 3a(1)] representing heterogeneous ice nucleation [Eqs. (1) and (7)] is modified by adding the temperature shift for each AP type to represent the ob-served time-dependent activation. More details are given by Jk22 (their section 3.2.2).

According to Jk22, the temperature shift is

$$\Delta T_X(t^*) = -A_X t^{*\beta}; \quad (6)$$

t^* is the time since the parcel entered the glaciating part of a cloud (the age of the cold parcel). Here, t^* is estimated by a passive tracer (Q) that decays exponentially with time following the motion of any parcel in a cold cloud [$T < 0°$C and ice water content (IWC) $> 10^{-6}$ kg m^{-3}]. The evolu-tion of Q is from numerical integration during the simula-tion of

$$\frac{DQ}{dt} = \begin{cases} \dfrac{-Q}{\tau_Q} & \forall\, T < 0°\mathrm{C} \quad \text{and} \quad \mathrm{IWC} > 10^{-6}\ \mathrm{kg\ m}^{-3} \\ 0 & \text{otherwise} \end{cases}. \quad (7)$$

Here, τ_Q is an arbitrary relaxation time and is set to 1800 s throughout the simulation. For an adiabatic parcel, the analytical solution of Eq. (6) gives t^*,

$$t^* \approx -\tau_Q \ln(Q/Q_0). \tag{8}$$

Outside of the cold cloud, $Q = Q_0 = 1 \text{ kg}^{-1}$ is prescribed everywhere. Effects on t^* from dilution of actual simulated parcels are approximately represented by virtue of in-cloud mixing and entrainment being treated in the numerical prediction of Q.

With this temperature shift $[\Delta T_X(t^*)]$, the time-dependent number mixing ratio of active INPs ($\tilde{n}_{\text{IN},X}$) in the Xth species from Eq. (1) is

$$\tilde{n}_{\text{IN},X}(T, S_i, \Omega_X, t) = n_{\text{IN},X}\{[T + \Delta T_X(t^*)],$$
$$S_i[T + \Delta T_X(t^*)], \Omega_X\}. \tag{9}$$

Similarly, the time-dependent number mixing ratio of INPs activated in heterogeneous raindrop freezing $[d(\Delta \tilde{n}_{\text{IN,rain}})]$ from Eq. (5) is obtained by summing over each raindrop size bin,

$$d[\Delta \tilde{n}_{\text{IN,rain}}(T, S_i, \Omega_X)] = d(\Delta n_{\text{IN,rain}}\{T + \Delta T_X(t^*),$$
$$S_i[T + \Delta T_X(t^*)], \Omega_X\}). \tag{10}$$

b. SIP mechanisms represented in AC

AC initiates secondary ice by four types of SIP mechanisms involving fragmentation. These four types are briefly described below.

1) THE HALLETT–MOSSOP PROCESS

The Hallett–Mossop (HM) process involves the emission of small ice splinters during the riming of supercooled cloud droplets between $-3°$ and $-8°C$ (Hallett and Mossop 1974). The maximum splinter emission rate was observed at $-5°C$ level and was 350 splinters per milligram of rime particle. This process mainly requires a warm base because another condition is that the cloud droplets emitting splinters must be larger than 24 μm in diameter (Mossop 1976). In AC, this dependence is treated with a cloud-droplet size-dependent factor, which is zero and unity for a mean droplet diameter less than 16 μm and greater than 24 μm, respectively. This factor is linearly interpolated in between. The factor multiplies the emission rate, together with another factor to represent temperature dependence.

2) FRAGMENTATION IN ICE–ICE COLLISIONS

The second mechanism by which AC forms secondary ice is fragmentation in ice–ice collisions (Phillips et al. 2017a,b). The formulation uses the principle of energy conservation to treat all types of ice particle collisions. A small fraction of the initial collision kinetic energy (CKE) is converted to create the ice fragments. These collisions depend on the size of the colliding ice particles, CKE, and temperature.

The formulation was modified considering a recent field campaign during winter in northern Sweden (Vindeln; 64.20°N, 19.71°E) to observe the fragmentation of natural snowflakes impacting an array of fixed ice spheres (Martanda 2022). The rime fraction was seen to be better treated by a uniform value at all sizes larger than 2 mm diameter and being linearly interpolated to zero at 0.2 mm.

3) RAINDROP FREEZING FRAGMENTATION

The empirical formulation by Phillips et al. (2018) which initiates secondary ice during the freezing of drizzle/raindrops by two modes is used in AC. In the first mode, there is quasi-spherical freezing when a supercooled drop (0.05–5 mm diameter) collides with a less massive ice particle or during heterogeneous raindrop freezing due to immersed INPs. Secondary splinters form when the outer ice shell breaks during freezing. In the second mode, collisions between a raindrop and a more massive ice particle result in the emission of secondary drops from a splash. Some of these contain ice such that they freeze (Phillips et al. 2018; James et al. 2021).

4) SUBLIMATION BREAKUP OF DENDRITIC SNOW AND GRAUPEL

Secondary ice has been observed to form during the sublimation of dendritic snow and graupel (Oraltay and Hallett 1989; Dong et al. 1994; Bacon et al. 1998). This is represented by the empirical formulation from Deshmukh et al. (2022) in AC. If present, sublimational breakup can be a prolific SIP mechanism in deep convective descent with a quasi equilibrium between emission and total sublimation of fragments (Deshmukh et al. 2022; Wa22).

c. Experimental setup

All three cases (section 2) have been simulated by AC for a 3D mesoscale domain for the horizontal and vertical resolution of about 2 and 0.5 km, respectively, with an integration time step of 10 s. A modeling study by Pauluis and Garner (2006) revealed that this 2 km horizontal resolution adequately represents the statistics of cloud properties and vertical velocity in deep convective clouds. Little sensitivity to alteration of this resolution was found.

The experimental design is as follows.

1) MC3E

The MC3E case (section 2a) is simulated with a domain of 80 km × 80 km. The LSF tendencies of potential temperature (θ) and vapor mixing ratio (q_v) were applied (Xie et al. 2014; Jensen et al. 2016). These tendencies were updated hourly and continuously interpolated over time between updates. Lateral boundary conditions (LBC) are periodic in both north–south and east–west directions. Convection is simulated in an idealized way, in the sense that no attempt is made to predict the exact locations of the cloud. Convection was initialized by adding random perturbations (of up to $\pm 0.06 \text{ g kg}^{-1}$) to the initial vapor mixing ratio in the PBL.

AC resolves nonbiological insoluble organics and five types of PBAPs as separate species including fungi (FNG), bacteria

TABLE 2. Aerosol mass mixing ratios near the ground, inferred from observations or from a global model, for various AP species of AC for the case of MC3E (averaged for 9 and 12 May 2011), ACAPEX, both from the IMPROVE measurements, and APPRAISE from the MERRA-2-GIOVANNI model monthly (February 2009) mean values. PBAP measurements from Amazonia (Patade et al. 2021) are used to partition the total PBAP mass (assumed to be 50% of the coincident insoluble organic mass) among the five PBAP groups according to the same ratio. None of these groups was either observed or available from global models.

	Mass concentrations (μg m^{-3})		
Aerosol species	MC3E	ACAPEX	APPRAISE
Ammonium sulfate	0.7	0.18	1.8
Sea salt	0.06	0.02	8.0
Mineral dust	0.17	0.030	8.7
soot	0.25	0.015	4.6
Soluble organic	1.36	0.28	1.24
Nonbiological insoluble organics (50% of insoluble organics)	0.17	0.011	0.14
PBAP (50% of insoluble organics)			
Fungi	0.17	0.0042	0.14
Bacteria	0.067	0.0014	0.055
Pollen	0.022	0.0018	0.018
Detritus	0.054	0.0033	0.024
Algae	4.3×10^{-5}	2.7×10^{-6}	3.58×10^{-5}

(BCT), pollen (PLN), detritus (DTS), and algae (ALG) (Patade et al. 2021, section 3.2 therein). It is parsimoniously assumed that about 50% of the measured loading of total insoluble organics consists of PBAPs in the absence of coincident observations of this fraction. Since the loadings of these five types were not measured in the MC3E, their ratio is assumed to follow measurements from Amazonia (Patade et al. 2021).

The Goddard Chemistry Aerosol Radiation and Transport (GOCART) model is used to prescribe the initial mass concentrations of various APs such as ammonium sulfate, sea salt, mineral dust, soot, soluble and insoluble organics for the same month and location. The vertical profiles of each AP are then rescaled by a constant factor to match with observations from the Interagency Monitoring of Protected Visual Environments (IMPROVE) located near the simulated domain. Table 2 summarizes the aerosol mass mixing ratio for each species observed at the ground.

2) ACAPEX

The case of orographic stratiform clouds observed during the ACAPEX campaign (section 2b) has been simulated for a horizontal area of 360 km × 80 km. The simulation was performed for 3 h (1915–2215 UTC 7 February 2015) and hourly thermodynamic soundings from the *Ron Brown* ship were applied. There were weak cells of embedded convection observed and these were represented by initializing the simulation with eight cold (about −5°C) dry bubbles oriented in a line parallel to the east and west boundaries. These cold
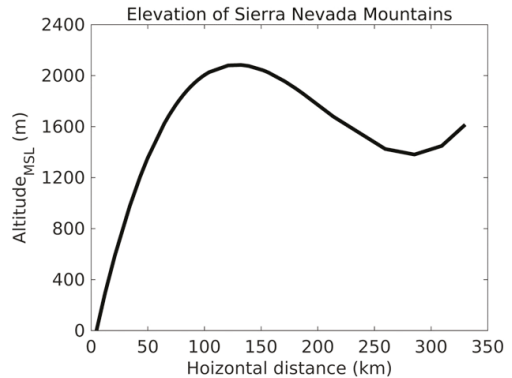

FIG. 4. Schematic picture of ground elevation represented in AC for the simulated ACAPEX case.

bubbles were each separated horizontally by 10 km and superimposed with many small warmer bubbles. Each cold bubble had maximum temperature perturbations of about −3 K. The same approach described in section 3c(1) is followed to obtain the initial mass concentrations of APs (Table 2). LBCs are open and periodic in the x and y directions, respectively.

Most of the length of the domain spanned the westernmost mountains in the Sierra Nevada range. The x and y axes were rotated by about 30° anticlockwise to orient the long edges of the domain to be perpendicular to the mountain chain (Fig. 2a). The western end of the domain was the Pacific coast. The elevation of the ground is represented in an idealized way as a function only of horizontal distance from the coast (Fig. 4).

3) APPRAISE

The case of supercooled, long-lived stratiform clouds observed during the APPRAISE campaign has been simulated for an area of 80 km × 80 km. Random perturbations of about ±0.8 g kg^{-1} were added to the initial vapor mixing ratio in the PBL to initialize convection. The simulation time is 48 h (0000 UTC 17 February–0000 UTC 19 February 2009), with the first 24 h as a spinup time of the model. LBCs are periodic in both the x and y directions.

Hourly fifth-generation European Centre for Medium-Range Weather Forecasts (ECMWF) atmospheric reanalysis (ERA5) data are used to derive the temperature, pressure, RH, and zonal (u) and meridional (v) wind in the x and y directions. The LSF advective tendencies in θ and q_v were applied to the simulation in view of the doubly periodic boundary conditions. These tendencies were estimated from the ERA5 dataset for every hour using

$$\left(\frac{\partial\theta}{\partial t}\right)_{LS} = \left[-\left(u\frac{\partial T}{\partial x} + v\frac{\partial T}{\partial y}\right) - \omega\left(\frac{\partial T}{\partial p} - \frac{\alpha}{C_p}\right)\right] \times \left(\frac{p}{p_{1000hPa}}\right)^{-0.286},$$
(11)

$$\left(\frac{\partial q_v}{\partial t}\right)_{LS} = -\left(u\frac{\partial q_v}{\partial x} + v\frac{\partial q_v}{\partial y}\right) - \omega\left(\frac{\partial q_v}{\partial p}\right),$$
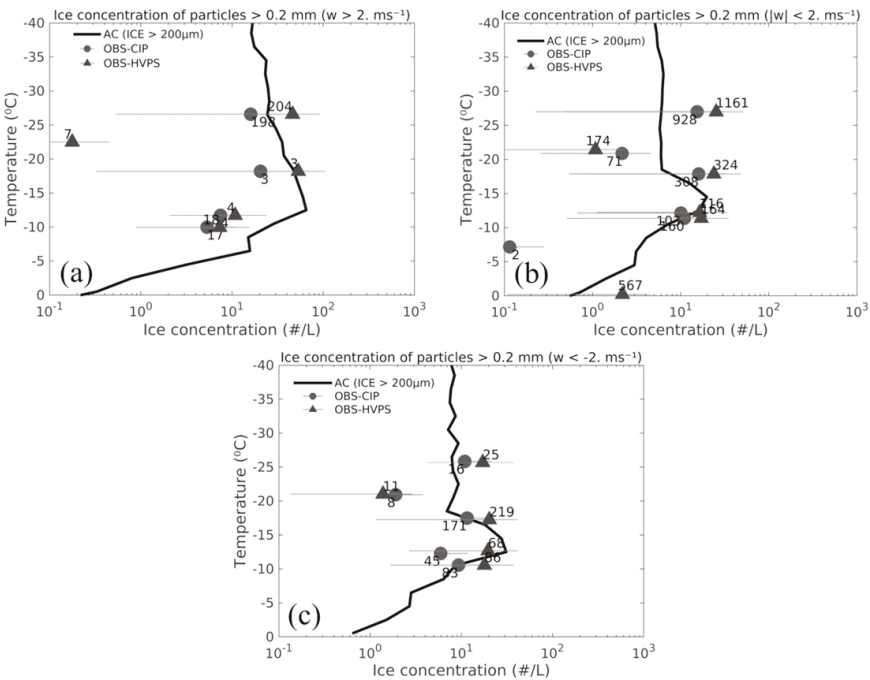(12)

FIG. 5. Comparison of predicted ice number concentrations for particles of maximum dimension bigger than 200 μm (NI$_{200}$) of all microphysical species (cloud ice, snow, and graupel/hail) from the control simulation of the simulated MC3E case (full black lines) with coincident aircraft observations from the CIP (circles) and HVPS-v3 (upward-pointing triangles) probes over cloudy convective (a) updrafts ($w > 2$ m s^{-1}), (b) downdrafts ($w < -2$ m s^{-1}), and (c) stratiform ($|w| < 2$ m s^{-1}) regions. Numbers by observational data points indicate the total number of seconds for which the aircraft sampled the cloud.

where ω is the vertical velocity in pressure coordinates, α is the specific volume, and C_p is the specific heat capacity of air at constant pressure. The values of θ and q_v are nudged toward observations for every hour in the lowest 2 km.

The GOCART model is used to prescribe the initial mass concentrations of various APs (Table 2). The vertical profiles of each AP are then rescaled by a constant factor to match with that from the Modern-Era Retrospective Analysis for Research and Applications version 2 (MERRA-2), 2D monthly mean data at the surface (~300 m MSL). Corrections were applied to MERRA-2-derived mass concentrations of soot and soluble organics to match the predicted cloud condensation nuclei (CCN) activity spectrum with previous maritime observations (e.g., Hoppel et al. 1990).

Furthermore, the initial 24 h are omitted from both the MC3E and APPRAISE simulations. This is because layer clouds advected into the study domain (in MC3E case; Jensen et al. 2015) and slowly evolving ($|w| < 1$ m s^{-1}) stratiform clouds (in APPRAISE case) cannot be well measured by sounding arrays that may potentially bias the LSF tendencies.

4. Results from the control simulations from all three cases

a. Model validation

1) MC3E

Figure 5 shows a comparison of the predicted filtered ice concentration, NI$_{200}$ from the control simulation (Table 3)

TABLE 3. List of simulations performed with AC.

Run performed	Description
Control	Including all four SIP processes and time-dependent heterogeneous freezing
No time-dependent INP	Including all four SIP mechanisms and excluding time dependence of heterogeneous freezing
No dust from droplet evaporation	Excluding contribution to mineral dust in the air from droplet evaporation from the control simulation

with the coincident aircraft observations. In cloudy convective regions (updrafts and downdrafts) and stratiform regions, the predicted NI_{200} is on the order of about $10\,L^{-1}$ at most observational levels, the same order of magnitude as in the aircraft data (Figs. 5a–c). Furthermore, in the dendritic regions of the stratiform (Fig. 5b) and downdraft (Fig. 5c) regions, the model agrees well with the observed NI_{200}, differing by less than ±15% from the aircraft observations at these levels.

Also, predictions of active CCN and INP concentrations, cloud-droplet properties, rainfall rate, radar reflectivity, top of the atmosphere radiative fluxes, and ascent statistics by AC of this MC3E case have already been validated with coincident aircraft, ground-based instruments, and satellite observations in Wa22.

2) ACAPEX

Figure 6 shows a comparison of the control simulation with the coincident aircraft and ground-based observations for the simulated ACAPEX case. All predicted microphysical properties (Figs. 6a–e) were averaged conditionally over cloudy convective updrafts ($w > 1\,\mathrm{m\,s^{-1}}$). Properties of cloud droplets such as mean diameter (Fig. 6a), and LWC (Fig. 6b) are in good agreement with observations from the CDP with errors of less than about 40%.

The predicted value of NI_{200} in cloudy convective updrafts has the same order of magnitude (about $10\,L^{-1}$) as observed by the 2DS probe. The predicted distribution of updraft speeds (Fig. 6d) and the domain-averaged surface precipitation rate at Lake Tahoe (Fig. 6e) each differ by less than 30% from the aircraft observations. Also, the difference between predicted microphysical properties (Figs. 6a–c) and aircraft observations at any level is less than that between the adjacent observational data points, signifying that the model agrees adequately with the observations.

3) APPRAISE

For the control simulation of the APPRAISE case, predicted microphysical properties such as NI_{100} and cloud droplets are compared with the aircraft (BAe146) observations from WI13.

Figure 7a shows adequate agreement of predicted CCN with previous studies such as Twomey and Wojciechowski (1969), Hoppel et al. (1990), and Jennings et al. (1998), in view of the spread of these observations. The number concentrations of cloud droplets (Fig. 7b), LWC (Fig. 7c), and NI_{100} (Fig. 7d) are all validated adequately with the coincident aircraft observations. The observed ice concentrations have been corrected for the shattering bias as noted above (section 2c). No in situ measurements were reported at levels below 3.6 km as the BAe146 aircraft mainly carried out measurements near cloud-top regions.

A distinct feature of the APPRAISE clouds is that they consisted of episodes of 1) weak embedded convection (~0000–1200 UTC) ("weak embedded convection episode"), and 2) supercooled, long-lived layer clouds (~1200–2400 UTC) ("long-lived layer-cloud episode"), as evident from the observed radar reflectivity (Figs. 7e,f). Our simulation predicts these clouds

adequately (Figs. 7g,h). Figure 7e shows adequate agreement of predicted radar reflectivity for the episodes of weak embedded convection with observations from the 3 GHz Doppler-polarization radar (1219–1221 UTC; C11). In these weak convective cells, the observed and predicted reflectivity values are between 7 and 30 dBZ. A time–height profile of the simulated radar reflectivity (Fig. 7f) is compared with the 35 GHz vertically pointing radar (adopted from C11) located at Chilbolton (Fig. 7i). At 1200 UTC 18 February 2009, the observed reflectivity is between -10 and 3 dBZ for altitudes between 2.5 and 3.8 km, over Chilbolton. The domainwide average of the predicted reflectivity at this time and altitude mostly varies between about -10 and 5 dBZ (Fig. 7g). Both observed (Figs. 7e,f) and predicted cloud tops were at about 4 km (Fig. 7g).

b. Other analyses of control simulations

1) CLOUD-MICROPHYSICAL QUANTITIES

Figures 8a and 8b show the vertical profiles of water contents of various microphysical species for the simulated MC3E, and ACAPEX cases in the stratiform regions ($|w| < 1\,\mathrm{m\,s^{-1}}$). A distinct feature of the simulated MC3E and ACAPEX cases is that the "ice-crystal process" is the dominant process of precipitation formation at all subzero levels. In both MC3E and ACAPEX cases (Figs. 10a,b), liquid water is predicted to dominate the cloud condensate at levels between the cloud base and $-5°C$, yet at levels between $-5°C$ and cloud top is dominated mostly by snow, graupel, and cloud ice (Figs. 8a,b; also Figs. 2, 3 in the online supplement). The presence of abundant snow, graupel, and cloud-ice mass along with strong vertical velocities ($w > 1\,\mathrm{m\,s^{-1}}$, Fig. 8c) and relatively strong wind shear (Fig. 8d) is predicted to enhance SIP through various mechanisms (section 3b). Similar results are predicted in the updraft and downdraft regions (not shown here).

By contrast, in the APPRAISE clouds, the ice-crystal process is predicted to be less active. This can be mainly attributed to relatively less liquid and ice hydrometeors mass (Fig. 8c) and weak vertical velocities ($|w| \sim 1\,\mathrm{m\,s^{-1}}$, Fig. 8d). However, C11 observed that in the episodes of weak embedded convection (~0000–1200 UTC, Fig. 7g), SIP (through the HM process) was mainly active. On the other hand, WI13 observed that in the episodes of long-lived supercooled layer clouds, heterogeneous ice nucleation is the most prolific ice initiation mechanism (Figs. 7e,f). WI13 further hypothesized that time-dependent freezing of available active INPs is the source for continuous ice nucleation and precipitation in such supercooled, long-lived layer clouds. We will test this hypothesis with different sensitivity tests in section 5.

2) RECIRCULATION OF DUST PARTICLES INTO SUPERCOOLED LAYER CLOUDS (APPRAISE)

Figure 9 shows the time–height profiles of various microphysical properties for the APPRAISE case (also see Fig. 1 in the online supplement). From Figs. 9a and 9b, it is evident that liquid and ice coexist at all levels in the episodes of weak embedded convection (~0000–1200 UTC) of the simulation
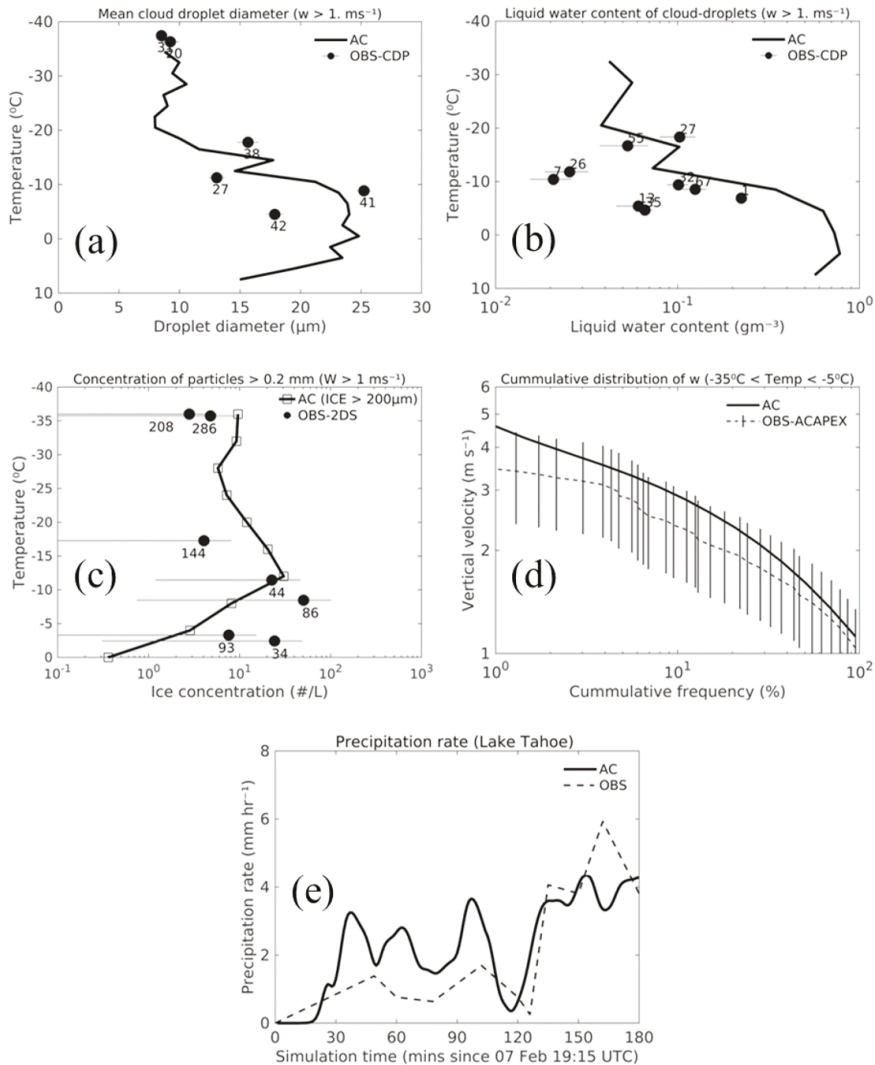
FIG. 6. Conditionally averaged predictions from the control simulation of the simulated ACAPEX case over regions of convective cloudy updrafts ($w > 1$ m s^{-1}) for (a) mean cloud droplet diameter (solid black line) and (b) LWC (solid black line) from the control simulation compared with the CDP observations (circles). (c) 2DS-measured ice concentrations for particles > 0.2 mm (NI$_{200}$) compared with the predicted ice concentrations (>0.2 mm) for all microphysical species (cloud ice, snow, and graupel/hail) in such updrafts. (d) Histogram of predicted vertical velocities ($w > 1$ m s^{-1}) with observations from the DOE G-1 aircraft and (e) predicted surface precipitation rate (mm h^{-1}) from the control simulation with observations from a rain gauge located at Lake Tahoe, California, United States. Standard errors of observational samples are shown as error bars in (a)–(d). Numbers by observation data points in (a)–(c) indicate the time in seconds for which the aircraft sampled the cloud at that level.

(Figs. 7e,g). As the simulation advances in its second half ($\sim$1200–2400 UTC), supercooled layer clouds are seen (Figs. 7f,h). These clouds are characterized by a thin ($\sim$400 m vertical extent) cloudy layer (Fig. 9a) at levels between the cloud top ($-13°$C) and $-7°$C. Below $-7°$C, the atmosphere is subsaturated (RH $<$ 70%) up to about 0°C (Fig. 9g). At levels warmer than 0°C, the air was saturated with respect to water (Figs. 3c and 9a). This water-saturated layer at lower levels

resulted in the formation of boundary layer stratiform clouds (~1 km thick) lasting about a day. By contrast, in the early simulation hours (0000–1200 UTC), the atmosphere was nearly saturated. Furthermore, these predicted weak convective and supercooled layer clouds are characterized by an ascent speed of about 1 m s^{-1} and less than 0.6 m s^{-1} (Fig. 9i), respectively, with continuous precipitation over several hours (Fig. 9h).

Consequently, we analyze how the quasi-steady state is maintained in the fixed domain for supercooled layer clouds over several hours. Figure 9a shows a layer of mixed-phase cloud continuing for about half a day between $-7°$ and $-13°$C. It is predicted that cloud droplets from this mixed-phase layer fall, and the smaller of these droplets may evaporate once they enter the region subsaturated with respect to both liquid and ice (Fig. 9g), releasing dust particles embedded in them. Moreover, at cloud-top levels, dust INPs initiate ice crystals and some of these crystals may grow to snow following vapor diffusion or aggregation. These ice (crystals and snow) particles may fall and some of them may sublimate away once they reach the subsaturation region. It is predicted that in the subsaturated environment, evaporation of droplets and sublimation of snow releases dust particles embedded in them, which form about 45% and 10% of the total dust mass, respectively, there. This is evident from Fig. 9c which shows that in the subsaturated environment, the upward mass flux [~10^{-11} kg m^{-2} s^{-1} (a particle flux of about 10^4 m^{-2} s^{-1})] of dust particles in the air is higher by about a factor of 5 than in the cloudy layer (e.g., near cloud top, Fig. 9e). This can be mainly attributed to evaporation of cloud droplets at subsaturated levels ($0°$ and $-7°$C, Fig. 9g), that releases dust particles embedded in them followed by an ascent in weak vertical motions (e.g., turbulence or weak convective cells), as simulated by AC.

5. Results from sensitivity tests in the simulated clouds

To evaluate the role of time dependence for heterogeneous ice nucleation, various sensitivity tests have been performed with AC (Table 3). These involved perturbation simulations from altering the control run in each of the three cases. Comparison with the control simulation revealed the effects from each prohibited process of ice initiation.

a. Role of time dependence of INP activity in overall ice production

Figure 10 shows the predicted number concentrations of active INPs, total and primary ice, and ice from various SIP processes in the stratiform regions ($|w| < 1$ m s^{-1}) with time-dependent INP activity prohibited (the "no time-dependent INP" run) for all three cases (section 2). These are compared with the three corresponding control runs that include this time dependence. These components of ice concentration were tracked by tagging tracers (section 3). Average number concentrations of active dust INPs are predicted to increase by a factor of 2 for the deep convective case (MC3E) and by about 0.5–1 order of magnitude for both layer-cloud cases (APPRAISE and ACAPEX), depending on the level (Figs. 10a,c,e) with inclusion of time dependence.

Also, active soot INPs show a similar sensitivity. However, active dust INPs are the most sensitive out of all the simulated INP species in this regard and have the maximum effect on the overall primary ice initiation. The same order-of-magnitude (0.5–1) increase is predicted also for the tagged concentrations of heterogeneously nucleated ice at colder levels ($< -7°$C) (Figs. 10a,c,e). The greater time dependence of INP activity in the layer-cloud cases (ACAPEX and APPRAISE) is due to longer lifetimes of such clouds with weaker ascent (Houze 2014), allowing more time for INPs to activate than in the convective case (MC3E).

In the APPRAISE control simulation of mixed-phase layer clouds in a frontal system, most of the primary ice is initiated by dust and soot INPs near cloud top ($-13°$C). The fractional increase in number concentrations of dust INPs from inclusion of time dependence has a maximum of about an order of magnitude at about $-6°$C (Fig. 10e). Yet the total ice concentration in such stratiform clouds is predicted to increase by only a factor of 2 between $-4°$ and $-8°$C in the control run relative to the "no time-dependent INP" run (Fig. 11f).

The weakness of this overall response of the cloud glaciation in APPRAISE is due to various SIP mechanisms, especially through the HM process and fragmentation in ice–ice collisions. Between $0°$ and $-7°$C, SIP mechanisms are predicted to create an ice enhancement (IE) ratio as high as 10^2 in the control run, greatly suppressing the response to time dependence of primary ice. However, in such thin clouds (APPRAISE, ~3 km in depth), SIP is less active than in the other two simulated cases (section 4b). At levels colder than $-10°$C where the heterogeneous ice nucleation occurs, there is an IE ratio of only about 3. This weak SIP is nevertheless sufficient again to reduce the response of total ice concentrations to the boosting of primary ice from time dependence of freezing INPs, with only a doubling of total and secondary ice concentrations.

By contrast, in the MC3E and ACAPEX clouds, no significant change in total ice concentrations is predicted from the inclusion of time dependence. This too can be attributed to various SIP processes dominating total ice initiation in both the simulated cases at all levels warmer than the $-36°$C isotherm. Both cases involved deeper clouds with more intense precipitation through ice-crystal process driving more vigorous SIP. Vertical profiles (Figs. 10b,d) of average concentration of ice particles from various initiation processes reveal that all SIP (section 3) initiates more than 99% and 90% of total nonhomogeneous ice (not from homogeneous freezing) at most levels warmer than the $-36°$C in MC3E and ACAPEX, respectively. At levels colder than $-8°$C, fragmentation in ice–ice collisions is the most prolific (>75% of the total nonhomogeneous ice concentration) SIP mechanism in both cases (MC3E and ACAPEX). The HM process is also active at temperatures between $-3°$ and $-8°$C, contributing about 85% to the total nonhomogeneous ice but only at these levels. Furthermore, fragmentation during raindrop freezing and sublimation together is predicted to contribute ~10% to the total nonhomogeneous ice initiated at levels colder than $-15°$C. In the ACAPEX simulation, fragmentation during sublimation is the second most dominant SIP mechanism in
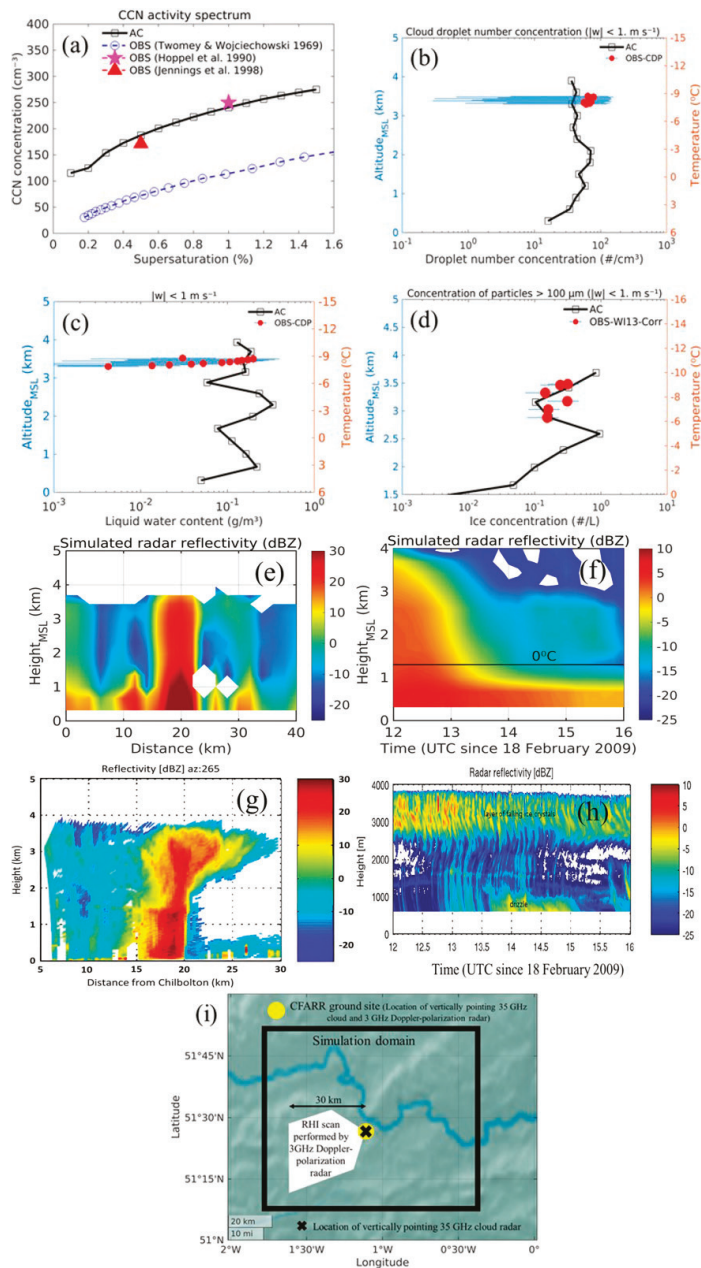
FIG. 7. (a) The CCN activity spectrum predicted by AC (solid black line) for the simulated APPRAISE case (18 Feb 2009) for the environment at about 100 m MSL from the prescribed vertical profiles of size distributions of various aerosol species. This is compared with maritime measurements made by Twomey and Wojciechowski (1969) (open circles), Hoppel et al. (1990) (pentagram), and Jennings et al. (1998, the geometric mean of observations shown in

downdraft regions (not shown here) in both cases. Similar results are predicted in the updraft and downdraft convective regions separately as for the stratiform regions for each of the simulated MC3E and ACAPEX cases (not shown here).

Regarding the time evolution at the lowest subzero levels ($-2°$ to $-10°$C) in layer cloud, Fig. 11 shows concentrations of ice particles conditionally averaged over all stratiform cloudy regions in the first 3 h after the onset of convection. Regarding the two deeper cloud cases (MC3E and ACAPEX), at times less than about 15 (in MC3E, Fig. 11a) and 40 min (in ACAPEX, Fig. 11b) after the onset of ice, the HM process is the only prolific SIP mechanism, creating IE ratios of about 10^2 during these times. The HM process is the most prolific SIP mechanism throughout the lifetime of the ACAPEX layer clouds. Later, as the deep convective cloud tops ascend through the mixed-phase region, fragmentation in ice–ice collisions becomes the most prolific SIP mechanism eventually in MC3E, creating IE ratios as high as 10^3 (Figs. 11a,b). This illustrates how fragmentation in ice–ice collisions tends to be slower but more persistent and prolific than the HM process in deep convection (Wa22, their Fig. 18). The ice concentrations in the simulated MC3E and ACAPEX cases reach their maxima after about 20 min, then become quasi steady for the rest of the lifetime of the clouds. Fragmentation during raindrop freezing and sublimation is predicted to form only about 5% of the total nonhomogeneous ice concentrations in all three cases.

Regarding these lower levels in the thin APPRAISE layer clouds (Fig. 11c), the HM process is predicted always to prevail (>150 min) in overall ice concentrations, creating sustained IE ratios as high as 10^2. About 40 min after the onset of convection, heterogeneous ice nucleation become the second most prolific type of ice initiation but forms only about 10% of the total nonhomogeneous ice concentrations between 40 and 100 min. Fragmentation in ice–ice collisions is active but has such a slow rate of explosive growth, owing to lack of ice precipitation, that it only contributes appreciably to the SIP at much longer times than those plotted (Fig. 11c).

Figure 12 shows a budget of ice particles initiated by various processes of ice initiation represented in AC (sections 3a and 3b), showing their contribution to the total ice at levels warmer

than the $-36°$C in the control and "no time-dependent INP" simulation (pie charts). The budget analysis shows that in all simulated cases (MC3E, ACAPEX, and APPRAISE), the number of heterogeneously nucleated ice crystals initiated increases by about 30% with a maximum of 45% (in APPRAISE) in the control simulation relative to the "no time-dependent INP" run (Fig. 12a).

The budget analysis also indicates that in all three simulated cases, SIP dominates overall ice production. In the APPRAISE clouds (Figs. 12a,b), fragmentation during ice–ice collisions and sublimation together with the HM process, are predicted to produce about 80% more fragments than those from heterogenous ice nucleation. In the MC3E (Figs. 12c,d) and ACAPEX simulations (Figs. 12e,f), fragmentation during ice–ice collisions and sublimation together initiate more than 95% of the total fragments implying an IE ratio of about 10^3. The budget analysis suggests that fragmentation in sublimation accounts for most of the fragments, creating IE ratios as high as 10^2. However, vertical profiles of tagging tracers (Fig. 10) reveal that fragmentation in sublimation is less prolific than fragmentation in ice–ice collisions (at levels colder than $-15°$C) and the HM process (between $-3°$ and $-8°$C levels). This is mainly attributed to the total sublimation of the vast majority ($>80\%$) of fragments initiated during the fragmentation in sublimation while descending.

To summarize, in all the simulated cases (MC3E, ACAPEX, and APPRAISE), the overall ice initiation is mostly dominated by various SIP mechanisms. Little effect ($<0.01\%$) on overall ice concentrations is predicted to arise from time-dependent INP activity.

b. Sources of quasi-steady precipitation in APPRAISE clouds

As discussed in sections 4a and 4b(1), our simulation for the APPRAISE case predicts two types of episodes during the evolution of the entire cloud system. First, weak embedded convection episode consisting of thermals with ascent of up to 1 m s^{-1} (section 4a). Second, long-lived layer-cloud episode, partly from convective outflow of the first episode, for which the stratiform ascent is only a few centimeters per second (section 4a). Both the episodes are predicted to be

---

$\leftarrow$

their Fig. 1; upward-pointing triangle). Comparison of predicted (b) droplet number concentrations (solid black line), (c) LWC (solid black line) with observations from the CDP, and (d) ice number concentrations for particles of maximum size dimension > 100 μm (NI$_{100}$) of all microphysical species (solid black line) with aircraft observations (circles) from the 2DS probe (adopted from WI13 and corrected following K11), conditionally averaged for the stratiform regions ($|w| < 1$ m s^{-1}). (e) Snapshot of the simulated radar reflectivity for the APPRAISE case compared with the observations from (g) 3 GHz Doppler-polarization radar at the CFARR ground site, which performed a range–height indicator scan along the 253° (adopted from C11) for the episodes of weak embedded convection, and (f) a time–height profile of the simulated radar reflectivity during the episodes of supercooled, long-lived layer clouds compared with the observations from (h) the 35GHz vertical pointing radar at the CFARR (adopted from C11). (i) Schematic diagram showing a view of the simulation domain (black box), the location of the vertically pointing 35 GHz cloud radar (black cross) and the area scanned by 3GHz Doppler-polarization radar located at CFARR ground site (yellow circle). Error bars in (b)–(d) are standard errors of observational samples.
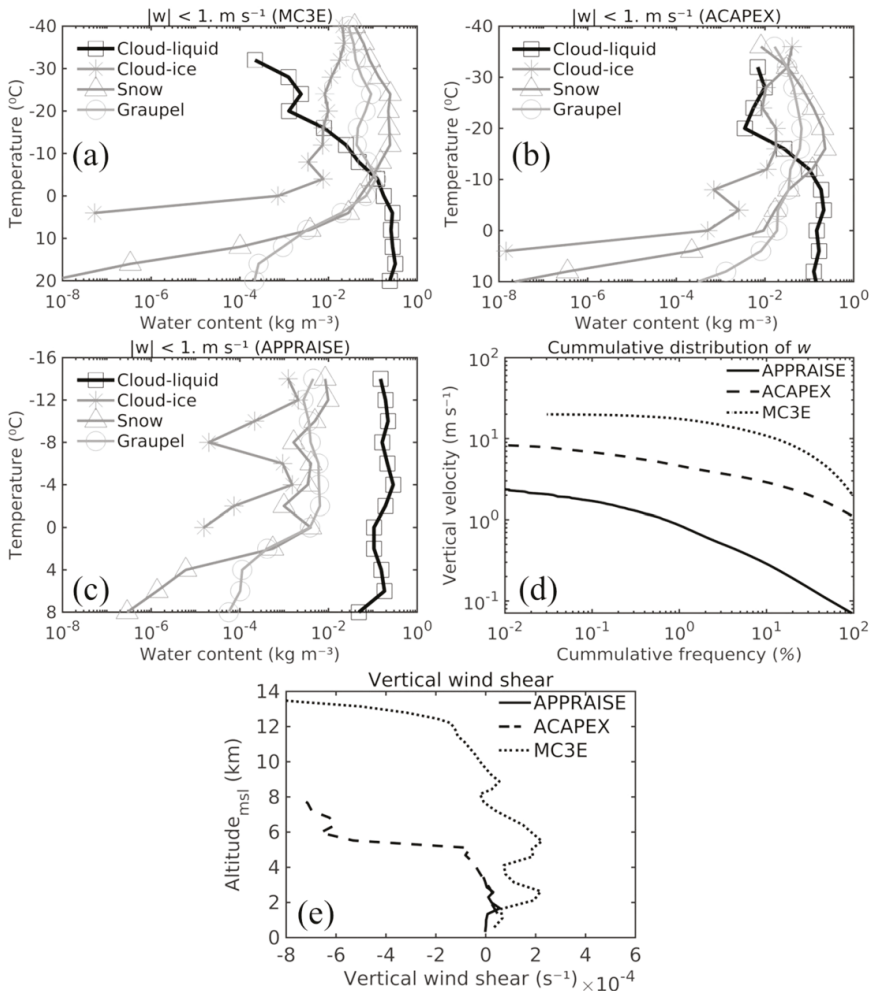
FIG. 8. The predicted water contents of cloud liquid (squares), cloud ice (asterisks), snow (upward-pointing triangles), and graupel (circles) in the stratiform regions ($|w| < 1$ m s^{-1}) from the control simulations of the (a) MC3E, (b) ACAPEX, and (c) APPRAISE cases. Also shown are (d) a vertical velocity histogram and (e) a profile of vertical wind shear from the control simulation of the APPRAISE (solid line), ACAPEX (dashed line), and MC3E (dotted line) cases.

precipitating continuously over several hours (Fig. 9h). However, ice initiation mechanisms influencing precipitation are predicted to differ between both types of episodes, as follows.

1) ICE INITIATION DURING THE WEAK EMBEDDED CONVECTION EPISODE

Figure 13 shows the total ice concentration (black lines) with time-dependent activity prohibited in the stratiform regions ($|w| < 1$ m s^{-1}) of the weak embedded convection episode (~0000–1200 UTC, section 4a) in comparison with the control run. In such clouds, the inclusion of time dependence causes only a slight increase (~30%) in the overall ice concentrations in the control simulation. This is because SIP is predicted to initiate about 75% of the total ice concentration at all subzero cloudy levels over several hours there. A similar extent of SIP was observed by C11 (their Fig. 11), attributing it to the HM process. In the control simulation, the HM process ($-3°$ to $-8°$C) and fragmentation in ice–ice collisions ($<-8°$C) contribute about 75% and 80%, respectively,
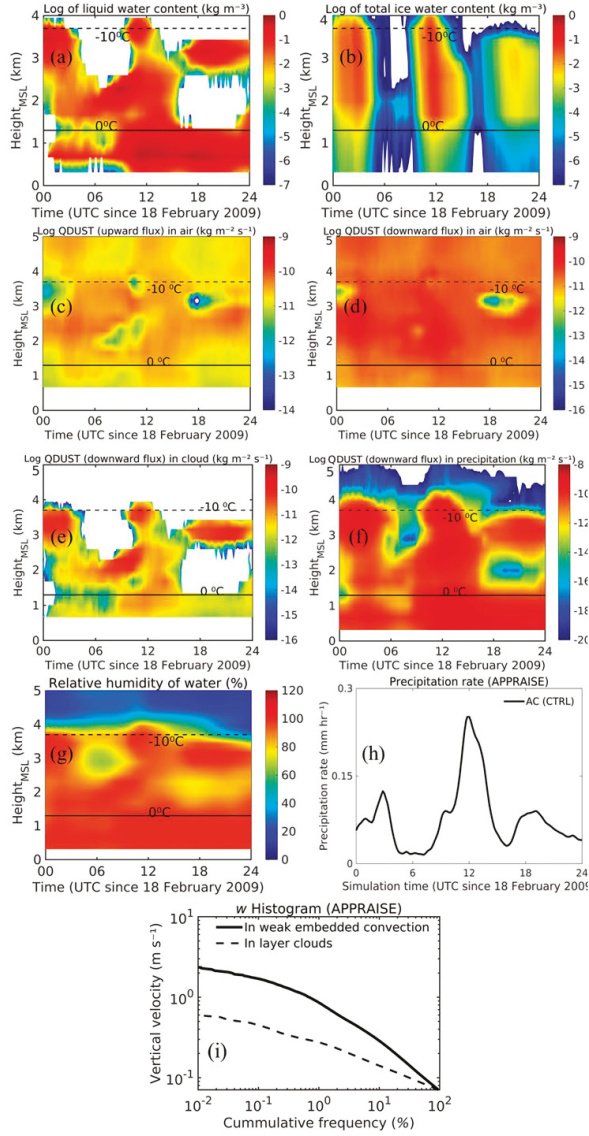
FIG. 9. Time–height profiles of the domain-averaged water contents of (a) cloud liquid, (b) total ice (cloud ice + snow + graupel), and (c) upward and (d) downward fluxes of the mass mixing ratio of dust particles in the air, and downward mass flux of dust mixing ratio in (e) cloud, and (f) precipitation, and (g) relative humidity with respect to water from the control simulation of the APPRAISE case between 0000 and 2400 UTC 18 Feb 2009. Also shown are the (h) precipitation rate, and (i) a vertical velocity histogram for the regions of weak convective cells (solid line) and supercooled layer clouds (dotted line) from the same simulation. All the quantities in (a)–(f) are plotted in log scale.
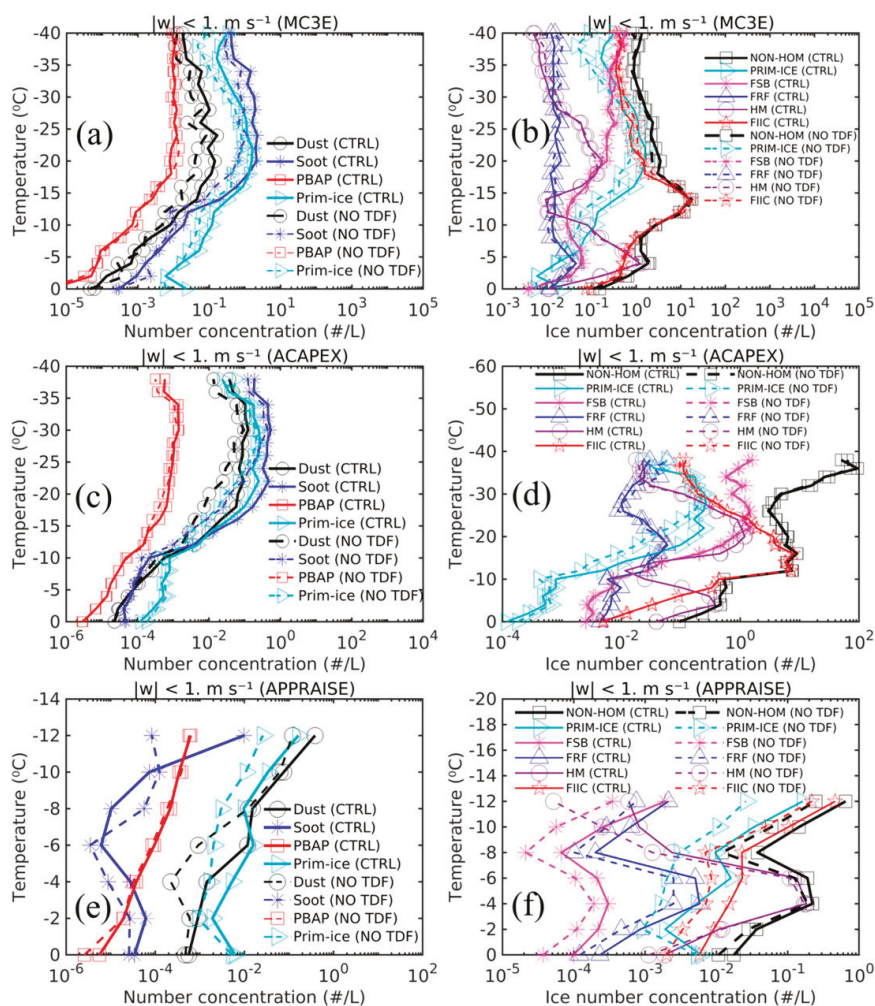
FIG. 10. (left) The predicted number concentrations of active INPs conditionally averaged over stratiform regions ($|w| < 1$ m s^{-1}) from mineral dust (solid line with open circles), soot (solid line with asterisks), and PBAP (solid line with squares), and concentrations of heterogeneously nucleated ice (PRIM-ICE, forward-pointing triangles) for the (a) MC3E, (c) ACAPEX, and (e) APPRAISE cases. The same information is shown with dotted lines for the "no time-dependent INP" run. (right) The concentrations of total nonhomogeneous ice (total cloud ice and snow minus total homogeneous ice; solid line with squares) and various tracer terms defining SIP processes such as fragmentation during sublimation (FSB; solid line with asterisks), ice–ice collisions (FIIC; solid line with pentagrams) and raindrop freezing (FRF; solid line with upward-pointing triangles), and the HM process (HM; solid line with open circles) for the (b) MC3E, (d) ACAPEX, and (f) APPRAISE case, respectively. The same information is shown with the dotted lines for the "no time-dependent INP" run. To compare the number concentrations of heterogeneously nucleated ice and total nonhomogeneous ice, heterogeneously nucleated ice (PRIM-ICE; forward-pointing triangles) is also shown in the right column.

to the total ice concentration (Fig. 13, grayscale lines) during this episode. However, heterogeneously nucleated ice forms only about 10%–20% of the overall ice concentrations (Fig. 13) at these levels.

Nevertheless, in both the control and no time-dependent INP case, ice crystals nucleated heterogeneously at levels near cloud top may become snow by vapor diffusion. This creates a positive feedback of ice multiplication by fragmentation
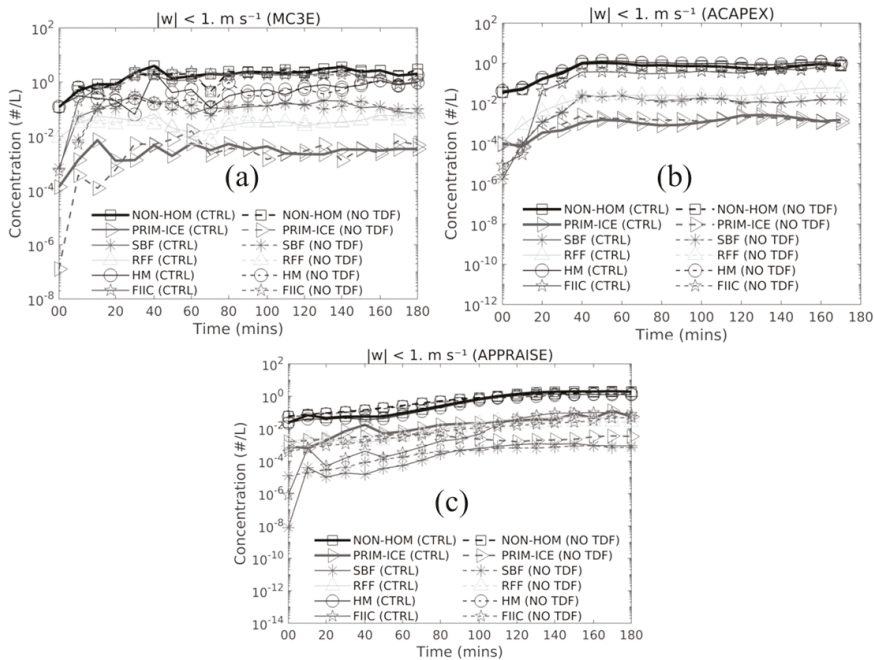
FIG. 11. Domain-averaged distributions with respect to time of the number concentrations of total nonhomogeneous ice (total ice from cloud ice and snow minus total homogeneous ice; squares), primary ice (forward-pointing triangles), and ice (cloud ice + snow) from tagging tracers of various SIP processes such as fragmentation during sublimation (SBF; asterisks), raindrop freezing (RFF; upward-pointing triangles), and fragmentation during ice–ice collisions (FIIC; pentagrams), and from the HM process (HM; circles) from the control simulation of (a) MC3E, (b) ACAPEX, and (c) APPRAISE cases. These concentrations are averaged for vertical velocities $|w| < 1$ m s^{-1} at temperatures between $-2°$ and $-10°$C. The same information is shown with dotted lines for the "no time-dependent INP" run. Time displayed is for the time after the first onset of ice.

in ice–ice collisions for up to several hours, causing a peak precipitation rate of about 0.3 mm h^{-1} at the surface (Fig. 9h) from the ice–crystal process. Hence, SIP (through the HM process and fragmentation in ice–ice collisions) is predicted to be the main source for the persistence of the weak embedded convection episode of the simulated APPRAISE clouds, which is also shown schematically in Fig. 14a.

In summary, during the weak embedded convection episode, this ice multiplication is promoted by the coexistence of cloud ice, snow, and graupel in proximity (Fig. 8c) and relatively strong vertical velocities ($|w| \sim 1$ m s^{-1}, Fig. 9i).

2) ICE INITIATION DURING THE LONG-LIVED LAYER-CLOUD EPISODE

In this section, focus is given to the duration of the simulation when weak convection is absent and there are only persistent long-lived layer clouds (~1200–2400 UTC, Fig. 7f) as observed by WI13. Our simulation approximately reproduced the quasi-steady state of the cloud top (Fig. 7h) for the long-lived layer-cloud episode which is consistent with the observations by WI13. The same is true for precipitation (Fig. 9h). WI13 proposed that

in such layer clouds, time-dependent freezing of available INPs is the main cause for continuous ice nucleation and precipitation.

In the long-lived layer-cloud episode, the inclusion of time dependence is predicted to increase the overall ice concentrations by only about 30% at levels near the cloud top ($-9°$ to $-13°$C) in the control simulation relative to the "no time-dependent INP" run. In this episode, heterogeneously nucleated ice and SIP (Fig. 15a) forms about 80% and 20% of the overall ice concentrations, respectively, at all subzero levels in the control simulation. A similar extent of heterogeneous ice was observed by WI13. However, contrary to the claim by WI13, time-dependent INP freezing would not be the cause for continuous ice nucleation and precipitation in such layer clouds, as it causes only a slight increase (~30%) in the overall ice production.

It is instead predicted that the recirculation of dust APs [section 4b(2)] is the main cause for the persistence of ice nucleation and precipitation in the long-lived layer-cloud episode. It is evident from Figs. 9c–f that dust APs that become free in droplet evaporation in the subsaturated environment (0° to $-7°$C, Fig. 9a) reach the saturated cloudy layer ($-7°$ to $-13°$C, Fig. 9a) following weak vertical motions and can
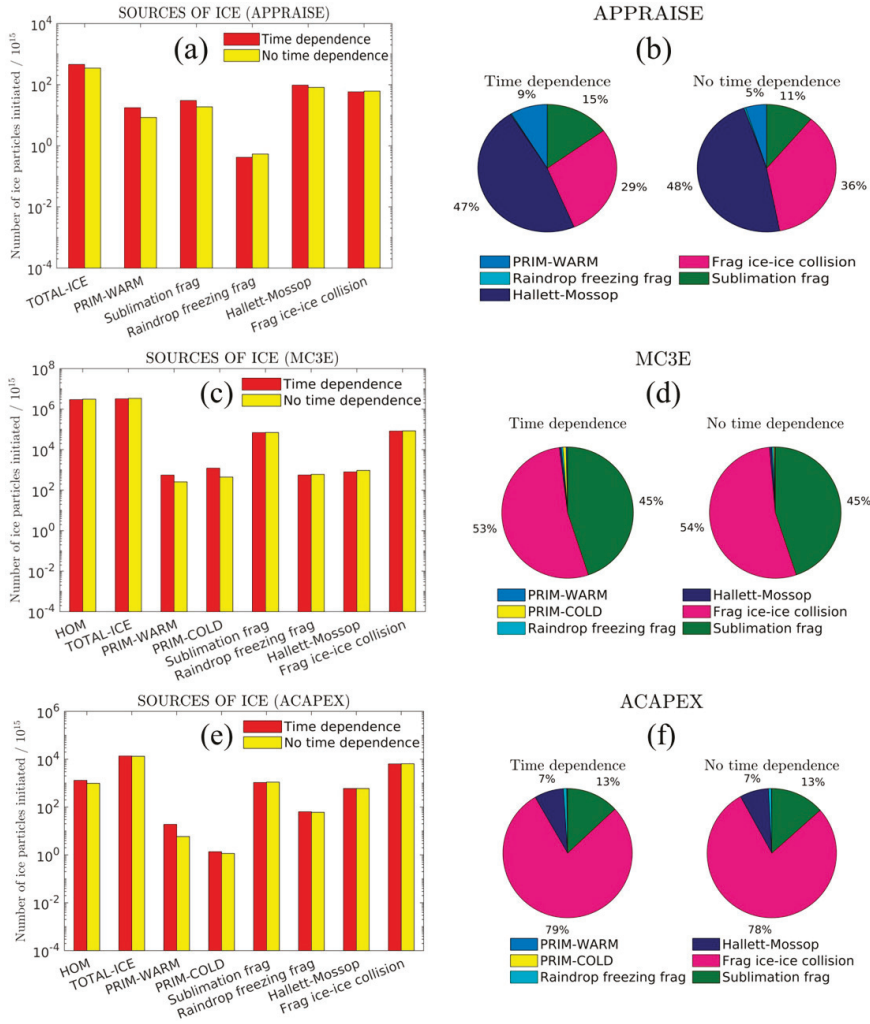
FIG. 12. (left) Bar charts showing a comparison of the budget of the number of ice crystals initiated from primary ice and SIP processes between the control and "no time-dependent INP" run for the (a) APPRAISE, (c) MC3E, and (e) ACAPEX cases. Shown are the sources of homogeneously nucleated ice ("HOM"), total ice from all ice initiation processes (TOTAL-ICE), heterogeneous ice nucleation at temperatures warmer than −30°C ("PRIM-WARM") and colder than −30°C ("PRIM-COLD"), and various SIP mechanisms active. These are fragmentation during raindrop freezing ("Raindrop freezing frag"), ice–ice collisions ("Frag ice–ice collisions") and sublimation ("Sublimation frag"), and the HM process ("Hallett–Mossop"). (right) The same information is shown (excluding "HOM" and "TOTAL-ICE") with the pie charts for the simulated (b) APPRAISE, (d) MC3E, and (f) ACAPEX simulations.

reactivate and nucleate ice there. Also, there is a significant downward flux of dust APs from levels above the cloud top (Fig. 9d) which again can initiate ice once a water-saturated cloudy layer is reached.

This reactivation following recirculation of dust APs (Fig. 14b) from the subsaturated environment is predicted to occur over a time scale (in-cloud dust mass concentration divided by the upward dust mass flux from below) of 1–2 h, which is much less than the time required (>10 h) for their INP activity to increase by about a factor of 10 according to the laboratory observations (Jk22). Furthermore, during this recirculation and reactivation, some of the hydrometeors may
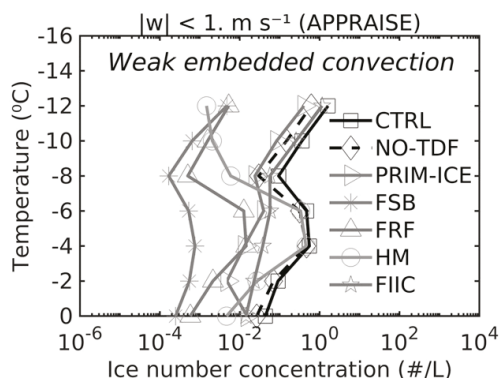
FIG. 13. Predicted number concentrations, during the weak embedded convection episode, of primary (forward pointing triangles) and total nonhomogeneous ice (total cloud ice and snow minus total homogeneous ice) from the control (squares) and "no time-dependent INP" (diamonds) run. Also shown are the ice particle number concentrations from various tracer terms defining SIP processes such as fragmentation during sublimation (FSB; asterisks), raindrop freezing (FRF; upward pointing triangles), and ice–ice collisions (FIIC; pentagrams), and the HM process (HM; circles). All quantities are conditionally averaged over the stratiform regions ($|w| < 1$ m s^{-1}), in APPRAISE clouds ($\sim$0000–1200 UTC 18 Feb 2009).

survive long enough and enter the liquid cloudy layer (1.2–0.3 km) leading to light precipitation in the form of drizzle or ice (Fig. 14b), as observed by WI13.

This is also evident from Fig. 15b which shows that in the long-lived layer-cloud episode, the overall ice concentration

decreases by about an order of magnitude in the "no dust from droplet evaporation" run relative to the control simulation. Hence, in such layer clouds (APPRAISE), it is predicted that reactivation following recirculation of dust APs is the main cause for the observed quasi-steady state of ice nucleation (WI13) over several hours, and not time-dependent freezing of available INPs.

6. Summary and conclusions

Three cloud cases have been simulated numerically with AC to investigate the effect from time-dependent INP activity on the total ice concentration. These are 1) an MCS consisting of deep convective clouds observed in MC3E over Oklahoma, United States, on 11 May 2011 (Wa22), 2) orographic stratiform layer clouds with embedded convection observed in ACAPEX over Northern California, United States, on 7 February 2015, and 3) thin, mixed-phase, supercooled stratiform clouds observed in APPRAISE on 18 February 2009 over the southern United Kingdom. All these simulations are validated adequately with coincident aircraft and ground-based observations. In all three simulated cases, cloud droplet properties such as mean droplet sizes, concentrations (in MC3E), and LWC differ no more than 40% from the coincident aircraft observations at most of the sampled levels where data are available.

A striking conclusion is that the filtered ice concentrations (NI$_{100}$ and NI$_{200}$) predicted by AC are also validated adequately at all sampled levels, differing by less than about a factor of 3 from the aircraft observations, in all three simulated cases. This is true for both the convective (ACAPEX and MC3E only) and stratiform regions of each case. The general realism of representations of all four SIP mechanisms (section 3b) in AC is the reason for the adequate validation of
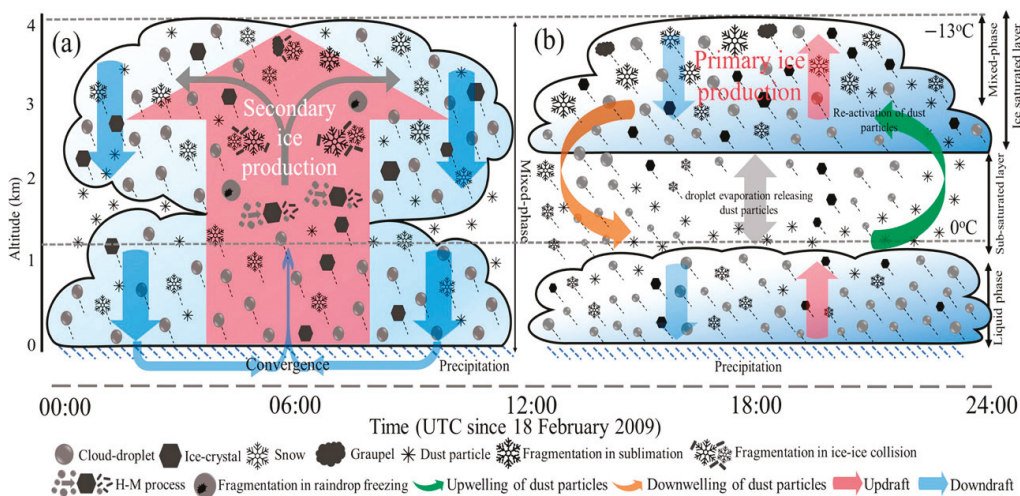

FIG. 14. A schematic of the APPRAISE clouds representing the sources of quasi-steady precipitation from the control simulation in the (a) weak embedded convection episode ($\sim$0000–1200 UTC) and (b) long-lived layer-cloud episode ($\sim$1200–2400 UTC) on 18 Feb 2009.
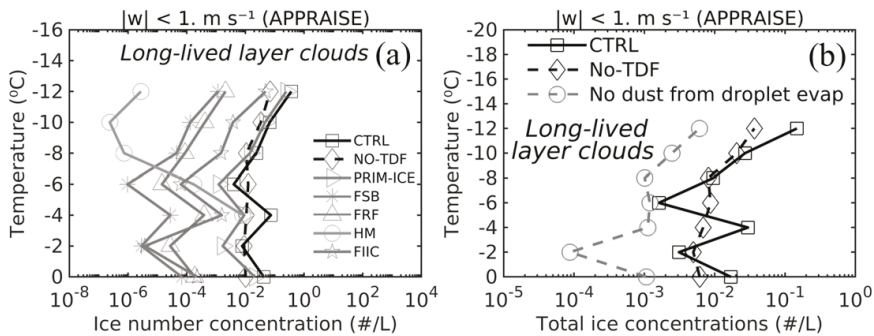
FIG. 15. During the long-lived layer-cloud episode of the APPRAISE case, conditionally averaged predicted number concentrations of the (a) total nonhomogeneous (total cloud ice and snow minus total homogeneous ice) ice from the control (squares) and "no time-dependent INP" (diamonds) run, heterogeneously nucleated ice (forward-pointing triangles), and various tracer terms defining SIP processes such as the Hallett–Mossop process (HM; circles), and fragmentation during ice–ice collisions (FIIC; pentagrams), sublimation of dendritic snow and graupel (FSB; asterisks), and raindrop freezing (FRF; upward-pointing triangles), over the stratiform regions ($|w| < 1$ m s^{-1}). Also shown are the total concentrations of nonhomogeneous ice from the (b) control (squares), "no time-dependent INP" (diamonds), and "no dust from droplet evaporation" (circles) simulations of the same clouds.

the number concentration of ice particles. Hence, there is no discrepancy between the observed and predicted ice concentrations as reported in some previous modeling studies (e.g., Fridlind et al. 2007, 2017; reviewed by Field et al. 2017).

Moreover, the vertical profiles of tagging tracers plotted for the control and "no time-dependent INP" runs reveal that the total ice concentrations in all the simulated clouds are mostly driven by ice formed in various SIP processes in all three cases. This is consistent with some previous studies (e.g., Lawson et al. 2015; Lasher-Trapp et al. 2016, 2021; Sotiropoulou et al. 2020; Qu et al. 2023). In all simulated clouds of the present study, fragmentation in ice–ice collisions contributes about 75%–95% to the total ice at most levels warmer than about −30°C. At levels between −3° and −8°C, the HM process initiates most of the ice particles (~70%) in the ACAPEX and APPRAISE simulations.

The budget analysis shows that the time dependence of INP activity makes no significant contribution (<10%) to the total number concentrations of ice particles initiated from all the processes in orographic and MCS clouds warmer than the −36°C level (MC3E, ACAPEX). In such clouds, fragmentation during ice–ice collisions (in updraft and stratiform regions) and during sublimation (in downdrafts only, counting fragments that survive) initiates more than 70% of the total ice particles. Consequently, the time dependence of INPs has little effect. In the case of the APPRAISE clouds, overall, the time dependence of INP activity is predicted to contribute about 30% of the total number of ice particles initiated, while SIP mechanisms active in such clouds initiate 70% of the total ice particles.

The conclusions of the present study are as follows:

1) Generally, for the total ice in precipitating clouds, the inclusion of time dependence is predicted to initiate about 10% of the total ice warmer than the −36°C level, whereas SIP mechanisms active in such clouds initiate more than 90% of the total ice at these levels in the mixed phase region (0° to −36°C).

2) In all three cases, for INP activity, including time dependence is predicted to have more impact for mineral dust and soot APs than for the other INP APs. This is consistent with the previous laboratory observations (Wright and Petters 2013; Herbert et al. 2014; Jk22). The INP activity of mineral dust and soot is predicted to increase by a factor of about 10 and 5, respectively, in the control simulation compared to the "no time-dependent INP" run at temperatures between −5° and −25°C. The least (only a factor of 2) increase is seen for PBAP groups from the inclusion of the time-dependent INP activity.

3) Specifically, in the simulated MCS (MC3E) system,

   (i) Overall, enhancement by a factor of up to about 4 (from dust APs) is seen in heterogeneously nucleated ice, whereas the total ice concentration is predicted to increase by only a factor of about 2 at levels colder than −15°C in all cloudy regions in the control run relative to the "no time-dependent INP" run.

   (ii) Regarding SIP, in updrafts, the HM process contributes about 30% to the total ice concentration at levels between −3° and −8°C, while this contribution is less (<10%) in the convective downdraft and stratiform regions. In the convective updraft and stratiform regions, fragmentation in ice–ice collisions is the most prolific SIP mechanism at levels colder than −8°C and initiates about 80% of the total ice at those levels. Fragmentation during sublimation is mostly active in stronger downdrafts ($w < −5$ m s^{-1}), initiating more than 15% of the total ice. All this SIP is far less sensitive to time-dependent INP activity than is primary ice itself.

4) In the case of orographic (ACAPEX) clouds,

 (i) Concentrations of heterogeneously nucleated ice are about half an order of magnitude higher in the control simulation relative to the "no time-dependent INP" run in all cloudy conditions. The same is true for the number concentrations of active dust INPs. However, no change is seen in the total ice concentration when the time dependence of INP activity is included.

 (ii) The HM process is the most prolific SIP mechanism at levels between $-3°$ and $-8°C$ and initiates more than 80% of the total ice concentration there in all cloudy conditions. In convective updrafts, fragmentation during ice–ice collisions contributes about 50% to the total ice concentration at levels colder than $-15°C$. While in convective downdrafts, fragmentation in sublimation is predicted to be more prolific and initiates about 40% of the overall ice concentration at these levels. Again, in this case, SIP acts to dampen the sensitivity of time dependence of INP activity.

5) In thin, long-lived mixed-phase stratiform (APPRAISE) clouds,

 (i) Overall, the total ice concentration is predicted to be about a factor of 3 higher, while the heterogeneously nucleated ice is about an order of magnitude higher, at all subzero levels when time dependence of INP activity is included.

 (ii) In the weak embedded convection episode, SIP (through the HM process and fragmentation ice–ice collisions) forms about 75% of the total ice concentration at all subzero levels, whereas in the long-lived layer-cloud episode, heterogeneously nucleated ice dominate (~80%) overall ice concentration.

 (iii) In the long-lived layer-cloud episode, it is predicted that the evaporation of droplets in the subsaturation region ($0°$ to $-7°C$) releases dust APs embedded in them, which forms about 45% of the total dust mass there. These released dust APs reactivate and nucleate ice once the mixed-phase cloudy layer ($-7°$ to $-13°C$) is reached following weak vertical motions. Furthermore, dust APs from levels above the cloud top also initiate ice once a saturated cloud layer is reached (Fig. 9d).

 (iv) This recirculation and reactivation of dust particles in the long-lived layer-cloud episode is predicted to happen over 1–2 h, which is much less than the times required for time-dependent INP freezing to alter the simulated ice concentrations appreciably (>10 h, Figs. 9 and 10).

 (v) Hence, the recirculation of dust APs back into the cloud from the subsaturated environment is the main reason for the simulated persistence of ice initiation and precipitation production in the long-lived layer-cloud episode, and not time-dependent freezing of available INPs, as claimed by WI13.

6) During the evolution of the simulated clouds (section 2) for tops warmer than $-15°C$ in the stratiform regions

($|w| < 1$ m s^{-1}), the initial (times < 20 min) explosive growth of numbers of ice crystals is from the fast HM process. Immediately after 20 min, this explosive growth is continued by fragmentation in ice–ice collisions, which prevails over a longer period. The effect of time dependence remains similar throughout the simulation.

In the simulated MC3E and ACAPEX clouds, SIP is predicted to dominate the overall ice concentrations at all levels colder than $-36°C$, whereas heterogeneously nucleated ice makes a negligible contribution (<1%) to the total ice concentration at these levels. This is mainly attributed to the relatively shorter lifetime of such clouds (60–90 min) and the presence of abundant large drops, snow, and graupel particles (Fig. 8) in association with strong convective ascent and descent ($|w| > 1$ m s^{-1}) in such clouds, which favor SIP at these levels.

By contrast, in the APPRAISE simulation of a thin layer cloud, the weakness and shallowness of the ascent ($|w| < 1$ m s^{-1}, Fig. 8d) causes less abundance (<10% of the total ice particles) of large snow and graupel particles than the other two (MC3E and ACAPEX) cases. Nevertheless, SIP is still predicted to prevail in overall ice initiation in the episodes of weak convection of this case (APPRAISE), albeit less prolifically than in the other two cases, and initiates about 75% (HM process and fragmentation in ice–ice collisions) of the total ice at all subzero levels there. Generally, treatment of ice initiation through various SIP processes has some uncertainty due to the incompleteness of laboratory studies (e.g., Field et al. 2017) and depends upon various parameters such as particle sizes, vertical velocities, temperature, and hydrometeor fall speed. Hence, the relative roles of various SIP processes in forming high ice concentrations differ among contrasting cloud types.

The present study generally finds little effect from time-dependent ice nucleation on the total ice concentration in a range of cloud types (deep convective, orographic, and long-lived stratiform clouds). In the case of thin, stratiform clouds (APPRAISE) there is at most a doubling of the average concentration of ice particles at levels colder than $-8°C$ from the inclusion of time dependence. Thus, time dependence alone cannot predict the observed steady state of such clouds. It is instead predicted that in the weak embedded convection episode of the APPRAISE clouds, SIP (through the HM process and fragmentation in ice–ice collisions) is the main source for quasi-steady state of ice formation and precipitation. On the other hand, in the long-lived layer-cloud episode of the APPRAISE clouds, the recirculation of dust particles (Fig. 14b and Fig. 15b) is predicted to be the main cause for continuous ice nucleation and precipitation.

In our simulation of summertime deep convection (MC3E) and wintertime orographic clouds (ACAPEX) with some weak embedded convection extending above the $-36°C$ level, SIP is predicted to initiate about 70%–80% of the total ice at all levels below this level, whereas primary ice only contributes less than 1.5%, implying an IE ratio of about 10^3. In such clouds, the effect of time-dependent ice nucleation on total ice is predicted to be the least. These more convective (MC3E

and less so for ACAPEX) clouds are characterized by typically shorter lifetimes (<90 min) due to stronger vertical motions, suppressing the modest effects from the time dependence of INP activity, relative to the APPRAISE clouds. In the simulated wintertime long-lived (~24 h) stratiform clouds (APPRAISE), the weakness of ascent and shallowness of cloud depth together support less precipitation and hence less SIP, with an IE ratio of only about 10.

To conclude, it is the combination of various SIP mechanisms, interrelated by positive feedbacks of ice multiplication (section 3b), that accurately explains the observed difference between the orders of magnitude of the measured concentrations of INPs and ice particles in the simulated cases. Fragmentation in ice–ice collisions and the HM process are especially pivotal to cloud glaciation. The present study suggests that time-dependent INP activity can be neglected in numerical simulations of clouds, as it has the least impact on the total number of ice particles out of all the ice initiation processes treated. This is consistent with previous laboratory studies (Vali 2014; Ka17; Jk22). Time dependence of INPs cannot explain either the observed ice enhancement in any of the cases of natural clouds studied here or the observed persistence of precipitation of the simulated layer clouds.

APPENDIX

List of Symbols Used in this Paper

Table A1 provides a list of symbols used in the present study along with their units and descriptions.

TABLE A1. Symbols used in the present study along with their units and descriptions.

Symbol	Description	Unit
A_X	Proportionality constant for a power law dependence of temperature shift on time	$\mathrm{K\ s}^{-\beta}$
D_X	Diameter of a given aerosol species	$\mu\mathrm{m}$
H_X	Fraction reducing INP activity at warm T and low s_i for various groups of aerosols in X	—
n_i	Number m.r. of ice crystals generated from EP	kg^{-1}
$n_{\mathrm{IN},1,*}$	Background-tropospheric reference activity spectrum number m.r. for water saturation	kg^{-1}
$n_{\mathrm{IN,rain}}$	Number mixing ratio of rain's activated INP	kg^{-1}
$n_{\mathrm{IN},X}$	Number m.r. of X INP species from the EP	kg^{-1}
n_X	Number mixing ratio (m.r.) of APs in group X (not depleted by ice nucleation while inside the cloud)	kg^{-1}
$n_{X,a}$	Number of aerosols in group X lost by ice nucleation	kg^{-1}
$\tilde{n}_{\mathrm{IN,rain}}$	Modified $n_{\mathrm{IN,rain}}$ representing time dependence INP activity	kg^{-1}
$\tilde{n}_{\mathrm{IN},X}$	Modified $n_{\mathrm{IN},X}$ representing time dependence INP activity	kg^{-1}
Q	Passive clock tracer	kg^{-1}
Q_0	Value of Q outside of the cold cloud (set to unity)	kg^{-1}
Q_r	Raindrop's mass mixing ratio	$\mathrm{kg\ kg}^{-1}$
S_i	Saturation ratio with respect to ice	—
S_i^w	Value of S_i at exact water saturation	—
S_w	Saturation ratio with respect to water	—

TABLE A1. (*Continued*)

Symbol	Description	Unit
t	Time	s
t^*	Time since the start of the isothermal phase of the laboratory experiment (Jk22)	s
T	Temperature of ambient air	°C
w	Vertical velocity of air	m s^{-1}
X	Aerosol species (X = DM, BC, sO, FNG, BCT, PLN, and DTS)	—
z	Height	m
α_X	Fraction of $n_{IN,1,*}$ ($H_X = 1$) from INP activity of AP group X	—
β	Exponent in power-law dependence of temperature shift on time	—
γ_X	Slope value of the fit for X in FNG, BCT, PLN, DTS	°C^{-1}
Ω_X	Total surface area of all APs of diameters larger than 0.1 μm from group X (not depleted by ice nucleation while inside the cloud)	(aerosol) m^2 (air) kg^{-1}
$\Omega_{X,1,*}$	Background tropospheric component of Ω_X for $0.1 \geq D_X \geq 1$ μm	(aerosol) m^2 (air) kg^{-1}
$\Omega_{X,\text{rain}}$	Total surface area of all APs bigger than 0.1 μm in group X immersed in liquid raindrops	(aerosol) m^2 (air) kg^{-1}
Δt	Model time step	s
ΔT_X	Shift in T in time-dependent approach of heterogeneous ice nucleation	K
μ_X	Average number of activated ice embryos per AP in group X	—
$\xi(T)$	The function that varies between 0 and 1 for $-5° < T < -2$°C	—
τ_Q	Relaxation time scale of $\bar{Q}$	s
υ_t	Fall speeds of raindrops in each size bin	m s^{-1}
$\omega_{X,1,*}$	Baseline coefficient of a group of aerosols from X = FNG, PLN, BCT, and DTS	m^2

REFERENCES

Bacon, N. J., B. D. Swanson, M. B. Baker, and E. J. Davis, 1998: Breakup of levitated frost particles. *J. Geophys. Res.*, **103**, 13 763–13 775, https://doi.org/10.1029/98JD01162.

Bigg, E. K., 1953: The supercooling of water. *Proc. Phys. Soc.*, **66B**, 688–694, https://doi.org/10.1088/0370-1301/66/8/309.

Cantrell, W., and A. Heymsfield, 2005: Production of ice in tropospheric clouds: A review. *Bull. Amer. Meteor. Soc.*, **86**, 795–808, https://doi.org/10.1175/BAMS-86-6-795.

Carte, A. E., 1959: Probability of freezing. *Proc. Phys. Soc.*, **73**, 324, https://doi.org/10.1088/0370-1328/73/2/126.

Chen, J.-P., A. Hazra, and Z. Levin, 2008: Parameterizing ice nucleation rates using contact angle and activation energy derived from laboratory data. *Atmos. Chem. Phys.*, **8**, 7431–7449, https://doi.org/10.5194/acp-8-7431-2008.

Clarke, A. D., and Coauthors, 2004: Size distributions and mixtures of dust and black carbon aerosol in Asian outflow: Physiochemistry and optical properties. *J. Geophys. Res.*, **109**, D15S09, https://doi.org/10.1029/2003JD004378.

Connolly, P. J., O. Möhler, P. R. Field, H. Saathoff, R. Burgess, T. Choularton, and M. Gallagher, 2009: Studies of heterogeneous freezing by three different desert dust samples. *Atmos. Chem. Phys.*, **9**, 2805–2824, https://doi.org/10.5194/acp-9-2805-2009.

Crosier, J., and Coauthors, 2011: Observations of ice multiplication in a weakly convective cell embedded in supercooled mid-level stratus. *Atmos. Chem. Phys.*, **11**, 257–273, https://doi.org/10.5194/acp-11-257-2011.

DeMott, P. J., 1990: An exploratory study of ice nucleation by soot aerosols. *J. Appl. Meteor.*, **29**, 1072–1079, https://doi.org/10.1175/1520-0450(1990)029<1072:AESOIN>2.0.CO;2.

Deshmukh, A., V. T. J. Phillips, A. Bansemer, S. Patade, and D. Waman, 2022: New empirical formulation for the sublimational breakup of graupel and dendritic snow. *J. Atmos. Sci.*, **79**, 317–336, https://doi.org/10.1175/JAS-D-20-0275.1.

Dong, Y., R. G. Oraltay, and J. Hallett, 1994: Ice particle generation during evaporation. *Atmos. Res.*, **32**, 45–53, https://doi.org/10.1016/0169-8095(94)90050-7.

Dudhia, J., 1989: Numerical study of convection observed during the Winter Monsoon Experiment using a mesoscale two-dimensional model. *J. Atmos. Sci.*, **46**, 3077–3107, https://doi.org/10.1175/1520-0469(1989)046<3077:NSOCOD>2.0.CO;2.

Dufour, L., and R. Defay, 1963: *Thermodynamics of Clouds*. Academic Press, 255 pp.

Ervens, B., and G. Feingold, 2013: Sensitivities of immersion freezing: Reconciling classical nucleation theory and deterministic expressions. *Geophys. Res. Lett.*, **40**, 3320–3324, https://doi.org/10.1002/grl.50580.

Field, P. R., and A. J. Heymsfield, 2015: Importance of snow to global precipitation. *Geophys. Res. Lett.*, **42**, 9512–9520, https://doi.org/10.1002/2015GL065497.

——, ——, and A. Bansemer, 2006: Shattering and particle interarrival times measured by optical array probes in ice clouds. *J. Atmos. Oceanic Technol.*, **23**, 1357–1371, https://doi.org/10.1175/JTECH1922.1.

——, and Coauthors, 2017: Secondary ice production: Current state of the science and recommendations for the future. *Ice Formation and Evolution in Clouds and Precipitation: Measurement and Modeling Challenges, Meteor. Monogr.*, No. 58, Amer. Meteor. Soc., https://doi.org/10.1175/AMSMONOGRAPHS-D-16-0014.1.

Freidenreich, S. M., and V. Ramaswamy, 1999: A new multiple-band solar radiative parameterization for general circulation models. *J. Geophys. Res.*, **104**, 31 389–31 409, https://doi.org/10.1029/1999JD900456.

Fridlind, A. M., A. S. Ackerman, G. McFarquhar, G. Zhang, M. R. Poellot, P. J. DeMott, A. J. Prenni, and A. J. Heymsfield, 2007: Ice properties of single-layer stratocumulus during the Mixed-Phase Arctic Cloud Experiment: 2. Model results. *J. Geophys. Res.*, **112**, D24202, https://doi.org/10.1029/2007JD008646.

——, and Coauthors, 2017: Derivation of aerosol profiles for MC3E convection studies and use in simulations of the 20 May squall line case. *Atmos. Chem. Phys.*, **17**, 5947–5972, https://doi.org/10.5194/acp-17-5947-2017.

Hallett, J., and S. C. Mossop, 1974: Production of secondary ice particles during the riming process. *Nature*, **249**, 26–28, https://doi.org/10.1038/249026a0.

Herbert, R. J., B. J. Murray, T. F. Whale, S. J. Dobbie, and J. D. Atkinson, 2014: Representing time-dependent freezing behaviour in immersion mode ice nucleation. *Atmos. Chem. Phys.*, **14**, 8501–8520, https://doi.org/10.5194/acp-14-8501-2014.

Hobbs, P. V., and J. D. Locatelli, 1969: Ice nuclei from a natural forest fire. *J. Appl. Meteor.*, **8**, 833–834, https://doi.org/10.1175/1520-0450(1969)008<0833:INFANF>2.0.CO;2.

——, M. K. Politovich, and L. F. Radke, 1980: The structures of summer convective clouds in eastern Montana. I: Natural clouds. *J. Appl. Meteor.*, **19**, 645–663, https://doi.org/10.1175/1520-0450(1980)019<0645:TSOSCC>2.0.CO;2.

Hong, S.-Y., and H.-L. Pan, 1996: Nonlocal boundary layer vertical diffusion in a medium-range forecast model. *Mon. Wea. Rev.*, **124**, 2322–2339, https://doi.org/10.1175/1520-0493(1996)124<2322:NBLVDI>2.0.CO;2.

Hoppel, W. A., J. W. Fitzgerald, G. M. Frick, R. E. Larson, and E. J. Mack, 1990: Aerosol size distributions and optical properties found in the marine boundary layer over the Atlantic Ocean. *J. Geophys. Res.*, **95**, 3659–3686, https://doi.org/10.1029/JD095iD04p03659.

Houze, R. A., Jr., 2014: *Cloud Dynamics*. 2nd ed. Elsevier/Academic Press, 496 pp.

Jakobsson, J. K. F., D. B. Waman, V. T. J. Phillips, and T. Bjerring Kristensen, 2022: Time dependence of heterogeneous ice nucleation by ambient aerosols: Laboratory observations and a formulation for models. *Atmos. Chem. Phys.*, **22**, 6717–6748, https://doi.org/10.5194/acp-22-6717-2022.

James, R. L., V. T. J. Phillips, and P. J. Connolly, 2021: Secondary ice production during the break-up of freezing water drops on impact with ice particles. *Atmos. Chem. Phys.*, **21**, 18519–18530, https://doi.org/10.5194/acp-21-18519-2021.

Jennings, S. G., M. Geever, and T. C. O'Connor, 1998: Coastal CCN measurements at Mace Head with enhanced concentrations in strong winds. *Atmos. Res.*, **46**, 243–252, https://doi.org/10.1016/S0169-8095(97)00066-5.

Jensen, M. P., and Coauthors, 2015: The Midlatitude Continental Convective Clouds Experiment (MC3E) sounding network: Operations, processing and analysis. *Atmos. Meas. Tech.*, **8**, 421–434, https://doi.org/10.5194/amt-8-421-2015.

——, and Coauthors, 2016: The Midlatitude Continental Convective Clouds Experiment (MC3E). *Bull. Amer. Meteor. Soc.*, **97**, 1667–1686, https://doi.org/10.1175/BAMS-D-14-00228.1.

Kanji, Z. A., L. A. Ladino, H. Wex, Y. Boose, M. Burkert-Kohn, D. J. Cziczo, and M. Krämer, 2017: Overview of ice nucleating particles. *Ice Formation and Evolution in Clouds and Precipitation: Measurement and Modeling Challenges, Meteor. Monogr.*, No. 58, Amer. Meteor. Soc., https://doi.org/10.1175/AMSMONOGRAPHS-D-16-0006.1.

Koop, T., B. Luo, A. Tsias, and T. Peter, 2000: Water activity as the determinant for homogeneous ice nucleation in aqueous solutions. *Nature*, **406**, 611–614, https://doi.org/10.1038/35020537.

Korolev, A. V., E. F. Emery, J. W. Strapp, S. G. Cober, G. A. Isaac, M. Wasey, and D. Marcotte, 2011: Small ice particles in tropospheric clouds: Fact or artifact? Airborne Icing Instrumentation Evaluation experiment. *Bull. Amer. Meteor. Soc.*, **92**, 967–973, https://doi.org/10.1175/2010BAMS3141.1.

Kudzotsa, I., and Coauthors, 2016: Aerosol indirect effects on glaciated clouds. Part I: Model description. *Quart. J. Roy. Meteor. Soc.*, **142**, 1958–1969, https://doi.org/10.1002/qj.2791.

Langham, E. J., and B. J. Mason, 1958: The heterogeneous and homogeneous nucleation of supercooled water. *Proc. Roy. Soc.*, **247A**, 493–504, https://doi.org/10.1098/rspa.1958.0207.

Lasher-Trapp, S., D. C. Leon, P. J. DeMott, C. M. Villanueva-Birriel, A. V. Johnson, D. H. Moser, C. S. Tully, and W. Wu, 2016: A multisensor investigation of rime splintering in tropical maritime cumuli. *J. Atmos. Sci.*, **73**, 2547–2564, https://doi.org/10.1175/JAS-D-15-0285.1.

——, E. L. Scott, E. Järvinen, M. Schnaiter, F. Waitz, P. J. DeMott, C. S. McCluskey, and T. C. Hill, 2021: Observations and modeling of rime splintering in Southern Ocean cumuli. *J. Geophys. Res. Atmos.*, **126**, e2021JD035479, https://doi.org/10.1029/2021JD035479.

Lau, K. M., and H. T. Wu, 2003: Warm rain processes over tropical oceans and climate implications. *Geophys. Res. Lett.*, **30**, 2290, https://doi.org/10.1029/2003GL018567.

Lawson, R. P., S. Woods, and H. Morrison, 2015: The microphysics of ice and precipitation development in tropical cumulus clouds. *J. Atmos. Sci.*, **72**, 2429–2445, https://doi.org/10.1175/JAS-D-14-0274.1.

Leung, L. R., 2016: ARM Cloud-Aerosol-Precipitation Experiment (ACAPEX) field campaign report. ARM Rep. DOE/SC-ARM-16-012, 24 pp., https://www.osti.gov/servlets/purl/1251152.

Levin, E. J. T., and Coauthors, 2019: Characteristics of ice nucleating particles in and around California winter storms. *J. Geophys. Res. Atmos.*, **124**, 11530–11551, https://doi.org/10.1029/2019JD030831.

Levine, J., 1950: Statistical explanation of spontaneous freezing of water droplets. NACA Tech. 2234, 28 pp., https://ntrs.nasa.gov/api/citations/19930082877/downloads/19930082877.pdf.

Lin, Y., and Coauthors, 2022: Modeling impacts of ice-nucleating particles from marine aerosols on mixed-phase orographic clouds during 2015 ACAPEX field campaign. *Atmos. Chem. Phys.*, **22**, 6749–6771, https://doi.org/10.5194/acp-22-6749-2022.

Lohmann, U., 2006: Aerosol effects on clouds and climate. *Space Sci. Rev.*, **125**, 129–137, https://doi.org/10.1007/s11214-006-9051-8.

Martanda, G., 2022: Fragmentation in graupel-snow collisions. M.S. thesis, Dept. of Physical Geography and Ecosystem Science, Lund University, 47 pp., http://lup.lub.lu.se/student-papers/record/9087233.

Ming, Y., V. Ramaswamy, L. J. Donner, and V. T. J. Phillips, 2006: A new parameterization of cloud droplet activation applicable to general circulation models. *J. Atmos. Sci.*, **63**, 1348–1356, https://doi.org/10.1175/JAS3686.1.

Monin, A. S., and A. M. Obukhov, 1954: Basic laws of turbulent mixing in the atmosphere near the ground. *Tr. Geofiz. Inst., Akad. Nauk SSSR*, **24**, 163–187.

Mossop, S. C., 1976: Production of secondary ice particles during the growth of graupel by riming. *Quart. J. Roy. Meteor. Soc.*, **102**, 45–57, https://doi.org/10.1002/qj.49710243104.

Murray, B. J., D. O' Sullivan, J. D. Atkinson, and M. E. Webb, 2012: Ice nucleation by particles immersed in supercooled cloud droplets. *Chem. Soc. Rev.*, **41**, 6519–6554, https://doi.org/10.1039/c2cs35200a.

Niedermeier, D., R. A. Shaw, S. Hartmann, H. Wex, T. Clauss, J. Voigtländer, and F. Stratmann, 2011: Heterogeneous ice nucleation: Exploring the transition from stochastic to singular

freezing behavior. *Atmos. Chem. Phys.*, **11**, 8767–8775, https://doi.org/10.5194/acp-11-8767-2011.

Oraltay, R. G., and J. Hallett, 1989: Evaporation and melting of ice crystals: A laboratory study. *Atmos. Res.*, **24**, 169–189, https://doi.org/10.1016/0169-8095(89)90044-6.

Patade, S., and Coauthors, 2021: Empirical formulation for multiple groups of primary biological ice nucleating particles from field observations over Amazonia. *J. Atmos. Sci.*, **78**, 2195–2220, https://doi.org/10.1175/JAS-D-20-0096.1.

——, and Coauthors, 2022: The influence of multiple groups of biological ice nucleating particles on microphysical properties of mixed-phase clouds observed during MC3E. *Atmos. Chem. Phys.*, **22**, 12 055–12 075, https://doi.org/10.5194/acp-22-12055-2022.

Pauluis, O., and S. Garner, 2006: Sensitivity of radiative–convective equilibrium simulations to horizontal resolution. *J. Atmos. Sci.*, **63**, 1910–1923, https://doi.org/10.1175/JAS3705.1.

Phillips, V. T. J., L. J. Donner, and S. T. Garner, 2007: Nucleation processes in deep convection simulated by a cloud-system-resolving model with double-moment bulk microphysics. *J. Atmos. Sci.*, **64**, 738–761, https://doi.org/10.1175/JAS3869.1.

——, P. J. DeMott, and C. Andronache, 2008: An empirical parameterization of heterogeneous ice nucleation for multiple chemical species of aerosol. *J. Atmos. Sci.*, **65**, 2757–2783, https://doi.org/10.1175/2007JAS2546.1.

——, and Coauthors, 2009: Potential impacts from biological aerosols on ensembles of continental clouds simulated numerically. *Biogeosciences*, **6**, 987–1014, https://doi.org/10.5194/bg-6-987-2009.

——, P. J. Demott, C. Andronache, K. A. Pratt, K. A. Prather, R. Subramanian, and C. Twohy, 2013: Improvements to an empirical parameterization of heterogeneous ice nucleation and its comparison with observations. *J. Atmos. Sci.*, **70**, 378–409, https://doi.org/10.1175/JAS-D-12-080.1.

——, A. Khain, N. Benmoshe, E. Ilotoviz, and A. Ryzhkov, 2015: Theory of time-dependent freezing. Part II: Scheme for freezing raindrops and simulations by a cloud model with spectral bin microphysics. *J. Atmos. Sci.*, **72**, 262–286, https://doi.org/10.1175/JAS-D-13-0376.1.

——, J. I. Yano, and A. Khain, 2017a: Ice multiplication by breakup in ice–ice collisions. Part I: Theoretical formulation. *J. Atmos. Sci.*, **74**, 1705–1719, https://doi.org/10.1175/JAS-D-16-0224.1.

——, and Coauthors, 2017b: Ice multiplication by breakup in ice–ice collisions. Part II: Numerical simulations. *J. Atmos. Sci.*, **74**, 2789–2811, https://doi.org/10.1175/JAS-D-16-0223.1.

——, S. Patade, J. Gutierrez, and A. Bansemer, 2018: Secondary ice production by fragmentation of freezing drops: Formulation and theory. *J. Atmos. Sci.*, **75**, 3031–3070, https://doi.org/10.1175/JAS-D-17-0190.1.

——, and Coauthors, 2020: Multiple environmental influences on the lightning of cold-based continental cumulonimbus clouds. Part I: Description and validation of model. *J. Atmos. Sci.*, **77**, 3999–4024, https://doi.org/10.1175/JAS-D-19-0200.1.

Qu, Z., and Coauthors, 2023: The impacts of secondary ice production on microphysics and dynamics in tropical convection. *EGUsphere*, https://doi.org/10.5194/egusphere-2022-235, in press.

Skamarock, W. C., J. B. Klemp, J. Dudhia, D. O. Gill, D. M. Barker, W. Wang, and J. G. Powers, 2005: A description of the Advanced Research WRF version 2. NCAR Tech. Note NCAR/TN-468+STR, 88 pp., https://doi.org/10.5065/D6DZ069T.

Sotiropoulou, G., S. Sullivan, J. Savre, G. Lloyd, T. Lachlan-Cope, A. M. Ekman, and A. Nenes, 2020: The impact of secondary ice production on Arctic stratocumulus. *Atmos. Chem. Phys.*, **20**, 1301–1316, https://doi.org/10.5194/acp-20-1301-2020.

Takahashi, T., 1978: Riming electrification as a charge generation mechanism in thunderstorms. *J. Atmos. Sci.*, **35**, 1536–1548, https://doi.org/10.1175/1520-0469(1978)035<1536:REAACG>2.0.CO;2.

Twomey, S., and T. A. Wojciechowski, 1969: Observations of the geographical variation of cloud nuclei. *J. Atmos. Sci.*, **26**, 648–651, https://doi.org/10.1175/1520-0469(1969)26<648:OOTGVO>2.0.CO;2.

Vali, G., 1994: Freezing rate due to heterogeneous nucleation. *J. Atmos. Sci.*, **51**, 1843–1856, https://doi.org/10.1175/1520-0469(1994)051<1843:FRDTHN>2.0.CO;2.

——, 2008: Repeatability and randomness in heterogeneous freezing nucleation. *Atmos. Chem. Phys.*, **8**, 5017–5031, https://doi.org/10.5194/acp-8-5017-2008.

——, 2014: Interpretation of freezing nucleation experiments: Singular and stochastic; sites and surfaces. *Atmos. Chem. Phys.*, **14**, 5271–5294, https://doi.org/10.5194/acp-14-5271-2014.

——, and E. J. Stansbury, 1966: Time-dependent characteristics of the heterogeneous nucleation of ice. *Can. J. Phys.*, **44**, 477–502, https://doi.org/10.1139/p66-044.

Vonnegut, B., and M. Baldwin, 1984: Repeated nucleation of a supercooled water sample that contains silver iodide particles. *J. Climate Appl. Meteor.*, **23**, 486–490, https://doi.org/10.1175/1520-0450(1984)023<0486:RNOASW>2.0.CO;2.

Waman, D., S. Patade, A. Jadav, A. Deshmukh, A. K. Gupta, V. T. J. Phillips, A. Bansemer, and P. J. DeMott, 2022: Dependencies of four mechanisms of secondary ice production on cloud-top temperature in a continental convective storm. *J. Atmos. Sci.*, **79**, 3375–3404, https://doi.org/10.1175/JAS-D-21-0278.1.

Westbrook, C. D., and A. J. Illingworth, 2013: The formation of ice in a long-lived supercooled layer cloud. *Quart. J. Roy. Meteor. Soc.*, **139**, 2209–2221, https://doi.org/10.1002/qj.2096.

Wright, T. P., and M. D. Petters, 2013: The role of time in heterogeneous freezing nucleation. *J. Geophys. Res. Atmos.*, **118**, 3731–3743, https://doi.org/10.1002/jgrd.50365.

Xie, S., Y. Zhang, S. E. Giangrande, M. P. Jensen, R. McCoy, and M. Zhang, 2014: Interactions between cumulus convection and its environment as revealed by the MC3E sounding array. *J. Geophys. Res. Atmos.*, **119**, 11 784–11 808, https://doi.org/10.1002/2014JD022011.

Yano, J.-I., and V. T. J. Phillips, 2011: Ice–collisions: An ice multiplication process in atmospheric clouds. *J. Atmos. Sci.*, **68**, 322–333, https://doi.org/10.1175/2010JAS3607.1.

Yau, M. K., and R. R. Rogers, 1996: *A Short Course in Cloud Physics*. 3rd ed. Elsevier, 304 pp.

Zhao, X., X. Liu, V. T. Phillips, and S. Patade, 2021: Impacts of secondary ice production on Arctic mixed-phase clouds based on ARM observations and CAM6 single-column model simulations. *Atmos. Chem. Phys.*, **21**, 5685–5703, https://doi.org/10.5194/acp-21-5685-2021.

Supplemental Material

Effects from time dependence of ice nucleus activity for contrasting cloud types

Deepak Waman[*1], Akash Deshmukh[1], Arti Jadav[1], Sachin Patade[1], Martanda Gautam[1], Vaughan Phillips[1], Aaron Bansemer[2], Jonas Jakobsson[3]

[1]Department of Physical Geography and Ecosystem Science, Lund University, Lund, Sweden

[2]National Center for Atmospheric Research, Boulder, Colorado, USA

[3]Division of Nuclear Physics, Department of Physics, Lund University, Lund, Sweden

*Corresponding author

Deepak Waman, Lund University, Sweden

email: deepak.waman@nateko.lu.se

Figure 1-3 shows the time-height profiles of water contents of microphysical properties such as cloud-liquid, cloud-ice, snow, graupel and rain for the simulated APPRAISE clouds. From Fig. 1a, it is predicted that liquid water exists at lower levels (between 0.3 to 1.5 km) over a period of day. In the second half of the simulation, two distinct cloud layers are seen at levels between about 0.3 and 1.5 km and between 2.5 to 3.9 km, whereas the atmosphere is subsaturated at levels between 1.5 and 2.5 km. The cloud layer near the surface (0.3 to 1.5 km) is saturated with respect to liquid water, whereas the layer near cloud-top (2.5 to 3.9 km) is predicted to contain both liquid water and ice.

In all the simulated cases (APPRAISE, ACAPEX and MC3E) (Fig. 1-3), it is predicted that the atmosphere is nearly saturated and both liquid and ice phase coexist. In all these simulated cases, it is evident that ice-crystals nucleated (through heterogeneous and/or homogeneous freezing) grow to snow following vapor diffusion which may rime to form graupel (Fig. 1-3). This snow and graupel may melt once it reaches levels warmer than freezing level (0°C) or precipitate on its own (Fig. 1-3). Moreover, water content of snow and graupel is predicted to be about 1-2 orders of magnitude higher in the simulated ACAPEX and MC3E clouds (characterized by strong vertical velocities) compared to that in APPRAISE clouds. Which signifies that the ice-crystal process is the dominant process of precipitation formation in ACAPEX and MC3E clouds at all subzero levels.

Fig. 1: Time-height profiles of the domain averaged water contents of (a) cloud-liquid, (b) cloud-ice, (c) snow, (d) graupel, and (e) rain for the simulated APPRAISE clouds on 18 February 2009 between 00:00 and 24:00 UTC. All the water contents are in log scale.

Fig. 2. Time-height profiles of the domain averaged water contents of (a) cloud-liquid, (b) cloud-ice, (c) snow, (d) graupel, and (e) rain for the simulated ACAPEX clouds on 07 February 2015 between 19:15 and 22:15 UTC. All the water contents are in log scale.
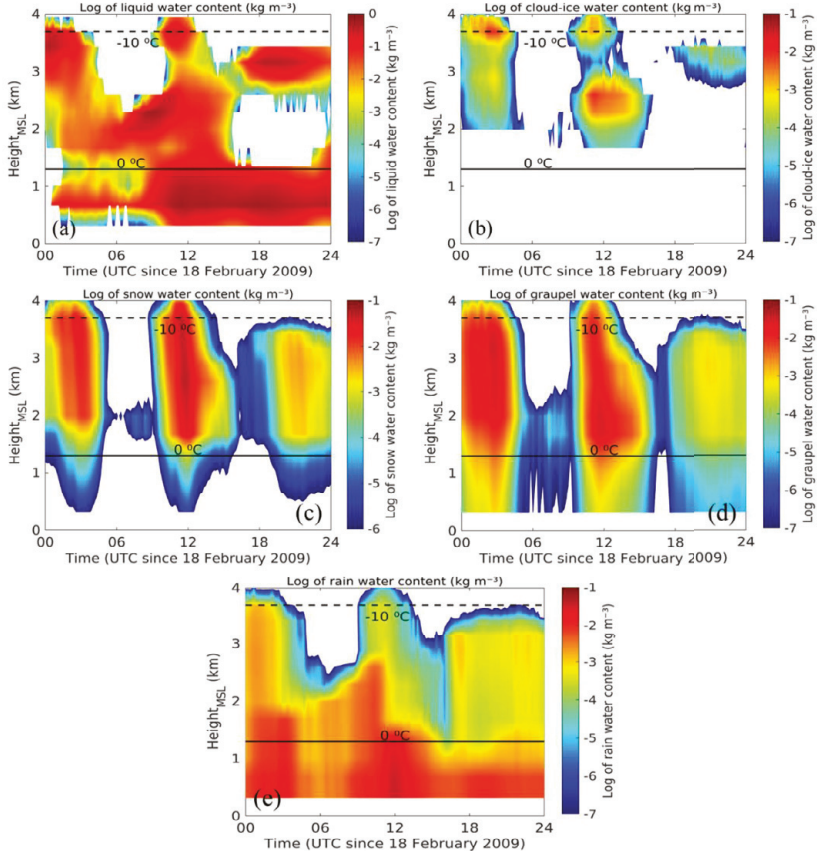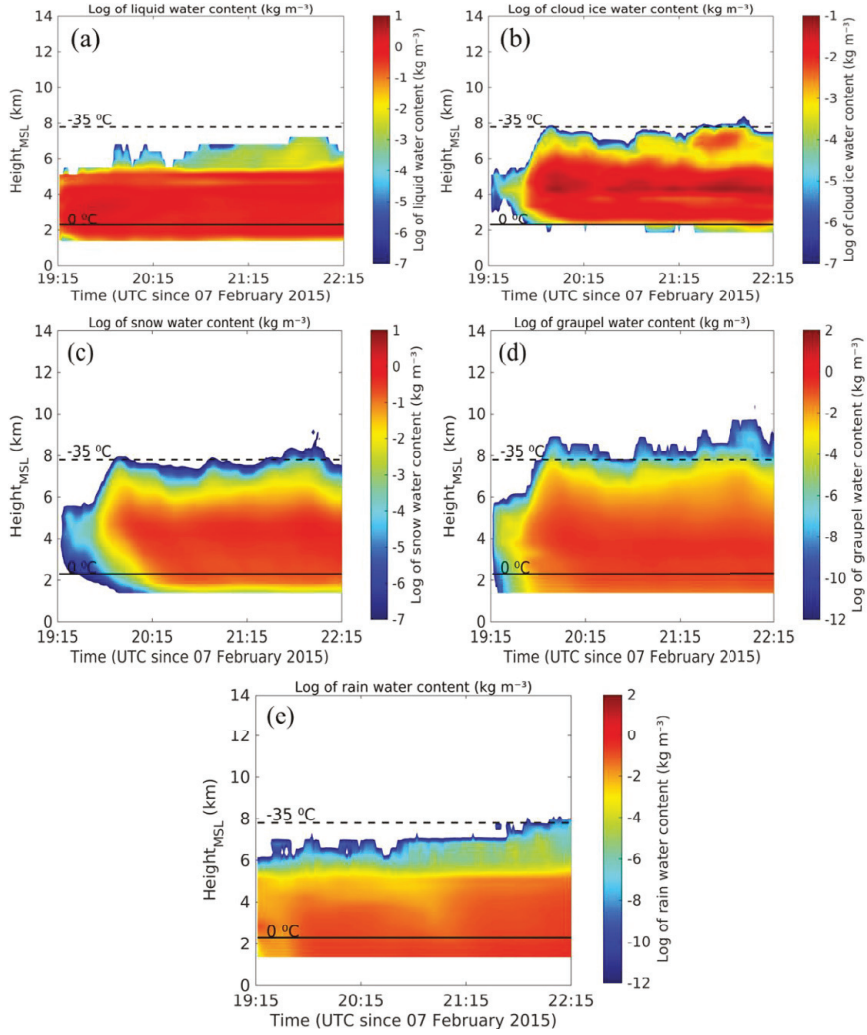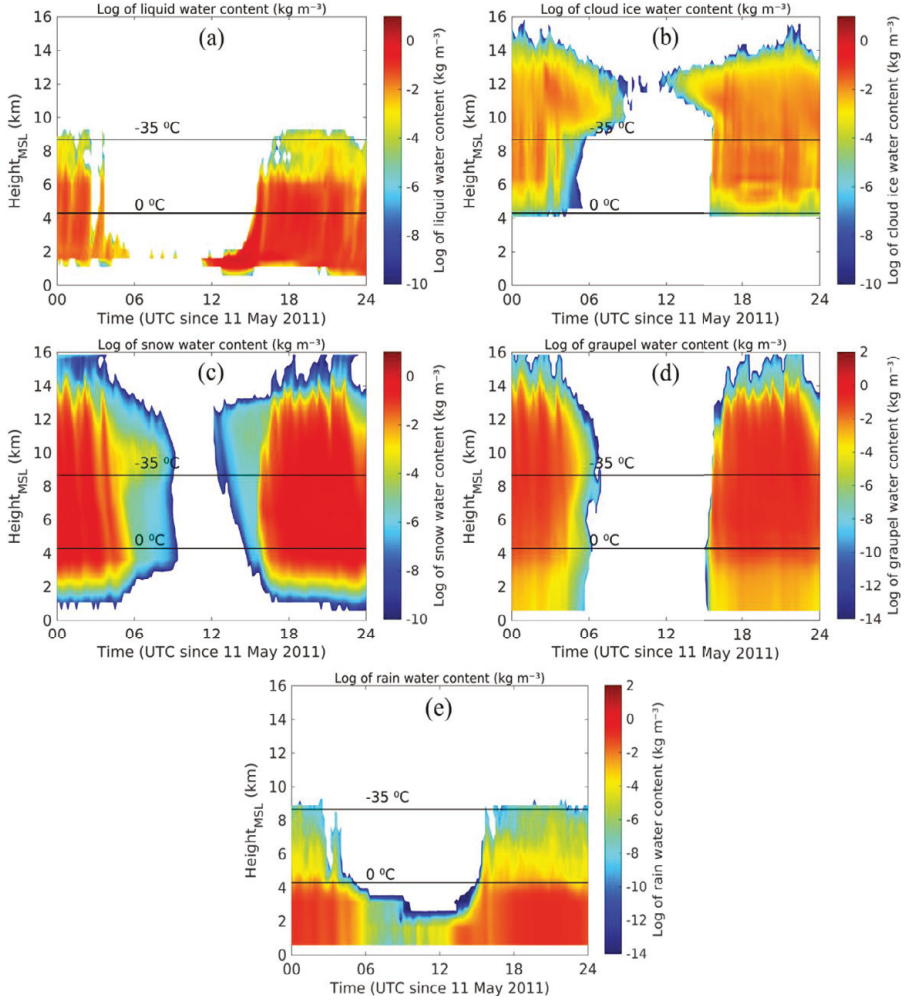
Fig. 3: Time-height profiles of the domain averaged water contents of (a) cloud-liquid, (b) cloud-ice, (c) snow, (d) graupel, and (e) rain for the simulated APPRAISE clouds on 11 May 2011 between 00:00 and 24:00 UTC. All the water contents are in log scale.

Paper 3

Dependencies of Four Mechanisms of Secondary Ice Production on Cloud-Top Temperature in a Continental Convective Storm

DEEPAK WAMAN,[a] SACHIN PATADE,[a] ARTI JADAV,[a] AKASH DESHMUKH,[a] ASHOK KUMAR GUPTA,[a,b]
VAUGHAN T. J. PHILLIPS,[a] AARON BANSEMER,[c] AND PAUL J. DEMOTT[d]

[a] Department of Physical Geography and Ecosystem Science, Lund University, Lund, Sweden
[b] Department of Earth and Environmental Sciences, Vanderbilt University, Nashville, Tennessee
[c] Mesoscale and Microscale Meteorology Laboratory, National Center for Atmospheric Research, Boulder, Colorado
[d] Department of Atmospheric Science, Colorado State University, Fort Collins, Colorado

ABSTRACT: Various mechanisms of secondary ice production (SIP) cause multiplication of numbers of ice particle, after the onset of primary ice. A measure of SIP is the ice enhancement ratio ("IE ratio") defined here as the ratio between number concentrations of total ice (excluding homogeneously nucleated ice) and active ice-nucleating particles (INPs). A convective line observed on 11 May 2011 over the Southern Great Plains in the Mesoscale Continental Convective Cloud Experiment (MC3E) campaign was simulated with the "Aerosol–Cloud" (AC) model. AC is validated against coincident MC3E observations by aircraft, ground-based instruments, and satellite. Four SIP mechanisms are represented in AC: the Hallett–Mossop (HM) process of rime splintering, and fragmentation during ice–ice collisions, raindrop freezing, and sublimation. The vertical profile of the IE ratio, averaged over the entire simulation, is almost uniform (10^2 to 10^3) because fragmentation in ice–ice collisions dominates at long time scales, driving the ice concentration toward a theoretical maximum. The IE ratio increases with both the updraft (HM process, fragmentation during raindrop freezing, and ice–ice collisions) and downdraft speed (fragmentation during ice–ice collisions and sublimation). As reported historically in aircraft sampling, IE ratios were predicted to peak near 10^3 for cloud-top temperatures close to the $-12°C$ level, mostly due to the HM process in typically young clouds with their age less than 15 min. At higher altitudes with temperatures of $-20°$ to $-30°C$, the predicted IE ratios were smaller, ranging from 10 to 10^2, and mainly resulted from fragmentation in ice–ice collisions.

KEYWORDS: Aerosols; Cloud microphysics; Ice particles; Clouds

1. Introduction

Hydrometeors in the atmosphere are either liquid or ice. Ice particles in clouds affect precipitation, radiative transfer, and cloud electrification (Rangno and Hobbs 2001; Cantrell and Heymsfield 2005). Mechanisms of ice initiation, which remain uncertain (Cantrell and Heymsfield 2005; Field et al. 2017), are fundamental for the climate. Precipitation globally is associated with the ice phase (Field and Heymsfield 2015) and controls cloud extent.

There are two possible mechanisms for precipitation production, and one of these is the "ice-crystal process," which involves the vapor growth of ice crystals to form snow (Yau and Rogers 1996). This snow may rime to form graupel which might subsequently melt to form ("cold") rain. The other process for precipitation formation involves the coalescence of cloud droplets to form "warm" rain ("warm rain process"), which may precipitate on its own, or freeze to form graupel that may also subsequently melt (e.g., Phillips et al. 2001; Sun et al. 2012). Note that the terms "warm" and "cold" applied to precipitation do not refer to its temperature but rather to its mechanism of origin.

Above the freezing level, formation of the first ("primary") ice requires activity of ice-nucleating particles (INPs) for precipitating clouds with tops warmer than $-36°C$. Active INPs are rare

with concentrations typically between about 10^{-5} and $1 \, L^{-1}$ near $-10°C$ (Hobbs 1969; DeMott et al. 2003; Möhler et al. 2005; Lasher-Trapp et al. 2016). It is commonly observed that in natural convective clouds with tops warmer than about $-36°C$, concentrations of ice are up to a factor of 10^4 higher than those of available active INPs (e.g., Harris-Hobbs and Cooper 1987; Jackson et al. 2018; Lasher-Trapp et al. 2021). For example, with modern optical probes and processing algorithms that eliminate any bias from artificial shattering (Field et al. 2006; Korolev et al. 2011), Ladino et al. (2017) observed that the discrepancy between number concentrations of active INP and total ice remains. Several similarly accurate studies of tropical cumulus clouds such as those by Lawson et al. (2015), Lasher-Trapp et al. (2016, 2021), and Huang et al. (2017) reported rapid glaciation in clouds with tops much warmer than $\sim-18°C$, with abundant ice.

It has long been proposed that some processes must exist following initial primary ice nucleation to enhance the number and mass concentration of ice. Such processes are termed "secondary ice production" (SIP) mechanisms (Langmuir 1948; Hobbs 1969). They are envisaged to create positive feedbacks with growth of fragments to form fragmenting precipitation ("ice multiplication"). In a recent study, Zhao and Liu (2021) included various SIP mechanisms in a global climate model with improved simulation of liquid and ice water paths. SIP mechanisms can alter the cloud properties, such as precipitation rate, cloud lifetime, glaciation, and electrification (e.g., Crawford et al. 2012; Lawson et al. 2015; Lasher-Trapp et al. 2016, 2021;

Phillips et al. 2017b, 2018, 2020; Sotiropoulou et al. 2021; Georgakaki et al. 2022).

Secondary ice production mechanisms

Various known SIP mechanisms in natural clouds depend on parameters such as vertical velocity, temperature, and particle size distributions (PSDs). As reviewed by Field et al. (2017), there are several possible SIP mechanisms:

1) The Hallett–Mossop ("HM"; Hallett and Mossop 1974) process of rime splintering
2) Fragmentation during ice–ice collisions (Vardiman 1978; Takahashi et al. 1995)
3) Shattering of freezing rain or drizzle, also including that of incident branched crystals in drop–ice collisions (e.g., Dye and Hobbs 1968)
4) Fragmentation during sublimation (e.g., Oraltay and Hallett 1989)
5) SIP production due to activation of INPs during transient fluctuations of supersaturation in wakes of warm precipitation particles (e.g., Prabhakaran et al. 2019)

The HM process is one of several known SIP mechanisms in which small ice splinters break away during riming of supercooled cloud droplets $> 24\ \mu$m, for the temperature range of $-3°$ to $-8°$C. At temperatures warmer than $-3°$C supercooled droplets do not form an ice shell (Dong and Hallett 1989). When colder than $-8°$C, their ice shells are hard to break by the internal pressure (Griggs and Choularton 1983). Field observations (Harris-Hobbs and Cooper 1987; Blyth and Latham 1993; Patade et al. 2016; Jackson et al. 2018; Lasher-Trapp et al. 2021) and numerical modeling (Blyth and Latham 1997; Huang et al. 2017; Gayatri et al. 2022; Lasher-Trapp et al. 2021) of cumulus clouds with warm cloud tops ($> -20°$C) showed that HM process can account for the observed high concentration of ice.

Yet several laboratory and field studies (Vardiman 1978; Takahashi et al. 1995; reviewed by Phillips et al. 2017a,b, 2021) have observed the fragmentation of ice particles in collisions. Takahashi et al. (1995) measured maximum ice production from ice–ice collisions at about $-16°$C. From field observations, Hobbs (1972) concluded that fragmentation in graupel–dendrite collisions might cause ice enhancement. Modeling studies such as those by Fridlind et al. (2007) (crystal–crystal collision), Yano and Phillips (2011) (graupel–graupel collisions), Phillips et al. (2017a) (all ice–ice collisions involving crystal, snow, and graupel), Sotiropoulou et al. (2021), and Zhao et al. (2021) reported fragmentation during ice–ice collisions. To simulate SIP during any ice–ice collision, Phillips et al. (2017a,b) developed a theoretical formulation based on the principle of energy conservation. The number of secondary fragments from a collision depends on the initial kinetic energy and habits of the colliding ice particles, which depend on factors such as temperature, particle size, and riming intensity of ice particles.

Another SIP mechanism active in clouds is shattering of freezing rain or drizzle, as seen in laboratory studies (Johnson and Hallett 1968; Pruppacher and Schlamp 1975; Leisner et al. 2014; Keinert et al. 2020). The liquid may get trapped inside an ice shell during raindrop freezing. Due to the density difference of ice and water, the excess pressure builds up in the trapped water, and if it exceeds a threshold during freezing, the external ice shell breaks, and spikes and fragments may get emitted. Aircraft observations by Rangno (2008) and Lawson et al. (2015) of frozen fragments of ice were consistent with fracturing of frozen raindrops. Phillips et al. (2018) provided an empirical formulation for secondary fragments from raindrop freezing, using laboratory observations only of drops in free-fall [section 2b(2)]. No laboratory observations of electrodynamically levitated drops were used, as Phillips et al. (2018) argued that the natural fall behavior governs the spherical symmetry of latent heat loss to the air, the ice shell geometry and hence the fragmentation in real clouds. Keinert et al. (2020) confirmed this.

Another idea is that ice formation upon collision of an ice crystal with a supercooled raindrop is seen to cause a breakup of the crystal (Dye and Hobbs 1968; King and Fletcher 1976a,b). We view this as an aspect of raindrop freezing fragmentation. It is already implicitly treated in part by our raindrop freezing fragmentation scheme (Phillips et al. 2018) since it is based on laboratory observations of raindrops that partly freeze in collisions with ice crystals. However, this process is not yet well understood.

Ice multiplication may also occur during sublimation of ice particles in subsaturated cloudy regions, as seen in laboratory studies (Oraltay and Hallett 1989; Dong et al. 1994; Bacon et al. 1998). Oraltay and Hallett (1989) observed that when the relative humidity over ice (RH$_i$) is less than 70% at subzero temperature, dendritic ice crystals break up. Dong et al. (1994) observed fragmentation of rimed ice particles during sublimation. Deshmukh et al. (2022) formulated fragmentation during the sublimation of dendritic crystals and rimed ice particles such as graupel based on these laboratory studies. Sublimation breakup can be significant in deep convective descent (Deshmukh et al. 2022).

Activation of preexisting INPs (Prabhakaran et al. 2019) in transient supersaturations in the wake of a warm falling hydrometeor, has been hypothesized in view of laboratory observations of activation of cloud condensation nuclei (CCN) (Prabhakaran et al. 2020) and numerical modeling of supersaturation fluctuations (Chouippe et al. 2019). We have chosen not to represent this mechanism since any high humidity above water saturation would first initiate a droplet around the INP, only activating it in a freezing mode. The high ambient relative humidity would then be expected to become irrelevant to the ice nucleation.

Aircraft observations of nimbostratus clouds over China by Yang et al. (2014) proposed several SIP mechanisms (the HM process, fragmentation in ice–ice collisions, raindrop freezing fragmentation) responsible for high ice particle number concentrations in such clouds. They showed that between $-10°$ and $-15°$C levels, the prominent SIP mechanism was likely dendritic crystal–crystal collisions. Images of irregularly shaped ice crystals between $-3°$ and $-10°$C suggested that drizzle/rain shattering along with the HM process are prolific.

Lawson et al. (2015) and Phillips et al. (2018) suggested that raindrop freezing fragmentation and the HM process could explain the rapid glaciation in tropical cumulus clouds with broad drop size distribution (DSD). By simulating the

HM process and fragmentation in ice–ice collisions, Sullivan et al. (2017) predicted the enhancement in number concentrations of ice particles by up to 10^4 relative to all ice from INP activity and delineated that the maximum ice enhancement occurred at moderate ascent speeds and moderate aerosol loadings. The study by Zhao et al. (2021) suggested that the dominant SIP mechanism in Arctic mixed-phase clouds is fragmentation during freezing of raindrops. This suggests that the role of each SIP mechanism in producing high ice number concentrations varies greatly with cloud types.

A major challenge for successful representation of cloud microphysical properties is the accurate prediction of number concentrations of ice particles by inclusion of SIP. Recent cloud models can predict two moments of the size distribution (both mass and number mixing ratio), and the most advanced discretize it with bins. SIP has received less attention than heterogeneous ice nucleation (Pruppacher and Klett 1997, hereafter PK97; Field et al. 2017).

The term we use here to quantify the effect of SIP on overall ice concentrations is "ice enhancement (IE) ratio." Hobbs et al. (1980, hereafter H80) defined as the ratio of the average ice concentration at any in-cloud level to the concentration of INPs active at cloud top. Figure 1 shows the IE ratio observed by the aircraft from H80, averaged for small cumulus, cumulus complexes, and embedded cumulus clouds. The geometric mean of the plotted IE ratios can be as large as 10^4 to 10^5 and generally decreases with decreasing cloud-top temperatures aloft, with a slight peak near $-12°C$.

The Optical Array Probe (OAP) has been widely used to measure sizes and concentrations of ice particles over the decades. Such aircraft probes have been biased by artificial shattering on impact, generating numerous tiny ice crystals less than 100 μm. Field et al. (2006) showed that short interarrival times indicate artificially fragmented ice particles. Korolev et al. (2011) made observations by mounting both shatter-corrected and unmodified probes on the same flight. It was observed that the artificial fragmentation was prone in ice particles smaller than 0.2–0.5 mm. Instead of OAPs, H80 used a formvar particle sampler typically mounted in a long decelerator tube ($\sim$1 m $\times$ 0.1 m) to minimize any shattering bias (Hobbs et al. 1971). However, it is unknown whether any shattering bias contaminated their data (Fig. 1). Also, there was less understanding then of contamination issues in measuring active INP concentrations with filter papers (H80).

Considering the uncertainties in the relationship between ice enhancement and cloud-top temperature in such observations, it is vital to investigate the role of various SIP mechanisms in ice enhancement using model simulations. Here we present a modeling study of continental, deep convective clouds to investigate the role of four SIP mechanisms (the HM process of rime splintering, and fragmentation during raindrop freezing, ice–ice collisions, and sublimation) in ice enhancement using the Aerosol–Cloud (AC) model. To our knowledge, this is the first time that all four SIP mechanisms have been included in a cloud model. Using AC, we also investigated the dependency of ice production from these SIP mechanisms on cloud-top temperature. This study elucidates the time evolution of activities of the four SIP mechanisms and their onset
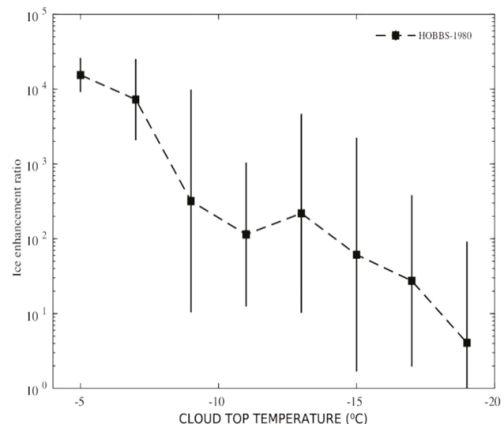
FIG. 1. Ice enhancement ratio (geometric mean), as a function of cloud-top temperature for updraft region (from H80, with changes).

times in the deep convection. Whereas a few earlier studies have observed SIP in maritime convective clouds (e.g., Heymsfield and Willis 2014; Lawson et al. 2015; Lloyd et al. 2020), the present study is focused solely on continental convective clouds.

2. Description of field campaign and observations

a. Description of case

The Midlatitude Continental Convective Cloud Experiment (MC3E) project was jointly led by the U.S. Department of Energy (DOE) Atmospheric Radiation Measurements (ARM) program and the National Aeronautics and Space Administration's (NASA) Global Precipitation Measurement (GPM) mission. It made observations for a total of 15 data missions focusing at and around the DOE ARM, Southern Great Plains (SGP) Central Facility (CF), and in north-central Oklahoma from 22 April to 6 June 2011. Data were collected from airborne and ground-based measurement (Jensen et al. 2016).

The Real-Time Mission Monitor (RTMM; Blakeslee et al. 2007) image (Fig. 2a) shows a radar picture of the simulated mesoscale convective system (MCS). The MCS was moving to the northeast (Jensen et al. 2016). The Citation aircraft sampled cloud bases only at takeoff and landing, mostly targeting the trailing stratiform region of the MCS. The aircraft observations were preliminary taken between 1800 and 2100 UTC as the system moved to the trailing stratiform mode as it passed over the CF (Jensen et al. 2016).

Figure 3 shows the observed profiles of initial air and dewpoint temperatures at 0000 UTC 10 May 2011. The lifting condensation level (LCL) was at 796 hPa. The case simulated here is the line of convective clouds observed in MC3E from 0900 to 2400 UTC 11 May 2011. It consisted of many cloud types, with deep convective clouds (e.g., cumulonimbi) with depths of 9–13 km and stratiform clouds. Convective clouds had relatively warm bases ($\sim$17°C) at about 1.5 km altitude above mean sea level (MSL). The ground level was about 350 m MSL. The case
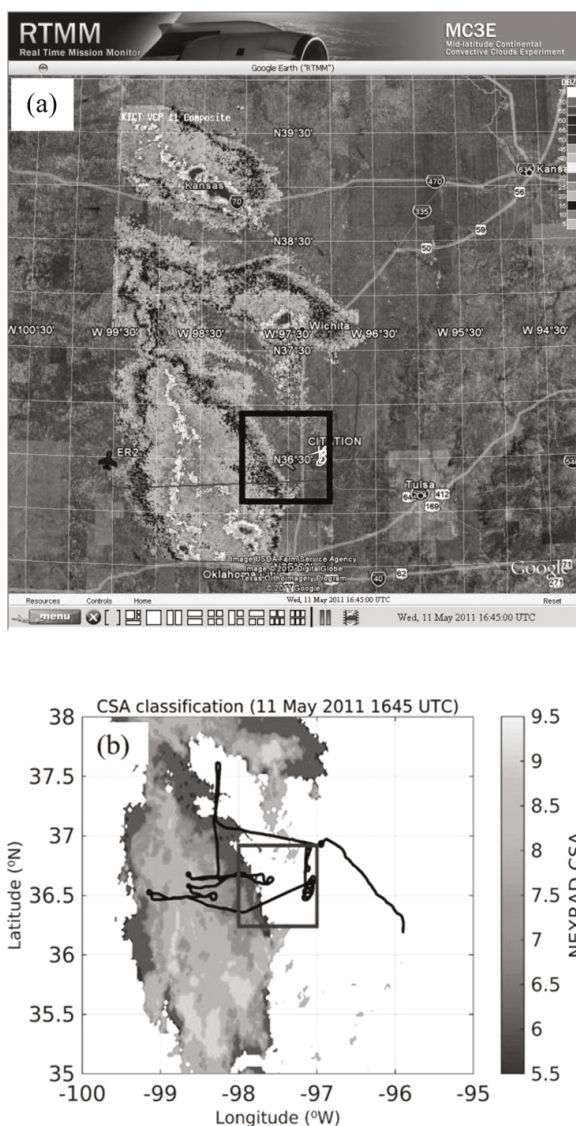
FIG. 2. (a) RTMM image during MC3E field campaign showing a plan position indicator of radar reflectivity from KICT radar at 1645 UTC with flight positions of citation (white line) and ER-2 aircraft (red line) (adapted from https://ghrc.nasa.gov/hydro), (b) convective–stratiform–anvil (CSA)-classified deep convective systems and Citation aircraft flight track (plotted for the entire flight duration, black line) superimposed on it for the simulated day of the MC3E at 1645 UTC. The CSA classification is based on Feng et al. (2011) (thick anvil: 5.5–7.5; stratiform: 7.5–8.5; convective: 8.5–9.5). The black boxes in (a) and (b) indicate the simulation domain.
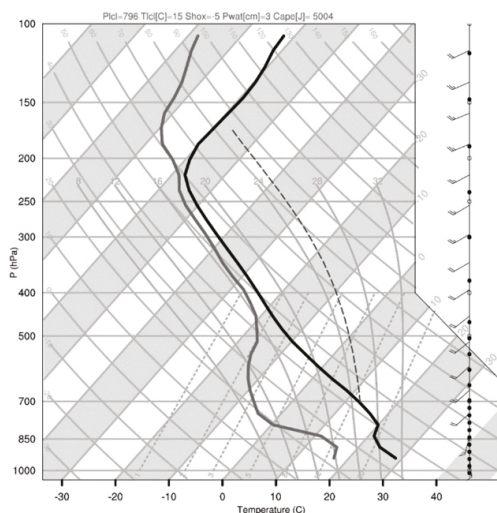
FIG. 3. Initial vertical dewpoint and temperature profiles at 0000 UTC 10 May 2011. A solid gray line represents the dewpoint, and a solid black line represents the air temperature. The thin dotted gray line indicates the moist adiabat.

had a high convective available potential energy (CAPE) (4000–5000 J kg^{-1}, Fig. 3) near the beginning of the simulated period (after 0000 UTC 10 May) when the lower troposphere was moistened by large-scale advection.

1) AIRBORNE MEASUREMENTS

Figures 2a and 2b show flight tracks of NASA ER-2 (red) and University of North Dakota (UND) Cessna Citation II (black) jet aircraft which were operational at 1645 UTC 11 May 2011 during the MC3E campaign. The optical probes (Table 1) carried by the UND Citation aircraft made measurements of in-cloud ice number concentrations, liquid water content (LWC), drop size and concentrations at altitudes between melting level and cloud top (~4–13 km).

The size and concentrations of droplets and LWC were measured by the cloud droplet probe (CDP). The Nevzorov and King hot-wire probes also measured the LWC during the MC3E campaign. However, these two probes were sensitive to ice in subsaturated regions, and conceivably also to any rain at warmer levels, so both probes were not used at all in the present study.

Moreover, the 2D cloud probe (2DC), cloud imaging probe (CIP), and high-volume precipitation spectrometer, version 3 (HVPS-3) were used to measure the ice concentration (Table 1). The combine spectrum ("COMB") uses the 2DC (or CIP) PSDs merged with the HVPS-3. During the aircraft measurements in MC3E, the 2DC and the HVPS-3 probes had "shattering corrected" tips, while the CIP was without any such antishatter tips. The 2DC and CIP probes used during the MC3E campaign were not able to measure particle size

TABLE 1. Instruments mounted on the Citation aircraft (Jensen et al. 2016).

Instrument	Range used
2DC	0.2–1.0 mm
CIP	0.2–1.5 mm
HVPS-3	0.2–19.2 mm
CDP	2–20 μm

and concentration in the size range of 50–200 μm accurately due to their coarse resolution (about 30 μm per pixel). To minimize the shattering of ice on the aircraft probes, shattered particles were identified and removed following the method described by Field et al. (2006) and Korolev et al. (2011). Only ice particles with a maximum size dimension >200 μm (NI$_{200}$) were included in plotted ice concentrations both in the simulation and observations to minimize any further shattering bias. However, in rest of the manuscript (other than model validation) the number concentrations of simulated ice include particles of all size ranges.

Furthermore, from Table 1, the impression that there is a measurement gap between particles of diameters between 50 (CDP maximum size) and 200 μm (2DC minimum size used). However, the coarse resolution of these probes and splashing of drops and shattering of ice can leave large uncertainties in the size range of 50–200 μm. Furthermore, the MC3E campaign did not use the Two-Dimensional Stereo (2DS) probe which could have measured particles in this size range, reasonably with 10 μm resolution. In addition to this, there are two extra sources of uncertainties associated with these probes i.e., optical response (since most of the small particles are out of focus) and electronic response. Though the limitation is there for measuring small particles, these optical probes (2DC and CIP) are still capable of measuring particles larger than 200 μm and most of the ice mass in convective clouds is typically in the larger size ranges (>200 μm). Moreover, the unfiltered 2DC size distribution plotted at levels near cloud base is consistent with that expected from the CDP size distribution (not shown here).

The Geostationary Operational Environmental Satellite (GOES) and Visible Infrared Solar-Infrared Split-Window Technique (VISST) measured the radiative fluxes at the top of the atmosphere (TOA).

Figure 4 shows PSD and corresponding images from the 2DC, CIP, and HVPS-3 probes at different in-cloud levels. The PSD changes from the cloud base (~17°C) to the upper half of the mixed-phase region, and corresponding images from the 2DC, CIP, and HVPS-3 probes at different in-cloud levels are shown in Fig. 4. Particles smaller than 200 μm are omitted from the PSDs because of the possibility of spurious fragments from artificial shattering on impact with the aircraft probes, which the antishatter tips might not fully eliminate (Field et al. 2006; Korolev et al. 2011) and poor time response of these probes at those smaller sizes (Gurganus and Lawson 2018). From these images (Figs. 4b,d), it can be seen that average size of particles (<1 mm) generally increases with height above cloud base (17°C) up to the −20°C level. The
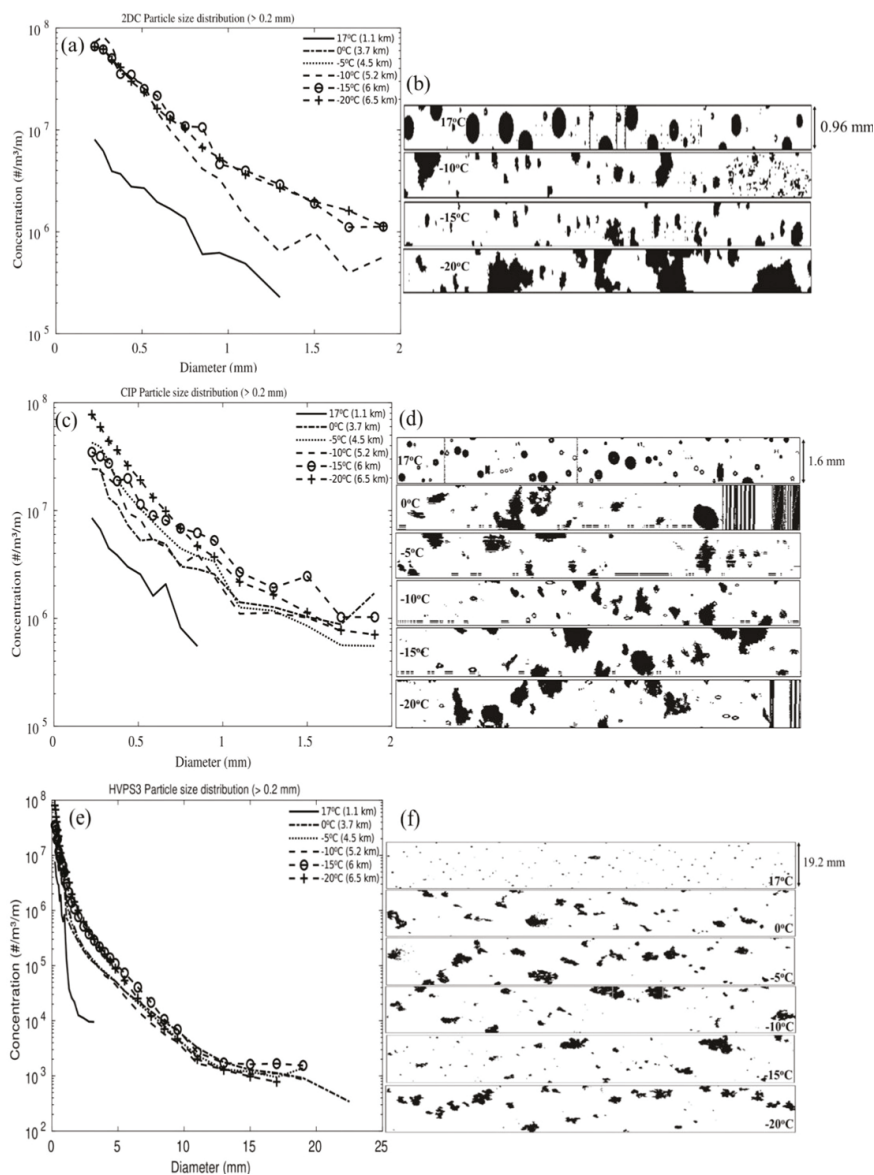
FIG. 4. (left) Particle size distribution for particles bigger than 0.2 mm and (right) corresponding images at various in-cloud levels from the (a),(b) 2DC, (c),(d) CIP, and (e),(f) HVPS3 probes on 11 May 2011 during MC3E.

warmest levels displayed correspond to mostly convective clouds whereas the colder levels are dominated by stratiform clouds.

Good agreement can be seen between PSDs from the 2DC probe (Fig. 4a) and CIP (Fig. 4c) for overlapping size bins.

The PSD generally broadens with decreasing subzero temperature, indicating numerous larger ice particles near the cloud top. There was the presence of raindrops (0.5 to 1 mm) near the cloud base as observed by the 2DC imagery. The 2DC and CIP images show the presence of aggregates and rimed

ice particles of diameter about 1 mm at levels colder than $-15°C$. Pristine ice crystals with diameters greater than 0.5 mm were relatively rare in the 2DC and CIP imagery, indicating the dominance of ice crystal growth by riming. Also, PSDs reveals that only ice particles are present among all detected particles bigger than 200 μm above the freezing level.

2) GROUND-BASED MEASUREMENTS

During the MC3E campaign, the CCN number concentration was measured by a CCN counter at seven supersaturation levels (Jefferson 2011; Uin 2016) at Lamont, Oklahoma ($\sim$300 m MSL). The predicted radar reflectivity is compared with the reflectivity measured by the Ka-band ARM zenith radar (KAZR).

Large-scale advective tendencies of heat and moisture ("large-scale forcing"), and the surface heat and moisture fluxes were all derived from the measurements by constrained variational analysis (Jensen et al. 2016). However, these advective tendencies might be biased due to advection of layer clouds in the simulated region, likely from the remote source, as Jensen et al. (2016) reported the presence of widespread stratiform clouds in the first peak (1800–2400 UTC 10 May). The presence of this layer cloud was not measured directly in the MC3E sounding, from which the large-scale forcing was derived.

b. Description of numerical model

This study used AC, and it has been previously used extensively (e.g., Phillips et al. 2017b, 2018, 2020).

AC represents clouds and aerosols with hybrid spectral bin–two-moment bulk microphysics, interactive radiation, and semiprognostic aerosol schemes (Phillips et al. 2007, 2009, 2017, 2020; Kudzotsa et al. 2016). AC uses emulated bin microphysics schemes to treat various microphysical processes such as homogeneous and primary ice initiation, SIP processes, and droplet activation (Phillips et al. 2007, 2008, 2009, 2013, 2015, 2017, 2018). The Weather Research and Forecasting (WRF) Model framework was used as a dynamical basis for schemes such as planetary boundary layer (PBL), dynamics, surface layer, and subgrid-scale mixing. AC follows the "two-moment" approach in which the total mass and number of each microphysical species are diffused and advected as bulk prognostic variables. This approach was extended for precipitation (Phillips et al. 2017b, 2020). Microphysical species are cloud liquid, cloud ice (or "crystals"), rain, snow, and graupel or hail. Prognostic variables were used to track ("tagging tracers") and estimate the mass and number concentrations of ice from each process of ice initiation (i.e., homogeneous freezing, primary and secondary) represented in the model. These variables are passive and do not interact with any other process in AC.

1) MODEL SETUP

The observed case of MCS has been simulated for a three-dimensional mesoscale domain of 40 × 40 grids with 2 km horizontal spacing with a time step of 10 s. A modeling study by Pauluis and Garner (2006) proved that in deep convective clouds, the statistics of vertical velocity and cloud properties

TABLE 2. Two-day-averaged (9 and 12 May) observed aerosol mass mixing ratios from IMPROVE observations used as input to AC at levels of about 350–700 m MSL. However, all PBAP observations are from Amazonia (Patade et al. 2021).

Aerosol species	Mass mixing ratio (μg m^{-3})
Ammonium sulfate	0.7
Sea salt	0.061
Mineral dust	0.175
Black carbon	0.25
Soluble organic (80% of total organic)	1.38
Insoluble organic (20% of total organic)	0.345
PBAP (50% of insoluble organic carbon)	
Fungi	0.067
Bacteria	0.023
Pollen	0.053
Detritus	0.029
Algae	4.3×10^{-5}

(e.g., ice concentration) can be adequately represented with 2 km horizontal resolution.

The simulation time is 72 h, from 0000 UTC 10 May to 0000 UTC 13 May 2011. The vertical model resolution is about 0.5 km at all levels. The lateral boundary conditions are periodic in both the east–west and north–south directions of the domain and updated hourly, since the aim was to study MCS over several days, requiring an idealized "cloud-system resolving" model framework. An "idealized mode" simulation was performed by adding random humidity perturbations of about $\pm 8 \times 10^{-4}$ kg kg^{-1} in the PBL. The large-scale forcing of advective tendencies of heat and moisture were applied following Xie et al. (2014). These tendencies were updated hourly with continuous interpolation over time in between. The temperature and humidity fields were nudged toward the observation at the lowest model level in the first 10 h of the simulation at the lowest model level in order to avoid an overshoot during the first peak of the simulation due to possible issues with the forcing [section 2a(2)] during the peak of the simulation.

Primary initiation of hydrometeors is governed by various aerosol particles (APs). These are ammonium sulfate, black carbon, sea salt, mineral dust, soluble and insoluble organics, and primary biological aerosol particles (PBAPs) group including, fungi, bacteria, detritus, pollen, and algae (Patade et al. 2021). AC predicts in-cloud aerosol size distribution (ASD) based on these APs (Table 2) and in-cloud supersaturation resolved on the model grid. The ASDs and resolved supersaturation are then input to the microphysics scheme to predict the number of cloud droplets and crystals nucleated (Phillips et al. 2017b).

Initial concentrations of APs are prescribed based on the Goddard Chemistry Aerosol Radiation and Transport (GOCART) model (Chin et al. 2000). Their vertical profiles were each rescaled by a constant factor to match with simultaneous measurements from the Interagency Monitoring of Protected Visual Environments (IMPROVE) at levels of stations (Ellis, Stilwell, and Wichita Mountains) near the simulated area. The present study used the IMPROVE aerosol mass

mixing ratios averaged for 9 and 12 May 2011. The rescaled initial mass mixing ratios of aerosol species are given in Table 2.

About 80% of the total organic carbon was assumed as soluble organic, and the remaining 20% was identified as insoluble organic carbon (Phillips et al. 2009). It was assumed that about 50% of insoluble organic aerosol particles were biological in origin. The contribution of these groups to the total PBAP mass is prescribed from the observations by Patade et al. (2021) over Amazonia (fungi: 39%; bacteria: 13%: pollen: 31%: detritus: 17%: algae: ~0.000 25%).

Droplets are activated both at cloud base (Ming et al. 2006) and by in-cloud droplet activation (Phillips et al. 2007, 2009). It depends on the size, number concentration, and chemistry of APs. AC predicts components of ASD of each APs that is immersed in (i) cloud particles and (ii) precipitation, and (iii) interstitial (Phillips et al. 2020).

The heterogeneous ice nucleation in AC takes place by APs such as mineral dust, black carbon, soluble organics, and PBAPs which predict INP activity from the "empirical parameterization" (EP) (Phillips et al. 2008, 2013). The EP represents all modes of INP activity such as contact freezing (outside-in and inside-out), deposition and immersion/condensation freezing, and heterogeneous raindrop freezing. Activation of ice crystals by these primary modes depend on temperature, supersaturation, and surface area mixing ratio for each APs.

There are two types of homogeneous freezing: cloud liquid/rain and solute aerosols (Phillips et al. 2007, 2009). Homogeneous freezing of cloud droplets near −36°C is treated by representing the preferential evaporation of smaller cloud droplets in the size distribution with a lookup table depending on the ascent and supersaturation in the mixed-phase updraft immediately below. This lookup table represents the fact that the larger cloud droplets freeze first homogeneously during ascent through the narrow temperature band of homogeneous freezing (e.g., PK97), with onset of supersaturation with respect to liquid causing the remainder to evaporate without freezing (Phillips et al. 2007).

2) REPRESENTATION OF SIP MECHANISMS IN AC

Four types of SIP mechanisms are treated in AC. These are as follows:

1) The HM process of rime splintering

The formation of secondary ice in the HM process depends on droplet size and temperature levels in the clouds (Hallett and Mossop 1974). Splinters of small ice particles are emitted during riming of supercooled cloud droplets (>24 μm) at levels between −3° and −8°C. The production rate of HM splinters is maximal at −5°C level. The HM process in AC is treated with a factor multiplying the fragment emission rate (350 splinters at −5°C mg^{-1} of rime) that depends on the mean cloud-droplet size (zero below 16 μm and unity above 24 μm, linearly interpolated in between).

2) Fragmentation in ice–ice collisions

AC can generate secondary ice by fragmentation in ice–ice collisions. AC treats fragmentation in all types of ice particle collisions (Phillips et al. 2017a) with dependencies on temperature, ice morphology/size, and collision

kinetic energy. The formulation of the fragmentation in ice–ice collisions is based on the principle of conservation of energy. Theoretically unknown parameters governing numbers of fragments emitted per collision are from field and laboratory studies by Vardiman (1978) and Takahashi et al. (1995). More details are from Phillips et al. (2017a, 2021).

3) Raindrop freezing fragmentation

In AC, secondary ice formation due to raindrop/drizzle freezing is treated with an empirical formulation by Phillips et al. (2018). This formulation proposed two modes of raindrop freezing fragmentation based on previous laboratory observations (Phillips et al. 2018, references therein):

(i) Fragmentation during freezing of spherical drop of drizzle or rain (mode 1): In this type, the quasi-spherical freezing may be initiated on collision of a supercooled drop (0.05–5 mm diameter) with a less massive ice particle or by heterogeneous raindrop freezing (immersed INP). In this mode, the spherical symmetry of the drop remains intact after collision with less massive ice particles, and it generates ice splinters when the outer shell breaks away following freezing. Both tiny and big fragments are generated.

(ii) Fragmentation during the collision between a supercooled raindrop and a more massive ice particle (mode 2): This mode involves the collision of a more massive ice particle and raindrop. In this type of non-spherical freezing, collision with an ice crystal can disrupt the spherical symmetry of the drop. Secondary splash drops are emitted, some of which later freeze, forming ice splinters (Phillips et al. 2018; James et al. 2021).

Both modes depend on the sizes of colliding hydrometeors and temperature. Fragmentation during raindrop freezing can create a high (~10^3) IE ratio when abundant large drops are present in the clouds (Phillips et al. 2018). More details are from Phillips et al. (2018).

4) Fragmentation during sublimation of snow and graupel

Another SIP mechanism empirically formulated in AC is fragmentation during sublimation of graupel and dendritic snow (Deshmukh et al. 2022). Fragmentation during sublimation depends on the initial size of the ice particle, ambient RH$_i$, and a ventilation factor depending on the fall speed (Deshmukh et al. 2022). A dedicated tagging tracer for dendritic snow was used to track the ice particles formed in the dendritic region (−12° to −17°C) by heterogeneous nucleation and other SIP processes. This is then input to the dendritic sublimation breakup formulation in AC. Deshmukh et al. (2022) give more details of the formulation.

3. Results from the control simulation

a. Model validation

The convective line observed on 11 May 2011 in MC3E (section 2a) has been simulated by AC (section 2b). Figure 5a show the CCN activity spectrum predicted by AC from the
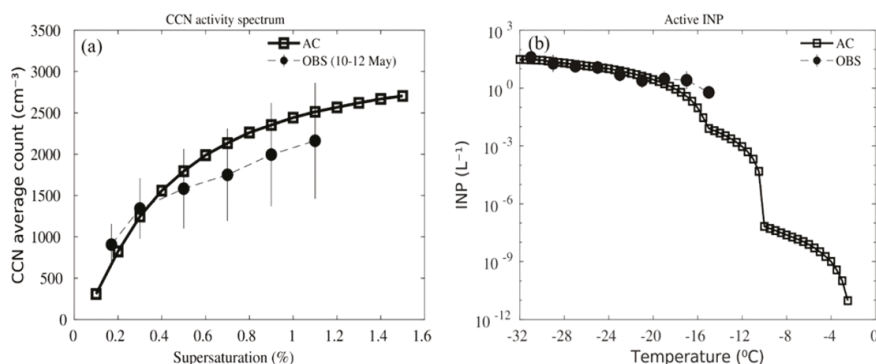
FIG. 5. (a) The CCN activity spectrum predicted by AC for the MC3E case (11 May 2011) for the environment at about 350 m MSL altitude, corresponding to the prescribed vertical profiles of size distributions of various species of aerosol (full line with squares). This is compared with the observed 3-day (9–12 May)-averaged CCN activity spectrum (dotted line with filled circles) from the CCN counter deployed at Lamont, Oklahoma. (b) The INP activity spectrum predicted by AC for 11 May 2011 MC3E case (full line with squares). This is compared with CFDC observation (dotted line with filled circles) taken at the SGP site in 2014 (adapted from DeMott et al. 2015, with changes). Standard deviations are plotted as a representative of error bars in (a) and (b).

prescribed ASD of soluble APs. It agrees with the observed CCN activity [section 2a(2)]. The MC3E campaign made no measurements of active INPs. However, DeMott et al. (2015) made continuous flow diffusion chamber (CFDC) measurements of active INPs in spring 2014 at SGP for a similar altitude. These data were reprocessed here for corrections and averaged over 2°C temperature bins for the same month as MC3E but for a different year (2014). Figure 5b shows that the number concentration of active INPs predicted by EP (AC) from the ASDs of insoluble aerosols (Table 2) is in good agreement with the observation.

Figures 6a and 6b show simulated domain averages of the accumulated surface precipitation and precipitation rate at

the ground, respectively. The peaks in the simulated precipitation rate are at 2400 UTC 10 and 1900 UTC 11 May. However, observations show a maximum precipitation rate at 2000 UTC 11 May. The predicted precipitation rate is higher than that observed by about 30% in the first peak (2400 UTC 10 May) and about 40% less in the second peak of the simulation (1900 UTC 11 May). This may partly because of possible biases in large-scale forcing [section 2a(2)]. Also, it may reflect the classic overshoot for the onset of convection in cloud models generally. The initial period (1200–2400 UTC 10 May) involved predicted high CAPE (3500–4000 J kg^{-1}). More precipitation is observed in the second peak than in the first, despite the predicted lower CAPE (1700 J kg^{-1}) (1500–2100 UTC 11 May).
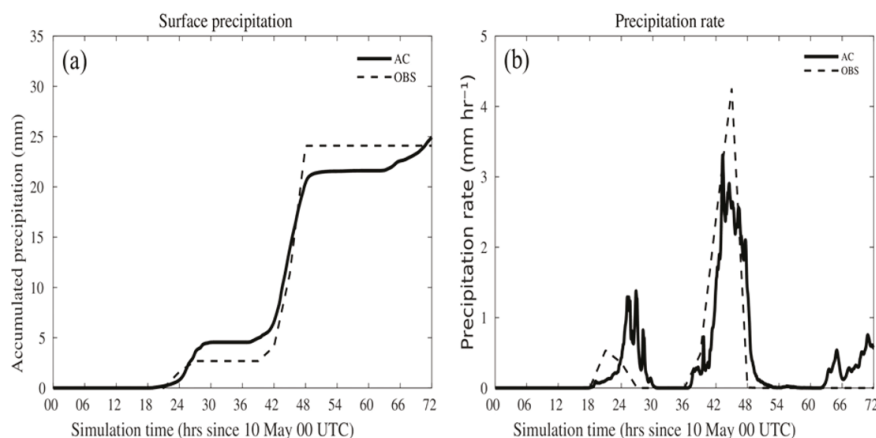

FIG. 6. Comparison of predicted (a) surface accumulation of precipitation and (b) surface precipitation rate from the control simulation with observations from rain gauge–adjusted WSR-88D over the SGP site.

For comparison, all predicted and observed cloud microphysical properties (Figs. 7 and 8) were averaged conditionally in an identical manner both for the same time period as the aircraft measurements (1600–2100 UTC 11 May 2011) and for regions of cloudy convective ascent, descent and of stratiform cloud. Since the Citation aircraft mostly flew in the stratiform region of the storm, a good agreement can be seen between the model and observations in the stratiform areas. For the simulation and aircraft observations, vertical velocities (w) exceeding 2 m s^{-1} were selected to identify convective updrafts, $w < -2$ m s^{-1} for downdrafts, and $|w| < 2$ m s^{-1} for stratiform conditions. The estimated errors in the vertical velocity from the aircraft observations are about ±30% from noise introduced by the aircraft maneuvers and the retrieval algorithms.

Considering the uncertainties involved in the measurements (as indicated by error bars), the predicted characteristics of cloud droplets such as droplet mean size, droplet concentration, and LWC are in fair agreement with the aircraft observations for cloudy convective ascent (Figs. 7a,d,h) and descent (Figs. 7c,f,j) as well as for stratiform regions (Figs. 7b,e,i). The observed LWC in the convective ascent below the freezing level appears much lower than in the simulation. This may reflect the tiny sample size (approximately a few seconds) of observational data points and lack of comprehensive sampling by the aircraft of cells at those low levels.

In cloudy convective updrafts, downdrafts, and stratiform conditions, the predicted NI$_{200}$ (ice concentrations of particles > 200 μm) is about 10 L^{-1} at observational levels, the same order of magnitude as the aircraft data (Figs. 8a–c). The predicted NI$_{200}$ in such regions has contributions from particles such as cloud ice (about 44%), graupel (about 32%), and snow (about 23%) with a minimal contribution from supercooled rain (<0.007%) in cloudy convective updrafts.

Supercooled cloud droplets in mixed-phase clouds will evaporate away if the supersaturation with respect to liquid water (s_w) becomes appreciably negative. Once the supercooled cloud liquid has evaporated, a deep mixed-phase cloud becomes ice-only, and there is cessation of vapor growth, riming, and production of ice precipitation, severing the positive feedbacks of ice multiplication (Yano and Phillips 2011). Evidence for precipitation being somehow necessary for any ice multiplication is that thin cold clouds without precipitation are observed by aircraft to have little difference between coincident concentrations of environmental INPs and total ice (Eidhammer et al. 2010).

At the onset of evaporation of liquid, $s_w = 0$, the theoretical critical ice particle concentration for this onset of subsaturation in the simulated storm is estimated following Korolev and Mazin [2003, Eq. (22) therein] in convective ascent. The predicted total ice concentration (Fig. 8a) is less than about a factor of 2 at warmer subzero temperatures (−5° to −25°C) from this coincident theoretical critical ice concentration, identically averaged conditionally in the convective ascent ($w > 2$ m s^{-1}). Comparatively, the agreement between these two parameters (theoretical and predicted ice concentrations) is much better at colder temperatures (<−25°C), because

during mixed-phase ascent from the freezing level it takes time for the explosive ice multiplication to occur.

Moreover, the predicted actual number concentrations of ice particles greater than 1 mm, conditionally averaged over fast updrafts ($w > 2$ m s^{-1}) (Fig. 8d) and downdrafts ($w < -2$ m s^{-1}) (Fig. 8f) differs no more than 40% from the observations. In stratiform conditions ($|w| < 2$ m s^{-1}) the observed particle number concentration is about 70% higher than the predicted concentration at temperatures between −11° and −26°C (Fig. 8e).

Predicted domainwide averages of net shortwave (SW) and longwave (LW) radiative fluxes measured at the TOA agree with satellite observations. Errors at any given time are less than 25% (Figs. 9a,b). The simulated distribution of updraft speeds (>2 m s^{-1}) differs by no more than 50% from the aircraft observations (Fig. 9c). The predicted radar reflectivity agrees with the observations (KAZR) with a difference of less than about 5 dBZ at most subzero levels (Fig. 9d). A time–height plot of the radar reflectivity from AC is shown in Fig. 9e to compare it with the KAZR radar. The maximum predicted radar reflectivity is 40 dBZ at lower levels around 2000 UTC 11 May. The observed reflectivity was maximum (36 dBZ) around 1800 UTC. It can be seen that the simulated cloud tops were reached up to about 14 km (Fig. 9e), and the observed cloud tops up to about 12 km (Fig. 9f) MSL around 2000 UTC.

b. Other analysis of control simulation

Passive tagging tracers (section 2b) were added to track the various sources of ice from homogeneous nucleation, primary, and secondary processes represented in AC [section 2b(2)]. From their vertical profiles in Figs. 10d–i, it can be seen that fragmentation in ice–ice collisions is the most prolific (~80%) at all subzero levels among all four SIP mechanisms in convective updraft, downdraft, and stratiform conditions and creates IE ratios as high as 10^3 (Figs. 10j–l), when considered over the duration of the simulation.

As the simulated MC3E case had relatively warm cloud bases (~17°C), the HM process is active at temperatures between −3° and −10°C in updrafts (Fig. 10d), creating IE ratios ~10^3 (Fig. 10j) at these temperatures. In downdrafts, fragmentation during sublimation is the second most prolific (~20%) SIP mechanism and creating IE ratios of up to about 10^2 (Fig. 10k). As the simulated MC3E case had relatively low mean droplet diameters (<18 μm, Fig. 7a) at levels colder than 0°C, there is less coalescence than the cold-rain process (Fig. 15 below), and raindrop freezing fragmentation (Figs. 10d–i) contributes less (<1%) than the cold-rain process to the SIP and creates less IE ratio (~10). It is also predicted that throughout the vertical levels in clouds, fragmentation in ice–ice collisions creates IE ratios on the order of 10^3 in convective cloudy updrafts, downdrafts, and stratiform conditions.

Figures 11a and 11b show the time series of predicted ice concentrations conditionally averaged over all cloudy vertical levels throughout the domain, and IE ratios in the first hour after the onset of the convection. At times less than 10 min after the onset of ice, the HM process dominates the overall
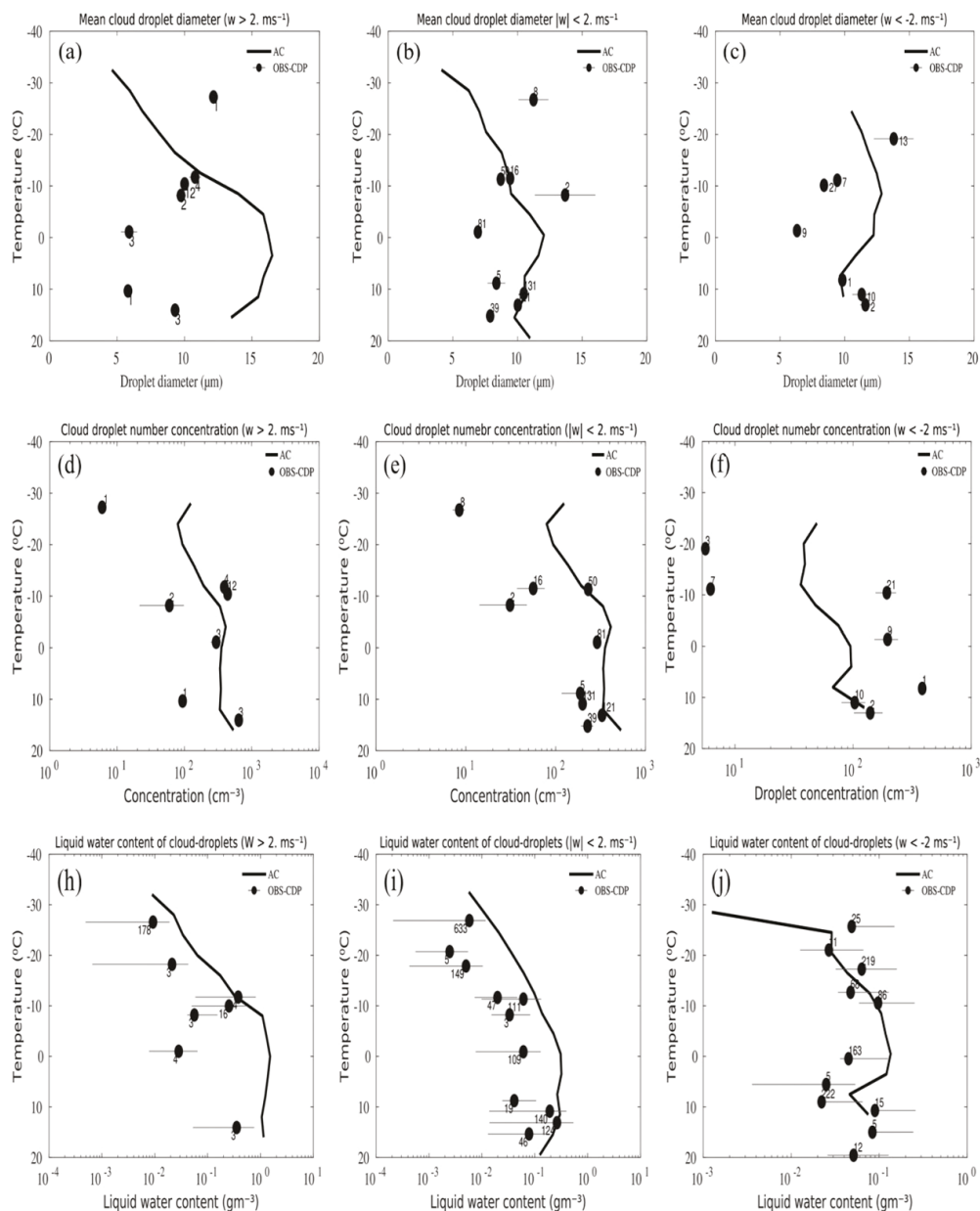
FIG. 7. Predicted (a)–(c) mean cloud droplet diameter and (d)–(f) droplet number concentrations compared with observations from the CDP probe and (g)–(i) liquid water content from the control simulation conditionally averaged over cloudy convective updrafts ($w > 2$ m s^{-1}), stratiform ($|w| < 2$ m s^{-1}) and downdrafts ($w < -2$ m s^{-1}) conditions compared with the aircraft observations from the CDP probe. Error bars shown in (a)–(i) are standard errors of observational samples. Numbers above each observation data point show the time (in s) for which the aircraft sampled the cloud at that level. Note that each observational data point consists of typically multiple up- and downdraft sampled for the convection.
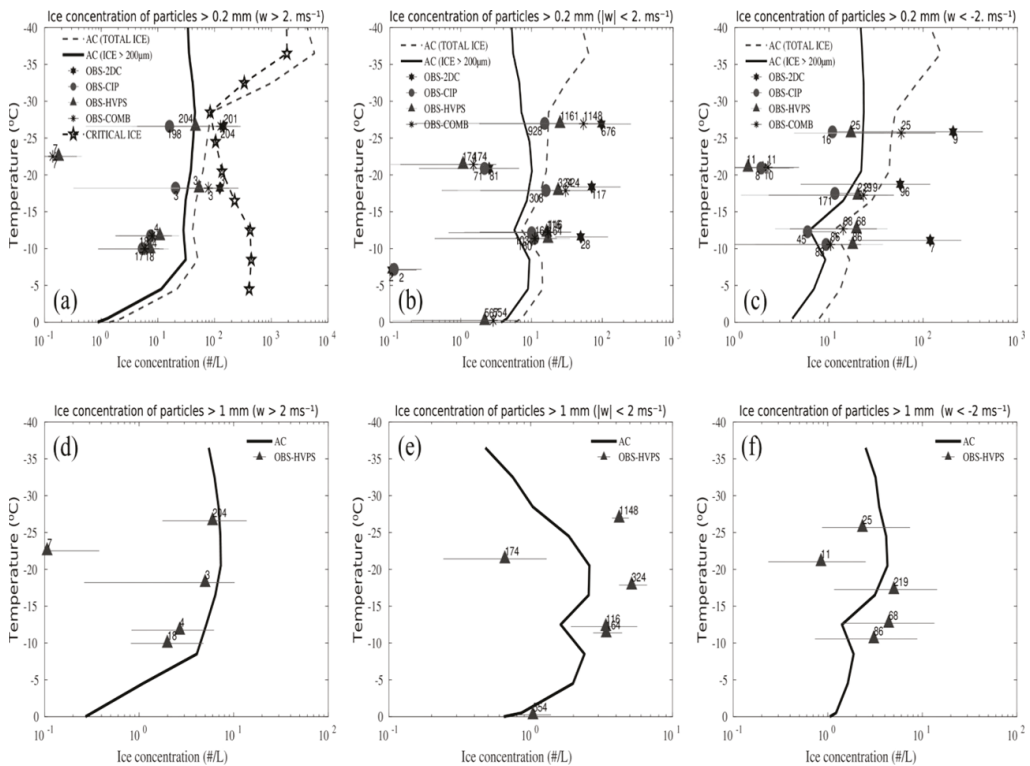
FIG. 8. Comparison of predicted ice number concentrations for particles of maximum dimension > 0.2 mm of all microphysical species (cloud ice, snow, and graupel/hail) (full black lines) over cloudy convective (a) updraft ($w > 2$ m s^{-1}), (b) stratiform ($|w| < 2$ m s^{-1}), and (c) downdraft ($w < -2$ m s^{-1}) regions with aircraft observations from the 2DC, CIP, HVPS-3 probes, and combined spectrum (COMB) of these three probes. Also shown in (a) is the theoretical critical concentration of ice particles (pentagrams) calculated from Korolev and Mazin [2003, Eq. (22) therein], conditionally averaged similarly for convective ascent. (d)–(f) Number concentrations of all ice particles bigger than 1 mm in such updrafts, stratiform, and downdrafts conditions compared with aircraft observations from the HVPS-3 probe. Error bars shown are standard errors of observational samples. The total duration (seconds) for which the aircraft sampled the cloud at any particular level is displayed with numbers on each observational data point.

ice concentration, causing an exponential growth of crystal numbers. Immediately in the first 10 min, it creates average IE ratios as high as 10^2 (Fig. 11b). As the clouds grow further with time and tops ascend through the mixed-phase region, the exponential growth is continued by fragmentation in ice–ice collisions, which becomes the most prolific SIP mechanism after 10 min as snow and larger graupel particles increase in concentration (Fig. 11c). The concentrations of activated INPs, from the tagging tracers required for the EP (as cloud top ascends), and total ice increase together, sustaining IE ratios $\sim 10^4$. The ice concentration attains its maximum after the first half hour, becoming quasi steady for the rest of the lifetime of the MCS. These quasi-steady ice concentrations are accompanied by declining IE ratios after the first half hour with a minimum (about 10^2) toward the end of the simulated MCS.

The dependency on the vertical velocity of predicted IE ratios conditionally averaged over the entire domain between

$0°$ and $-30°C$ is shown in Fig. 12b. The total IE ratios have the same order of magnitude in the updraft and downdraft (>-5 m s^{-1}) regions, whereas in the stratiform region, the IE ratio is minimal (about 40). The balance among various SIP mechanisms in convection differs between ascent and descent (Fig. 12a). The SIP mechanism of fragmentation in ice–ice collisions dominates overall ice concentrations in convective ascent and descent, throughout the simulation. However, in most convective downdrafts, fragmentation during sublimation of ice is the second most prevalent process of SIP, creating IE ratios as high as 10^2 in the fastest downdrafts (<5 m s^{-1}). Generally, the faster the ascent or descent in all simulated cold clouds, the greater the IE ratio.

Figures 13a and 13b show a number budget of ice particles initiated by all processes represented throughout the control simulation. Fragmentation in ice–ice collisions generates 100 times more particles than heterogeneous ice nucleation at all
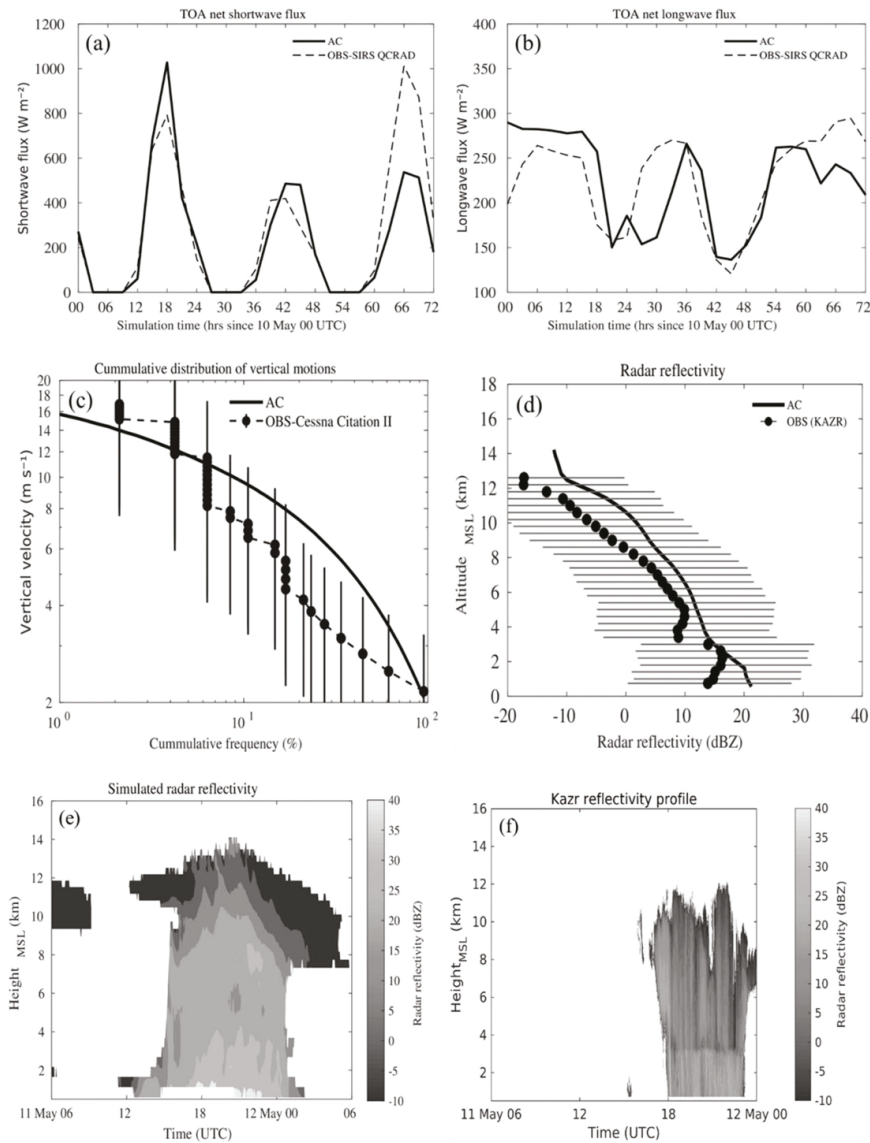
FIG. 9. Comparison of predicted (a),(b) TOA net shortwave and longwave radiation flux compared with that from GOES-VISST data, (c) vertical velocity histogram in fast convective updrafts (>2 m s^{-1}) compared with observations from the Citation aircraft, and (d) the simulated and observed vertical profiles of radar reflectivity conditionally averaged over the regions of significant reflectivity (>-10 dBZ) at each level, from the ground-based (KAZR) radar, which was functional at CF, Lamont, Oklahoma (36.605°N, 97.485°W). Error bars in (c) and (d) are standard errors of observational samples. Comparison of (e) simulated radar reflectivity profile with (f) reflectivity observed by KAZR.
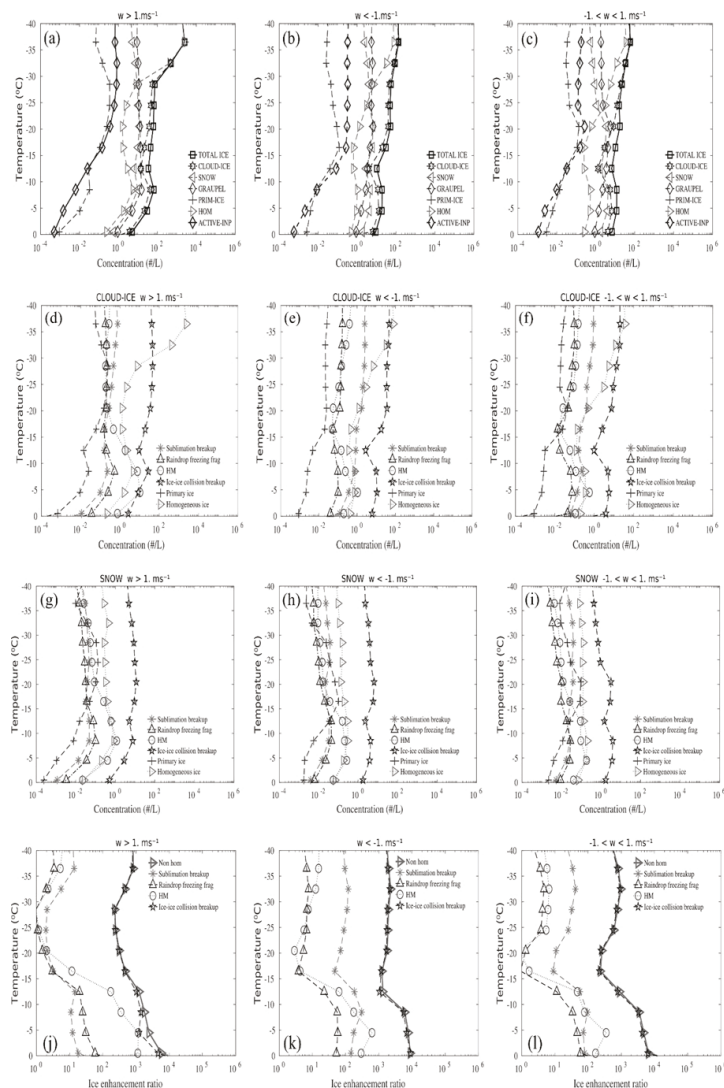
FIG. 10. Number concentrations for different microphysical species and various tracer terms defining SIP processes in the control simulation of AC, conditionally averaged over regions of cloudy convective (left) updrafts (>1 m s^{-1}) and (center) downdrafts (<-1 m s^{-1}) and (right) stratiform cloud ($-1 < w < 1$ m s^{-1}). Properties displayed for these three regions are (a)–(c) number concentrations of activated INPs (solid line with diamonds), ice number concentrations (L^{-1}) of all particles (solid line with squares) and individual microphysical species; cloud ice, snow, and graupel (dotted lines with hexagons, downward-pointing triangles, diamonds, respectively), (d)–(f) concentration of cloud ice from the tagging tracers of fragmentation during sublimation breakup (asterisks), shattering due to raindrop freezing (upward-pointing triangles), the HM process (open circles), and fragmentation in ice–ice collisions (pentagrams) averaged for (g)–(i) snow concentration from these tracer terms, and (j)–(l) IE ratios from nonhomogeneous ice and tracer terms of various SIP processes. Number concentrations of primary ice (plus signs) from heterogeneous ice nucleation and homogeneous ice (right-pointing triangles) are shown in (d)–(i).
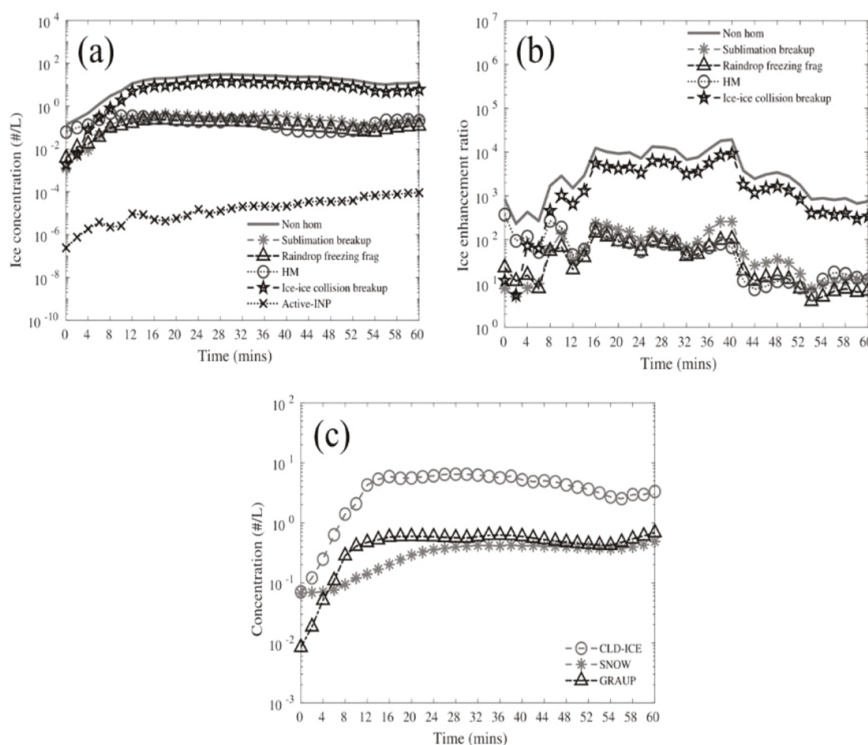
FIG. 11. The number concentration of ice particles (a) for total nonhomogeneous ice (total ice from cloud ice and snow minus total homogeneously nucleated ice) (solid line) and various tracer terms defining SIP processes such as the HM process (open circles) and fragmentation during sublimation (asterisks), raindrop freezing (upward-pointing triangles) and ice–ice collisions (pentagrams) and activated INP (crosses) in the control simulation of AC, (b) IE ratio defined from (a) for nonhomogeneous ice and ice from various tagging tracers used to track SIP processes and (c) concentration of cloud ice (open circles), snow (asterisks), and graupel (upward-pointing triangles). All concentrations in (a)–(c) are conditionally averaged between temperatures 0° and −30°C for nonzero values. The plotted time is relative to the second onset of the convection at 1400 UTC 11 May 2011.

temperatures warmer than −30°C. Among all types of fragmentation in ice–ice collisions, fragmentation due to collisions of snow with graupel or hail is the most prolific (∼44% of all fragments from all ice–ice collisions, Fig. 13c). Also, collisions of graupel with either graupel or hail (∼10% fragments from all ice–ice collision) and collisions of snow on snow are predicted to have appreciable impacts on the budget (∼27% of fragments from fragmentation in ice–ice collisions, Fig. 13c).

At first glance, the budget gives the impression that the fragmentation during sublimation of graupel is the most prolific SIP mechanism as it generated about 400 times more ice particles than the heterogeneous ice nucleation at temperatures warmer than −30°C. However, as noted above (section 3b, Fig. 10), the tagging tracers reveal that the fragmentation during sublimation of ice is less prolific than the HM process and fragmentation in ice–ice collisions. A separate budget (Fig. 13a, black bar) shows that the vast majority (∼80%) of

such fragments from fragmentation during sublimation are sublimated away completely while descending, so never reach the updrafts for growth and survival, and only about 20% of these emitted fragments survive (Fig. 13a, yellow bar).

Figure 13a also shows that homogeneous freezing produces most ice particles (∼94% of the total budget) in the entire storm as clouds reach above the −36°C level. This is much greater than the total ice formed in all SIP processes (∼3% of all ice initiated). Primary ice crystals formed at warmer temperatures (>−30°C) contribute only about 0.05% to the total ice formed.

Figure 14 shows the dependency of the total number of ice particles initiated in the simulated storm from the HM process and fragmentation in ice–ice collisions on vertical velocity and temperature. Most of the splinters from the HM process (∼80%) were emitted between temperatures −5° and −8°C and weak convective ascent vertical velocities between 1 and
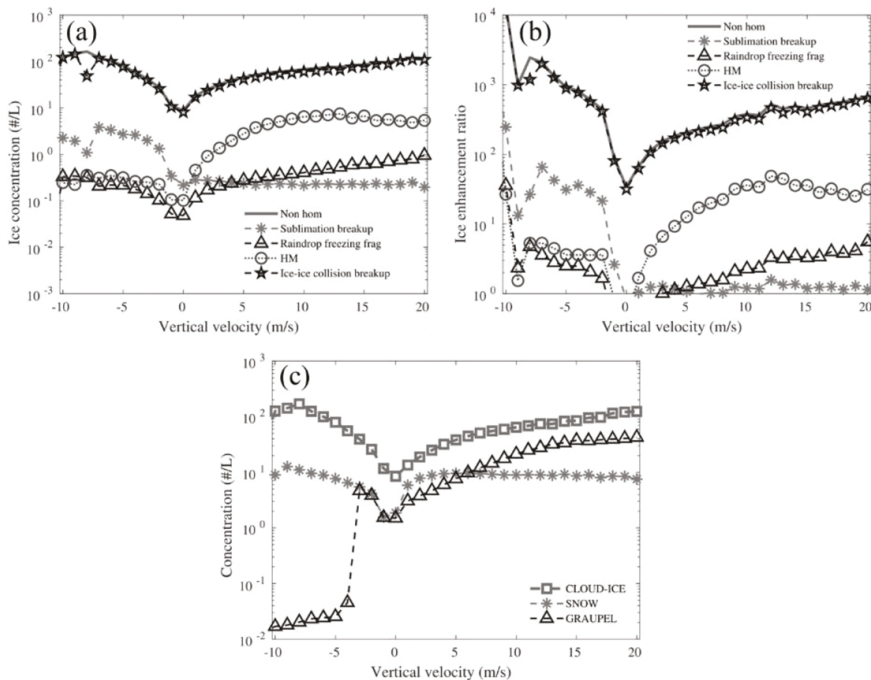
FIG. 12. Domain-averaged distributions with respect to the ascent of (a) the predicted nonhomogeneous ice (total ice from cloud ice and snow minus total homogeneously nucleated ice) (solid line) and ice (cloud ice + snow) from tagging tracers of various SIP processes such as the HM process (open circles) and fragmentation during sublimation (asterisks), raindrop freezing (upward-pointing triangles), and ice–ice collisions (pentagrams) averaged for vertical velocities between −10 and 20 m s⁻¹ over 1 m s⁻¹ bin at temperatures between 0° and −30°C. (b) IE ratios at these vertical velocity bins were estimated from (a),(c) concentrations of cloud ice (squares), snow (asterisks), and graupel (upward-pointing triangles).

5 m s^{-1} (Fig. 14a). About 20% of all HM ice splinters were generated in stronger updrafts (>5 m s^{-1}) at those temperatures. Fragmentation in ice–ice collisions generated about two orders of magnitude more ice particles than the HM process (Fig. 14a) in the entire simulation and is the most prolific mechanism of SIP overall. Fragmentation in ice–ice collisions mostly happens in convective ascent greater than 1 m s^{-1} (~70%) and temperatures in the central third of the mixed-phase region (−15° to −30°C). In a faster convective ascent, emission of fragments occurs at colder temperatures (Fig. 14b), as expected from graupel and snow being upwelled to higher levels. In the stratiform clouds, the peak in fragmentation in ice–ice collisions is in the lower third of the mixed-phase region (0° to −10°C).

Figure 14b illustrates how fragmentation in ice–ice collisions is ubiquitous throughout the storm. This budget of fragments initiated is consistent with the vertical profiles noted above, showing fragments from fragmentation in ice–ice collisions at all subzero temperatures (Fig. 10a). Fragmentation in ice–ice collisions is more evenly distributed over temperatures (Fig. 14d) than the HM process. It has a broad thermal peak

in the central mixed-phase region (near −20°C) due to an interplay between supercooled cloud liquid for riming and the fallout of graupel during upwelling. About 70% of the fragments are generated in the upper half (−20° to −36°C) of the mixed-phase region due to the upwelling of both large graupel and snow particles (Fig. 10a). Most of the fragments (about 65%) from fragmentation in ice–ice collisions are emitted in weak to moderate convective ascent (<10 m s^{-1}) (Fig. 14c), partly because the weaker ascent is more ubiquitous. By contrast, raindrop freezing fragmentation and the HM process contribute only about 1% of all fragments from all four SIP mechanisms (Figs. 13a,b).

Figure 15 shows the components of graupel from the two precipitation mechanisms (section 1), namely, the warm rain and ice-crystal processes ("warm" and "cold" graupel, respectively), diagnosed with passive tagging tracers. The lack of warm rain causes a lack of raindrop freezing, and hence cold graupel is more prolific than warm graupel. This can be attributed to typically high CCN concentrations (>2000 cm^{-3}, Fig. 5a) suppressing coalescence and related raindrop freezing. The continental aerosol conditions act to boost the mass
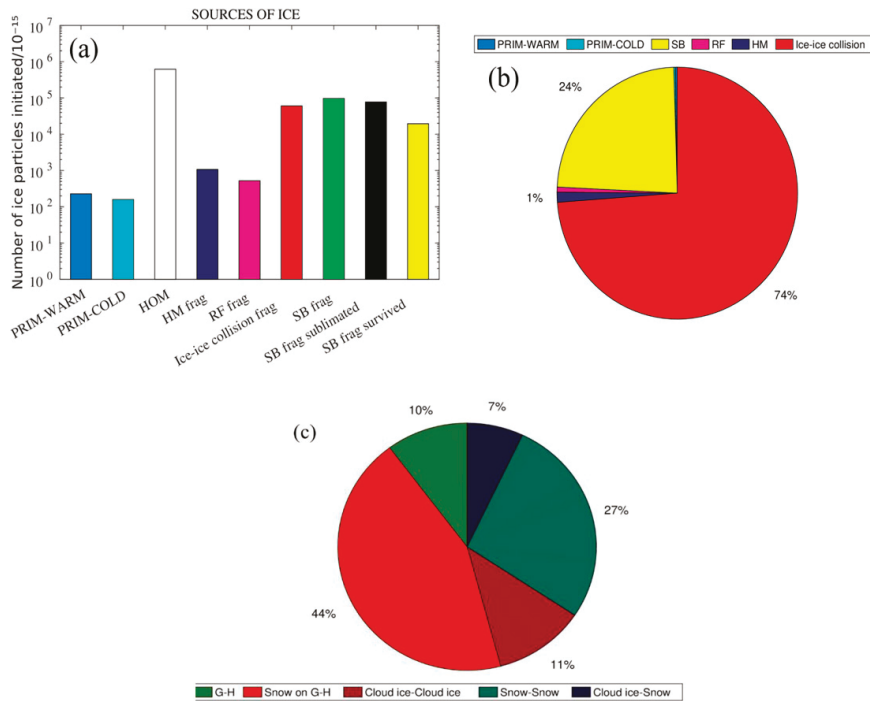
FIG. 13. (a) Bar chart for budgets of the number of ice crystals from homogeneous, primary, and secondary initiation in the control simulation of the AC for 11 May 2011 MC3E case. From left to right, bars are the sources of heterogeneous ice nucleation at temperatures warmer ("PRIM-WARM") and colder ("PRIM-COLD") than −30°C, homogeneous freezing at temperatures colder than −36°C ("HOM"), and various SIP mechanisms. These are the HM process of rime splintering ("HM frag"), fragmentation of freezing rain/drizzle ("RF frag"), fragmentation in ice–ice collision (ice–ice collision frag) from all types of collision, fragmentation during sublimation of dendritic snow and graupel (SB frag). The number of sublimationally generated fragments (SB frag) that are sublimated away is also shown ("SB frag sublimated"). Still, only a few of them can reach the updrafts and survive since most of them must melt in the downdrafts ("SB frag survived"). (b) the same information, but in a pie chart without including homogeneously nucleated ice. (c) Another pie chart shows the relative contributions of various types of fragmentation in ice–ice collisions including collisions of graupel with either graupel or hail (G–H), snow on graupel or hail (Snow on G–H), ice crystal on ice crystal (Cloud ice–Cloud ice), snow on snow (Snow–Snow) and crystal on snow (Cloud ice–Snow).

of supercooled cloud liquid available for riming (Saleeby et al. 2016; Braga et al. 2017) yet may also decrease the graupel–drop collision kernel (Cui et al. 2011). However, raindrop freezing is not insignificant in the MC3E control run and can accelerate any SIP process. Collisions between ice crystals and trace amounts of supercooled warm rain can reduce the onset time of both the HM process and fragmentation in ice–ice collisions (e.g., Phillips et al. 2001; Yano and Phillips 2011).

c. Cloud-top dependency of SIP

Airborne measurements by H80 in Miles City, Montana, sampled developing cumulus clouds at levels warmer (by between 2 and 17 K) than the instantaneous cloud tops. To estimate the IE ratio, H80 used the PBL measurements of active INPs and the temperature of activation was assumed to be cloud-top temperature. This yielded the classic plot of IE ratio as the function of cloud-top temperature (Fig. 1) with peaks at characteristic temperatures (e.g., ∼−12°C).

Consequently, to analyze the causes of that classic plot, we have inferred a similar relation from the control simulation, partly using tagging tracers noted above (section 2b). In the present study, the simulated clouds sampled were mostly young and convective (Fig. 16c) with ascending tops. The estimated average age of these clouds was typically between 5 and 30 min. Figure 16a shows predicted number concentrations of active INPs and ice particles derived from the cloud-top algorithm (appendix), plotted against temperatures of coincident cloud tops warmer than −30°C. Only cloud tops below the −36°C level were chosen to exclude all ice from homogeneous freezing. Tagging tracers of cloud ice and
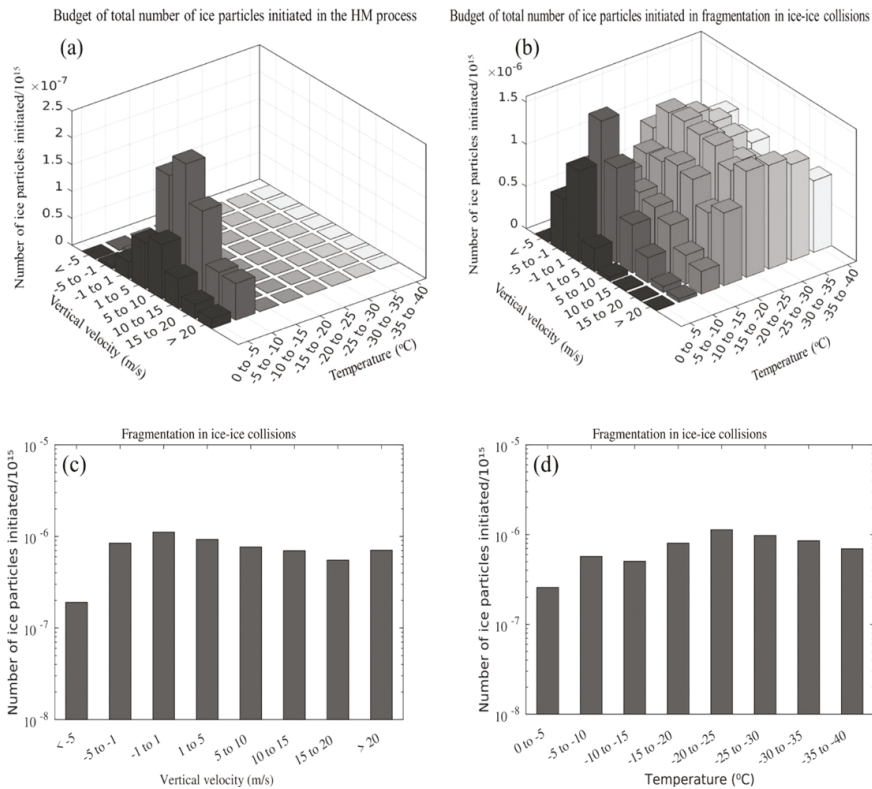
FIG. 14. Budget of the total number of ice particles initiated in the (a) HM process and (b) ice–ice collisions in ranges of vertical velocity (m s^{-1}) and temperature (°C) for the entire simulation. (c),(d) The same information is shown for fragmentation in ice–ice collisions.

snow from homogeneous freezing were deducted from the predicted total concentrations of cloud ice and snow to ensure no homogeneous ice in the IE ratio analysis at levels warmer than −36°C. From the simulation output, coincident values of concentrations of active INPs (prognostic scalars from the EP) and ice particles were taken from the nearest level (up to 7 K warmer) below the cloud top, where both were nonzero. Figure 16b shows the profile of the IE ratio derived from Fig. 16a. It can be seen that the IE ratios (Fig. 16b) generally tend to decrease with decreasing temperature of cloud top, as seen by H80 (Fig. 1, section 1).

Moreover, the predicted and observed (H80, Fig. 25 therein) IE ratios show a peak at similar cloud-top temperatures (∼−12°C). This peak chiefly arises from the HM process but partly also from fragmentation during ice–ice collisions and raindrop freezing (Fig. 16b). However, the contribution to the IE ratio is predicted to be strongly dependent on vertical velocity. For example, with vertical velocity > 1 m s^{-1} (not shown here), the peak (∼10^3) in IE ratio is mainly from the HM process and fragmentation in ice–ice collisions.

However, at higher updraft speeds ($w > 5$ m s^{-1}, not shown here), the raindrop freezing fragmentation becomes the second most prolific SIP mechanism after the HM process. It is predicted that the splinters from the HM process tend to accumulate near the −12°C level due to increased stability of the atmosphere above this level (Fig. 17). While any typical cloud is growing (e.g., as cumulus congestus) toward the mature stage, fragmentation in ice–ice collisions becomes the most prolific SIP mechanism after the cloud top ascends above the −20°C level, as mentioned below (section 5).

This explanation for the observed peak in IE ratio is consistent with previous aircraft studies (Hallett et al. 1978; Harris-Hobbs and Cooper 1987; Blyth and Latham 1993). Such studies suggested that the HM process is the dominant SIP mechanism in convection. Inspection of such studies shows that they tended to sample in young, developing cumulus clouds, typically less than about 15 min after the ascending cloud top first goes above the freezing level, and with warm bases such that large cloud droplets (>24 μm) are present in the HM generation region (−3° to −8°C).

FIG. 15. Domain-averaged profile of mass mixing ratio of total graupel (solid line), cold graupel (open circles), and warm graupel (asterisks) conditionally averaged over cloudy convective updrafts ($w > 1$ m s^{-1}).

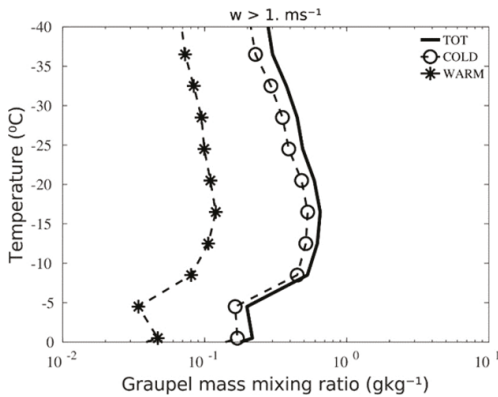The HM process is predicted to prevail in the overall SIP for ascending cloud tops between the $-7°$ and $-12°$C levels and creates IE ratios as high as 10^3 in such young growing convective clouds (Fig. 16b). This situation for convective cells in their growth stage contrasts with the vertical profiles averaged for the entire simulation (Figs. 10d,g), during which the mature stage dominates over long times. Essentially, the HM process is faster than fragmentation in the ice–ice collisions and can prevail in younger clouds with warmer cloud tops (Fig. 13a). The HM process is proportional to the total riming rate of graupel. In contrast, fragmentation in ice–ice collisions is slower yet eventually more powerful, with its positive feedback between riming of snow to become graupel, snow–graupel collisions, and growth of fragments to become snow (Yano and Phillips 2011, their Fig. 4; Phillips et al. 2017b). This difference in natural time scales of the explosive growth of ice concentrations among these SIP mechanisms explains why studies by aircraft of warm-topped (warmer than $-36°$C) ascending turrets have frequently reported strong correlations of observed ice concentrations with the HM process (Hallett et al. 1978; Harris-Hobbs and Cooper 1987; Blyth and Latham 1993; Blyth et al. 1997; Huang et al. 2017; Gayatri et al. 2022; Lasher-Trapp et al. 2021) as noted above. Such warm-topped turrets tend to be young. For example, in the present simulation, a turret with a top ascending through the $-20°$C level and a peak updraft speed of about 10 m s^{-1} has spent typically only about 10 min above the freezing level.

A wide range of intensities of various SIP mechanisms is evident in cloud-top spectrum of ice concentrations shown in Fig. 16a. The peak from the HM process noted above consists of IE ratios as high as 10^3 at $-7°$ to $-12°$C in the lower half of the mixed-phase region. Fragmentation during ice–ice collisions and raindrop freezing are each jointly the second most prolific SIP mechanism for ascending cloud tops near $-12°$C with IE ratios $\sim 10^2$. Later as cloud tops ascend toward the upper half of the mixed-phase region, going above the $-15°$C

level, the explosive growth of ice crystal concentrations is mainly from the fragmentation in ice–ice collisions and contributes more than 90% to the total ice formed in all SIP processes (Fig. 16a), sustaining IE ratios $\sim 10^2$ at these temperatures ($< -15°$C). This is consistent with laboratory observations by Vardiman (1978) and Takahashi et al. (1995) for fragmentation in ice–ice collisions, showing a strong dependency on temperature with a maximum rate of splinter ejection at about $-15°$C for dendritic cloud ice and snow. Moreover, fragmentation during raindrop freezing and sublimation can be ranked as the third and fourth most prolific SIP mechanisms, respectively, creating IE ratios of about $\sim 10^2$ and 10, at temperatures between $-7°$ and $-15°$C.

H80 used the PBL measurements of active INP and assumed that the activation temperature is simply the instantaneous cloud-top temperature. Although elsewhere in the present study a more accurate estimate of active INP is followed, for the sake of comparison with H80, their approach is now followed in Fig. 18a. Predicted active INP concentrations were obtained from the PBL during convection, and the temperature of activation was assumed to be the cloud-top temperature. Corresponding predicted IE ratios for cloudy convective updrafts (>2 m s^{-1}) are shown in Fig. 18b. IE ratios predicted and observed by H80 are on the same order of magnitude, as differences are comparable to errors in the IE ratio observed by H80. From Fig. 18b, it can be seen that the peak in the IE ratio (10^3) observed by them is due mainly to the HM process, if it is assumed that the warm-based continental deep convection of our MC3E case resembles that observed by H80.

4. Results from sensitivity tests

Various sensitivity tests (Table 3) were performed to evaluate the role of different SIP mechanisms for the IE ratio. This involved modifying the control run to create various perturbation simulations, which were then compared with the control run.

Figures 19a and 19b show the cloud-top dependency of ice concentration and IE ratios for various tests. In the absence of either the HM process or fragmentation in ice–ice collisions, the IE ratio decreases by a factor of about 20 compared to the control simulation in the middle and upper half of the mixed-phase region (Fig. 19b). In the case of no fragmentation in ice–ice collisions, IE ratios in the upper half of the mixed-phase region decrease sharply with minimum 1° at $-23°$C cloud-top temperature. However, only a factor of about 2 change is seen in the IE ratios in the case of "no raindrop freezing fragmentation" case and "no fragmentation in sublimation" case at cloud-top temperatures near $-10°$C (Fig. 19b).

Ice concentrations are plotted against cloud-top temperatures for various sensitivity tests (Figs. 19c–f). It can be seen that the HM process is the dominant SIP mechanism at cloud-top temperatures warmer than $-12°$C contributing $\sim 80\%$ to the total nonhomogeneous ice from all four SIP processes at these temperatures in "no fragmentation in ice–ice collisions" case, "no raindrop freezing fragmentation" case, and "no fragmentation
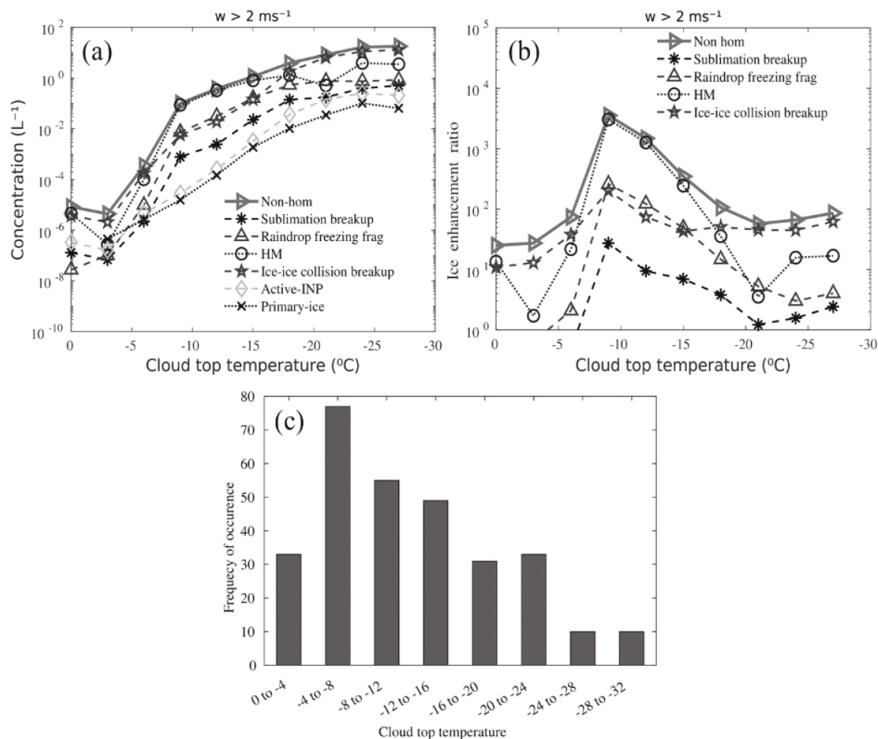
FIG. 16. (a) Predicted concentration of active INP (diamonds) from the EP, heterogeneously nucleated ice (crosses), total nonhomogeneous ice (total ice from cloud ice and snow minus total homogeneous ice) (right-pointing triangles) as a function of cloud-top temperatures conditionally averaged over cloudy convective updrafts (>2 m s^{-1}), ice concentration tracked by tracers (cloud ice + snow) from sublimation breakup of dendritic snow and graupel (asterisks), fragmentation during raindrop freezing (upward-pointing triangles), the Hallett–Mossop (open circles), and fragmentation in ice–ice collisions (pentagrams). Concentrations of active INP and total ice from control and individual SIP mechanism are at temperatures warmer ($1°–7°C$) than the cloud top. All the concentrations are the geometric means of nonzero values. (b) Predicted IE ratio as a function of cloud-top temperatures for cloudy convective updrafts (>2 m s^{-1}) of clouds sampled by the cloud-top algorithm for the simulated MC3E case, and (c) frequency of occurrence of cloud tops at various temperature ranges.

during sublimation" case (Figs. 19d–f). Fragmentation in ice–ice collisions is the most prolific, contributing over 70% to the total nonhomogeneous ice formed in all SIP processes at all cloud-top temperatures in the absence of the HM process (Fig. 19c). When present in young cumulus clouds whose tops are growing, the fragmentation in ice–ice collisions contributes $< 30\%$ to the total nonhomogeneous ice at cloud-top temperatures between $0°$ and $-15°C$. The HM process contributes over 50% to nonhomogeneous ice at cloud-top temperature $\sim -7°C$.

The radiative response of cloud depends on multiple factors such as cloud type and cover, hydrometeor concentrations and habits, liquid, and ice water path (Kinne and Liou 1989; Hong et al. 2016; Young et al. 2019). The enhanced ice due to SIP reduces the cloud cover and increases the SW flux reaching the climate system (Young et al. 2019). Figure 20 shows the TOA

SW and LW for the control and various sensitivity test runs (Table 3). It reveals that clouds in which SIP or fragmentation in ice–ice collisions is not active show a significant drop in both net SW (by about 8%, Fig. 20a) and LW (by about 12%) radiative fluxes at the TOA (Fig. 20b). This change can be attributed to the increase in cloud cover and LWC (not shown here) at the middle and upper half of the mixed-phase region. The rapid glaciation ceases in the absence of these processes, increasing cloud cover and lifetime.

Schematic picture of multiple SIP processes

A schematic structure of growing cloud with cloud base $\sim 15°C$ and cloud tops extending from $-5°$ to $-50°C$ from the control simulation is shown in Fig. 21a. It can be seen that in a typically young cloud with a top $\sim -5°C$, SIP processes are absent. As the cloud grows further, with its tops reaching
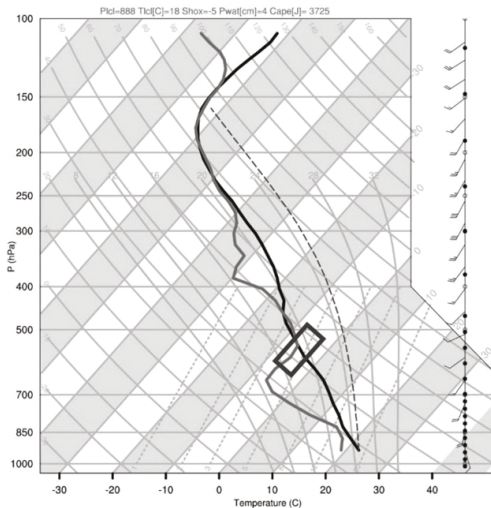
FIG. 17. The instantaneous profile of thermodynamic sounding plotted for the simulation in convection when the HM process was active showing stability at levels above the HM region ($-3°$ to $-8°C$). The lines shown are environment temperature (black line), dewpoint temperature (gray line), and pseudoadiabat (dotted black line). The black box indicates the HM generation region.

up to $-15°C$ level, the HM process is active ($-3°$ to $-8°C$) and dominates ($\sim 96\%$, Fig. 21b) overall ice concentrations, even at levels up to the cloud top due to upwelling of the splinters formed below. Other SIP mechanisms such as the fragmentation in ice–ice collisions, raindrop freezing fragmentation, and fragmentation during sublimation are also present but contribute less ($<2\%$) to the total ice than the HM process in clouds with relatively warm ($\sim -15°C$) tops. When the cloud becomes older with tops reaching above the $-30°C$ level, these other SIP mechanisms become more active than they were before. The fragmentation in ice–ice collisions is the most prolific at all the temperatures throughout the cloud structure, contributing more than 90% to total ice at temperatures $< -15°C$. Second, fragmentation during sublimation and raindrop freezing are primarily active at temperatures colder than $-10°C$ and contribute $<2\%$ to the total ice concentration. Homogeneous freezing is the dominant process of ice initiation as convection reaches above the $-36°C$ level.

Figure 21b shows a pie chart corresponding to each cloud growing from cloud-top temperature $-15°$ to $-50°C$. In the early developing stage, when the cloud grows from top $\sim -5°$ to $-15°C$ in 5–10 min, under the suitable condition, splinters can be produced by the HM process and is the dominant SIP mechanism in such clouds. When clouds grow further in 15–20 min, reaching up to level $-30°C$ large-sized graupel number increases, and as a result, the fragmentation in ice–ice collisions becomes faster than the HM process. When a convective cloud enters its mature stage (cumulonimbi), the fragmentation in ice–ice collisions becomes even faster, contributing $\sim 95\%$ to the total ice formed in all SIP processes.

5. Summary and conclusions

A case of a squall line consisting of deep convective and trailing stratiform clouds, observed over Oklahoma on 11 May 2011, has been simulated with AC. This simulation adequately compares with the coincident aircraft and ground-based observations of the MCS from the MC3E (section 3a). In the vertical profiles, predicted averages of the filtered ice concentration (NI_{200}) and cloud droplet concentrations at all levels differ by less than 30% from the coincident aircraft observations for stratiform and convective regions in the storm. Previous modeling studies (e.g., Fridlind et al. 2017) have reported underprediction in the observed ice concentration (by about an order of magnitude) for the MC3E squall line. The present study has closed this gap between the predicted and observed ice concentrations. Also, domainwide averages of the TOA radiative fluxes have errors of less than about 30% at any instant both in the shortwave and longwave throughout the entire simulated period. This is consistent with the accuracy of predicted particle concentrations of droplets and ice because AC represents the dependency of radiative fluxes on particle size and concentration.

The budget analysis of total numbers of ice particles initiated shows that, for clouds with tops warmer than $-36°C$, fragmentation in ice–ice collisions dominates among all four SIP mechanisms [section 2b(2)]. As the simulated MC3E case is deep convection (cloud tops $\sim -60°C$) with abundant snow, graupel, or hail, the collisions between snow and graupel/hail and snow–snow collision contribute $\sim 44\%$ and 27%, respectively, to the total ice formed in fragmentation in ice–ice collisions. In this budget, only fragments from sublimational breakup that survived (about 20% of the true total) descent to reach the ascent are counted.

In the present study, the IE ratio is defined as the ratio between the number concentrations of total nonhomogeneously nucleated ice and active INP. Using this metric, following the progression of convective clouds growing to become cumulonimbi, the total intensity of ice multiplication and its balance of multiple SIP processes is predicted to evolve with the age of the clouds. Our simulation shows the dependency on cloud-top temperature of the IE ratio, which is typically between 10 and 10^3, and is dominated by the younger growing convective turrets. The corresponding contributions to this dependency from the SIP processes are diagnosed with dedicated tagging tracers. This explains the high concentrations of ice particles in young cumuli and mature clouds in MC3E.

The conclusions from the validated simulation of the MC3E storm are as follows:

1) Simulated IE ratios were between 10 and 10^3 for cloud tops between $0°$ and $-30°C$ with a peak (10^3) at cloud tops of about $-10°C$ and a minimum value (50) at $-22°C$. At most cloud-top temperatures, the IE ratios are about 10^2. Similar orders of magnitude for the IE ratio were observed by H80, who reported a peak at cloud-top temperatures close to $-12°C$.
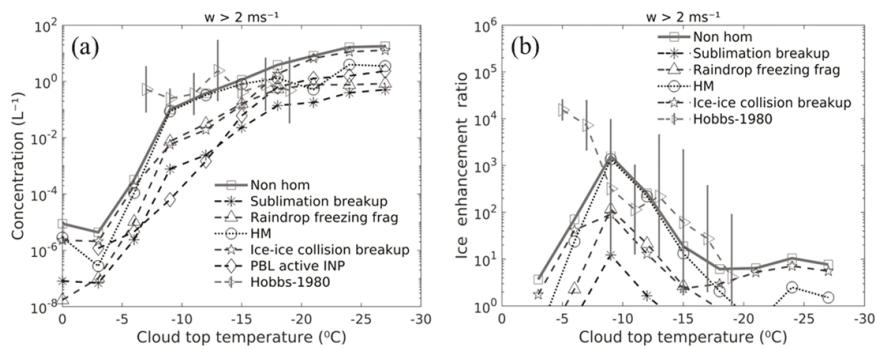
FIG. 18. (a) Predicted total nonhomogeneous ice (total ice from cloud ice and snow minus total homogeneous ice) (full line with squares) concentration is shown, as well as ice concentrations tracked by tracers (cloud ice + snow) from dendritic and graupel sublimation breakup (asterisks), fragmentation in raindrop freezing (upward-pointing triangles), the HM process (open circles), and fragmentation in the ice–ice collision (pentagrams), the PBL predicted active INP concentration (diamonds) in the convection and ice concentration observed by H80 (right-pointing triangles) as a function of cloud-top temperature. Also shown are (b) predicted ice enhancement ratios from total ice (cloud ice + snow) (full line with squares) and various tracers plotted as in (a) corresponding to these PBL-derived active INPs as a function of cloud-top temperature and compared with observed IE ratios by H80 (right-pointing triangles). Error bars are standard errors of ice concentration and IE ratios. All predicted ice concentrations were conditionally averaged over cloudy convective updrafts (>2 m s^{-1}). Geometric means of nonzero values of concentrations are shown here.

2) The predicted IE ratio decreases with decreasing cloud-top temperatures down to $-22°C$ and is higher (10^4) for faster convective ascent and descent.

3) As expected for the relatively warm bases (17°C), the HM process of rime splintering dominates overall ice concentrations in young convective clouds (~15 min since cloud tops first rise above the freezing level). In contrast, fragmentation in ice–ice collisions prevails in the less young convective clouds with tops reaching above the $-20°C$ level and for long times (>30–45 min) of MCS of multiple cells.

4) Regarding vertical profiles of tagging tracers averaged over the entire simulation, fragmentation in ice–ice collisions dominates overall ice concentrations above the $-15°C$ level.

 (i) In convective updrafts and downdrafts, fragmentation in ice–ice collisions dominates the overall ice concentration and contributes about 70% to the concentrations of all secondary ice.

 (ii) Fragmentation during sublimation only occurs in downdrafts, where it is the second most dominant SIP mechanism, creating IE ratios of 10^2. In convective updrafts, it only contributes an IE ratio of about 10, which is much smaller than the total IE ratio.

5) During the evolution of the storm, the initial explosive growth of ice concentrations (cloud tops warmer than $-15°C$) of is due to the fast HM process and subsequent fragmentation in ice–ice collisions that prevails at longer times. The growth is slower for warmer cloud tops (warmer than $-5°C$). The HM process prevails in young cumulus turrets ascending into subzero levels (e.g., Yano and Phillips 2011).

6) The ranking of SIP mechanisms in order of importance, according to contributions to the predicted IE ratio as a function of cloud-top temperature, is as follows:

 (i) In young, growing convective clouds, the HM process can be ranked as the first, fragmentation in ice–ice collisions to be second, raindrop freezing fragmentation as the third and fragmentation during sublimation as the fourth most prolific SIP mechanism.

 (ii) In stratiform clouds, the dependency of IE ratio on cloud-top temperature is similar to that for convective clouds. Fragmentation in ice–ice collisions can

TABLE 3. List of various simulations performed with AC.

Run performed	Description
Control	Included all the SIP processes [section 2b(2)]
No HM case	HM process prohibited from the control run
No fragmentation in ice–ice collisions case	Fragmentation in ice–ice collisions process prohibited from the control run
No raindrop freezing fragmentation case	Raindrop freezing fragmentation process prohibited from the control run
No fragmentation during sublimation case	Fragmentation during sublimation is prohibited from the control run
No SIP case	All the SIP mechanisms were prohibited from the control run
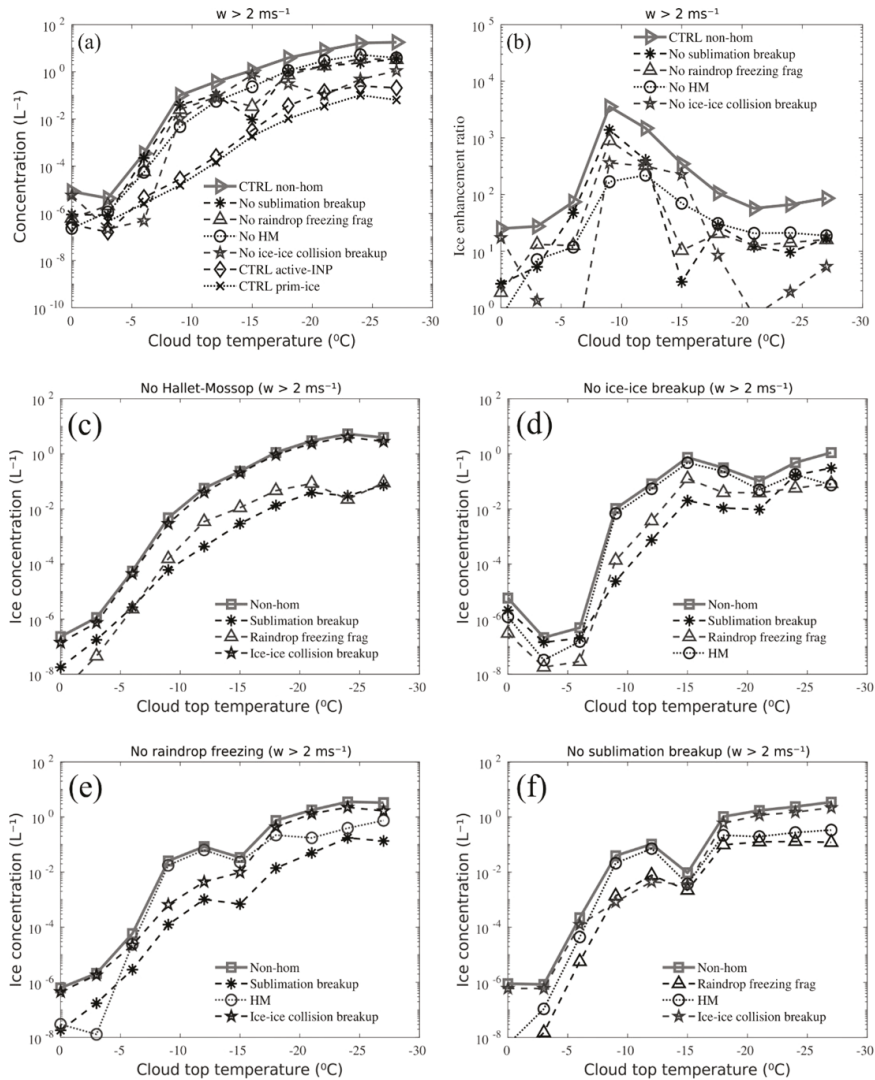
FIG. 19. Predicted active INPs, total nonhomogeneous ice (total ice from cloud ice and snow minus total homogeneous ice) concentrations, and IE ratio vs cloud-top temperature averaged over fast convective cloudy updrafts (>2 m s^{-1}) for the simulated MC3E case from the control run and sensitivity tests. (a) Concentrations of active INPs (diamonds) and nonhomogeneous ice (solid line with right-pointing triangles) from the control simulation, and nonhomogeneous ice concentrations from no sublimation breakup (asterisks), no raindrop freezing (upward-pointing triangles), no HM (open circles), and no fragmentation in ice–ice collisions (pentagrams). (b) Predicted IE ratio as a function of cloud-top temperatures for cloudy convective updrafts (>2 m s^{-1}) from the control and various sensitivity tests runs. Contribution in ice number concentration from tracers of individual SIP process in the absence of (c) the HM process, (d) fragmentation in ice–ice collisions, (e) raindrop freezing fragmentation, and (f) fragmentation during sublimation breakup. All concentrations are geometric means of the nonzero values.
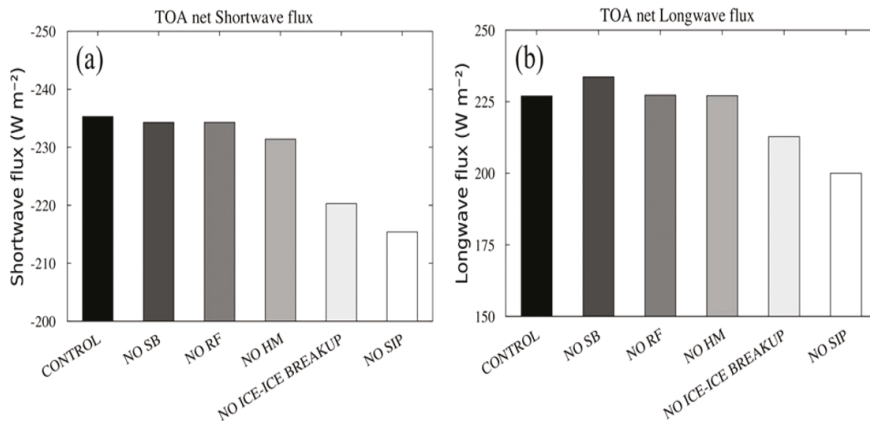
FIG. 20. The domain averaged TOA net (a) SW and (b) LW radiative flux from the control and various sensitivity tests runs (NO-SB: no sublimation breakup; NO-RF: no raindrop freezing fragmentation; NO-HM: no HM process; NO-ICE-ICE BREAKUP: no fragmentation in ice–ice collisions; and NO-SIP).

be ranked as the first most prolific SIP mechanism, the HM process as the second, fragmentation during sublimation as the third, and fragmentation during raindrop freezing as the fourth most prolific SIP mechanism.

(iii) In mature convective clouds with the coldest tops (Fig. 21b), the fragmentation in ice–ice collisions is the first most prolific SIP mechanism, whereas the HM process is the second, raindrop freezing fragmentation being the third and fragmentation during sublimation the fourth. This is consistent with fragmentation in ice–ice collisions being ubiquitous above the freezing level, without the restrictive conditions of the HM process.

7) There is a reduction in both SW (by about 8%) and LW (by about 12%) net radiative fluxes predicted at the TOA in the "no SIP" and no "fragmentation in ice–ice collisions" case relative to the control run. This is because of increasing cloud cover and LWC especially in the upper half of the mixed-phase region.

8) Most of the graupel is generated by the ice-crystal process with riming of snow. There is less contribution (by about 0.5–1 order of magnitude) to the total amount of graupel from the freezing of rain from the warm rain process (coalescence).

9) The predicted average ice concentration is never greater than the theoretical maximum for the onset of subsaturation with respect to liquid water at all levels warmer than about $-30°C$, where SIP is more prolific than homogeneous freezing. The order of magnitude is the same at most levels above $-15°C$ so the theoretical maximum can be used as a rough approximation of total ice. This is explicable in terms of the explosive growth of ice particle number concentrations from ice multiplication ceasing shortly after the onset of subsaturation with respect to

liquid, when the simulated mixed-phase cloud becomes "ice-only." This collapse of the humidity to near ice saturation inhibits both the vapor growth of fragments and all riming, preventing them from growing to become ice precipitation, and severing all positive feedbacks of ice multiplication by almost all of the SIP mechanisms, as theorized by Yano and Phillips (2011) (see also Phillips et al. 2017).

Regarding point 3, the young age of convective turrets sampled in past field studies explains why the HM process seemingly appeared to dominate ice concentrations in correlations from analysis of aircraft observations (Hallett et al. 1978; Harris-Hobbs and Cooper 1987; Blyth and Latham 1993). For example, Blyth and Latham (1993) report that ice concentrations were orders of magnitude lower when the conditions for the HM process were not met. In such field studies, their aircraft preferentially sampled younger clouds. The different rankings of SIP mechanisms depending on cloud age between points 3 and 4 suggests the importance of sampling convective clouds in a manner that is irrespective of their age in aircraft campaigns.

Under suitable conditions ($-3°$ to $-8°C$ and cloud droplets $>$ 24 μm), HM splinters are predicted to form from graupel with a typical onset time of 10–15 min and the typical onset time of fragmentation in ice–ice collisions is predicted to be 45 min. This is consistent with the theory (Yano and Phillips 2011). In deep convective clouds, raindrop freezing fragmentation can accelerate fragmentation in ice–ice collisions by reducing its onset time, because collisions between ice crystals and supercooled rain immediately form large graupel (Phillips et al. 2001). It can also radically reduce the time required for the onset of the HM process (Phillips et al. 2001, 2002). Splinters formed in all SIP mechanisms can be either upwelled or downwelled (sublimation breakup) to higher or lower levels in the cloud. So, the most likely SIP mechanism responsible
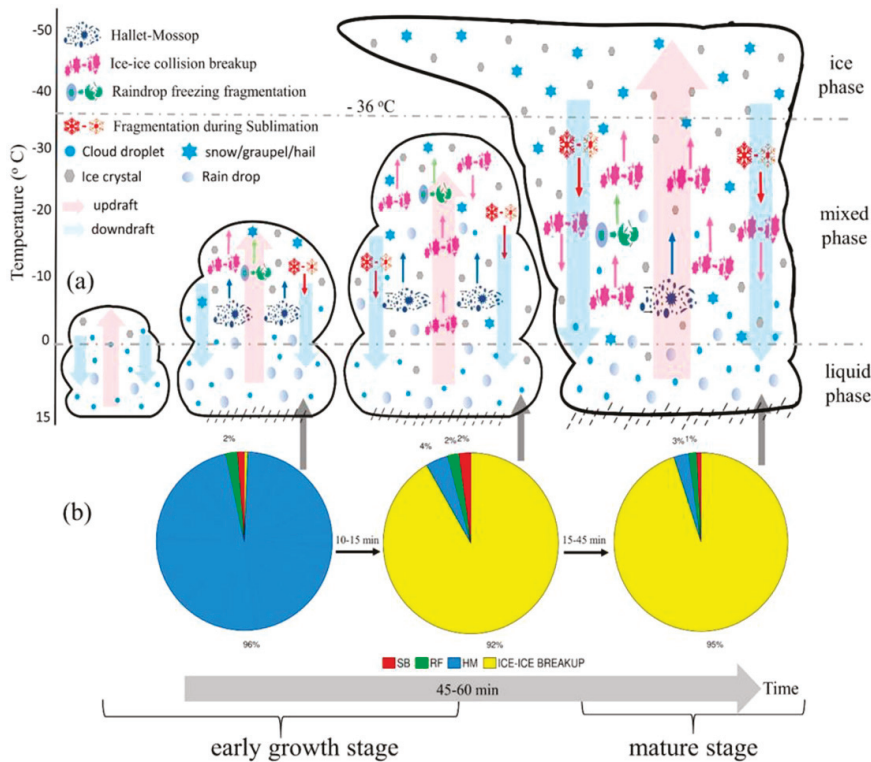
FIG. 21. (a) The schematic cloud structure in MC3E with cloud top growing from $-5°$ to $-50°C$ from the control simulation showing different SIP mechanisms active and vertical velocity (shown with upward- and downward-pointing arrows). Upwelling (downwelling) of the splinters formed is shown with a small upward (downward)-pointing arrow on top (bottom) of each SIP process. (b) Pie chart showing the relative contribution of various SIP mechanisms (SB: fragmentation in sublimation of ice; RF: fragmentation in raindrop freezing; HM: the HM process; and ICE–ICE BREAKUP: fragmentation in ice–ice collisions) to the total ice formed in all secondary processes for each cloud shown in (a). The time arrow at the bottom indicates the typical time required for the cloud to reach in mature stage from its early growth stage.

for the peak in IE ratio observed by H80 near a cloud-top temperature of $-12°C$ is the HM process, because such clouds sampled by them were relatively young.

Currently, most numerical models consider only the HM process of rime splintering as representative of SIP in natural clouds. The present study suggests that SIP in warm-based young, convective clouds in their early growth stage (tops above the freezing level) can be attributed mainly to the HM process. However, the HM process is active only in a narrow temperature range ($-3°$ to $-8°C$). Moreover, the mean droplet size is often insufficient for the observed ice enhancement to be accounted for by the HM process. This enhancement is seen to be several orders of magnitude aloft in natural convective clouds that are developing (e.g., cumulus congestus) or mature (e.g., cumulonimbi). The HM process can be inactive in cold-based, mixed-phase clouds (Morrison et al. 2005; Yano and Phillips 2011), such as those in the polar regions, and in clouds

with scarce availability of larger cloud drops (Phillips et al. 2017b; Sotiropoulou et al. 2020; Zhao et al. 2021). In such clouds, the explosive growth of ice crystals can be governed by other SIP mechanisms (section 1a). Here our AC simulations reveal that, along with the HM process, several other SIP mechanisms must be active in the simulated MCS case, causing such high ice concentrations (10^2–10^3 L^{-1}) observed by the aircraft.

Regarding the ranking of SIP mechanisms (point 6 and 7), all the analysis with sensitivity tests (section 4) and with tagging tracers (section 3b) shows that the fragmentation in ice–ice collisions makes the maximum contribution (>75%) to the total ice below the $-36°C$ level. Thus, fragmentation in ice–ice collisions is essential for accuracy of predicted ice concentrations aloft in the upper half of the mixed-phase region. This indicates that the HM process alone cannot create the high ice concentrations typically seen ($\sim 10^2$–10^3 L^{-1}),

especially in deep convective clouds (e.g., cumulonimbi), in the present MC3E case.

Generally, the raindrop freezing fragmentation (Rangno 2008; Phillips et al. 2018) can be a prolific SIP mechanism, especially in maritime or tropical deep convective clouds, if larger cloud drops are present. Yet, in the present study, the high CCN concentrations ($\sim$2000 cm^{-3}, Fig. 4a) inhibit the warm rain process despite the warm cloud base, so that raindrop freezing fragmentation is less prolific and only ranked in third place overall. However, for warmer cloud tops ($>-15°C$), raindrop freezing fragmentation shares the joint second place with fragmentation in ice–ice collisions, creating IE ratios as high as 10^2. Subsequently, the fragmentation during sublimation can significantly contribute to the total ice, especially in stronger downdrafts (<-4 m s^{-1}, Fig. 12a).

The upwelling of large snow and graupel into the upper half of the mixed-phase region results in copious fragmentation in ice–ice collisions (section 3b). The predicted budget of fragmentation in ice–ice collisions strongly depends on vertical velocity for the stratiform versus convective contrast, more so than on temperature. Most ($\sim$70%) splinters from fragmentation in ice–ice collisions are emitted in weak or moderate convective ascent (<10 m s^{-1}) and in the upper half of the mixed-phase region ($<-20°C$). This is consistent with total ice concentrations in ascending cloud tops above the $-16°C$ level being driven mainly by fragmentation in ice–ice collisions, because such cloud-top regions have had at least 10 min of prior glaciation for this slower yet persistent process to prevail, relative to the HM process (accelerated by collisional raindrop freezing).

To conclude, this study predicts the classic dependency observed by H80 (Fig. 25 therein) of IE ratio on cloud-top temperature in young convective turrets (Fig. 1). In our simulation of similar summertime deep convection (2011) in the continental United States, two SIP mechanisms (the HM process and fragmentation in ice–ice collisions) are responsible for the explosive growth of ice concentrations in convective ascent and descent, accounting for this pattern of IE ratio. The prediction includes the same observed peak from H80 (in the vicinity of about $-12°C$ of cloud-top temperature) in terms of upwelled splinters from the HM process, accelerated by raindrop freezing in collisions between supercooled raindrops and the HM splinters. The present study also concludes that the age of a cloud as it goes through its life cycle is of paramount importance for the relative balance of activities among the various mechanisms of SIP.

Finally, it is the concerted combination of multiple SIP mechanisms represented here that together accurately explains the observed disparity between concentrations of ice and INPs in our simulated line of convection (Fig. 8). Dependencies of these SIP mechanisms on quantities, such as droplet size, temperature, vertical velocity, and hydrometeor fall speed, make their relative importance for ice initiation differ among different cloud types. This highlights the need for continued innovation of new laboratory experiments and theoretical representations of various SIP mechanisms (section 1a) to inform formulations in atmospheric models. This is especially true for breakup in collisions among ice particles.

Data availability statement. The "cloud-top algorithm" code is available from the corresponding author on a request. The data that support and are used in this study are also available on a request. The codes representing SIP in the cloud model are freely available on request.

APPENDIX

Cloud-Top Detection and Classification

The convective line observed in MC3E has been simulated by AC (section 2). The cloud-top temperature for the simulation is detected by our cloud-top detection algorithm. The algorithm is described as follows.

In the cloud-top algorithm, convective cores are first automatically identified using the partitioning method by Xu (1995). According to this method, a convective core satisfies one of the following four conditions:

(i) the horizontal distribution of maximum cloud draft strength below the melting level ($|w_{max}|$) is twice as large as the average over the four adjacent grid columns, or

(ii) $|w_{max}|$ is greater than 3 m s^{-1}, or

(iii) surface precipitation rate ($\langle P \rangle$) is greater than 25 mm h^{-1}, or

(iv) rain rate twice as greater as the average taken over the surrounding four grid points ($\langle P \rangle$) (Tao and Simpson 1989).

Grid columns other than the convective core and for which the total liquid water path (TLWP) is positive were chosen as convective grid columns. A region including a core and immediately adjacent convective grid columns is then defined as a convective region following Tao and Simpson (1989). The grid columns where TLWP exceeds 0.2 kg m^{-2} were identified as stratiform regions, and the remaining grid columns were defined as clear regions.
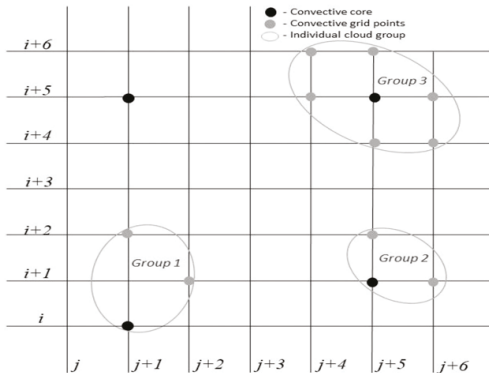
FIG. A1. Schematic diagram representing cloud grouping in the control simulation of AC. Filled black circles are cores, and filled gray circles represents convective grids adjacent to an individual core.

a. Step 1: Instantaneous grouping of grid points

Once the convective region (core and adjacent convective columns) was identified, links between pairs of convective adjacent grid points were established at any given time. These links were then used to expand each convective region. Such links of grid points were then stored in individual cloud groups. For example, group 1 consist of a core and two convective grids where a core at $(i, j + 1)$ creates a link with a convective grid at $(i + 1, j + 2)$ and this convective grid can be linked to another convective grid at $(i + 2, j + 1)$ as shown in Fig. A1.

b. Step 2: Iterative grouping

A convective region may split into more convective regions as clouds evolve with time in the simulation. This splitting then later forms "extra clouds." This was done by defining "spatial–temporal links" between pairs of convective grid points $[\mathrm{abs}(w) > 1 \ \mathrm{m \ s^{-1}}]$ that are adjacent in the spatial–temporal sense (in 4D). Clusters of contiguous spatial–temporal links in space–time were grouped.

c. Step 3: True cloud groups

A problem now arose that the expanded convective regions may have overlapped even though they are different clouds. So, there can be multiple clouds for a given convective region formed in steps 1 and 2. Consequently, we partitioned all the convective regions into distinct "sub–cloudy regions." To avoid overlapping convective regions found in step 2, two subgroups of convective regions were defined for a given time instance. If the grid points of these two subgroups were the same, they were said to be overlapped, and if not, then there was no overlap at a given time. These no-overlapped "sub–cloudy regions" are stored in "true cloud" groups.

d. Step 4: Actual cloud

Once the "true cloud" grid points (regions) associated with a core were found, convective columns in such a core

were collected along with the convective grids adjacent to these columns to form an actual cloud shown in Fig. 21a.

REFERENCES

Bacon, N. J., B. D. Swanson, M. B. Baker, and E. J. Davis, 1998: Breakup of levitated frost particles. *J. Geophys. Res.*, **103**, 13 763–13 775, https://doi.org/10.1029/98JD01162.

Blakeslee, R., J. Hall, M. Goodman, P. Parker, L. Freudinger, and M. He, 2007: The Real Time Mission Monitor: A situational awareness tool for managing experiment assets. *NASA Science Technology Conf.*, College Park, MD, NASA.

Blyth, A. M., and J. Latham, 1993: Development of ice and precipitation in New Mexican summertime cumulus clouds. *Quart. J. Roy. Meteor. Soc.*, **119**, 91–120, https://doi.org/10.1002/qj.49711950905.

——, and ——, 1997: A multi-thermal model of cumulus glaciation via the Hallett-Mossop process. *Quart. J. Roy. Meteor. Soc.*, **123**, 1185–1198, https://doi.org/10.1002/qj.49712354104.

——, R. E. Benestad, P. R. Krehbiel, and J. Latham, 1997: Observations of supercooled raindrops in New Mexico summertime cumuli. *J. Atmos. Sci.*, **54**, 569–575, https://doi.org/10.1175/1520-0469(1997)054<0569:OOSRIN>2.0.CO;2.

Braga, R. C., and Coauthors, 2017: Further evidence for CCN aerosol concentrations determining the height of warm rain and ice initiation in convective clouds over the Amazon basin. *Atmos. Chem. Phys.*, **17**, 14 433–14 456, https://doi.org/10.5194/acp-17-14433-2017.

Cantrell, W., and A. Heymsfield, 2005: Production of ice in tropospheric clouds: A review. *Bull. Amer. Meteor. Soc.*, **86**, 795–808, https://doi.org/10.1175/BAMS-86-6-795.

Chin, M., R. B. Rood, S.-J. Lin, J.-F. Müller, and A. M. Thompson, 2000: Atmospheric sulfur cycle simulated in the global model GOCART: Model description and global properties. *J. Geophys. Res.*, **105**, 24 671–24 687, https://doi.org/10.1029/2000JD900384.

Chouippe, A., M. Krayer, M. Uhlmann, J. Dušek, A. Kiselev, and T. Leisner, 2019: Heat and water vapor transfer in the wake of a falling ice sphere and its implication for secondary ice formation in clouds. *New J. Phys.*, **21**, 043043, https://doi.org/10.1088/1367-2630/ab0a94.

Crawford, I., and Coauthors, 2012: Ice formation and development in aged, wintertime cumulus over the UK: Observations and modelling. *Atmos. Chem. Phys.*, **12**, 4963–4985, https://doi.org/10.5194/acp-12-4963-2012.

Cui, Z., S. Davies, K. S. Carslaw, and A. M. Blyth, 2011: The response of precipitation to aerosol through riming and melting in deep convective clouds. *Atmos. Chem. Phys.*, **11**, 3495–3510, https://doi.org/10.5194/acp-11-3495-2011.

DeMott, P. J., D. J. Cziczo, A. J. Prenni, D. M. Murphy, S. M. Kreidenweis, D. S. Thomson, R. Borys, and D. C. Rogers, 2003: Measurements of the concentration and composition of nuclei for cirrus formation. *Proc. Natl. Acad. Sci. USA*, **100**, 14 655–14 660, https://doi.org/10.1073/pnas.2532677100.

——, and Coauthors, 2015: Integrating laboratory and field data to quantify the immersion freezing ice nucleation activity of mineral dust particles. *Atmos. Chem. Phys.*, **15**, 393–409, https://doi.org/10.5194/acp-15-393-2015.

Deshmukh, A., V. T. J. Phillips, A. Bansemer, S. Patade, and D. Waman, 2022: New empirical formulation for the

sublimational breakup of graupel and dendritic snow. *J. Atmos. Sci.*, **79**, 317–336, https://doi.org/10.1175/JAS-D-20-0275.1.

Dong, Y. Y., and J. Hallett, 1989: Droplet accretion during rime growth and the formation of secondary ice crystals. *Quart. J. Roy. Meteor. Soc.*, **115**, 127–142, https://doi.org/10.1002/qj.49711548507.

——, R. G. Oraltay, and J. Hallett, 1994: Ice particle generation during evaporation. *Atmos. Res.*, **32**, 45–53, https://doi.org/10.1016/0169-8095(94)90050-7.

Dye, J. E., and P. V. Hobbs, 1968: The influence of environmental parameters on the freezing and fragmentation of suspended water drops. *J. Atmos. Sci.*, **25**, 82–96, https://doi.org/10.1175/1520-0469(1968)025<0082:TIOEPO>2.0.CO;2.

Eidhammer, T., and Coauthors, 2010: Ice initiation by aerosol particles: Measured and predicted ice nuclei concentrations versus measured ice crystal concentrations in an orographic wave cloud. *J. Atmos. Sci.*, **67**, 2417–2436, https://doi.org/10.1175/2010JAS3266.1.

Feng, Z., X. Dong, B. Xi, C. Schumacher, P. Minnis, and M. Khaiyer, 2011: Top-of-atmosphere radiation budget of convective core/stratiform rain and anvil clouds from deep convective systems. *J. Geophys. Res.*, **116**, D23202, https://doi.org/10.1029/2011JD016451.

Field, P. R., and A. J. Heymsfield, 2015: Importance of snow to global precipitation. *Geophys. Res. Lett.*, **42**, 9512–9520, https://doi.org/10.1002/2015GL065497.

——, ——, and A. Bansemer, 2006: Shattering and particle inter-arrival times measured by optical array probes in ice clouds. *J. Atmos. Oceanic Technol.*, **23**, 1357–1371, https://doi.org/10.1175/JTECH1922.1.

——, and Coauthors, 2017: Secondary ice production: Current state of the science and recommendations for the future. *Ice Formation and Evolution in Clouds and Precipitation: Measurement and Modeling Challenges*, Meteor. Monogr., No. 58, Amer. Meteor. Soc., https://doi.org/10.1175/AMSMONOGRAPHS-D-16-0014.1.

Fridlind, A. M., A. S. Ackerman, G. McFarquhar, G. Zhang, M. R. Poellot, P. J. DeMott, A. J. Prenni, and A. J. Heymsfield, 2007: Ice properties of single-layer stratocumulus during the Mixed-Phase Arctic Cloud Experiment: 2. Model results. *J. Geophys. Res.*, **112**, D24202, https://doi.org/10.1029/2007JD008646.

——, and Coauthors, 2017: Derivation of aerosol profiles for MC3E convection studies and use in simulations of the 20 May squall line case. *Atmos. Chem. Phys.*, **17**, 5947–5972, https://doi.org/10.5194/acp-17-5947-2017.

Gayatri, K., S. Patade, J. Fan, and T. Prabhakaran, 2022: Pathways of precipitation formation in different thermodynamic and aerosol environments over the Indian Peninsula. *Atmos. Res.*, **266**, 105934, https://doi.org/10.1016/j.atmosres.2021.105934.

Georgakaki, P., G. Sotiropoulou, E. Vignon, A.-C. Billault-Roux, A. Berne, and A. Nenes, 2022: Secondary ice production processes in wintertime Alpine mixed-phase clouds. *Atmos. Chem. Phys.*, **22**, 1965–1988, https://doi.org/10.5194/acp-22-1965-2022.

Griggs, D. J., and T. W. Choularton, 1983: Freezing modes of riming droplets with application to ice splinter production. *Quart. J. Roy. Meteor. Soc.*, **109**, 243–253, https://doi.org/10.1002/qj.49710945912.

Gurganus, C., and P. Lawson, 2018: Laboratory and flight tests of 2D imaging probes: Toward a better understanding of instrument performance and the impact on archived data.

J. Atmos. Oceanic Technol., **35**, 1533–1553, https://doi.org/10.1175/JTECH-D-17-0202.1.

Hallett, J., and S. C. Mossop, 1974: Production of secondary ice particles during the riming process. *Nature*, **249**, 26–28, https://doi.org/10.1038/249026a0.

——, R. I. Sax, D. Lamb, and A. S. R. Murty, 1978: Aircraft measurements of ice in Florida cumuli. *Quart. J. Roy. Meteor. Soc.*, **104**, 631–651, https://doi.org/10.1002/qj.49710444108.

Harris-Hobbs, R. L., and W. A. Cooper, 1987: Field evidence supporting quantitative predictions of secondary ice production rates. *J. Atmos. Sci.*, **44**, 1071–1082, https://doi.org/10.1175/1520-0469(1987)044<1071:FESQPO>2.0.CO;2.

Heymsfield, A., and P. Willis, 2014: Cloud conditions favoring secondary ice particle production in tropical maritime convection. *J. Atmos. Sci.*, **71**, 4500–4526, https://doi.org/10.1175/JAS-D-14-0093.1.

Hobbs, P. V., 1969: Ice multiplication in clouds. *J. Atmos. Sci.*, **26**, 315–318, https://doi.org/10.1175/1520-0469(1969)026<0315:IMIC>2.0.CO;2.

——, 1972: Fragmentation of ice particles in clouds. *J. Rech. Atmos.*, **6**, 245–258.

——, and Coauthors, 1971: Studies of winter cyclonic storms over the Cascade Mountains (1970–71). University of Washington Dept. of Atmospheric Sciences Rep. VI, 312 pp.

——, M. K. Politovich, and L. F. Radke, 1980: The structures of summer convective clouds in eastern Montana. I: Natural clouds. *J. Appl. Meteor.*, **19**, 645–663, https://doi.org/10.1175/1520-0450(1980)019<0645:TSOSCC>2.0.CO;2.

Hong, Y., G. Liu, and J.-L. F. Li, 2016: Assessing the radiative effects of global ice clouds based on *CloudSat* and *CALIPSO* measurements. *J. Climate*, **29**, 7651–7674, https://doi.org/10.1175/JCLI-D-15-0799.1.

Huang, Y., A. M. Blyth, P. R. A. Brown, T. W. Choularton, and Z. Cui, 2017: Factors controlling secondary ice production in cumulus clouds. *Quart. J. Roy. Meteor. Soc.*, **143**, 1021–1031, https://doi.org/10.1002/qj.2987.

Jackson, R., J. R. French, D. C. Leon, D. M. Plummer, S. Lasher-Trapp, A. M. Blyth, and A. Korolev, 2018: Observations of the microphysical evolution of convective clouds in the southwest of the United Kingdom. *Atmos. Chem. Phys.*, **18**, 15329–15344, https://doi.org/10.5194/acp-18-15329-2018.

James, R. L., V. T. J. Phillips, and P. J. Connolly, 2021: Secondary ice production during the break-up of freezing water drops on impact with ice particles. *Atmos. Chem. Phys.*, **21**, 18519–18530, https://doi.org/10.5194/acp-21-18519-2021.

Jefferson, A., 2011: Aerosol Observing System (AOS) handbook. ARM Tech. Rep. ARM-TR-014, 32 pp, https://www.arm.gov/publications/tech_reports/handbooks/aos_handbook.pdf.

Jensen, M. P., and Coauthors, 2016: The Midlatitude Continental Convective Clouds Experiment (MC3E). *Bull. Amer. Meteor. Soc.*, **97**, 1667–1686, https://doi.org/10.1175/BAMS-D-14-00228.1.

Johnson, D. A., and J. Hallett, 1968: Freezing and shattering of supercooled water drops. *Quart. J. Roy. Meteor. Soc.*, **94**, 468–482, https://doi.org/10.1002/qj.49709440204.

Keinert, A., D. Spannagel, T. Leisner, and A. Kiselev, 2020: Secondary ice production upon freezing of freely falling drizzle droplets. *J. Atmos. Sci.*, **77**, 2959–2967, https://doi.org/10.1175/JAS-D-20-0081.1.

King, W. D., and N. H. Fletcher, 1976a: Thermal shock as an ice multiplication mechanism. Part I. Theory. *J. Atmos. Sci.*, **33**, 85–96, https://doi.org/10.1175/1520-0469(1976)033<0085:TSAAIM>2.0.CO;2.

——, and ——, 1976b: Thermal shock as an ice multiplication mechanism. Part II. Experimental. *J. Atmos. Sci.*, **33**, 97–102, https://doi.org/10.1175/1520-0469(1976)033<0097:TSAAIM>2.0.CO;2.

Kinne, S., and K.-N. Liou, 1989: The effects of the nonsphericity and size distribution of ice crystals on the radiative properties of cirrus clouds. *Atmos. Res.*, **24**, 273–284, https://doi.org/10.1016/0169-8095(89)90049-5.

Korolev, A. V., and I. P. Mazin, 2003: Supersaturation of water vapor in clouds. *J. Atmos. Sci.*, **60**, 2957–2974, https://doi.org/10.1175/1520-0469(2003)060<2957:SOWVIC>2.0.CO;2.

——, E. F. Emery, J. W. Strapp, S. G. Cober, G. A. Isaac, M. Wasey, and D. Marcotte, 2011: Small ice particles in tropospheric clouds: Fact or artifact? Airborne Icing Instrumentation Evaluation Experiment. *Bull. Amer. Meteor. Soc.*, **92**, 967–973, https://doi.org/10.1175/2010BAMS3141.1.

Kudzotsa, I., and Coauthors, 2016: Aerosol indirect effects on glaciated clouds. Part I: Model description. *Quart. J. Roy. Meteor. Soc.*, **142**, 1958–1969, https://doi.org/10.1002/qj.2791.

Ladino, L. A., A. Korolev, I. Heckman, M. Wolde, A. M. Fridlind, and A. S. Ackerman, 2017: On the role of ice-nucleating aerosol in the formation of ice particles in tropical mesoscale convective systems. *Geophys. Res. Lett.*, **44**, 1574–1582, https://doi.org/10.1002/2016GL072455.

Langmuir, I., 1948: The production of rain by a chain reaction in cumulus clouds at temperatures above freezing. *J. Atmos. Sci.*, **5**, 175–192, https://doi.org/10.1175/1520-0469(1948)005<0175:TPORBA>2.0.CO;2.

Lasher-Trapp, S., D. C. Leon, P. J. DeMott, C. M. Villanueva-Birriel, A. V. Johnson, D. H. Moser, C. S. Tully, and W. Wu, 2016: A multisensor investigation of rime splintering in tropical maritime cumuli. *J. Atmos. Sci.*, **73**, 2547–2564, https://doi.org/10.1175/JAS-D-15-0285.1.

——, E. L. Scott, E. Järvinen, M. Schnaiter, F. Waitz, P. J. DeMott, C. S. McCluskey, and T. C. J. Hill, 2021: Observations and modeling of rime splintering in Southern Ocean cumuli. *J. Geophys. Res. Atmos.*, **126**, e2021JD035479, https://doi.org/10.1029/2021JD035479.

Lawson, R. P., S. Woods, and H. Morrison, 2015: The microphysics of ice and precipitation development in tropical cumulus clouds. *J. Atmos. Sci.*, **72**, 2429–2445, https://doi.org/10.1175/JAS-D-14-0274.1.

Leisner, T., T. Pander, P. Handmann, and A. Kiselev, 2014: Secondary ice processes upon heterogeneous freezing of cloud droplets. *14th Conf. on Cloud Physics and Atmospheric Radiation*, Boston, MA, Amer. Meteor. Soc., 2.3, https://ams.confex.com/ams/14CLOUD14ATRAD/webprogram/Paper250221.html.

Lloyd, G., and Coauthors, 2020: Small ice particles at slightly supercooled temperatures in tropical maritime convection. *Atmos. Chem. Phys.*, **20**, 3895–3904, https://doi.org/10.5194/acp-20-3895-2020.

Ming, Y., V. Ramaswamy, L. J. Donner, and V. T. J. Phillips, 2006: A new parameterization of cloud droplet activation applicable to general circulation models. *J. Atmos. Sci.*, **63**, 1348–1356, https://doi.org/10.1175/JAS3686.1.

Möhler, O., and Coauthors, 2005: Effect of sulfuric acid coating on heterogeneous ice nucleation by soot aerosol particles. *J. Geophys. Res.*, **110**, D11210, https://doi.org/10.1029/2004JD005169.

Morrison, H., J. A. Curry, M. D. Shupe, and P. Zuidema, 2005: A new double-moment microphysics parameterization for application in cloud and climate models. Part II: Single-column modeling of Arctic clouds. *J. Atmos. Sci.*, **62**, 1678–1693, https://doi.org/10.1175/JAS3447.1.

Oraltay, R. G., and J. O. H. N. Hallett, 1989: Evaporation and melting of ice crystals: A laboratory study. *Atmos. Res.*, **24**, 169–189, https://doi.org/10.1016/0169-8095(89)90044-6.

Patade, S., S. Shete, N. Malap, G. Kulkarni, and T. V. Prabha, 2016: Observational and simulated cloud microphysical features of rain formation in the mixed phase clouds observed during CAIPEEX. *Atmos. Res.*, **169**, 32–45, https://doi.org/10.1016/j.atmosres.2015.09.018.

——, and Coauthors, 2021: Empirical formulation for multiple groups of primary biological ice nucleating particles from field observations over Amazonia. *J. Atmos. Sci.*, **78**, 2195–2220, https://doi.org/10.1175/JAS-D-20-0096.1.

Pauluis, O., and S. Garner, 2006: Sensitivity of radiative-convective equilibrium simulations to horizontal resolution. *J. Atmos. Sci.*, **63**, 1910–1923, https://doi.org/10.1175/JAS3705.1.

Phillips, V. T. J., 2021: Ice multiplication by fragmentation during quasi-spherical freezing of raindrops: A theoretical investigation. *J. Atmos. Sci.*, **78**, 3215–3228, https://doi.org/10.1175/JAS-D-20-0309.1.

——, A. M. Blyth, P. R. A. Brown, T. W. Choularton, and J. Latham, 2001: The glaciation of a cumulus cloud over New Mexico. *Quart. J. Roy. Meteor. Soc.*, **127**, 1513–1534, https://doi.org/10.1002/qj.49712757503.

——, T. W. Choularton, A. M. Blyth, and J. Latham, 2002: The influence of aerosol concentrations on the glaciation and precipitation of a cumulus cloud. *Quart. J. Roy. Meteor. Soc.*, **128**, 951–971, https://doi.org/10.1256/0035900021643601.

——, L. J. Donner, and S. T. Garner, 2007: Nucleation processes in deep convection simulated by a cloud-system-resolving model with double-moment bulk microphysics. *J. Atmos. Sci.*, **64**, 738–761, https://doi.org/10.1175/JAS3869.1.

——, P. J. DeMott, and C. Andronache, 2008: An empirical parameterization of heterogeneous ice nucleation for multiple chemical species of aerosol. *J. Atmos. Sci.*, **65**, 2757–2783, https://doi.org/10.1175/2007JAS2546.1.

——, and Coauthors, 2009: Potential impacts from biological aerosols on ensembles of continental clouds simulated numerically. *Biogeosciences*, **6**, 987–1014, https://doi.org/10.5194/bg-6-987-2009.

——, P. J. Demott, C. Andronache, K. A. Pratt, K. A. Prather, R. Subramanian, and C. Twohy, 2013: Improvements to an empirical parameterization of heterogeneous ice nucleation and its comparison with observations. *J. Atmos. Sci.*, **70**, 378–409, https://doi.org/10.1175/JAS-D-12-080.1.

——, A. Khain, N. Benmoshe, E. Ilotoviz, and A. Ryzhkov, 2015: Theory of time-dependent freezing. Part II: Scheme for freezing raindrops and simulations by a cloud model with spectral bin microphysics. *J. Atmos. Sci.*, **72**, 262–286, https://doi.org/10.1175/JAS-D-13-0376.1.

——, J.-I. Yano, and A. Khain, 2017a: Ice multiplication by breakup in ice–ice collisions. Part I: Theoretical formulation. *J. Atmos. Sci.*, **74**, 1705–1719, https://doi.org/10.1175/JAS-D-16-0224.1.

——, and Coauthors, 2017b: Ice multiplication by breakup in ice–ice collisions. Part II: Numerical simulations. *J. Atmos. Sci.*, **74**, 2789–2811, https://doi.org/10.1175/JAS-D-16-0223.1.

——, S. Patade, J. Gutierrez, and A. Bansemer, 2018: Secondary ice production by fragmentation of freezing drops: Formulation and theory. *J. Atmos. Sci.*, **75**, 3031–3070, https://doi.org/10.1175/JAS-D-17-0190.1.

——, and Coauthors, 2020: Multiple environmental influences on the lightning of cold-based continental cumulonimbus clouds.

Part I: Description and validation of model. *J. Atmos. Sci.*, **77**, 3999–4024, https://doi.org/10.1175/JAS-D-19-0200.1.

Prabhakaran, P., G. Kinney, W. Cantrell, R. A. Shaw, E. Bodenschatz, 2019: Ice nucleation in the wake of warm hydrometeors. arXiv, 1906.06129, https://arxiv.org/abs/1906.06129.

——, A. S. M. Shawon, G. Kinney, S. Thomas, W. Cantrell, and R. A. Shaw, 2020: The role of turbulent fluctuations in aerosol activation and cloud formation. *Proc. Natl. Acad. Sci. USA*, **117**, 16 831–16 838, https://doi.org/10.1073/pnas.2006426117.

Pruppacher, H. R., and R. J. Schlamp, 1975: A wind tunnel investigation on ice multiplication by freezing of waterdrops falling at terminal velocity in air. *J. Geophys. Res.*, **80**, 380–386, https://doi.org/10.1029/JC080i003p00380.

——, and J. Klett, 1997: *Microphysics of Clouds and Precipitation.* 2nd ed. Atmospheric and Oceanographic Sciences Library, Vol. 18, Kluwer Academic, 954 pp.

Rangno, A. L., 2008: Fragmentation of freezing drops in shallow maritime frontal clouds. *J. Atmos. Sci.*, **65**, 1455–1466, https://doi.org/10.1175/2007JAS2295.1.

——, and P. V. Hobbs, 2001: Ice particles in stratiform clouds in the Arctic and possible mechanisms for the production of high ice concentrations. *J. Geophys. Res.*, **106**, 15 065–15 075, https://doi.org/10.1029/2000JD900286.

Saleeby, S. M., S. C. van den Heever, P. J. Marinescu, S. M. Kreidenweis, and P. J. DeMott, 2016: Aerosol effects on the anvil characteristics of mesoscale convective systems. *J. Geophys. Res. Atmos.*, **121**, 10 880–10 901, https://doi.org/10.1002/2016JD025082.

Sotiropoulou, G., S. Sullivan, J. Savre, G. Lloyd, T. Lachlan-Cope, A. M. Ekman, and A. Nenes, 2020: The impact of secondary ice production on Arctic stratocumulus. *Atmos. Chem. Phys.*, **20**, 1301–1316, https://doi.org/10.5194/acp-20-1301-2020.

——, É. Vignon, G. Young, H. Morrison, S. J. O'Shea, T. Lachlan-Cope, A. Berne, and A. Nenes, 2021: Secondary ice production in summer clouds over the Antarctic coast: An underappreciated process in atmospheric models. *Atmos. Chem. Phys.*, **21**, 755–771, https://doi.org/10.5194/acp-21-755-2021.

Sullivan, S. C., C. Hoose, and A. Nenes, 2017: Investigating the contribution of secondary ice production to in-cloud ice crystal numbers. *J. Geophys. Res. Atmos.*, **122**, 9391–9412, https://doi.org/10.1002/2017JD026546.

Sun, J., P. A. Ariya, H. G. Leighton, and M. K. Yau, 2012: Modeling study of ice formation in warm-based precipitating shallow cumulus clouds. *J. Atmos. Sci.*, **69**, 3315–3335, https://doi.org/10.1175/JAS-D-11-0344.1.

Takahashi, T., Y. Nagao, and Y. Kushiyama, 1995: Possible high ice particle production during graupel–graupel collisions. *J. Atmos. Sci.*, **52**, 4523–4527, https://doi.org/10.1175/1520-0469(1995)052<4523:PHIPPD>2.0.CO;2.

Tao, W.-K., and J. Simpson, 1989: Modeling study of a tropical squall-type convective line. *J. Atmos. Sci.*, **46**, 177–202, https://doi.org/10.1175/1520-0469(1989)046<0177:MSOATS>2.0.CO;2.

Uin, J., 2016: Cloud Condensation Nuclei Particle Counter (CCN) instrument handbook. ARM Rep. DOE/SC-ARM-TR-168, 16 pp.

Vardiman, L., 1978: The generation of secondary ice particles in clouds by crystal–crystal collision. *J. Atmos. Sci.*, **35**, 2168–2180, https://doi.org/10.1175/1520-0469(1978)035<2168:TGOSIP>2.0.CO;2.

Xie, S., Y. Zhang, S. E. Giangrande, M. P. Jensen, R. McCoy, and M. Zhang, 2014: Interactions between cumulus convection and its environment as revealed by the MC3E sounding array. *J. Geophys. Res. Atmos.*, **119**, 11 784–11 808, https://doi.org/10.1002/2014JD022011.

Xu, K.-M., 1995: Partitioning mass, heat, and moisture budgets of explicitly simulated cumulus ensembles into convective and stratiform components. *J. Atmos. Sci.*, **52**, 551–573, https://doi.org/10.1175/1520-0469(1995)052<0551:PMHAMB>2.0.CO;2.

Yang, J., H. Lei, Z. Hu, and T. Hou, 2014: Particle size spectra and possible mechanisms of high ice concentration in nimbostratus over Hebei Province, China. *Atmos. Res.*, **142**, 79–90, https://doi.org/10.1016/j.atmosres.2013.12.018.

Yano, J.-I., and V. T. J. Phillips, 2011: Ice–ice collisions: An ice multiplication process in atmospheric clouds. *J. Atmos. Sci.*, **68**, 322–333, https://doi.org/10.1175/2010JAS3607.1.

Yau, M. K., and R. R. Rogers, 1996: *A Short Course in Cloud Physics.* 3rd ed. Elsevier, 304 pp.

Young, G., T. Lachlan-Cope, S. J. O'Shea, C. Dearden, C. Listowski, K. N. Bower, T. W. Choularton, and M. W. Gallagher, 2019: Radiative effects of secondary ice enhancement in coastal Antarctic clouds. *Geophys. Res. Lett.*, **46**, 2312–2321, https://doi.org/10.1029/2018GL080551.

Zhao, X., and X. Liu, 2021: Global importance of secondary ice production. *Geophys. Res. Lett.*, **48**, e2021GL092581, https://doi.org/10.1029/2021GL092581.

——, ——, V. T. J. Phillips, and S. Patade, 2021: Impacts of secondary ice production on Arctic mixed-phase clouds based on ARM observations and CAM6 single-column model simulations. *Atmos. Chem. Phys.*, **21**, 5685–5703, https://doi.org/10.5194/acp-21-5685-2021.

Paper 4

Mechanisms for Indirect Effects from Solid Aerosol Particles on Continental Clouds and Radiation

Deepak Waman[1*], Akash Deshmukh[1], Arti Jadav[1], Sachin Patade[1], Martanda Gautam[1,2], and Vaughan Phillips[1]

[1]Department of Physical Geography and Ecosystem Science, Lund University, Lund, Sweden

[2]Johannes Gutenberg University, Mainz, Germany

*Corresponding author
Deepak Waman, Lund University, Sweden
Email: deepak.waman@nateko.lu.se, deepakwaman11@gmail.com

Abstract

Mechanisms of the aerosol indirect effects (AIE) from ice nucleating particles (INPs) are investigated by using a cloud-resolving 'Aerosol-Cloud' (AC) model with a hybrid bin-bulk microphysics scheme coupled with a radiation scheme in: 1) continental deep convection observed during the Midlatitude Continental Convective Cloud Experiment (MC3E) over Oklahoma, and 2) supercooled stratiform clouds observed during Aerosol Properties, Processes And Influences on the Earth's climate (APPRAISE) campaign over Larkhill, UK. In both cases, the sensitivity of cloud micro-, macrophysical and associated radiative properties are examined with respect to anthropogenic INPs. For both cases, anthropogenic INPs reduce the mean sizes of cloud-droplets and ice-crystals, boosting their concentrations by 10-30%. Furthermore, in both cases, cloud extents and optical thicknesses increases with anthropogenic solid APs.

For both cases, anthropogenic INPs cause a net cooling (~ -0.4 W m^{-2}) in APPRAISE, and a net warming (~ 4.5 W m^{-2}) in MC3E, chiefly from glaciated clouds ($\sim 80\%$ of the net AIE). The role of ice formation processes, such as secondary ice production (SIP) and time dependent INP freezing in the simulated AIEs are estimated. Artificially prohibiting SIP causes little change in the net AIE (1% increase) in APPRAISE whereas this change is stronger for MC3E (50% decrease), chiefly from glaciated clouds. In the absence of time dependence, the absolute magnitude of the AIE is weakened by about 30% in APPRAISE and by about 80% in MC3E, relative to control AIEs, mainly due to a strong reversal ($> \pm 105\%$) in the aerosol-sensitivity of the AIE from glaciated clouds.

Keywords: Aerosol indirect effects, cloud radiative effects, anthropogenic aerosols, ice nucleating particles, secondary ice, cloud-resolving model

1. Introduction

Anthropogenic activity can greatly influence the tropospheric loading of aerosol particles (APs) such as sulfate, mineral dust, and black carbon (soot), (Haywood and Boucher 2000). These APs can affect the radiative budget of the Earth by modifying the microphysical and hence radiative properties of the clouds, affecting also the cloud lifetimes and extent (Haywood and Boucher 2000; Cantrell and Heymsfield, 2005; Koren *et al*., 2010; Bollasina *et al*., 2011; Wang *et al*. 2014; Kudzotsa *et al*. 2016; Phillips *et al*., 2022). Hence, they can act as an important driver of climate forcing (Boucher et al., 2013; Chen *et al*. 2000).

Clouds are a major regulator of the Earth's radiation budget and cover about 30-50% of the globe (Flossmann, 1998; King et al., 2013) and significantly modulate solar radiative heating (Lohmann and Feichter, 2005; Chen *et al*. 1999). On a global scale, clouds cause a net cooling by modifying the net radiative flux entering the earth system, predominantly by reflecting incoming solar radiation to space (Lohmann and Feichter 2005). However, depending on its altitude and cover in the atmosphere, any cloud can cause a net cooling (low to mid-level clouds) or a net warming (high-level clouds) (Koch and Genio, 2010).

The change in the net radiative flux at the top of the atmosphere (TOA) is known as the radiative forcing (RF), (e.g., Lohmann 2006). RF from changes in aerosol loading can occur through mainly two mechanisms: 1) a *direct effect* in which APs cause absorption and scattering of the incoming shortwave (SW) radiation and absorption and re-emission of the longwave (LW) radiation; 2) APs can influence climate *indirectly* through various aerosol-cloud feedbacks, known as the *aerosol indirect effect* (AIE) (Twomey 1974; Penner *et al*., 2001; Grabowski 2006; Hill and Dobbie, 2008; Gettelman *et al*., 2012; Boucher *et al*., 2013).

In its first indirect effect, known as the '*Twomey effect*' (Twomey 1974; Penner *et al*., 2001; Boucher *et al*., 2013) or '*cloud albedo effect',* APs can modify the cloud microphysical structure by acting as cloud condensation nuclei (CCN) or ice nucleating particles (INP) and thereby affecting the cloud albedo (fraction of incoming solar radiation reflected to space). This TOA radiative flux change involves a change in cloud properties, and occurs even if the cloud extent is unaltered. A similar effect must occur with absorption of long-wave radiation, depending on the emissivity of the cloud being altered (e.g. Kudzotsa et al. 2016). Thus, we refer to this extended effect as the '*cloud-albedo/emissivity effect*', instead of the Twomey effect.

APs can also affect the extent of the clouds and hence their lifetime through the changes to the precipitation efficiency, which is known as the second indirect effect ('*cloud lifetime effect*'), (Quaas *et al*. 2006; Hill and Dobbie, 2008). In addition to these two effects, APs also have a *semi-direct effect* in which absorbing APs can cause heating which may lead to the evaporation of cloud hydrometeors (Lohmann and Feichter, 2001; Hill and Dobbie 2008; Johnson *et al*. 2003; Koch and Genio, 2010). An observational study with satellite data by Toll *et al*. (2019) estimated that the Twomey effect dominates over the cloud lifetime effect as heating due to absorbing APs cause the evaporation of cloud droplets. However, such purely observational studies can be challenged by the task of inferring causation because only correlations are observed.

Compared to pre-industrial times, the global loading of anthropogenic APs has increased in the present day by about 50 to 90%, depending on the species (Lohmann and Feichter, 2005; Takemura 2012; also Sec. 2, Table 4). Although the residence time of any given AP is of the order of magnitude of a week, the approximate balance between global emissions into the

atmosphere and removal by wet and dry deposition (depending on the loading) implies that stronger emissions boost the average AP loading. Higher aerosol loadings in the earth's atmosphere cause smaller mean sizes and higher number concentrations of cloud droplets, enhancing the cloud albedo and causing a net cooling in global simulations by the cloud albedo effect (Lohmann and Feichter, 2005; Christensen *et al*. 2016).

Below the -36°C level, the INP activity of solid APs such as mineral dust, soot, insoluble organics, and primary biological aerosol particles (PBAPs) initiates primary ice (DeMott 1990; Phillips *et al*. 2008, 2009, 2013; Patade *et al*. 2021). Mineral dust is an effective INP (Hoose & Möhler, 2012; Kanji *et al*. 2017). Anthropogenic emissions of soluble aerosol material can be closely related to the distribution and INP activity of solid APs due to their internal mixing (Cziczo *et al*. 2009; Bellouin *et al*. 2019). Also, at these levels, various mechanisms of secondary ice production (SIP) can cause an explosive production of ice-crystals (Hobbs et al. 1980; Field et al. 2017; Lawson et al. 2017; Phillips et al. 2017, 2018; Lasher-Trapp et al. 2021), especially in clouds with relatively high convective motions and high mass of cloud-liquid and cloud-ice (Waman et al. 2022, 'Wa22'; 2023, 'Wa23'). However, in thin layer clouds with weak precipitation (< 1 mm/hr), SIP is weak (Westbrook and Illingworth, 2013) or can be completely absent (Eidhammer et al. 2010).

At levels colder than the -36°C, overall ice initiation is dominated by homogenous freezing of haze/cloud droplets and solute aerosols typically in the convective cores and cirriform weak ascent of deep convective systems (Phillips *et al*. 2007, 2009). This suggests that at cirrus levels, increasing emission of soluble APs such as sulfate may enhance the number concentrations of haze/cloud droplets, boosting the number concentrations of ice crystals through homogeneous freezing (Kudzotsa *et al*. 2016b, 2018; Bellouin *et al.* 2019). This increasing ice crystal numbers in cirriform clouds trap more LW and reflect more SW radiation, with a net warming of the atmosphere. However, the radiative response of cirriform clouds strongly depends on updrafts and the process of ice nucleation through which they form (Bellouin *et al*. 2019). A modelling study by DeMott *et al*. (1997) suggests that heterogeneous INP activity can significantly influence the cloud radiative forcing in cirriform clouds compared to homogeneous freezing. A recent study by Krämer *et al*. (2016) shows that homogeneously formed thin cirrus clouds with mild updrafts induce a net warming effect whereas thick cirrus clouds associated with fast updrafts and formed by heterogeneous freezing cause a net cooling.

The present study aims to investigate the responses of cloud micro-, macrophysical and radiative properties to anthropogenically increased solid APs. This is done by performing various sensitivity tests involving modifications in the solid aerosol fields. This study, using a 3D mesoscale domain, evaluates the role of cloud microphysical processes on glaciated cloud indirect effects arising from anthropogenically boosted solid APs. Here, the term 'glaciated clouds' refers to clouds that are either in mixed-phase or ice-only. A hypothesis being tested is that solid aerosol pollution modifies glaciated clouds via homogeneous freezing of aerosols and supercooled droplets. Furthermore, the impact on the simulated AIEs from the ice formation processes such as SIP and time dependence of INP freezing are also estimated.

The structure of the paper is as follows. Section 2 describes the cases of storms that were simulated with our 'Aerosol-Cloud' (AC) model. The case setup and description of AC are given in Sec. 3. Results from various sensitivity tests are discussed in Sections 4. Finally, Sec. 5 discusses conclusions.

2. Details of Field Campaigns and Numerical Model

The present study focuses on two different campaigns from different periods and geographical locations. These are: 1) the wintertime supercooled stratiform clouds observed during Aerosol Properties, Processes And Influences on the Earth's climate (APPRAISE) campaign over the southern UK, and 2) summertime deep convective clouds with widespread stratiform precipitation observed during the Midlatitude Continental Convective Cloud Experiment (MC3E) over Oklahoma, USA. The MC3E and APPRAISE campaigns are described in detail by Wa22, Wa23, respectively, and are briefly discussed as follows.

2.1 Field campaigns
2.1.1 APPRAISE

APPRAISE observed a case of supercooled stratiform clouds covering an area of about 100 km in width with embedded convection over the southern UK on 18 February 2009 (Crosier *et al.* 2011). These clouds were observed to precipitate for a period of more than a day (Westbrook and Illingworth 2013). The cloud base and top were at about 6 and −13°C respectively, whereas the atmosphere above the cloud top was characterized by a temperature inversion with a difference of about 4 K. Above cloud top, the environment was dry with a relative humidity of less than about 30%. Horizontal and vertical wind speeds were weak (< 3 m s^{-1}) throughout the atmosphere up to the cloud top.

2.1.2 MC3E

The MC3E campaign was carried out by the National Aeronautics and Space Administration's (NASA) global precipitation measurement and Department of Energy (DoE) Atmospheric Radiation Measurement (ARM) program over north-central Oklahoma, USA between 22 April and 6 June 2011. In the present study, the case of the mesoscale convective system (MCS), consisting of deep convective clouds observed on 11 May 2011 (0900 to 2400 UTC) during the MC3E campaign has been analyzed. Jensen *et al.* (2016) and Wa22 and Wa23 provide details about the aircraft and ground-based measurements, observed properties of cloud hydrometeors, and large-scale forcing (LSF) conditions of the selected case.

2.2 Aerosol-Cloud model

The numerical model used in the present study is AC which is a type of non-hydrostatic, cloud-resolving model. It uses the software infrastructure and dynamical core of the Weather Research and Forecasting (WRF) model (Dudhia 1989; Skamarock *et al.* 2005), with a hybrid spectral bin-two-moment bulk microphysics package (Phillips *et al.* 2007; 2008; 2009; 2013; 2014; 2015b; 2017a, 2018; 2020). AC uses a semiprognostic aerosol scheme and predicts mass and number mixing ratios (double-moment approach) of cloud hydrometeors such as cloud-liquid, cloud-ice (crystals), and precipitation particles such as rain, snow, and graupel/hail. AC tracks components of APs in the air interstitially and immersed in precipitation and in clouds. AC initiates cloud droplets at the cloud-base (Ming *et al.* 2006) and at in-cloud levels far above the cloud-base from the supersaturation resolved on the model grid through the activity of soluble APs such as ammonium sulfate, sea salt, and soluble organics.

Insoluble APs such as mineral dust, soot, and groups of PBAPs [fungi, bacteria, pollen, algae, and detritus (Patade *et al.* 2021)] initiate primary ice in AC through heterogeneous ice nucleation. These insoluble APs can also initiate droplets as they tend to have hydrophilic coatings or are wettable, with activity predicted by kappa-Kohler theory (Petters and Kreidenweis 2007). The empirical parameterization [EP, Phillips *et al.* 2008, 2013] predicts the INP activity of these APs which represents all modes of INP activation (e.g., contact,

deposition, condensation, and immersion freezing) depending on the surface area mixing ratio of each AP type and supersaturation. Improvements to the EP described in Jakobsson *et al.* (2022) and Wa23 is also incorporated in AC, such as representation of time-dependence of INP activity.

AC uses our own implementation of the Geophysical Fluid Dynamics Laboratory (GFDL) radiation scheme (Friedreich and Ramaswamy, 1999) in which scattering of SW and LW radiation depends on the effective and generalized effective size of cloud-liquid and cloud-ice. The GFDL radiation scheme used in AC takes mean sizes of cloud droplets and ice-crystals as inputs to calculate the SW and LW fluxes at model levels. This scheme does not predict the direct effect of aerosols.

Homogeneous ice nucleation in AC occurs through two mechanisms above the -36°C level. First, spontaneous freezing of APs, supercooled cloud drops, and raindrops. There is preferential evaporation of the smaller cloud droplets in the size distribution that freeze later during ascent through the layer of homogeneous freezing of cloud liquid (about -35 to -37°C), with a lookup table (Phillips et al. 2007). Second, homogeneous freezing of soluble AP that occurs at colder temperatures as soon as a critical supersaturation is exceeded with respect to ice which depends on the temperature and size of APs (Koop *et al.* 2000; Phillips *et al.* 2007). Finally, components of mass and number concentrations of ice-crystals and snow formed in various ice formation processes were tracked by passive variables ('tagging tracers'). These tagging tracers do not interact with other processes.

2.2.1 Experimental setup

For both cases (APPRAISE and MC3E), the initial vertical profiles of mass concentrations of various APs described above are prescribed using the Goddard Chemistry Aerosol Radiation and Transport (GOCART) model for the same month and location. These vertical profiles are then rescaled using a constant factor at the surface to match them with the observations from the Interagency Monitoring of Protected Visual Environments (IMPROVE) sites close to the simulation domain for the MC3E (Table 1). For the APPRAISE case, monthly mean data from the Modern-Era Retrospective analysis for Research and Applications version-2 (MERRA2) at the surface ($\sim$ 300 m MSL) (Table 1). Corrections were applied to MERRA2-derived mass concentrations of soot and soluble organics to match the predicted CCN activity spectrum with previous maritime observations (e.g., Hoppel *et al.* 1990; Jennings *et al.* 1998).

Aerosol species	Mass concentrations (μg m^{-3})	
	APPRAISE	MC3E
Ammonium sulfate	1.8	0.7
Sea salt	8.0	0.06
Mineral dust	8.7	0.17
soot	4.6	0.25
Soluble organic	1.24	1.36
Non-biological insoluble organics (50% of insoluble organics)	0.28	0.17
PBAP (50% of insoluble organics) 1. Fungi 2. Bacteria 3. Pollen 4. Detritus 5. Algae	 0.14 0.055 0.0018 0.0033 3.58×10^{-5}	 0.17 0.067 0.022 0.054 4.3×10^{-5}

Table 1: Aerosol mass mixing ratios near the ground, inferred from the observations for various APs in AC for the case of (a) APPRAISE, monthly mean (February 2009) values from the MERRA2-GIOVANNI model, and for (b) MC3E (averaged for 09 and 12 May 2011), both from the IMPROVE measurements at stations near the study domain. PBAP measurements from Amazonia (Patade et al. 2021) are used to prescribe the total PBAP mass (assumed to be about 50% of the coincident organic mass) among the five PBAP groups, according to the same ratio. None of the PBAP groups is either observed or available from global models.

Both APPRAISE and MC3E cases have been simulated by AC for a 3D mesoscale domain in an idealized way, in the sense that no attempt is made to predict the exact locations of the clouds. For both simulations, the LSF tendencies in vapor mixing ratio (q_v) and potential temperature (θ) are applied and updated hourly and interpolated continuously over time between updates. Lateral boundary conditions are periodic in both east-west and east-west directions. Table 2 summarises the details of the experimental set-up followed to simulate the observed cases (Sec. 2.1) and are described briefly as follows.

i.   APPRAISE

The APPRAISE case (Sec. 2.1.1) is simulated over a domain of 80 x 80 km with 2 km grid-spacing along x and y directions for 48 hours (17 Feb 2009 00:00 UTC to 19 Feb 2009 00:00 UTC). Convection was initialized by adding random perturbations of about $\pm$ 0.8 g kg^{-1} to the initial vapor mixing ratio in the lowest 2 km. The first 24 hours is considered as a spin-up time of the model (Wa23).

ii.   MC3E

The observed MC3E case (Sec. 2.1.2) is simulated for a domain of 80 x 80 km for a 2 km grid resolution. Periodic lateral boundary conditions are applied in both the x and y directions. Also, the observed fluxes of moisture and heat are prescribed at the surface. To dampen the reflection of gravity waves at the model top, a sponge layer with a thickness of 6 km is applied. Random perturbations ($\sim \pm$0.06 g kg^{-1}) are added to the initial vapor mixing ratio in the first 2 km of the atmosphere from the surface.

Domain properties	Simulated case	
	APPRAISE	**MC3E**
date	18 February 2009	11 May 2011
Simulation time (hours)	48 (From 17 Feb 00:00 UTC to 19 Feb 00:00 UTC)	72 (From 10 May 00:00 UTC to 13 May 00:00 UTC)

Domain width (km) along
  i. x direction
  ii. y direction
	80
	80	

Boundary conditions	Periodic along x and y directions	
Horizontal resolution (dx and dy) (km)	2.0	
vertical resolution (dz) (km)	0.5	
Model top (km)	16 MSL	
time-step (sec)	10	

Table 2. Details of the domain for the simulated APPRAISE and MC3E cases.

2.3   Secondary ice production mechanisms

Four SIP processes incorporated in AC to form secondary ice (Phillips *et al*. 2017a, b, 2018; Deshmukh *et al*. 2021; Wa22; Wa23) and are as follows:

i.   The Hallett-Mossop process of rime-splintering

AC treats the rime-splintering process (Hallett and Mossop [HM] 1974) in which small splinters of ice get emitted during the riming of supercooled cloud droplets between −3 and −8°C. This HM process mainly occurs in clouds with a warm base (e.g., Lawson *et al*. 2015; Wa22) as it requires cloud droplets bigger than 24 μm (Mossop 1976). AC treats this process with a factor dependent on cloud-droplet size. This factor is zero and unity for mean cloud-droplet diameters less than 16 μm and greater than 24 μm, respectively, and is interpolated linearly in between. The maximum rate of splinter emission was seen to be 350 splinters per mg of rime particle and is at the −5°C level.

ii.   Fragmentation in ice-ice collisions

AC represents fragmentation in ice-ice collisions and is based on the principle of conservation of energy. It is dependent on ice particle morphology/size, temperature, and collision kinetic energy. More details can be found in Phillips *et al*. (2017a, b). The treatment was recently updated in light of observations by Martanda (2022), indicating more breakup by dendritic crystals/snow than treated previously.

iii.   Fragmentation in raindrop freezing

The third mechanism by which AC forms secondary ice is fragmentation during drizzle/raindrop freezing (Phillips *et al*. 2018). There are two modes of fragmentation in raindrop freezing. In the first mode ('quasi-spherical freezing'), during freezing of a supercooled drop (0.05 to 5 mm in diameter), following its collision with a less massive ice particle, splinters of secondary ice are emitted when the outer shell breaks. In its second mode ('non-spherical freezing'), a collision between a more massive ice particle and a raindrop emits

8

secondary droplets (e.g. in a splash). Some of these (30%) contain ice such that they freeze. More details can be found in Phillips *et al*. (2018) and James *et al*. (2021).

iv.   Fragmentation in sublimation of dendritic snow and graupel

Another empirical formulation that forms secondary ice in AC is fragmentation during the sublimation of dendritic snow and graupel (Deshmukh *et al*. 2021). This formulation is based on previous studies such as those by Oraltay and Hallett (1989), Dong *et al*. (1994), and Bacon *et al*. (1998). Fragmentation during sublimation is found to be more prolific in deep convective descent and requires a minimum subsaturation with respect to ice (Deshmukh *et al.* 2021; Wa22).

3. Methodology of simulations to analyze indirect effects

The focus of the present study is to investigate the mechanisms for AIE via glaciated clouds due to anthropogenic emissions of solid APs. In the present study, any cloud containing any ice is considered a 'glaciated cloud' and it can be either ice-only or mixed-phase.

For APPRAISE and MC3E, both present-day and pre-industrial runs (Sec. 2.2) are simulated with the present-day thermodynamic conditions for a model forcing. For APPRAISE and MC3E, two simulations have been performed. These are: 1) present-day run simulated with the present-day aerosol loadings, and 2) pre-industrial run simulated with the pre-industrial aerosol conditions from 1850s. The purpose of the present study is to study the indirect effects from changing aerosol loadings.

Pre-industrial conditions of solid aerosol follow a modeling study of the global distribution of APs from the pre-industrial (1850) to the future (2100) by Takemura (2012). The adjustment factor, modifying the present-day loading, for each solid AP is shown in Table 3 for pre-industrial simulations. The same factor is applied to both cases (MC3E and APPRAISE). Among all the solid APs, soot is the most affected AP among all solid aerosol species whereas soluble organic and biological APs have no change.

However, there is no unique way to estimate the pre-industrial aerosol loading. For example, previous studies (Morrison and Grabowski 2011; Fan *et al*. 2013) have used a single arbitrary factor (of up to about 6) to all aerosol species to derive pre-industrial aerosol concentrations. Hence, the present study may have uncertainties in deriving pre-industrial aerosol conditions.

Solid aerosol species	Adjustment factor
Mineral dust	0.9
Soot	0.4
Soluble organics	1.0
Biological	1.0

Table 3. Fractional changes in mass concentrations of solid aerosol species from pre-industrial (1850) times to the present day (2000) were inferred from Takemura (2012).

To estimate the cloud albedo-emissivity and lifetime indirect effects, for the deep convection (MC3E) and supercooled stratiform clouds (APPRAISE), various sensitivity tests have been performed following Kudzotsa *et al*. (2016b). We classified these tests under '*Test A'* which predicts the net and albedo-emissivity AIE, and '*Test B'* which gives lifetime AIE. A range of simulations (Table 5) were carried out with Tests A and B to estimate the net indirect effects, and impact on these simulated AIEs from processes of ice initiation such as 1) time dependent INP freezing, and 2) SIP.

Simulation	Description
Control	Includes all SIP processes, time dependent INP freezing and homogeneous freezing
No time dependent INP	Excludes time dependent INP freezing from the control run.
No SIP	Excludes all SIP processes from the control run.

Table 4. *Description of simulations performed for the simulated APPRAISE and MC3E cases.*

These sensitivity tests are described as follows for the control simulation.

3.1.1 Test A: The Total and Albedo-Emissivity AIE

i. The total aerosol indirect effect

To estimate the total AIE, a pair of simulations have been performed for each of both cases (APPRAISE and MC3E): 1) present-day, and 2) pre-industrial simulation as described above (Table 5). For the simulated mesoscale region, the difference in net radiative fluxes at the top of the atmosphere (TOA, at the model top) between the present-day ($Q_{PRESDAY}$) and pre-industrial (Q_{PREIND}) simulations gives the total or net aerosol indirect effect (Q_{net}) (Gettelman *et al.* 2012; Lohmann *et al.* 2006; Kudzotsa *et al.* 2016).

$$Q_{net} = Q_{PRESDAY} - Q_{PREIND} \qquad (1)$$

ii. Albedo-Emissivity AIE

The albedo-emissivity indirect effect is evaluated by changing the mean sizes of cloud particles that are the inputs to the GFDL radiation scheme (Sec. 2.2) with passive extra calls to it. The first calls are active calls that influence the meteorology of the simulations. The difference in net radiative fluxes at the TOA between the present-day and pre-industrial simulations predicted using these first calls gives the net radiative flux (Q_{net}), as discussed above.

The second call to the radiation driver is designed for diagnostic purposes only and it does not alter the microphysics of the simulation. In this call, the response of cloud radiative properties to changes in aerosol loadings is eliminated by using temperature and vertical velocity-dependent look-up tables of the mean sizes of cloud droplets and cloud-ice, instead of the mean sizes predicted by the model. Applying Eq (1) to the second calls of both the present-day and pre-industrial runs gives a hypothetical net radiative flux at the TOA (Q_{net_life}), which is the total lifetime AIE. Finally, subtracting Q_{net_life} from Q_{net} gives the total albedo-emissivity indirect effect (Q_{net_alb}).

By using the technique discussed above, the albedo-emissivity and lifetime indirect effects can be calculated for a targeted cloud type by repeating the above procedure, except with the passive call to the radiation scheme (look-up table of particle mean sizes) being only applied inside the targeted cloud type. Note that the same lookup tables, derived from the present-day run, have been used for both the present-day and pre-industrial simulations.

In a given time step, a model grid point is said to be glaciated when the cloud-liquid and/or cloud-ice mixing ratios are non-zero. To simplify the analysis, clouds that are supercooled but liquid-only are counted as glaciated. On the other hand, model grids containing non-zero cloud-ice and zero cloud-liquid mixing ratios are identified as *ice-only* clouds.

Specifically, to estimate the albedo-emissivity indirect effect of glaciated clouds (Q_{alb_glc}), the cloud droplet and ice crystal mean sizes are prescribed using look-up tables in glaciated clouds and the technique described above is repeated. The albedo-emissivity effect of ice-only clouds (Q_{alb_ice}) is estimated by fixing the mean sizes of ice crystals in ice-only clouds. The aerosol indirect effects for the mixed-phase clouds are estimated by subtracting the indirect effects of ice-only clouds from that of glaciated clouds.

3.1.2 Test B: The Lifetime AIE

To determine the lifetime indirect effects from aerosols of a targeted cloud type, the sensitivity of certain microphysical processes with respect to changes in solid aerosol loading is eliminated

by using look-up tables of sizes and/or number concentrations of cloud droplets and ice crystals. These look-up tables are temperature and vertical velocity dependent and the same look-up tables have been used for both the present-day and pre-industrial simulations. Application of these look-up tables during each simulation affects the predicted meteorology.

i.   Lifetime indirect effects for glaciated clouds

To isolate all indirect effects from glaciated clouds, first all indirect effects from liquid-only clouds are eliminated. This is done by simultaneously fixing the sizes or number concentrations of cloud droplets in the microphysical processes associated with liquid-only clouds. These microphysical processes are collision-coalescence, sedimentation, and auto-conversion that depend on cloud droplet number concentrations, and radiative properties that depend on cloud droplet sizes.

The difference in the TOA net radiative fluxes between the present-day and pre-industrial simulations, performed with look-up tables for these microphysical processes and with passive second calls to the radiation scheme in liquid-only cloud, gives the net radiative flux without any indirect effects from liquid-only clouds at levels warmer than $0°C$ (Q_{hyp_glc}). Finally, by subtracting the Q_{alb_glc} (test A) from Q_{hyp_glc} gives the estimate of the lifetime indirect effects from glaciated clouds (Q_{life_glc}).

ii.   Lifetime indirect effects for ice-only and mixed-phase clouds

To estimate the lifetime indirect effects from ice-only clouds, the responses of the aerosol-dependent microphysical processes of ice-only clouds are eliminated from the present-day and pre-industrial simulations by using look-up tables of ice crystal number concentrations and sizes. Yet responses of microphysical processes to changes in aerosol loading are allowed in mixed-phase and liquid-only clouds. The microphysical processes associated with ice-only clouds are auto-conversion of cloud-ice to snow, sedimentation of cloud-ice, aggregation of graupel and cloud-ice, aggregation of cloud-ice with snow. Additionally, the passive second call to the radiation scheme is used with the same look-up table for ice-only clouds to eliminate their albedo-emissivity effect.

The difference in the TOA net radiative fluxes between the present-day and pre-industrial simulations, performed using look-up tables for these microphysical processes and radiative properties in ice-only clouds, gives a hypothetical net radiative flux for liquid-only and mixed-phase clouds ($Q_{hyp\_net\_liq\_mix}$). By subtracting $Q_{hyp\_net\_liq\_mix}$ from the Q_{net} determined in Test A gives the net indirect effects from ice-only clouds (Q_{net_ice}). Finally, by subtracting Q_{alb_ice} from Q_{net_ice} gives the lifetime indirect effects from ice-only clouds (Q_{life_ice}).

The indirect effects from mixed-phase clouds are determined by subtracting the indirect effects of ice-only clouds from those of glaciated clouds (Sec. 3.1.2i).

3.1.3 The radiative effects from the time dependence of INP freezing

To estimate the effects on the net AIEs predicted above (Sec. 3.1.1-3.1.2) arising from the time dependence of heterogeneous ice nucleation, a sensitivity test is performed. In this test, the time dependent approach of INP freezing is prohibited from the control simulation ('no time dependent INP' run, Table 4). This 'no time dependent INP' run is simulated with both present-day and pre-industrial aerosol conditions. Then, by applying the techniques discussed in Tests

A and B, the alteration of indirect effects of solid aerosols arising from inclusion of time-dependent freezing of INPs is estimated.

For each targeted cloud type, these indirect effects from 'no time dependent INP' runs are subtracted from those of the control runs (Sec. 3.1.1-3.1.2). Note that the same look-up tables for particle mean sizes and number concentrations from the present-day control simulation are used to perform 'no time dependent INP' simulations.

3.1.4 The radiative effects from secondary ice production

To analyze the impact from SIP on the net AIEs predicted from the control runs, a sensitivity test ('no SIP' run, Table 4) is performed with both present-day and pre-industrial solid aerosol loadings (Table 4). Since SIP significantly affects the mean sizes and number concentrations of cloud-droplets and ice-crystals, separate look-up tables are used to estimate the contributions from SIP to the net indirect effects. These look-up tables involve dependencies on temperature and vertical velocity and are made from the present-day 'no SIP' simulation.

By repeating Tests A and B (Sec. 3.1.1-3.1.2) for targeted cloud types without SIP, their indirect effects from solid aerosol can be estimated following similar technique. Finally, the relative contribution to the net indirect effects from the SIP activity in the control simulation is calculated by subtracting the indirect effects predicted in 'no SIP' simulations from those of the control runs (Sec. 3.1.1-3.1.2).

4. Results from simulations of supercooled layer clouds (APPRAISE) and deep convection (MC3E)

In this section, the responses of cloud microphysical properties and radiative fluxes to changes in solid aerosol loadings are analyzed in the simulated supercooled layer (APPRAISE) and continental deep convective clouds (MC3E). Note that for both cases, microphysical properties such as the mean sizes and number concentrations of cloud droplets, liquid water contents, and filtered ice concentrations predicted in the present-day control simulation have been adequately validated against coincident aircraft and ground-based observations, as shown by Wa22 (for MC3E) and Wa23 (for MC3E and APPRAISE).

4.1   Net Aerosol Indirect Effect

4.1.1 Response of Microphysical Properties

The control run (Table 5) is performed with the present day and pre-industrial aerosol loadings (Test A, Sec. 3.1.1). The responses of microphysical properties from changing aerosol loadings for the simulated supercooled stratiform and deep convective clouds are discussed here. All the plots (Fig. 1a-d) shown below include solid black and dotted red lines, representing the results from the present-day and pre-industrial aerosol conditions, respectively.

Figure 1 shows a comparison of the mean diameters (Fig.1a-b) and number concentrations (Fig. 1c-d) of cloud-droplets between the present-day and pre-industrial simulations in the stratiform regions ($|w| < 1$ m s^{-1}). It is predicted that the droplet mean sizes are lower by 20% in the present-day run compared to the pre-industrial simulations of the APPRAISE and MC3E clouds at most levels (Fig.1a-b). Moreover, the droplet number concentrations are predicted to increase by 20% in the present-day run relative to the pre-industrial simulation of these clouds (Fig.1c-d). These changes in mean sizes and number concentrations of cloud droplets arise mainly from the CCN activity of solid APs at all levels both above and below the freezing level.

Also, in the stratiform regions ($|w| < 1$ m s^{-1}) of the APPRAISE and MC3E clouds, changes in solid aerosol loadings are predicted to slightly alter the mass mixing ratios of the cloud hydrometeors. In supercooled layer clouds (APPRAISE), the present-day cloud-liquid mass is predicted to increase by about 4% relative to pre-industrial simulation (Fig. 2a) whereas the present-day rain mass is predicted to be 20% lower at all levels (Fig. 2a). Also, little increase ($\sim$ 2-5%) is predicted in the present-day for cloud-ice and snow mass whereas the mass of graupel is 30% higher (Fig. 2b).

In the deep convective clouds (MC3E, Fig. 2c-d), at warmer levels ($> -10^{\circ}$C), changes in solid aerosols causes no change in the mass mixing ratios of the hydrometeors in all microphysical species. On the other hand, above the -10°C level, the present-day simulation has amounts of cloud-liquid, rain and cloud-ice that are lower by a factor of 3, and by 20% and 30%, respectively. Furthermore, graupel mass is predicted to be unchanged.
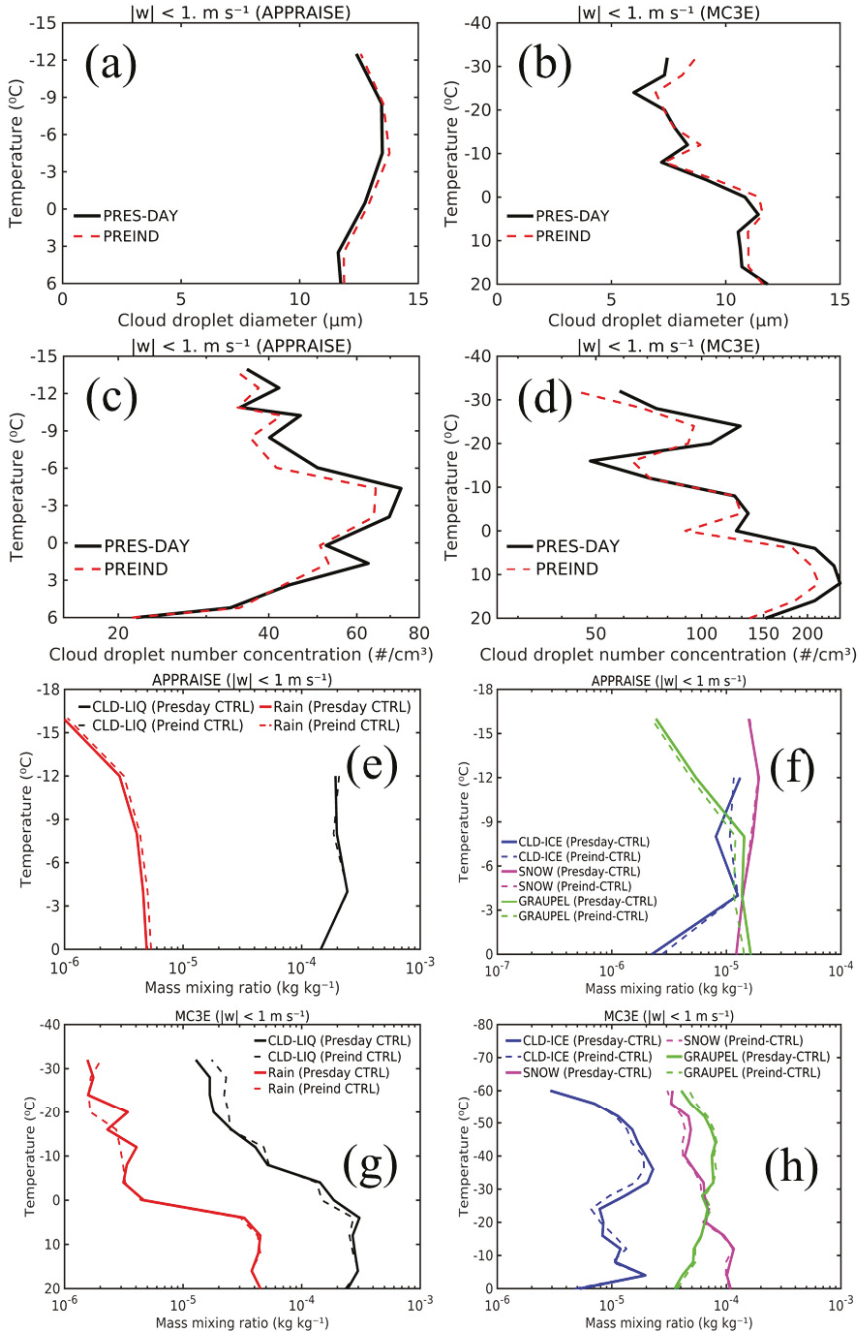
Fig. 1. *Predicted mean diameters and number concentrations of cloud droplets for the control simulations (present-day and pre-industrial) (a, c) APPRAISE and (b, d) MC3E cases. All the profiles are conditionally averaged over stratiform regions (|w| < 1 m s⁻¹). The solid black line shows the result from the control run whereas the dotted red line shows the results from the pre-industrial simulation. Also shown are the predicted mass mixing ratios of (e) cloud-liquid (black lines) and rain (red lines), and of (f) cloud-ice (blue lines), snow (magenta lines), and graupel (green lines) for the APPRAISE case*

conditionally averaged for stratiform regions (|w| < 1 m s⁻¹). The same information is shown in (g) and (h) for the MC3E case. The solid and dotted lines in (a-d) show the water contents from the control (PRESDAY) and pre-industrial (PREIND) simulation, respectively.

Figure 2 shows number concentrations of primary and total ice, and their components from various SIP processes tracked using tagging tracers (Sec. 2), in the stratiform regions ($|w| < 1$ m s⁻¹). For APPRAISE and MC3E, at levels near the cloud top, the present-day primary ice is predicted to be about 30% and 50% higher respectively than in the pre-industrial run due to more soot and dust INPs. Also, similar changes are predicted in the number concentrations of total ice particles and ice from fragmentation during ice-ice collisions and sublimation in both MC3E and APPRAISE cases.

Moreover, in both APPRAISE and MC3E cases, the ice concentrations from the HM process and raindrop freezing are about 30% lower due to the reduction in droplet sizes (Fig. 1a-b) from CCN activity of the extra soot and dust in the present-day environment. However, above the $-36°C$ level, there is less homogeneously nucleated ice by about 20% in the present-day conditions, reflecting stronger depletion of supercooled cloud-liquid upwelled from below through the mixed-phase region.
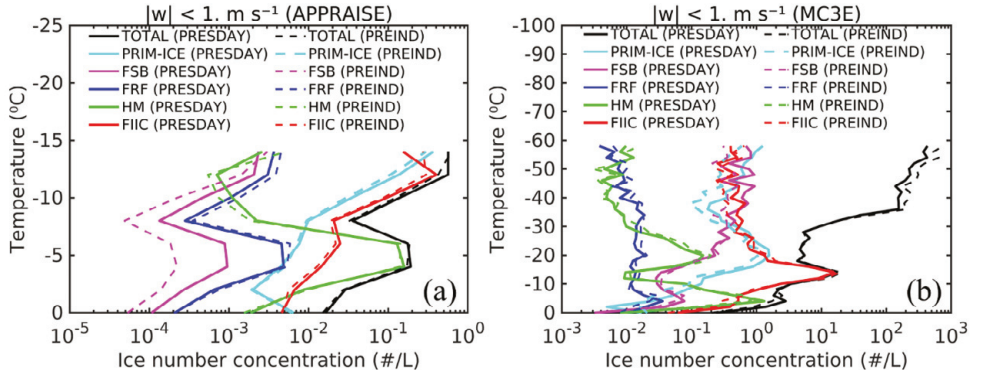
Fig. 2. *Comparison of total number concentrations of ice particles (black lines) and ice number concentrations from SIP processes such as the HM process (HM, green lines) and fragmentation during ice-ice collisions (FIIC, red lines), raindrop freezing (FRF, blue lines) and sublimation (FSB, magenta lines) predicted in the control run simulated with the present-day (solid lines) and pre-industrial (dotted lines) solid aerosol conditions for (a) APPRAISE and (b) MC3E cases conditionally averaged for cloudy stratiform regions (|w| < 1 m s⁻¹).*

4.1.2 Response of Macrophysical Properties

Anthropogenically increased solid APs are also predicted to affect the macrophysical properties of the simulated MC3E and APPRAISE clouds. Figure 3(a-b) shows changes (present-day minus pre-industrial) in domain-averaged cloud fraction for the control simulations of APPRAISE and MC3E clouds. This is the fraction of horizontal domain, covered by grid columns with the targeted cloud type. Furthermore, the change in volumetric cloud fraction (present-day minus pre-industrial) is also shown (Fig. 3c-d), which is the fraction of the volume of 3D domain for a targeted cloud type. Hence, domain-averaged cloud fraction indicates horizontal extent whereas volumetric cloud fraction highlights the lifetime and 3D extent.

There is a strong contrast between both APPRAISE and MC3E cases. In the simulated APPRAISE case, the horizontal extent of the present-day layer clouds increases by about 2% relative to the pre-industrial clouds (Fig. 3a), chiefly due to more coverage by liquid-only clouds, reflecting extra incoming SW radiation to space. Also, inclusion of anthropogenic INPs causes an increase by about 1% in their volumetric extent, mainly due to deepening of glaciated clouds (Fig. 3c). Moreover, for MC3E, both horizontal and volumetric (Fig. 3b, d) extents of the clouds increase (~ 2%) with anthropogenic aerosols due to a deepening of ice-only clouds. However, the more radiatively important mixed-phase clouds have less (by about 10%) volumetric and horizontal coverage (Fig. 3b, d). This is mainly because of more numerous secondary ice particles (~ 7% higher) in the present-day mixed-phase clouds growing and depleting the supercooled cloud-liquid (e.g., by riming and evaporation).

Figure 3(e-f) shows the components of the surface accumulation of precipitation from warm-rain and ice-crystal processes for APPRAISE and MC3E. In the simulated present-day APPRAISE clouds, the warm-rain and ice-crystal processes form about 54% and 46% of the total surface precipitation, respectively (Fig. 3e), with a slight strengthening (by ~10%) of the ice-crystal process relative to the pre-industrial run. In APPRAISE, the ice-crystal process is weaker than the warm rain process mainly because the SIP activity is curbed by weakness of ascent (~ few cm s^{-1}) of these stratiform layer clouds and their thinness, while the CCN aerosols are fewer than in MC3E. Also, the extra INPs in the present-day condition act to enhance the ice-crystal process by initiating more ice-crystals.

On the other hand, in MC3E clouds of vigorous deep convection (Fig. 3f), the ice-crystal process is the most prolific mechanism of precipitation production forming about 83% of the total accumulation of surface precipitation. This is mainly because of the high mass of ice hydrometeors (Fig. 2c-d) and strong deep vertical ascent ($|w| > 1$ m s^{-1}) (Waman *et al*. 2023, their Fig. 8d) in such clouds. Moreover, in such clouds, a slight change (~ 1% decrease) is predicted in the warm rain and ice-crystal processes in the present-day run compared to the pre-industrial simulation.

Figure 3(g-h) shows the change (present-day minus pre-industrial) in the optical thickness for each cloud type in the simulated APPRAISE and MC3E cases. In both cases, it is predicted that anthropogenic INPs form more dense clouds by suppressing precipitation. Furthermore, solid aerosol pollution causes the mixed-phase and liquid-only clouds (in APPRAISE), and liquid-only, mixed-phase and ice-only clouds (in MC3E) (Fig. 3g-h) to become denser. This is mainly because these clouds have relatively high mass contents of cloud condensate and they grow horizontally extensively (Fig. 3a-b) in the present-day environment. It is further predicted that the present-day ice-only APPRAISE clouds tend to be optically thin (Fig. 3g), mainly due to lower mass contents of ice particles and their low cloud-tops.
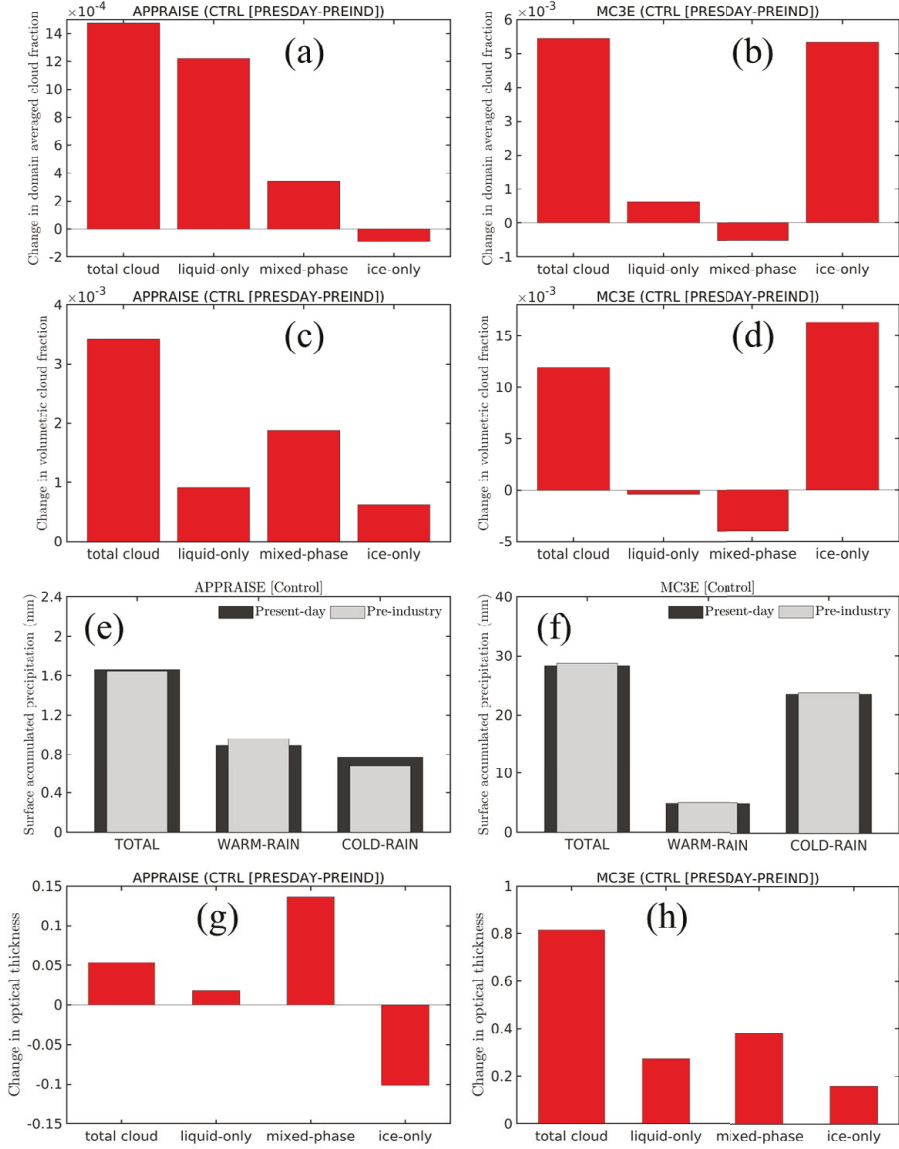
Fig. 3. *Bar chart showing the changes (present day−pre-industry) in the horizontal (a, c) and volumetric (b, d) cloud extents for each cloud type for the simulated APPRAISE and MC3E clouds from their corresponding control simulations. A given grid point is defined as liquid-only when the mass mixing ratio of cloud-liquid and cloud-ice is non-zero and zero respectively. A grid point is said to be in mixed-phase when both cloud-liquid and cloud-ice mass mixing ratios are non-zero. Also, a grid point is said to be ice-only if cloud-liquid and cloud-ice mass mixing ratios are zero and non-zero respectively. Furthermore, predicted domain averaged precipitation accumulated at the surface from the components of the warm rain (WARM-RAIN) and ice-crystal (COLD-RAIN) processes for the (e) APPRAISE and (f) MC3E clouds simulated with the present-day and pre-industrial solid aerosol conditions. Moreover, changes in the optical thicknesses (present day−pre-industry) for each cloud type from the control simulation are shown for the simulated (g) APPRAISE and (h) MC3E cases. The optical thickness for*

each cloud type in the present-day and pre-industrial run is averaged unconditionally over the entire domain and duration of the simulation.

4.1.3 Response of Radiative Fluxes at TOA

Figure 4(a, c) shows the TOA net AIE flux change from the control simulations of the APPRAISE and MC3E clouds, for the total and glaciated clouds. Also, the contributions from the albedo-emissivity and lifetime AIEs are shown from glaciated clouds. The corresponding components of SW and LW radiation are shown in Fig. 4b, d. Note that the term 'AIE' refers to the flux change between present-day and pre-industrial solid aerosol conditions.

For the supercooled stratiform clouds in APPRAISE (Fig. 4a), a net cooling of the present-day climate system with a net AIE of about -0.39 W m^{-2}, chiefly from glaciated clouds (~ -0.33 W m^{-2}) is predicted. This net cooling is mainly because of more reflection of incoming SW radiation to space from liquid-only and mixed-phase clouds as they are optically thicker in the present-day than pre-industrially. Furthermore, ice-only clouds also exert a net cooling (~ -0.15 W m^{-2}) as their ice water path decreases with inclusion of anthropogenic aerosols, reducing their absorption (lower emissivity) of LW radiation in the present-day. This allows more outgoing LW radiation (~ -0.27 W m^{-2}) from the surface to space.

Furthermore, for such layer clouds (APPRAISE, Fig. 4a), the third and fourth clusters of bars show the albedo-emissivity and lifetime AIEs from glaciated, ice-only and mixed-phase clouds. The albedo-emissivity (~ -0.3 W m^{-2}) AIE from ice-only clouds dominates over their lifetime (~ -0.15 W m^{-2}) AIE, mainly due to the relatively weaker response of macrophysical properties (Fig. 4a-d) and precipitation production than the microphysical properties (Fig. 1a-b, Fig. 2a-b) governing cloud emissivity (e.g., ice water content). It is further predicted that, the albedo-emissivity effect via glaciated clouds is mostly dominated by ice-only clouds whereas their lifetime indirect effect is dominated by mixed-phase clouds, which have stronger aerosol-sensitive precipitation production than ice-only clouds.

By contrast, for the simulated convective storm (MC3E, Fig. 4c), the net AIE is much stronger and is a warming (~ 4.8 W m^{-2}) of the present-day climate system. The main contribution is from the mixed-phase component of glaciated clouds (~ 4.6 W m^{-2}) whereas that from liquid-only clouds is relatively weak (~ 0.2 W m^{-2}). Furthermore, in such deep convective clouds, the lifetime indirect effect (~ 3.4 W m^{-1}) from glaciated-clouds is predicted to dominate over their albedo-emissivity effect (~ 1.2 W m^{-2}, Fig. 4c). This contrasts with APPRAISE because mixed-phase clouds, which have aerosol-sensitive precipitation production, cloud extent and optical thickness, prevail in the overall AIE in MC3E.

It is further predicted that in MC3E clouds, the net indirect effect is mainly dominated by changes in SW radiative flux chiefly from the mixed-phase component of glaciated clouds (fifth cluster, Fig. 5d), due to their lower horizontal and volumetric cloud fractions (Fig. 3b and d). Furthermore, ice-only (third cluster, Fig. 4d) and mixed-phase (fourth cluster, Fig. 4d) clouds show opposite responses in their SW and LW flux changes, which is consistent with changes in horizontal (Fig. 3b) and volumetric (Fig. 3d) cloud fractions. Although for each of both cloud types (mixed-phase and ice-only) the LW flux change is more important than SW, for all glaciated clouds the SW change prevails in total because both LW changes almost cancel out.
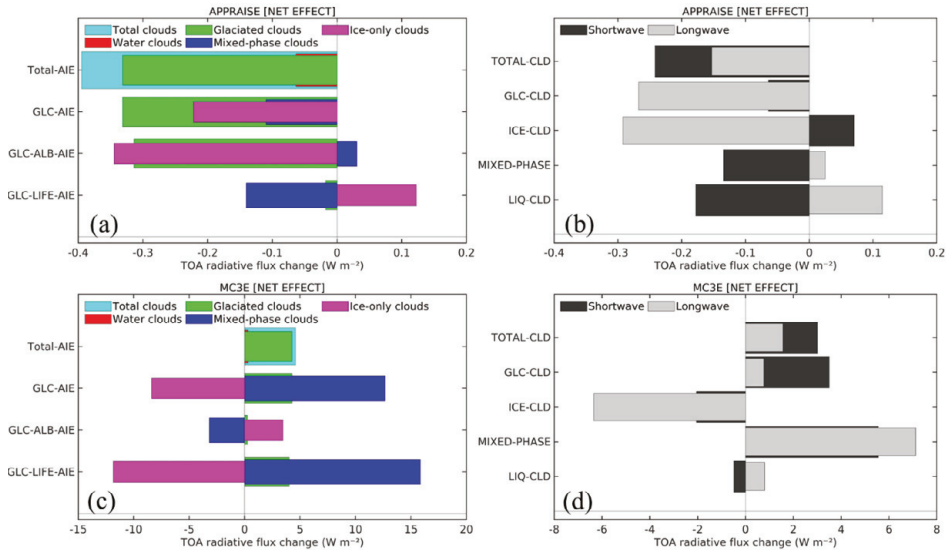
Fig. 4. *Net aerosol indirect effects at the TOA from solid aerosols on glaciated clouds predicted from Test A and Test B (Sec. 3) from the control simulations of (a) APPRAISE and (c) MC3E cases. Corresponding changes in the shortwave and longwave components of radiation, unconditionally averaged over the whole domain, are shown for (b) APPRAISE and (d) MC3E cases. Here, abbreviations: GLC-AIE= Glaciated Clouds AIE, GLC-ALB-AIE= Glaciated cloud Albedo-Emissivity AIE, GLC-LIFE-AIE= Glaciated Cloud Lifetime AIE.*

4.2   Changes in AIE from Exclusion of Secondary Ice

To estimate the role of SIP (Sec. 2) in the simulated AIEs, various sensitivity tests have been performed by modifying the control run for the present-day and pre-industrial solid aerosol conditions to create various perturbation simulations (Table 5, Sec. 3.1.3). To determine the albedo-emissivity and lifetime indirect effects of clouds without SIP, simulations discussed in Tests A and B (Sec. 3) were repeated for the 'no SIP' runs.

4.2.1 Response of Microphysical Properties

Figure 5(a-d) shows a comparison of the predicted cloud-droplet sizes and number concentrations between the control and 'no SIP' runs performed with the present-day and pre-industrial simulations for the APPRAISE and MC3E clouds, in the stratiform regions ($|w| < 1$ m s^{-1}).

In both simulated cases (APPRAISE and MC3E), at levels warmer than -15°C, the droplet mean sizes are 10% higher without SIP, with both the present-day and pre-industrial aerosol conditions. For MC3E deep convection, at levels colder than -15°C, the droplet mean sizes are 50% higher without SIP, both in the present-day and pre-industrially, mainly due to less intense accretion by precipitation and less evaporation from a weakened Bergeron-Findeisen effect.

Moreover, in APPRAISE clouds, in the absence of SIP, the present-day droplet number concentrations are about 10% higher than pre-industrially whereas they are lower than the corresponding present-day and pre-industrial control runs (Fig. 5b). For the MC3E clouds without SIP, the droplet number concentrations are about 10-30% higher in the present-day than

pre-industrially whereas they increase by the same amount (10-30%) compared to the present-day control run (Fig. 5d). These sensitivities are similar to those seen with SIP (Sec. 4.1.1).

Figure 5(e-h) shows vertical profiles of the predicted mass mixing ratios of microphysical species of cloud and precipitation, averaged conditionally over stratiform conditions ($|w| < 1$ m s^{-1}). For MC3E, there is a strong sensitivity (increase with more INPs) of cloud-liquid mass without SIP, with respect to inclusion of anthropogenic INPs, but including it in the control run greatly damps this aerosol sensitivity (Fig. 5g). In fact, inclusion of SIP reduces the cloud-liquid mass by about half an order of magnitude in the lower half of the mixed-phase region for each aerosol scenario, whether present-day or pre-industrial. Similarly, there is more sensitivity (increase with more INPs) of the rain mass without SIP with respect to anthropogenic solid aerosol conditions (a change of about 10-20% below the freezing level) than with it (a change of about 1-3%). This is explicable in terms of increased cold rain (melting of snow and cold graupel) from the ice-crystal process of precipitation, which is boosted by extra INPs. The intensified cold rain more nearly becomes limited by the supply of condensate, hence the damping of response to INPs.

In the stratiform regions of MC3E clouds, the ice phase is drastically altered by inclusion of SIP, in a way that damps the sensitivity with respect to anthropogenic solid APs. Inclusion of SIP boosts snow mass by about 10% because there are more crystals growing to become snow in the water saturated mixed-phase clouds but the consequent depletion of supercooled cloud-liquid (e.g., by intensified evaporation or riming) causes less graupel mass. This lack of sensitivity of supercooled cloud-liquid noted above, with respect to solid aerosol conditions, when SIP is present, similarly damps the aerosol sensitivity of snow and graupel mass, which is derived mostly from riming.

In summary, this sensitivity of all species of precipitation aloft, which is derived from the ice-crystal process in MC3E, with respect to anthropogenic solid APs, is drastically damped by inclusion of SIP. This has repercussions for the lifetime indirect effects, which SIP would be expected to suppress.
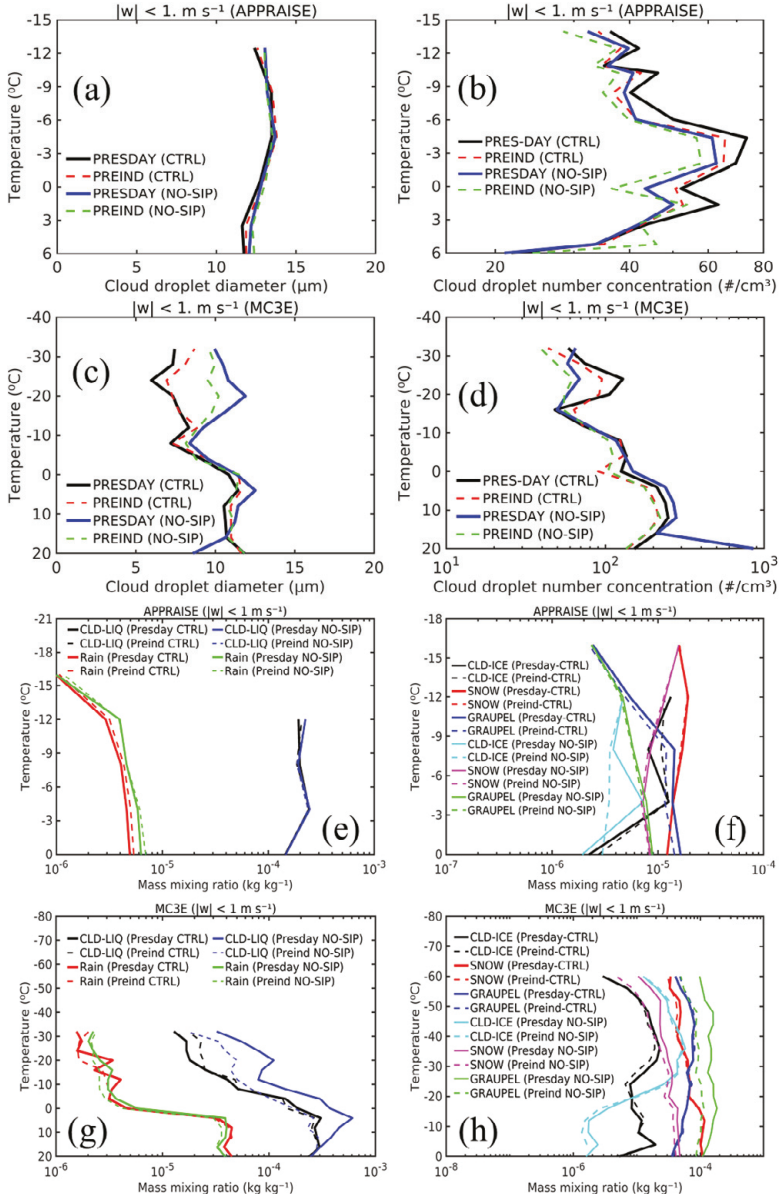
Fig. 5. *Predicted mean diameters and number concentrations of cloud droplets for the 'control' and 'no SIP' simulations (present-day and pre-industrial) (a, c) APPRAISE and (b, d) MC3E cases. All the profiles are conditionally averaged over stratiform regions (|w| < 1 m s⁻¹). The solid black line shows the result from the control run whereas the dotted red line shows the results from the pre-industrial simulation. Also shown are the predicted mass mixing ratios of (e) cloud-liquid (black lines) and rain (red lines), and of (f) cloud-ice (blue lines), snow (magenta lines), and graupel (green lines) for the APPRAISE case conditionally averaged for stratiform regions (|w| < 1 m s⁻¹). The same information is shown in (g) and (h) for the MC3E case. The solid and dotted lines in (a-d) show the water contents from the 'control' and 'no SIP' (PRESDAY) and pre-industrial (PREIND) simulation, respectively.*

22

Furthermore, in APPRAISE and MC3E (between 0 and −20°C), exclusion of SIP causes the predicted ice concentrations in stratiform regions to be about 0.5 and 1 orders of magnitude lower, respectively than with SIP (Fig. 6a-b). However, above the −20°C level in MC3E, exclusion of SIP boosts the overall ice concentrations in the stratiform region (Fig. 6b) due to more outflow of homogenously nucleated ice from convective regions (Fig. 6c). The sensitivity with respect to anthropogenic INPs is reduced (from an increase of about 20% to that of 10%) by inclusion of SIP in APPRAISE. For MC3E in stratiform regions, there is little sensitivity (~ 2% increase) of the overall ice concentration with respect to anthropogenic solid APs, whether or not SIP is included.

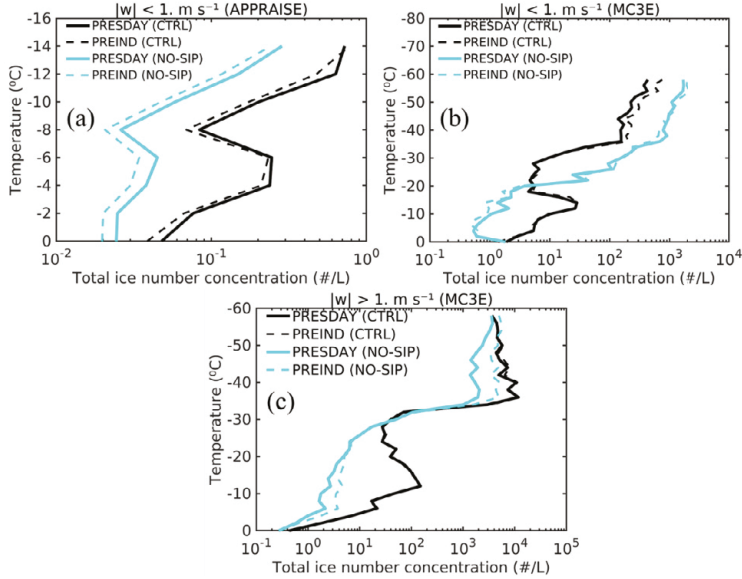**Fig. 6.** *Comparison of total number concentrations of ice particles predicted in the control (black lines) and 'no SIP' (cyan lines) runs simulated with the present-day (solid lines) and pre-industrial (dotted lines) solid aerosol conditions for (a) APPRAISE and (b) MC3E cases conditionally averaged for cloudy stratiform regions (|w| < 1 m s⁻¹) and over (c) convective regions (|w| > 1 m s⁻¹) for MC3E.*

4.2.2 Response of Macrophysical Properties

For APPRAISE and MC3E, Figure 7 shows how the response of macrophysical properties with respect to inclusion of anthropogenic aerosols depends on the presence of SIP, in comparison with Fig. 4.

For APPRAISE, without SIP, inclusion of anthropogenic INPs causes an increase of about 0.5% in the horizontal extent of clouds whereas this increase is about 2% with SIP. This is due to more coverage by glaciated clouds with less sensitivity with respect to anthropogenic INPs in the absence of SIP. Also, the volumetric extent of clouds is increased by about 0.5% with inclusion of these INPs, both with and without SIP, a response due mainly due to glaciated clouds. Essentially, including anthropogenic INPs reduced the depth and horizontal extent of glaciated clouds without SIP, but more so when SIP is included (Fig. 3a, c).

For MC3E, in the absence of SIP, inclusion of anthropogenic solid APs causes a decrease by about 1% and 2.4% in the horizontal and volumetric extent of clouds, respectively. This is

mostly due to less coverage by ice-only clouds from less homogeneous freezing when heterogeneous ice nucleation is intensified by extra INPs (Fig. 7c) and also from less extent of mixed-phase clouds. Moreover, this sensitivity with respect to anthropogenic INPs is increased (~ 1%) when SIP is included (Fig. 4b, d).

For APPRAISE, without SIP, inclusion of anthropogenic INPs by their CCN activity reduces overall surface precipitation by 2%, because cloud-droplets are smaller, and by only 0.8% with SIP. This damping of the aerosol sensitivity by the presence of SIP is consistent with the microphysical responses noted above for cloud-liquid and rain. As noted above, in APPRAISE, the surface precipitation is dominated by warm rain. The minor contribution from cold rain is boosted by 10% with anthropogenic aerosols, both with and without SIP.

For MC3E, inclusion of anthropogenic solid APs causes an increase only by about 0.2% in the surface accumulated precipitation without SIP whereas it decreases by about 1% with SIP. This reversal of the aerosol sensitivity is chiefly due to both warm rain (~ 16% decrease) and ice-crystal (~ 11% increase) processes that have a higher aerosol sensitivity without SIP than with it, as noted above for the microphysical species aloft.

For APPRAISE and MC3E, in the absence of SIP, inclusion of anthropogenic solid APs causes a decrease by about 1% in the overall optical thickness. However, with SIP, the optical thickness of the present-day APPRIASE and MC3E clouds is boosted by about 3% and 17%, respectively, chiefly due mixed-phase clouds with more aerosol-sensitivity in the presence of SIP than without it.

In summary, for APPRAISE and MC3E, inclusion of SIP acts to amplify the aerosol-sensitivity of cloud extents (~ 1-3%) and optical thickness (~3-17%). This can be chiefly because of more numerous ice particles and reduction in surface precipitation in both cases.
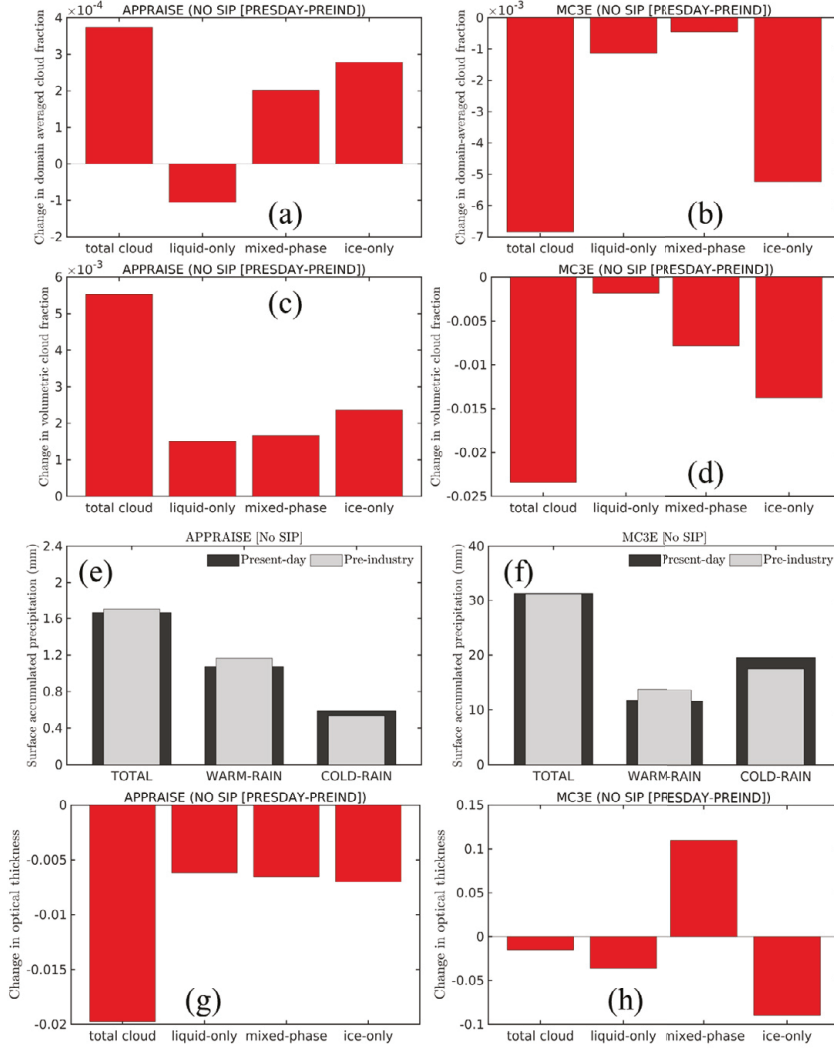
Fig. 7. *Bar chart showing the changes (present day−pre-industry) in the horizontal (a, c) and volumetric (b, d) cloud extents for each cloud type for the simulated APPRAISE and MC3E clouds from their corresponding 'no SIP' simulations. Furthermore, predicted domain averaged precipitation accumulated at the surface from the components of the warm rain (WARM-RAIN) and ice-crystal (COLD-RAIN) processes for the (e) APPRAISE and (f) MC3E clouds simulated with the present-day and pre-industrial solid aerosol conditions. Moreover, changes in the optical thicknesses (present day−pre-industry) for each cloud type from the 'no SIP' simulation are shown for the simulated (g) APPRAISE and (h) MC3E cases. The optical thickness for each cloud type in the present-day and pre-industrial run is averaged unconditionally over the entire domain and duration of the simulation.*

4.2.3 Response of Radiative fluxes at TOA

Figure 8 shows the predicted net AIE flux at TOA from 'no SIP' simulations for APPRAISE and MC3E, for all clouds and for individual cloud types (liquid-only, mixed-phase, and ice-

only). Also, the corresponding changes in the SW and LW radiative fluxes are shown in Fig. 8b, d. All these quantities are predicted from Tests A and B repeated without SIP (Sec. 3).

For APPRAISE, without SIP, inclusion of anthropogenic INPs causes a net cooling of the climate system with a net AIE of about -0.39 W m^{-2} at the TOA (Fig. 8a) which is similar to that with SIP (Fig. 4a). This net cooling is chiefly from glaciated clouds, both with (-0.37 W m^{-2}) and without (~ -0.8 W m^{-2}) SIP. Hence, in APPRAISE, the presence of SIP has little impact on the net AIE. However, without SIP, the net AIE from liquid-only clouds is artificially boosted ($\sim 40\%$ more warming) than with ($\sim 8\%$ cooling) SIP, offsetting the boosted cooling from the glaciated clouds. This reversal in liquid-only AIE, when SIP is included, is consistent with the changes in the horizontal and volumetric extents of these clouds, as noted above (Fig. 3a, c).

For MC3E, in the absence of SIP, anthropogenic INPs cause a net warming (~ 2.2 W m^{-2}) of the climate system (Fig. 8c) which is about 48% of the net AIE with SIP (Fig. 4c). Hence in such deep convective clouds, the net AIE has a higher sensitivity (more warming) with respect to anthropogenic INPs in the presence of SIP than without it. Also, this warming (~ 2.2 W m^{-2}) is mainly from glaciated clouds, both with (~ 4 W m^{-2}) and without (~ 7 W m^{-2}) SIP. This is because without SIP, both ice-only and mixed-phase clouds becomes horizontally and vertically less extensive (Fig. 7b and d), allowing more SW radiation to enter the climate system (Fig. 8d). Furthermore, with SIP, the net AIE from liquid-only clouds is damped ($\sim 6\%$ warming) relative to that without ($\sim 50\%$ more cooling) it.

Furthermore, for APPRAISE, the net AIE is mainly dominated by the albedo-emissivity AIE (-0.9 W m^{-2}) from glaciated clouds. This is mainly because in the absence of SIP, the microphysical properties of such clouds (Sec. 4.2.1) show a strong sensitivity with respect to anthropogenic solid APs than their extents and optical thickness (Sec. 4.2.2). By contrast, for MC3E, the lifetime indirect effect from glaciated clouds (8.8 W m^{-2}) dominates over their albedo-emissivity indirect effects (-2 W m^{-2}). This is mainly because without SIP, the horizontal and volumetric extents of these clouds show a higher sensitivity with respect to anthropogenic INPs than with SIP (Fig. 3), as discussed above (Sec. 4.2.2).
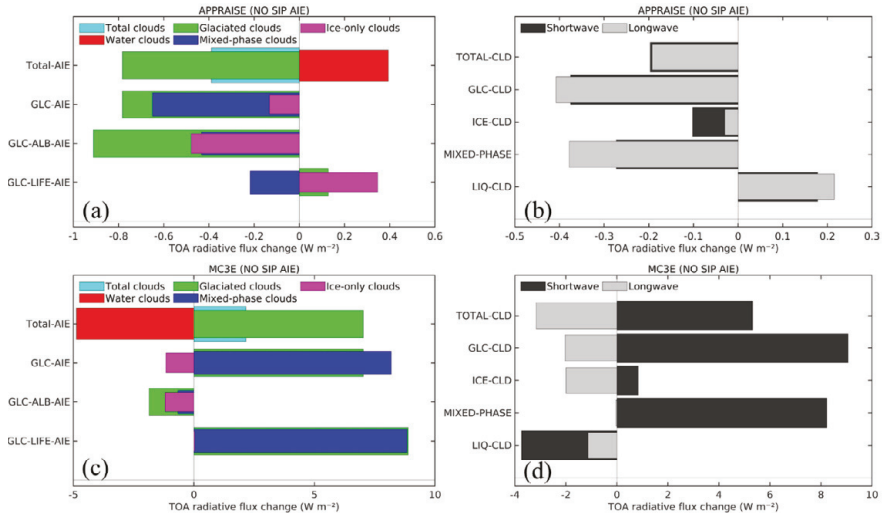
Fig. 8. *Net aerosol indirect effects at the TOA from solid aerosols on glaciated clouds predicted from Test A and Test B (Sec. 3) from the 'no SIP' simulations of (a) APPRAISE and (c) MC3E cases. Corresponding changes in the shortwave and longwave components of radiation, unconditionally averaged over the whole domain, are shown for (b) APPRAISE and (d) MC3E cases. Here, abbreviations: GLC-AIE= Glaciated Clouds AIE, GLC-ALB-AIE= Glaciated cloud Albedo-Emissivity AIE, GLC-LIFE-AIE= Glaciated Cloud Lifetime AIE.*

4.3 Changes in AIE from exclusion of Time-dependent INP Freezing

To estimate the role of time dependent heterogeneous ice nucleation in the simulated AIEs (Sec. 4.1.3), various sensitivity tests described in Sec. 3.1.3 have been performed (Table 5, Sec. 3.3). To determine the albedo and lifetime indirect effects of clouds without time dependent INP freezing, simulations discussed in tests A and B (Sec. 3) were repeated for 'no time dependent INP' runs.

Sections 4.3.1-4.3.3 below analyze the changes in the micro-, macrophysical and radiative properties, respectively in the no time-dependent INP run from inclusion of anthropogenic solid APs.

4.3.1 Response of microphysical properties

For APPRAISE and MC3E, in the stratiform regions ($|w| < 1$ m s^{-1}), Fig. 9(a-d) shows a comparison of the mean sizes and number concentrations of cloud-droplets between the control and 'no time dependent INP' runs simulated with the present-day and pre-industrial aerosol conditions.

For supercooled layer clouds in APPRAISE, at levels warmer than 0°C, without time dependence, inclusion of anthropogenic solid APs causes an increase (at levels warmer than 0°C) and a decrease (at levels colder than 0°C) of about 1% in the mean sizes of cloud-droplets whereas with time dependence, they are predicted to decrease by the same fraction at all levels (Fig. 9a). However, both with and without time dependence, inclusion of anthropogenic solid APs causes an increase by 10-20% in droplet number concentration (Fig. 9b).

27

For MC3E, at levels warmer than -20°C, both with and without time dependence, droplet mean sizes again have little sensitivity (~ 2% decrease) with respect to anthropogenic solid APs (Fig. 9c). However, above this level, this aerosol sensitivity is higher, with a decrease of about 8% in the droplet mean sizes. Also, droplet number concentration shows similar aerosol sensitivities at these levels, both with and without time dependence (Fig. 9d).

In the stratiform regions ($|w| < 1$ m s^{-1}) of the layer clouds in APPRAISE, inclusion of anthropogenic solid aerosols causes little sensitivity of cloud-liquid mass both with and without time dependence. Also, at levels warmer than -10°C, the rain mass is little sensitive to anthropogenic solid APs (~ < 2% decrease). Above this level, there is a strong sensitivity (increase by 6%) of rain mass without time dependence, with respect to anthropogenic solid aerosols, whereas it decreases by the same fraction with time dependence. Also, in APPRAISE, the absence of time dependence causes a strong aerosol sensitivity (~ 10-20% increase with more INPs) of cloud-ice and snow masses whereas graupel mass has little aerosol sensitivity (~ < 1% increase).

For MC3E in stratiform regions ($|w| < 1$ m s^{-1}), with and without time dependence, inclusion of anthropogenic solid aerosols causes little sensitivity of cloud-liquid and rain masses at all levels (Fig. 9f). Furthermore, a high aerosol sensitivity (decrease by 20% with more INPs) of cloud-ice mass is seen without time dependence, which with time dependence is reversed (increase of about 10%). Also, without time dependence, inclusion of anthropogenic INPs causes an increase of about 15-20% in snow and graupel masses which is about 10% more than with time dependence.

Fig. 9. *Predicted mean diameters and number concentrations of cloud droplets for the 'control' and 'no time dependent INP' simulations (present-day and pre-industrial) (a, c) APPRAISE and (b, d) MC3E cases. All the profiles are conditionally averaged over stratiform regions ($|w| < 1\ m\ s^{-1}$). The solid black line shows the result from the control run whereas the dotted red line shows the results from the pre-industrial simulation. Also shown are the predicted mass mixing ratios of (e) cloud-liquid (black lines) and rain (red lines), and of (f) cloud-ice (blue lines), snow (magenta lines), and graupel (green lines) for the APPRAISE case conditionally averaged for stratiform regions ($|w| < 1\ m\ s^{-1}$). The same information is shown in (g) and (h) for the MC3E case. The solid and dotted lines in (a-d) show the water contents from the 'control' and 'no time dependent INP' (PRESDAY) and pre-industrial (PREIND) simulation, respectively.*

In the stratiform regions of the APPRAISE, without time dependence, at levels colder than $-4°C$, the overall ice concentration is about 10-30% lower than with it, both with the present-day and pre-industrially (Fig. 10a). However, with time dependence, inclusion of anthropogenic INPs causes a higher sensitivity (~ 20% increase) of overall ice concentration than without it (~10% increase), mainly due to an increase in INP activity of dust and PBAP INPs (Waman *et al.* 2023, their Fig. 10e).

For MC3E at levels warmer than $-40°C$ in the stratiform regions ($|w| < 1 \text{ m s}^{-1}$), inclusion of anthropogenic INPs causes little change ($< \pm5\%$) in the overall ice concentration, both with and without time dependence (Fig. 10b). Above this level, without time dependence, anthropogenically boosted INPs causes an increase of about 30% in the overall ice concentration, mainly due to boosted (~ 15% increase) homogeneously nucleated ice. However, at these levels, with time dependence, inclusion of anthropogenic INPs causes a decrease of about 20% in the overall ice concentration. This is mainly because of the relatively less homogeneous freezing of supercooled cloud droplets due to weak updraft speeds in the present-day conditions, with time dependence included in the control run. Furthermore, in convective regions ($|w| > 1 \text{ m s}^{-1}$) at all levels, inclusion of anthropogenic INPs causes a low sensitivity of overall ice concentration, both with and without time dependence.
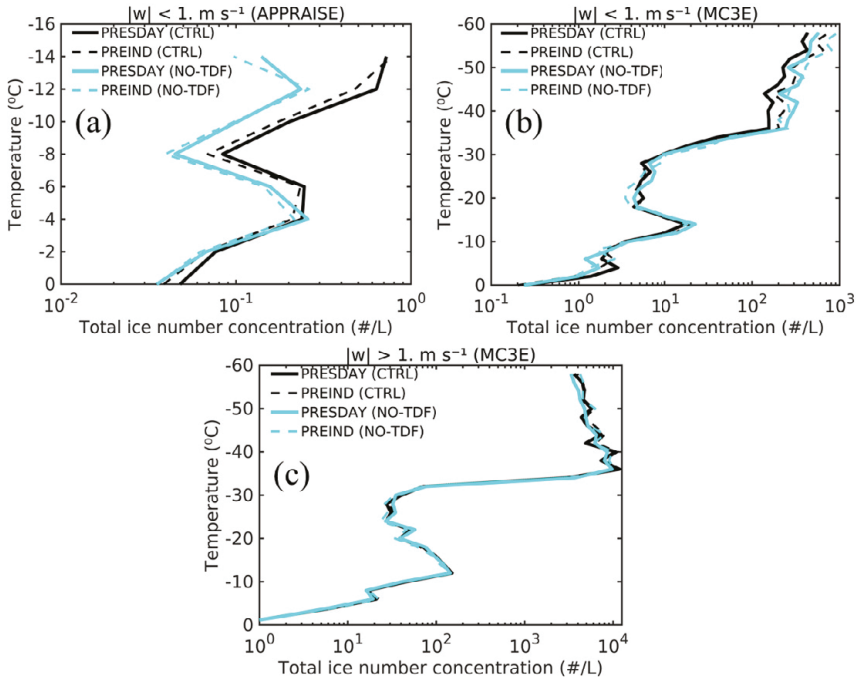
Fig. 10. Comparison of total number concentrations of ice particles predicted in the control (black lines) and 'no time dependent INP' (cyan lines) runs simulated with the present-day (solid lines) and pre-industrial (dotted lines) solid aerosol conditions for (a) APPRAISE and (b) MC3E cases conditionally averaged for cloudy stratiform regions ($|w| < 1 \text{ m s}^{-1}$) and over (c) convective regions ($|w| > 1 \text{ m s}^{-1}$) for MC3E.

To summarize, in both the simulated cases (APPRAISE and MC3E), inclusion of time dependence of INP freezing in the present-day as well as pre-industrial control runs predicts modest changes in all the microphysical properties (Fig. 9 and 10).

4.3.2 Response of Macrophysical Properties

Figure 11, in comparison with Fig. 4, shows how the response of macrophysical properties with respect to inclusion of anthropogenic solid aerosols depends on the presence of time dependent freezing of INPs in the simulated APPRAISE and MC3E cases. The 'no time dependent INP' runs are compared with the control runs (Table 5).

For supercooled layer clouds in APPRAISE (Fig. 11a), without time dependence, inclusion of anthropogenic INPs causes a decrease of about 2% in the horizontal extent of clouds, mostly involving liquid-only clouds (1% decrease). However, with time dependence included in the control run, the response is reversed with an increase by about 2%. Since the glaciated and liquid-only clouds become less deep due to fewer droplets at levels warmer than 0°C (Fig. 9b), in the presence of extra INPs, the volumetric extent is decreased by about 0.7% without time dependence. However, it increases by about 0.4% with time dependence (Fig. 11c). When time dependence is prohibited from the control run, there is a stronger aerosol sensitivity of the 3D volumetric cloud extent because removal of condensate by precipitation (~ 2% decrease) is also highly sensitive due to the corresponding sensitivities of the surface accumulation of warm rain (reduced by 6%) and cold rain (increased by 8%) (Fig. 11e). However, with time dependence, this aerosol sensitivity of the overall surface precipitation is weakened (~ 0.8% increase). With time dependence, the stronger deepening of clouds from intensified INP activity and more latent heating of ice growth also cause them to grow horizontally extensive since the cloud volume is significantly changed (0.4%) (Fig. 3f).

For APPRAISE, the surface precipitation is slightly dominated by warm rain, as noted above (Fig. 3e). In such layer clouds, without time dependence, inclusion of anthropogenic solid APs causes a decrease by 2% in the overall surface precipitation. However, with time dependence the overall surface precipitation is increased by about 0.8%. Also, both with and without time dependence, inclusion of anthropogenic solid APs causes a decrease of about 6% in the precipitation from the warm rain process (Fig. 11e), mainly due to relatively small droplet sizes. Furthermore, without time dependence, there is a slightly weaker sensitivity (~ 8% increase) with respect to anthropogenic solid APs of the surface precipitation from the ice-crystal process than with it (~ 10% increase), mainly because with time dependence, INP activity is much stronger (Fig. 10a), boosting the cold rain sensitivity.

For MC3E, without time dependence, anthropogenically boosted INPs cause an increase by about 3% in the overall surface precipitation (Fig. 11f) whereas it decreases by about 1% when time dependence is included (Fig. 3f). This reversal in aerosol sensitivity is chiefly due to the ice-crystal process that has a higher aerosol-sensitivity of surface precipitation (~ 3% increase) without time dependence than with it (~ 1% decrease). This is because without time dependence, the overall ice concentration is lower and has a stronger sensitivity (~ 30% increase) with respect to anthropogenic solid APs than with it (~ 7% increase). Without time dependence, INPs are scarcer and crystals from extra INPs will tend to convert, to precipitation, moisture that would otherwise not be converted. Conversely, with time dependence included, the more numerous crystals from extra INPs, are smaller due to more competition for the available moisture during growth, being less likely to grow to precipitation, hence the reversal in aerosol sensitivity.

For APPRAISE and MC3E, without time dependence, anthropogenically emitted solid APs cause an increase by about 2.5 and 5% respectively in the overall optical thicknesses. However, in the presence of time dependence, the optical thickness is increased by about 5% in APPRAISE and about 8% in MC3E when the extra APs are added. With time dependence, this stronger sensitivity with respect to anthropogenic aerosols is mainly because there are more ice crystals for a given change in aerosol conditions and hence there is a greater fractional aerosol sensitivity of the cloud condensate mass content (Fig. 10g).

To summarise, for both APPRAISE and MC3E, without time dependence, the macrophysical properties such as cloud 3D extent, overall surface precipitation and optical thickness shows a higher sensitivity with respect to anthropogenic INPs than with it. This cause a higher impact on the simulated net AIEs (Sec. 4.1.3), mainly from the lifetime indirect effect, when time dependence of INP freezing is prohibited from the control runs, as discussed below (Sec. 4.3.3).
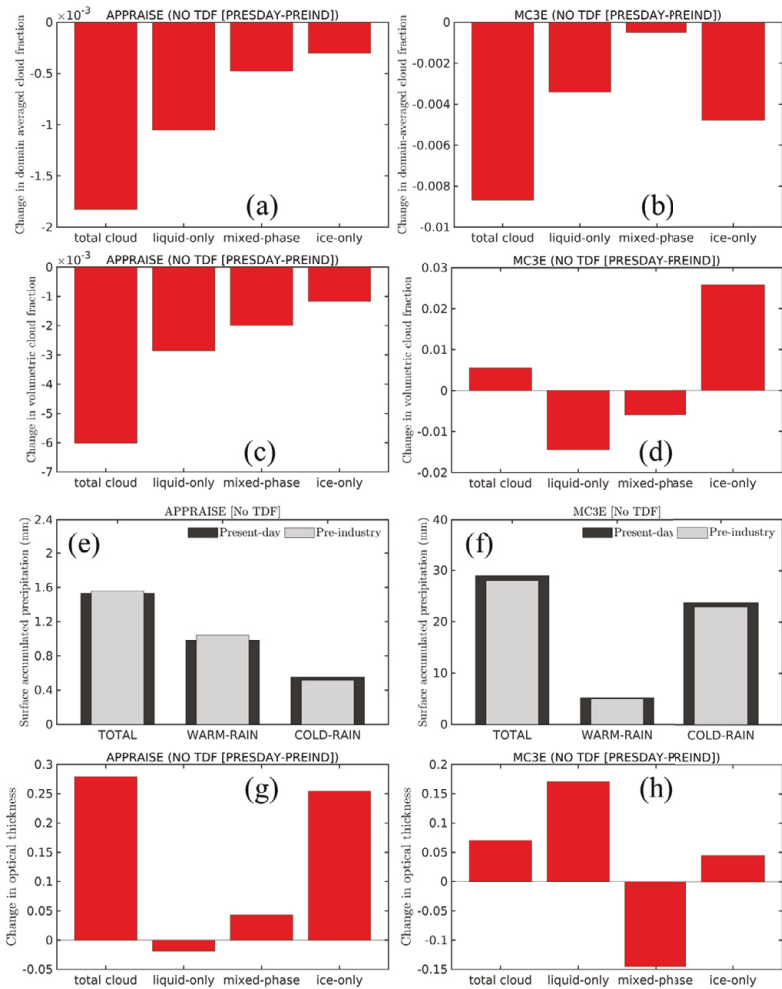

Fig. 11. Bar chart showing the changes (present day−pre-industry) in the horizontal (a, c) and volumetric (b, d) cloud extents for each cloud type for the simulated APPRAISE and MC3E clouds from their corresponding 'no time dependent INP' simulations. Predicted domain averaged precipitation

accumulated at the surface from the components of the warm rain (WARM-RAIN) and ice-crystal (COLD-RAIN) processes for the (e) APPRAISE and (f) MC3E clouds simulated with the present-day and pre-industrial solid aerosol conditions. Moreover, changes in the optical thicknesses (present day−pre-industry) for each cloud type from the 'no time dependent INP' simulation are shown for the simulated (g) APPRAISE and (h) MC3E cases. The optical thickness for each cloud type in the present-day and pre-industrial run is averaged unconditionally over the entire domain and duration of the simulation.

4.3.3 Response to Radiative Fluxes at TOA

For APPRAISE and MC3E, Fig. 12(a, c) shows the predicted TOA AIE fluxes (present-day−pre-industrial) from 'no time dependent INP' simulations, for all clouds and for individual cloud types. Also, corresponding changes in the SW and LW fluxes are shown in Fig. 12(b, d). All these quantities are predicted from Tests A and B which are repeated for 'no time dependent INP' runs (Sec. 3.1.3).

Regarding the net AIEs, for APPRAISE, without time dependence (Fig. 12a), anthropogenic solid APs cause a net cooling of the climate system with a net AIE of about -0.26 W m^{-2}, mainly from liquid-only clouds that cause more reflection of incoming SW flux (-0.37 W m^{-2}). Furthermore, this net AIE is about 65% of the net cooling with time dependence (Fig. 4a). Also, in the absence of time dependence, inclusion of anthropogenic aerosols causes a net warming (0.45 W m^{-2}) from glaciated clouds. However, with time dependence, it causes a net cooling of about -0.34 W m^{-2}. This reversal in sensitivity with respect to anthropogenic INPs, without time dependence, is mainly due a corresponding reversal in the macrophysical properties of glaciated clouds, as discussed in Sec. 4.3.2.

Furthermore, in such layer clouds (APPRAISE), without time dependence, the lifetime indirect effect (0.85 W m^{-2}) from glaciated clouds dominate over their albedo-emissivity indirect effect (-0.38 W m^{-2}). This is explicable in terms of a strong sensitivity of anthropogenic INPs of the overall surface precipitation ($\sim$ 2% decrease) that increases the lifetime of such layer clouds in the absence of time dependence. However, with time dependence, this sensitivity with respect to anthropogenic INPs of surface accumulated precipitation is weaker ($\sim$ 0.8% increase) and hence weaker lifetime indirect effect.

For the deep convective clouds in MC3E, without time dependence, inclusion of anthropogenic INPs cause a net warming ($\sim$ 0.93 W m^{-2}), mainly from liquid-only clouds ($\sim$ 1.2 W m^{-2}). This warming is about 20% of the net warming with time dependence (Fig. 4c, Sec. 4.1.3). Hence, in MC3E, the net AIE has a strong sensitivity with respect to anthropogenic INPs ($\sim$ 80% more warming) in the presence of time dependence. Furthermore, without time dependence, the net AIE from glaciated clouds is weakened ($\sim$ cooling by -0.18 W m^{-2}) than with it (warming by $\sim$ 4.3 W m^{-2}). In the absence of time dependence, this reversal in glaciated cloud AIE is consistent with a strong sensitivity with respect to anthropogenic solid APs of the macrophysical properties as noted above (Fig. 11b, d, h). A strong decrease in the horizontal and volumetric extent of liquid-only and glaciated clouds, from inclusion of anthropogenic INPs, in the absence of time dependence allows more incoming SW radiation to enter the climate system, hence a net warming (Fig. 12d).

For MC3E, with time dependence, inclusion of anthropogenic INPs causes an increase by about 5% in the lifetime indirect effect from glaciated clouds (Fig. 4c) whereas it decreases by about 0.5% without it (Fig. 12c). This reversal in sensitivity with respect to anthropogenic INPs of lifetime indirect effect from glaciated clouds is chiefly due a corresponding sensitivity of the

overall surface precipitation, with (~ 1% decrease, Fig. 3f) and without (~ 5% increase, Fig. 11f) time dependence. By contrast, both with and without time dependence, little sensitivity with respect to anthropogenic INPs (< 1% increase) is predicted in the albedo-emissivity indirect effect from glaciated clouds. This is explicable in terms of the corresponding sensitivities with respect to anthropogenic INPs in the mean sizes of the cloud droplets and ice-crystals without time dependence (Fig. 9c). It is further predicted that in such convective clouds, without time dependence, AIEs from mixed-phase clouds cancels out the corresponding AIEs on ice-only clouds, causing relatively weak radiative response from glaciated clouds than liquid-only clouds (Fig. 12c). However, this cancelling out is relatively weak in the presence of time dependence (Fig. 4c), prevailing the lifetime indirect effect from glaciated clouds.

To summarise, for supercooled layer clouds in APPRAISE, overall, no significant impact from the presence of time dependent INP freezing is predicted on the net AIEs (Fig. 4a) from inclusion of anthropogenic solid APs. However, a strong reversal in the sensitivities of the AIEs from glaciated and liquid-only clouds is seen, with respect to inclusion of anthropogenic INPs, mainly because the corresponding aerosol sensitivities of their macrophysical properties, as discussed in Sec. 4.3.3. By contrast, for the deep convective clouds in MC3E, when time dependence is included in the control run, anthropogenic solid APs cause a strong climate warming (Fig. 4c, Sec. 4.1.3), mainly from glaciated clouds, which, in the absence of time dependence would damped by 80% (Fig. 12c, Sec. 4.3.3).
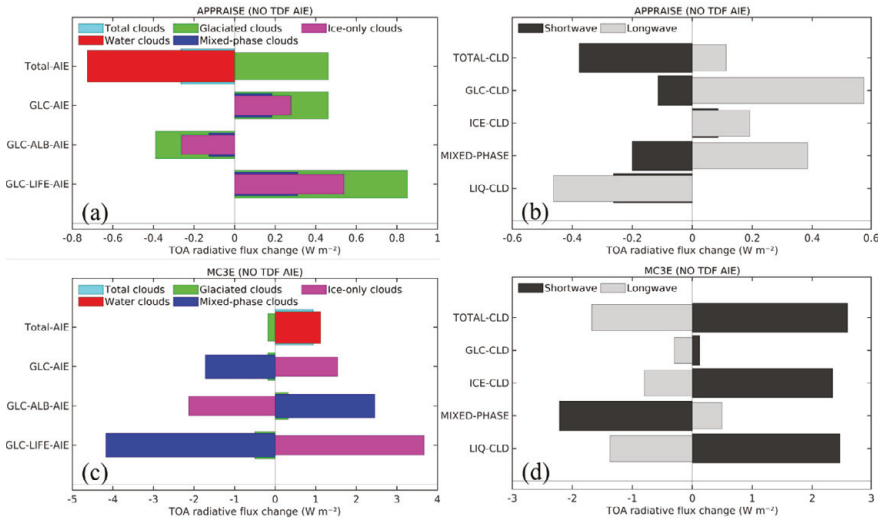
Fig. 12. *Net aerosol indirect effects at the TOA from solid aerosols on glaciated clouds predicted from Test A and Test B (Sec. 3) from the 'no time dependent INP' simulations of (a) APPRAISE and (c) MC3E cases. Corresponding changes in the shortwave and longwave components of radiation, unconditionally averaged over the whole domain, are shown for (b) APPRAISE and (d) MC3E cases. Here, abbreviations: GLC-AIE= Glaciated Clouds AIE, GLC-ALB-AIE= Glaciated cloud Albedo-Emissivity AIE, GLC-LIFE-AIE= Glaciated Cloud Lifetime AIE.*

5. Summary and Conclusions

In the present study, two cloud cases have been simulated (APPRAISE and MC3E) numerically using a mesoscale numerical model (AC) to evaluate the responses of cloud micro- and macrophysical properties from inclusion of anthropogenic solid APs. Also, the changes in these properties of the simulated clouds, due to changes in solid aerosol loading, are predicted to significantly alter their radiative properties (e.g., albedo and lifetime AIEs). To estimate these indirect effects on the simulated clouds (APPRAISE and MC3E), various sensitivity tests have been performed (Sec. 3). Moreover, this study also investigates the impact from ice formation processes such as the time dependent INP freezing and SIP on the simulated net AIEs.

In both simulated cases (APPRIASE and MC3E), through their CCN activity, inclusion of anthropogenic solid APs in the control run causes an increase by about 15% in the number concentration of cloud-droplets whereas their mean sizes are predicted to decrease by a similar fraction. This can be mainly attributed to the fact that in the polluted environment, the extra cloud droplets compete more for the available vapor and hence are smaller. Also, at levels warmer than -15°C (in APPRAISE) and -36°C (in MC3E), inclusion of anthropogenic solid APs causes a little increase ($\sim$ 1-3%) in the overall ice concentrations, which is explicable in terms of their enhanced INP activity at these levels.

In MC3E, on the other hand, at levels colder than -36°C, inclusion of anthropogenic INPs in the control run causes a decrease by about 20% in the overall ice concentration. This can be chiefly attributed to less upwelling of supercooled cloud droplets at these levels due to relatively weaker ascent by $\sim$ 5%) and hence less homogeneous freezing, when anthropogenic INPs are included. This proved the hypothesis that anthropogenically increased solid APs modifies glaciated clouds via homogeneous ice nucleation. Also, in the polluted environment, the masses of cloud-liquid and ice-crystal increases by about 1% (in APPRAISE) and about 20% (in MC3E) whereas the masses of rain, snow and graupel decreases by about 5-10% from anthropogenically boosted INPs in both cases.

Additionally, for both cases, the changes in the cloud droplets and ice properties in the polluted environment also alter the overall surface accumulation of precipitation. For APPRAISE, inclusion of anthropogenic solid APs in the control run causes an increase by about 1% in the overall surface precipitation, mainly from the ice-crystal process ($\sim$ 10% increase) whereas the contribution to the overall surface precipitation from the warm rain process is weakened by about 8%. By contrast, for MC3E, the overall surface precipitation, from inclusion of anthropogenic INPs, is weakened by 1.5%, due to weaker warm rain and ice-crystal process. More numerous cloud droplets and ice crystals are smaller, with more intense competition for moisture, curbing growth to precipitation, both in APPRAISE (warm rain) and MC3E (both warm rain and cold rain).

Moreover, for both APPRAISE and MC3E, inclusion of anthropogenic INPs increases the cloud extents (1-3%) and optical thicknesses (4% and 30% respectively) due to weakened removal of condensate by precipitation. All these macrophysical properties are predicted to greatly affect the downward SW and outgoing LW radiation at the TOA and hence their radiative properties.

The conclusions of the present study are as follows:
1) For the simulated supercooled layer clouds in APPRAISE at the TOA:
   i. Inclusion of anthropogenic INPs causes a net cooling of the climate system with a net AIE of about -0.39 W m^{-2} at the TOA. This net AIE is mainly dominated by the albedo-

emissivity AIE from glaciated clouds (~ -0.3 W m^{-2}), chiefly because increased reflectivity of such clouds as they consist of more numerous cloud particles (higher by $\sim 20\%$) with slightly higher ($\sim 5\%$) water contents of cloud-liquid and cloud-ice. By contrast, the lifetime AIE (~ -0.018 W m^{-2}) of such clouds is relatively weak due to corresponding weakness in the aerosol-sensitivity of their extents, as noted above.

ii. For such stratiform clouds, in the presence of anthropogenic solid APs, artificially prohibiting SIP causes little impact ($\sim 2\%$ decrease) on the net AIE (~ -0.39 W m^{-2}), mainly due to weakness of SIP processes in such layer clouds (Wa23). Furthermore, without SIP, similar sensitivity ($\sim 2\%$ decrease) of the SW and LW radiative fluxes is seen with respect to anthropogenic INPs.

iii. Also, when SIP is prohibited from the control runs, anthropogenically boosted INPs form about 50% in the net AIE, chiefly due to the albedo-emissivity indirect effect of glaciated clouds (-0.8 W m^{-2}). This is explicable in terms of a higher sensitivity with respect to anthropogenic solid APs of the microphysical properties of these clouds (± 10-20% change) than their extents ($< \pm 2\%$ change), as noted in Sec. 4.2. Also, the net AIE from glaciated clouds is compensated by the corresponding AIE from liquid-only clouds (~ 0.4 W m^{-2}).

iv. Moreover, when time dependent INP freezing is prohibited from the control runs, anthropogenic solid APs causes a net cooling (by -0.26 W m^{-2}) of the climate system, which is about 65% of the net AIE from the control run. Also, without time dependence, this cooling is chiefly due to artificially boosted reflection of the incoming SW radiation from liquid-only (~ -0.26 W m^{-2}) and mixed-phase clouds (~ -0.2 W m^{-2}) as they are optically thicker (Sec. 4.2.3).

2) For the simulated deep convective clouds in MC3E at the TOA:

i. In the control run, anthropogenically boosted INPs causes a net warming of the climate system, with a net AIE of about 4.5 W m^{-2} (Fig. 4c) which is consistent with the previous modelling study by Fan *et al*. (2012). Moreover, this net AIE is mainly from the lifetime AIE of glaciated clouds (~ 4.3 W m^{-2}) as anthropogenic solid APs causes less extensive mixed-phase clouds, allowing more incoming SW flux (~ 5.5 W m^{-2}) to enter the climate system as well as being optically thicker, these clouds cause more re-emission of LW flux (~ 7 W m^{-2}) to the surface (Fig. 4d).

ii. Also, this net warming from mixed-phase clouds (12.5 W m^{-2}) is compensated by a net cooling from ice-only clouds (~ -8.4 W m^{-2}), mainly because with extra INPs, ice-only clouds are denser and horizontally extensive, reflecting more downward SW flux to space.

iii. For such convective clouds, when SIP is artificially prohibited, anthropogenic INPs causes a warming (~ 2.2 W m^{-2}) of the climate system, which is 48% of the net AIE with SIP (~ 4.58 W m^{-2}).

iv. Moreover, in the absence of SIP, the net AIE is mainly dominated by the lifetime AIE from glaciated clouds (7 W m^{-2}). This is chiefly because in the absence of SIP, anthropogenic INPs cause glaciated clouds to grow less extensive and optically thinner (~ 2-10% decrease), allowing more incoming SW flux (~ 9 W m^{-2}) to enter the climate system.

v. Furthermore, for such convective clouds, when time dependent INP freezing is artificially prohibited from the control runs, anthropogenically increased INPs causes a strong aerosol-sensitivity ($\sim 80\%$ less warming) of the net AIE (4.58 W m^{-2}). This is mainly attributed to a decrease by about 105% in the net AIE from glaciated clouds, when anthropogenic INPs are included, in the absence of time dependence.

vi. Also, when time dependence is prohibited from the control run, anthropogenic INPs causes an increase by about 70% in the net AIE from liquid-only clouds. This is mainly because anthropogenic INPs cause a decrease ($\sim 0.6\%$) in the horizontal extent of these clouds,

without time dependence than with it (~ 0.05% increase), allowing more incoming SW flux to enter the climate system.

vii. However, this aerosol-sensitivity of the net AIE from liquid-only clouds (~ 70% increase) is much less than that from glaciated clouds (~ 105% decrease) (Figs. 4c and 12c).

viii. Also, in the absence of time dependence, ice-only clouds cause a net solar warming (~ 2.3 W m^{-2}) of the climate system mainly because they are horizontally less extensive (Fig. 11b). However, this warming from ice-only clouds is cancelled out by more reflection of incoming SW flux (~ −2.2 W m^{-2}) to space from mixed-phase clouds due to increased mass of cloud condensate in the upper half of the mixed-phase levels (Sec. 4.3.2).

For supercooled stratiform clouds in APPRAISE with tops warmer than −15°C, anthropogenically boosted INPs cause a weaker sensitivity of the net AIE (weak cooling), which is mainly dominated by the albedo-emissivity indirect effect from glaciated clouds. This is chiefly because the microphysical properties of such clouds show the relatively high sensitivity (± 20% change) than their macrophysical properties (± 5% change), with respect to anthropogenic solid APs. Furthermore, in such layer clouds, overall, the impact on the net AIE predicted in the control run, from inclusion of the ice formation processes such as SIP and time dependence INP freezing, is relatively weak, forming less than 30% of the net AIE. For APPRAISE, the layer clouds were thin that causes very light precipitation (~ 0.2 mm/hr). This causes SIP to be relatively weak in such clouds and hence weak lifetime AIE. The opposite is true for MC3E.

On the other hand, for the deep convective clouds in MC3E with tops reaching up to −60°C, the lifetime indirect effect from glaciated clouds dominates the overall AIE in the control run. This can be chiefly attributed to the relatively high sensitivity of the extents and of the optical thickness of these clouds (Sec. 4.1.3), with respect to anthropogenic INPs. This can be mainly because of weakening in the precipitation from both warm rain and cold rain processes (~ 2% decrease), from inclusion of anthropogenic INPs, giving rise to their lifetime indirect effect. Furthermore, for such deep convective clouds, in the presence of SIP and time dependent INP freezing, anthropogenically increased solid APs boosts the net warming by more than 50%, mainly due to corresponding radiative responses of glaciated clouds. In the mixed-phase regions of such convective clouds, the rapid glaciation due to various SIP mechanisms reduces the overall cloud extents and hence allowing more incoming SW flux to enter the climate system in the present-day conditions, causing a strong climate warming. These results are consistent with the previous modelling studies by Young *et al*. (2019) and Wa22. Hence, this study underpins the importance of these ice formation mechanisms in studying the aerosol indirect effects.

To conclude, the present study found that increasing solid aerosol loadings due to anthropogenic activities cause a moderate cooling of the climate system via supercooled stratiform clouds. However, through their indirect effects on the deep convective clouds in MC3E, anthropogenic solid aerosols cause a strong solar warming at the TOA. Furthermore, for the simulated cases, both with and without SIP, the net indirect effects are mainly from glaciated clouds. The presence of SIP and time dependent INP freezing in the deep convective clouds enhances the net warming at the TOA. The same is true for the predicted net cooling from supercooled stratiform clouds (APPRAISE).

The consistency and accuracy of the results presented here are dependent on the factors such as the nature of the model, selection of parameterization schemes, assumptions considered to prescribe the aerosol loadings as well as the nature of the large scale forcing. This study finds

the relative importance of ice initiation processes such as time dependent heterogeneous ice nucleation and SIP in modifying the cloud radiative properties. However, the role of various SIP mechanisms may differ among different cloud types due to their dependency on factors such as droplet sizes, vertical velocity, hydrometeor fall speeds and temperature as well as of time dependent INP freezing that is dependent on freezing temperature and surface area of freezing AP. This suggests the need of more accurate laboratory experiments and theoretical formulations of these ice initiation processes to represent them precisely in atmospheric models.

Acknowledgments

Data availability statement

The codes representing all four mechanisms of SIP, and original and modified empirical parameterization in AC and postprocessing scripts for both simulated cases are freely available at https://doi.org/10.5281/zenodo.7654587 and at https://doi.org/10.5281/zenodo.8156134. For the simulated MC3E clouds, the observational datasets for microphysical cloud properties are obtained from https://ghrc.nsstc.nasa.gov/home/field-campaigns/mc3e/data_access and radar data and the LSF tendencies are obtained from https://adc.arm.gov/discovery/. The sounding profiles for the simulation of APPRAISE clouds are taken from the ECMWF ERA5 data over the study domain whereas the observations for cloud microphysical properties are obtained from Crosier *et al*. (2011) and Westbrook and Illingworth (2013).

References

Bellouin, N., Quaas, J., Gryspeerdt, E., Kinne, S., Stier, P., Watson-Parris, D., Boucher, O., Carslaw, K.S., Christensen, M., Daniau, A.L. and Dufresne, J.L., 2020. Bounding global aerosol radiative forcing of climate change. *Reviews of Geophysics*, *58*(1), p.e.2019RG000660.

Boucher, O., D. Randall, P. Artaxo, C. Bretherton, G. Feingold, P. Forster, V.-M. Kerminen, Y. Kondo, H. Liao, U. Lohmann, P. Rasch, S.K. Satheesh, S. Sherwood, B. Stevens and X.Y. Zhang, 2013: Clouds and Aerosols. In: Climate Change 2013: The Physical Science Basis. Contribution of Working Group I to the Fifth Assessment Report of the Intergovernmental Panel on Climate Change [Stocker, T.F., D. Qin, G.-K. Plattner, M. Tignor, S.K. Allen, J. Boschung, A. Nauels, Y. Xia, V. Bex and P.M. Midgley (eds.)]. Cambridge University Press, Cambridge, United Kingdom and New York, NY, USA.

Chen, W.T., Lee, Y.H., Adams, P.J., Nenes, A. and Seinfeld, J.H., 2010. Will black carbon mitigation dampen aerosol indirect forcing? *Geophysical Research Letters*, *37*(9).

Crosier, J., Bower, K.N., Choularton, T.W., Westbrook, C.D., Connolly, P.J., Cui, Z.Q., Crawford, I.P., Capes, G.L., Coe, H., Dorsey, J.R. and Williams, P.I., 2011. Observations of ice multiplication in a weakly convective cell embedded in supercooled mid-level stratus. *Atmospheric Chemistry and Physics*, *11*(1), pp.257-273.

Cziczo, D.J., Froyd, K.D., Gallavardin, S.J., Moehler, O., Benz, S., Saathoff, H. and Murphy, D.M., 2009. Deactivation of ice nuclei due to atmospherically relevant surface coatings. *Environmental Research Letters*, *4*(4), p.044013.

Deshmukh, A., Phillips, V.T., Bansemer, A., Patade, S. and Waman, D., 2022. New empirical formulation for the sublimational breakup of graupel and dendritic snow. *Journal of the Atmospheric Sciences*, *79*(1), pp.317-336.

Eidhammer T, DeMott PJ, Prenni AJ, Petters MD, Twohy CH, Rogers DC, Stith J, Heymsfield A, Wang Z, Pratt KA, Prather KA. Ice initiation by aerosol particles: Measured and predicted ice nuclei concentrations versus measured ice crystal concentrations in an orographic wave cloud. Journal of the Atmospheric Sciences. 2010 Aug;67(8):2417-36.

Fan, J., Leung, L.R., Rosenfeld, D., Chen, Q., Li, Z., Zhang, J. and Yan, H., 2013. Microphysical effects determine macrophysical response for aerosol impacts on deep convective clouds. *Proceedings of the National Academy of Sciences*, *110*(48), pp.E4581-E4590.

Hoppel, W.A., Fitzgerald, J.W., Frick, G.M., Larson, R.E. and Mack, E.J., 1990. Aerosol size distributions and optical properties found in the marine boundary layer over the Atlantic Ocean. *Journal of Geophysical Research: Atmospheres*, *95*(D4), pp.3659-3686.

Jakobsson, J.K., Waman, D.B., Phillips, V.T. and Bjerring Kristensen, T., 2022. Time dependence of heterogeneous ice nucleation by ambient aerosols: laboratory observations and a formulation for models. *Atmospheric Chemistry and Physics*, *22*(10), pp.6717-6748.

Jensen, M.P., Petersen, W.A., Bansemer, A., Bharadwaj, N., Carey, L.D., Cecil, D.J., Collis, S.M., Del Genio, A.D., Dolan, B., Gerlach, J. and Giangrande, S.E., 2016. The midlatitude continental convective clouds experiment (MC3E). *Bulletin of the American Meteorological Society*, *97*(9), pp.1667-1686.

Kanji, Z.A., Ladino, L.A., Wex, H., Boose, Y., Burkert-Kohn, M., Cziczo, D.J. and Krämer, M., 2017. Overview of ice nucleating particles. *Meteorological Monographs*, *58*, pp.1-1.

Koren, I., Remer, L.A., Altaratz, O., Martins, J.V. and Davidi, A., 2010. Aerosol-induced changes of convective cloud anvils produce strong climate warming. *Atmospheric Chemistry and Physics*, *10*(10), pp.5001-5010.

Krämer, M., Rolf, C., Luebke, A., Afchine, A., Spelten, N., Costa, A., Meyer, J., Zoeger, M., Smith, J., Herman, R.L. and Buchholz, B., 2016. A microphysics guide to cirrus clouds–Part 1: Cirrus types. *Atmospheric Chemistry and Physics*, *16*(5), pp.3463-3483.

Kudzotsa, I., Phillips, V.T., Dobbie, S., Formenton, M., Sun, J., Allen, G., Bansemer, A., Spracklen, D. and Pringle, K., 2016. Aerosol indirect effects on glaciated clouds. Part I: Model description. *Quarterly Journal of the Royal Meteorological Society*, *142*(698), pp.1958-1969.

Lasher-Trapp, S., Scott, E.L., Järvinen, E., Schnaiter, M., Waitz, F., DeMott, P.J., McCluskey, C.S. and Hill, T.C., 2021. Observations and modeling of rime splintering in Southern Ocean cumuli. *Journal of Geophysical Research: Atmospheres*, *126*(23), p.e2021JD035479.

Patade, S., Phillips, V.T., Amato, P., Bingemer, H.G., Burrows, S.M., DeMott, P.J., Goncalves, F.L., Knopf, D.A., Morris, C.E., Alwmark, C. and Artaxo, P., 2021. Empirical formulation for multiple groups of primary biological ice nucleating particles from field observations over Amazonia. *Journal of the Atmospheric Sciences*, *78*(7), pp.2195-2220.

Patade, S., Waman, D., Deshmukh, A., Gupta, A.K., Jadav, A., Phillips, V.T., Bansemer, A., Carlin, J. and Ryzhkov, A., 2022. The influence of multiple groups of biological ice nucleating particles on microphysical properties of mixed-phase clouds observed during MC3E. *Atmospheric Chemistry and Physics*, *22*(18), pp.12055-12075.

Penner, J.E., Andreae, M.O., Annegarn, H., Barrie, L., Feichter, J., Hegg, D., Jayaraman, A., Leaitch, R., Murphy, D., Nganga, J. and Pitari, G., 2001. Aerosols, their direct and indirect effects. In *Climate change 2001: the scientific basis. Contribution of working group I to the third assessment report of the intergovernmental panel on climate change* (pp. 289-348). Cambridge University Press.

Phillips, V.T., Andronache, C., Christner, B., Morris, C.E., Sands, D.C., Bansemer, A., Lauer, A., McNaughton, C. and Seman, C., 2009. Potential impacts from biological aerosols on ensembles of continental clouds simulated numerically. *Biogeosciences*, *6*(6), pp.987-1014.

Phillips, V.T., Demott, P.J., Andronache, C., Pratt, K.A., Prather, K.A., Subramanian, R. and Twohy, C., 2013. Improvements to an empirical parameterization of heterogeneous ice nucleation and its comparison with observations. *Journal of the Atmospheric Sciences*, *70*(2), pp.378-409.

Phillips, V.T., Formenton, M., Bansemer, A., Kudzotsa, I. and Lienert, B., 2015. A parameterization of sticking efficiency for collisions of snow and graupel with ice crystals: Theory and comparison with observations. *Journal of the Atmospheric Sciences*, *72*(12), pp.4885-4902.

Phillips, V.T., Formenton, M., Kanawade, V.P., Karlsson, L.R., Patade, S., Sun, J., Barthe, C., Pinty, J.P., Detwiler, A.G., Lyu, W. and Tessendorf, S.A., 2020. Multiple environmental influences on the lightning of cold-based continental cumulonimbus clouds. Part I: Description and validation of model. *Journal of the Atmospheric Sciences*, *77*(12), pp.3999-4024.

Phillips, V.T., Yano, J.I., Formenton, M., Ilotoviz, E., Kanawade, V., Kudzotsa, I., Sun, J., Bansemer, A., Detwiler, A.G., Khain, A. and Tessendorf, S.A., 2017. Ice multiplication by breakup in ice–ice collisions. Part II: Numerical simulations. *Journal of the Atmospheric Sciences*, *74*(9), pp.2789-2811.

Waman, D., Deshmukh, A., Jadav, A., Patade, S., Gautam, M., Phillips, V., Bansemer, A. and Jakobsson, J., 2023. Effects from time dependence of ice nucleus activity for contrasting cloud types. *Journal of the Atmospheric Sciences*.

Waman, D., Patade, S., Jadav, A., Deshmukh, A., Gupta, A.K., Phillips, V.T., Bansemer, A. and DeMott, P.J., 2022. Dependencies of Four Mechanisms of Secondary Ice Production on Cloud-Top Temperature in a Continental Convective Storm. *Journal of the Atmospheric Sciences*, *79*(12), pp.3375-3404.

Field, P.R., Lawson, R.P., Brown, P.R., Lloyd, G., Westbrook, C., Moisseev, D., Miltenberger, A., Nenes, A., Blyth, A., Choularton, T. and Connolly, P., 2017. Secondary ice production: Current state of the science and recommendations for the future. *Meteorological Monographs*, *58*, pp.7-1.

Gettelman, A., Liu, X., Barahona, D., Lohmann, U. and Chen, C., 2012. Climate impacts of ice nucleation. *Journal of geophysical research: Atmospheres*, *117*(D20).

Phillips, V.T., Andronache, C., Morris, C.E. and Sands, D.C., 2008. Impacts from ice-nucleating bacteria on deep convection: implications for the biosphere-atmosphere interaction in climate change. *Biogeosciences Discussions*, *5*(2), pp.1035-1067.

Hallett, J. and Mossop, S.C., 1974. Production of secondary ice particles during the riming process. *Nature*, *249*(5452), pp.26-28.

Twomey, S.J.A.E., 1974. Pollution and the planetary albedo. *Atmospheric Environment (1967)*, *8*(12), pp.1251-1256.

Mossop, S.C., 1976. Production of secondary ice particles during the growth of graupel by riming. *Quarterly Journal of the Royal Meteorological Society*, *102*(431), pp.45-57.

Hobbs, P.V., Politovich, M.K. and Radke, L.F., 1980. The structures of summer convective clouds in eastern Montana. I: Natural clouds. *Journal of Applied Meteorology and Climatology*, *19*(6), pp.645-663.

Oraltay, R.G. and Hallett, J.O.H.N., 1989. Evaporation and melting of ice crystals: A laboratory study. *Atmospheric research*, *24*(1-4), pp.169-189.

DeMott, P.J., 1990. An exploratory study of ice nucleation by soot aerosols. *Journal of Applied Meteorology and Climatology*, *29*(10), pp.1072-1079.

Dong, Y., Oraltay, R.G. and Hallett, J., 1994. Ice particle generation during evaporation. *Atmospheric research*, *32*(1-4), pp.45-53.

DeMott, P.J., Rogers, D.C. and Kreidenweis, S.M., 1997. The susceptibility of ice formation in upper tropospheric clouds to insoluble aerosol components. *Journal of Geophysical Research: Atmospheres*, *102*(D16), pp.19575-19584.

Bacon, N.J., Swanson, B.D., Baker, M.B. and Davis, E.J., 1998. Breakup of levitated frost particles. *Journal of Geophysical Research: Atmospheres*, *103*(D12), pp.13763-13775.

Jennings, S.G., Geever, M. and O'Connor, T.C., 1998. Coastal CCN measurements at Mace Head with enhanced concentrations in strong winds. *Atmospheric research*, *46*(3-4), pp.243-252.

Freidenreich, S.M. and Ramaswamy, V., 1999. A new multiple-band solar radiative parameterization for general circulation models. *Journal of Geophysical Research: Atmospheres*, *104*(D24), pp.31389-31409.

Chen, T., Rossow, W.B. and Zhang, Y., 2000. Radiative effects of cloud-type variations. *Journal of climate*, *13*(1), pp.264-286.

Haywood, J. and Boucher, O., 2000. Estimates of the direct and indirect radiative forcing due to tropospheric aerosols: A review. *Reviews of geophysics*, *38*(4), pp.513-543.

Koop, T., Luo, B., Tsias, A. and Peter, T., 2000. Water activity as the determinant for homogeneous ice nucleation in aqueous solutions. *Nature*, *406*(6796), pp.611-614.

Lohmann, U. and Feichter, J., 2001. Can the direct and semi-direct aerosol effect compete with the indirect effect on a global scale? *Geophysical Research Letters*, *28*(1), pp.159-161.

Johnson, B.T., Shine, K.P. and Forster, P.M., 2004. The semi-direct aerosol effect: Impact of absorbing aerosols on marine stratocumulus. *Quarterly Journal of the Royal Meteorological Society*, *130*(599), pp.1407-1422.

Cantrell, W. and Heymsfield, A., 2005. Production of ice in tropospheric clouds: A review. *Bulletin of the American Meteorological Society*, *86*(6), pp.795-808.

Lohmann, U. and Feichter, J., 2005. Global indirect aerosol effects: a review. *Atmospheric Chemistry and Physics*, *5*(3), pp.715-737.

Grabowski, W.W., 2006. Indirect impact of atmospheric aerosols in idealized simulations of convective–radiative quasi equilibrium. *Journal of climate*, *19*(18), pp.4664-4682.

Lohmann, U., 2006. Aerosol effects on clouds and climate. *Space Science Reviews*, *125*, pp.129-137.

Ming, Y., Ramaswamy, V., Donner, L.J. and Phillips, V.T., 2006. A new parameterization of cloud droplet activation applicable to general circulation models. *Journal of the atmospheric sciences*, *63*(4), pp.1348-1356.

Quaas, J., Boucher, O. and Lohmann, U., 2006. Constraining the total aerosol indirect effect in the LMDZ and ECHAM4 GCMs using MODIS satellite data. *Atmospheric Chemistry and Physics*, *6*(4), pp.947-955.

Petters, M.D. and Kreidenweis, S.M., 2007. A single parameter representation of hygroscopic growth and cloud condensation nucleus activity. *Atmospheric Chemistry and Physics*, *7*(8), pp.1961-1971.

Phillips, V.T., Donner, L.J. and Garner, S.T., 2007. Nucleation processes in deep convection simulated by a cloud-system-resolving model with double-moment bulk microphysics. *Journal of the atmospheric sciences*, *64*(3), pp.738-761.

Hill, A.A. and Dobbie, S., 2008. The impact of aerosols on non-precipitating marine stratocumulus. II: The semi-direct effect. *Quarterly Journal of the Royal Meteorological Society: A journal of the atmospheric sciences, applied meteorology and physical oceanography*, *134*(634), pp.1155-1165.

Koch, D. and Del Genio, A.D., 2010. Black carbon semi-direct effects on cloud cover: review and synthesis. *Atmospheric Chemistry and Physics*, *10*(16), pp.7685-7696.

Bollasina, M.A., Ming, Y. and Ramaswamy, V., 2011. Anthropogenic aerosols and the weakening of the South Asian summer monsoon. *science*, *334*(6055), pp.502-505.

Morrison, H. and Grabowski, W.W., 2011. Cloud-system resolving model simulations of aerosol indirect effects on tropical deep convection and its thermodynamic environment. *Atmospheric Chemistry and Physics*, *11*(20), pp.10503-10523.

Hoose, C. and Möhler, O., 2012. Heterogeneous ice nucleation on atmospheric aerosols: a review of results from laboratory experiments. *Atmospheric Chemistry and Physics*, *12*(20), pp.9817-9854.

Takemura, T., 2012. Distributions and climate effects of atmospheric aerosols from the preindustrial era to 2100 along Representative Concentration Pathways (RCPs) simulated using the global aerosol model SPRINTARS. *Atmospheric Chemistry and Physics*, *12*(23), pp.11555-11572.

Westbrook, C.D. and Illingworth, A.J., 2013. The formation of ice in a long-lived supercooled layer cloud. *Quarterly Journal of the Royal Meteorological Society*, *139*(677), pp.2209-2221.

Phillips, V.T., Khain, A., Benmoshe, N. and Ilotoviz, E., 2014. Theory of time-dependent freezing. Part I: Description of scheme for wet growth of hail. *Journal of the Atmospheric Sciences*, *71*(12), pp.4527-4557.

Wang, Y., Lee, K.H., Lin, Y., Levy, M. and Zhang, R., 2014. Distinct effects of anthropogenic aerosols on tropical cyclones. *Nature Climate Change*, *4*(5), pp.368-373.

Lawson, R.P., Woods, S. and Morrison, H., 2015. The microphysics of ice and precipitation development in tropical cumulus clouds. *Journal of the Atmospheric Sciences*, *72*(6), pp.2429-2445.

Christensen, M.W., Chen, Y.C. and Stephens, G.L., 2016. Aerosol indirect effect dictated by liquid clouds. *Journal of Geophysical Research: Atmospheres*, *121*(24), pp.14-636.

Kudzotsa, I., Phillips, V.T. and Dobbie, S., 2016. Aerosol indirect effects on glaciated clouds. Part 2: Sensitivity tests using solute aerosols. *Quarterly Journal of the Royal Meteorological Society*, *142*(698), pp.1970-1981.

Phillips, V.T., Yano, J.I. and Khain, A., 2017. Ice multiplication by breakup in ice–ice collisions. Part I: Theoretical formulation. *Journal of the Atmospheric Sciences*, *74*(6), pp.1705-1719.

Lawson, P., Gurganus, C., Woods, S. and Bruintjes, R., 2017. Aircraft observations of cumulus microphysics ranging from the tropics to midlatitudes: Implications for a "new" secondary ice process. *Journal of the Atmospheric Sciences*, *74*(9), pp.2899-2920.

Kudzotsa, I., Phillips, V.T. and Dobbie, S., 2018. Effects of solid aerosols on partially glaciated clouds. *Quarterly Journal of the Royal Meteorological Society*, *144*(717), pp.2634-2649.

Phillips, V.T., Patade, S., Gutierrez, J. and Bansemer, A., 2018. Secondary ice production by fragmentation of freezing drops: Formulation and theory. *Journal of the Atmospheric Sciences*, *75*(9), pp.3031-3070.

Toll, V., Christensen, M., Quaas, J. and Bellouin, N., 2019. Weak average liquid-cloud-water response to anthropogenic aerosols. *Nature*, *572*(7767), pp.51-55.

James, R.L., Phillips, V.T. and Connolly, P.J., 2021. Secondary ice production during the break-up of freezing water drops on impact with ice particles. *Atmospheric Chemistry and Physics*, *21*(24), pp.18519-18530.

Martanda, G., 2022: Fragmentation in graupel-snow collisions. M.S. thesis, Dept. of Physical Geography and Ecosystem Science, Lund University, 47 pp., http://lup.lub.lu.se/studentpapers/record/9087233.

Phillips, V.T. and Patade, S., 2022. Multiple Environmental Influences on the Lightning of Cold-Based Continental Convection. Part II: Sensitivity Tests for Its Charge Structure and Land–Ocean Contrast. *Journal of the Atmospheric Sciences*, *79*(1), pp.263-300.

Avhandlingar från Institutionen för naturgeografi och ekosystemanalys (INES), Lunds universitet

----

Dissertations from Department of Physical Geography and Ecosystem Science, University of Lund

Martin Sjöström, 2012: Satellite remote sensing of primary production in semi-arid Africa.

Zhenlin Yang, 2012: Small-scale climate variability and its ecosystem impacts in the sub-Arctic.

Ara Toomanian, 2012: Methods to improve and evaluate spatial data infrastructures.

Michal Heliasz, 2012: Spatial and temporal dynamics of subarctic birch forest carbon exchange.

Abdulghani Hasan, 2012: Spatially distributed hydrological modelling: wetness derived from digital elevation models to estimate peatland carbon.

Julia Bosiö, 2013: A green future with thawing permafrost mires?: a study of climate-vegetation interactions in European subarctic peatlands. (Lic.)

Anders Ahlström, 2013: Terrestrial ecosystem interactions with global climate and socio-economics.

Kerstin Baumanns, 2013: Drivers of global land use change: are increasing demands for food and bioenergy offset by technological change and yield increase? (Lic.)

Yengoh Genesis Tambang, 2013: Explaining agricultural yield gaps in Cameroon.

Jörgen Olofsson, 2013: The Earth: climate and anthropogenic interactions in a long time perspective.

David Wårlind, 2013: The role of carbon-nitrogen interactions for terrestrial ecosystem dynamics under global change: a modelling perspective.

Elin Sundqvist, 2014: Methane exchange in a boreal forest: the role of soils, vegetation and forest management.

Julie Mari Falk, 2014: Plant-soil-herbivore interactions in a high Arctic wetland: feedbacks to the carbon cycle.

Finn Hedefalk, 2014: Life histories across space and time: methods for including geographic factors on the micro-level in longitudinal demographic research. (Lic.)

Sadegh Jamali, 2014: Analyzing vegetation trends with sensor data from earth observation satellites.

Cecilia Olsson, 2014: Tree phenology modelling in the boreal and temperate climate zones : timing of spring and autumn events.

Jing Tang, 2014: Linking distributed hydrological processes with ecosystem vegetation dynamics and carbon cycling: modelling studies in a subarctic catchment of northern Sweden.

Wenxin Zhang, 2015: The role of biogeophysical feedbacks and their impacts in the arctic and boreal climate system.

Lina Eklund, 2015: "No Friends but the Mountains": understanding population mobility and land dynamics in Iraqi Kurdistan.

Stefan Olin, 2015: Ecosystems in the Anthropocene: the role of cropland management for carbon and nitrogen cycle processes.

Thomas Möckel, 2015: Hyperspectral and multispectral remote sensing for mapping grassland vegetation.

Hongxiao Jin, 2015: Remote sensing phenology at European northern latitudes: from ground spectral towers to satellites.

Bakhtiyor Pulatov, 2015: Potential impact of climate change on European agriculture: a case study of potato and Colorado potato beetle.

Christian Stiegler, 2016: Surface energy exchange and land-atmosphere interactions of Arctic and subarctic tundra ecosystems under climate change.

Per-Ola Olsson, 2016: Monitoring insect defoliation in forests with time-series of satellite based remote sensing data: near real-time methods and impact on the carbon balance.

Jonas Dalmayne, 2016: Monitoring biodiversity in cultural landscapes: development of remote sensing- and GIS-based methods.

Balathandayuthabani Panneer Selvam, 2016: Reactive dissolved organic carbon dynamics in a changing environment: experimental evidence from soil and water.

Kerstin Engström, 2016: Pathways to future cropland: assessing uncertainties in socio-economic processes by applying a global land-use model.

Finn Hedefalk, 2016: Life paths through space and time: adding the micro-level geographic context to longitudinal historical demographic research.

Ehsan Abdolmajidi, 2016: Modeling and improving Spatial Data Infrastructure (SDI).

Giuliana Zanchi, 2016: Modelling nutrient transport from forest ecosystems to surface waters.

Florian Sallaba, 2016: Biophysical and human controls of land productivity under global change: development and demonstration of parsimonious modelling techniques.

Norbert Pirk, 2017: Tundra meets atmosphere: seasonal dynamics of trace gas exchange in the High Arctic.

Minchao Wu, 2017: Land-atmosphere interactions and regional Earth system dynamics due to natural and anthropogenic vegetation changes.

Niklas Boke-Olén, 2017: Global savannah phenology: integrating earth observation, ecosystem modelling, and PhenoCams.

Abdulhakim M. Abdi, 2017: Primary production in African drylands: quantifying supply and demand using earth observation and socio-ecological data.

Nitin Chaudhary, 2017: Peatland dynamics in response to past and potential future climate change.

Ylva van Meeningen, 2017: Is genetic diversity more important for terpene emissions than latitudinal adaptation?: using genetically identical trees to better understand emission fluctuations across a European latitudinal gradient.

Patrik Vestin, 2017: Effects of forest management on greenhouse gas fluxes in a boreal forest.

Mohammadreza Rajabi, 2017: Spatial modeling and simulation for disease surveillance.

Jan Blanke, 2018: European ecosystems on a changing planet: integrating climate change and land-use intensity data.

Min Wang, 2018: Characteristics of BVOC emissions from a Swedish boreal forest: using chambers to capture biogenic volatile organic compounds (BVOCs) from trees and forest floor.

Wilhelm Dubber, 2018: Natural and social dimensions of forest carbon accounting.

Emma Johansson, 2018: Large-Scale Land Acquisitions as a Driver of Socio-Environmental Change: From the Pixel to the Globe.

Helen Eriksson, 2018: Harmonisation of geographic data: between geographic levels, hierarcic structures and over time. (Lic.)

Zhendong Wu, 2018: Modelling the terrestrial carbon cycle: drivers, benchmarks, and model-data fusion.

Zhanzhang Cai, 2019: Vegetation observation in the big data era: Sentinel-2 data for mapping the seasonality of land vegetation.

Fabien Rizinjirabake, 2019: Dissolved organic carbon in tropical watersheds: linking field observation and ecohydrological modelling.

Jeppe Ågård Kristensen, 2019: Biogeochemistry in Subarctic birch forests: perspectives on insect herbivory.

Yanzi Yan, 2019: The role of hydrological cycle in forest ecosystems: flow path, nutrient cycling and water-carbon interaction.

George Oriangi, 2019: Urban resilience to climate change shocks and stresses in Mbale municipality in Eastern Uganda.

Alex Paulo Lubida, 2019: Investigating spatial data infrastructure planning in Tanzania using system modelling and social concepts.

Weiming Huang, 2020: Geospatial data and knowledge on the Web: knowledge-based geospatial data integration and visualisation with Semantic Web technologies.

Oskar Löfgren, 2020: Remote sensing of grassland communities: integrated effects of soil nutrients and habitat age.

Altaaf Mechiche-Alami, 2020: Food security in a changing climate: the role of cropland intensification and land acquisitions across Africa.

Helen Eriksson, 2020: Harmonisation of 3D geodata – a prerequisite for a digital information flow for applications in the planning and building sector.

Augustus Aturinde, 2020: GIS and Health: Enhancing Disease Surveillance and Intervention through Spatial Epidemiology.

Geert Hensgens, 2020: Dissolved organic matter dynamics across terrestrial and aquatic systems: sources, chemistry and microbial processing.

Enass Said Al-Kharusi, 2021: Broad-Scale Patterns in CDOM and Total Organic Matter Concentrations of Inland Waters – Insights from Remote Sensing and GIS.

Tetiana Svystun, 2021: Understanding the environmental regulation of tree phenology.

Pearl Mzobe, 2021: Bearing the brunt of warming: Interactions between carbon and hydrology in northern Sweden.

Tomas Karlsson, 2021: The variability in Salix BVOC emissions and possible consequences for managed SRC plantations.

Olive Niyomubyeyi, 2022: Metaheuristic Algorithms for Spatial Multi-Objective Decision Making.

Veronika Kronnäs, 2022: Modelling effects of climate change and forestry on weathering rates and base cation cycling in forest soils.

Didac Pascual, 2022: The Torneträsk System - A basis for predicting future subarctic ecosystems.

Bernice Hwang, 2022: Impacts and drivers of insect herbivory on element cycling in forests globally.

Joel White, 2023: The functional potential of methane producing and consuming microorganisms in a changing world.

Alexandra Pongracz, 2023: Quantifying the impact of winter warming on the Arctic carbon cycle.

Sofia Junttila, 2023: Modelling carbon uptake in Nordic forest landscapes using remote sensing.

Deepak Waman, 2023: Mechanisms for the Influence from Ice Nucleus Aerosols on Clouds and their indirect effects: Cloud modelling.